Sedimentology and Geochemistry of the 2.93 Ga Basinal Facies of the Red Lake Carbonate Platform

Munira Afroz

Submitted in partial fulfillment of the requirement for the degree of

Master of Science - Geology

Supervisor: Dr. Philip Fralick

Geology Department

Lakehead University

Thunder Bay, Ontario, P7B 5E1

Canada

April 2019

Abstract

The Mesoarchean Red Lake carbonate platform is the oldest (~2.93 Ga) known carbonate platform on Earth. It is comprised of a variety of chemical sedimentary rocks including: limestone, dolostone, chert, oxide iron formation, and sulfide iron formation. This study deals with its five different types of deeper water lithofacies, including four chemical sedimentary rocks and siliciclastic black slate, to delineate Mesoarchean ocean chemistry and comprehend the localized depositional settings. Geochemical analysis of selected elements in the chemical sediments were used to constrain depositional processes. Of these positive Eu anomalies in REE patterns suggests that the ocean was heavily influenced by hydrothermal activity and positive Ce anomalies in oxide iron formation indicate that a redoxcline existed in the depositional environment. Zirconium and hafnium in oxide facies iron formation were mostly derived from seawater, and their sorption was dependent on the rate of precipitation of iron hydroxide. Multiple sulfur isotope analyses revealed that mass-independent fractionation of sulfur was operating along with bacterial sulfate reduction, and the source of sulfur was diverse. Organic carbon isotopes increase from ~ -27 ‰ to ~ -20 ‰ up-section towards the shallow portion of the carbonate shelf, possibly reflecting the presence of anoxic phototrophs in the shallows. Inorganic carbon isotopic ratios averaging ~ -1.5 ‰ fall within the range of Archean carbonate and reflect seawater values. Also, $\delta^{18}O$ data reveals that dolomitization occurred in a freshwater influenced environment. Evidence such as increasing Mn concentration towards the carbonate platform and positive Ce anomaly in oxide iron formation, as well as redox-sensitive element enrichment in the chemical sedimentary rocks, suggests that bacterial O_2 production was somewhat active in the Mesoarchean sea. The interlayering of various types of chemical sediments at differing stratigraphic scales indicates that localized ocean chemistry changed repeatedly over both short and long time intervals. Carbonates were perhaps formed in the slightly oxic shallow water environment, while magnetite and chert were precipitated in a suboxic environment distal to any venting fluids and iron sulfides accumulated in a reducing, anoxic environment during intervals of intense venting of hydrothermal fluids. Shale was deposited as background sediment and accumulated during cessation of chemical sedimentation. Finally, the deeper water sediments repeatedly interlayered with the shallow water stromatolitic carbonate successions, which suggests multiple events of carbonate platform flooding.

Acknowledgments

First and foremost, I would like to acknowledge my supervisor Dr. Philip Fralick at Lakehead University for his consistent guidance, encouragement, and support throughout my entire thesis. Weekly discussions with him have greatly improved my understanding of Archean geology and helped me to think scientifically. Without his persistent guidance and advice, this research would not have been accomplished. I am grateful to Dr. Roger Mitchell and Dr. Mary Louise Hill for their scholarly feedback on my work. I would also like to thank the lab technicians and all other support people for helping me during the research. I should thank my lab mates who offered friendship and cooperativeness in my Thunder Bay life.

My sincere appreciation goes to Lakehead University and the European Research Council for providing funding for this research.

I am thankful to my spouse, Siddhartho Shekhar Paul for his inspiration and continuous support to keep me confident. I appreciate my family, especially my father and my elder sister, Samina Afroz who always acknowledge my effort and feel proud of me.

Table of Contents

Sedimentology and Geochemistry of the 2.93 Ga Basinal Facies of the Red Lake Carbonate Platform

List of figures

List of tables

Chapter 1: Introduction

1.1 Overview

The relationships between the primitive atmosphere, hydrosphere, and emerging life in the Archean Era have remained poorly understood. The free oxygen level in the atmosphere during this time interval was probably less than ~10^{-5} PAL (present atmospheric level), and ocean chemistry in Earth's early history was very different from today's (Kasting et al., 2001; Pavlov & Kasting, 2002; Holland, 2006). The early ocean was largely anoxic, except for possible local oxygen oases in shallow seas, and was heavily influenced by hydrothermal activity (Bau & Dulski, 1995; Bolhar et al., 2004; Holland, 2006). The composition of the Archean deeper ocean was primarily ferruginous to silica-rich (Poulton, 2011; Delvigne, 2012), while carbonate deposition was possible in the shallow ocean. Juxtapositions of these compositions were caused by the deposition of iron-rich minerals, chert, and carbonate in different parts of the ocean or at different times due to changes in water chemistry. Hence, chemical sediments can be used as a tracer, providing significant clues to ancient oceanic processes and helping to determine the specific conditions required for the precipitation of different chemical sediments. In particular, the geochemistry of rare earth elements (REE) is very important because the REE composition of sediments reflects the REEs present in the ancient ocean from which they precipitated (Shields & Stille, 2001; Kamber et al., 2004; Bolhar et al., 2004; Allwood et al., 2010; Planavsky et al., 2010). In addition, analysis of organic and inorganic $\delta^{13}C$ carbon and multiple sulfur isotopes gives insights into the ancient ocean's carbon and sulfur sources and their role in evolving biologic activity (Shegelski, 1978; Thode & Goodwin, 1983; Schidlowski, 1988; Hayes et al., 1989; Thode et al., 1991; Canfield, 2001; Ono et al., 2003).

In this connection, the Red Lake area provides ample opportunity to study the 2.93 Ga old (Corfu & Wallace, 1986) chemical sedimentary rocks deposited adjacent to the Earth's oldest known carbonate platform and to explore the deeper basinal facies. Previous work in the Red Lake area was conducted by Hofmann et al. (1985) on stromatolites, and by McIntyre & Fralick (2017), mostly on peritidal stromatolites and partially on deep subtidal to upper slope chemical sediments. No comprehensive study has been done so far on the various chemical sediments belonging to the offshore area of this carbonate platform. As a step towards rectifying the lack of in-depth research on the Red Lake platform, this study aimed to examine the sedimentological aspects and geochemistry of the ~200 m thick sedimentary assemblage beneath the carbonate platform and inter-fingering with it.

1.2 Objectives

This study focusses on the Archean chemical sediments of Earth's oldest, carbonate platform, which is at Red Lake, in northwest Ontario. It investigates the nature of the chemical and siliciclastic sediments lying below and interlayered with the carbonate portion of the platform and gathers information about the water chemistry of the ancient ocean and processes that operated during the formation of this Archean carbonate platform. The 2.93 Ga Red Lake carbonate platform consists of a variety of chemical and siliciclastic sediments including chert, oxide iron formation, sulfide iron formation, carbonate, siliciclastic black shale, sandstone, and conglomerate. This research describes the facies of the non-carbonate units and delineates the geochemistry of each facies to understand Archean ocean water chemistry and sediment-water interaction.

1.3 Regional Geology

The Superior Province is the largest known Archean craton in the world, which covers about 23% of the exposed Archean crust of the Earth (Thurston et al., 1991). It is in the south-central area of the Canadian Shield and extends from the northwestern part of Quebec to the shores of Lake Superior in Ontario and extends south into the northern fringes of USA. Card & Ciesielski (1986) divided Superior Province into various subprovinces based on unique rock types which were of mainly Meso-Neoarchean age and underwent significant deformation. The Superior Province includes the Berens River subprovince, the Sachigo subprovince, the Uchi subprovince, the English River subprovince, the Winnipeg River subprovince, the Wabigoon subprovince, the Quetico subprovince, the Western Abitibi subprovince and the Wawa subprovince (Figure 1.1) (Thurston et al., 1991).

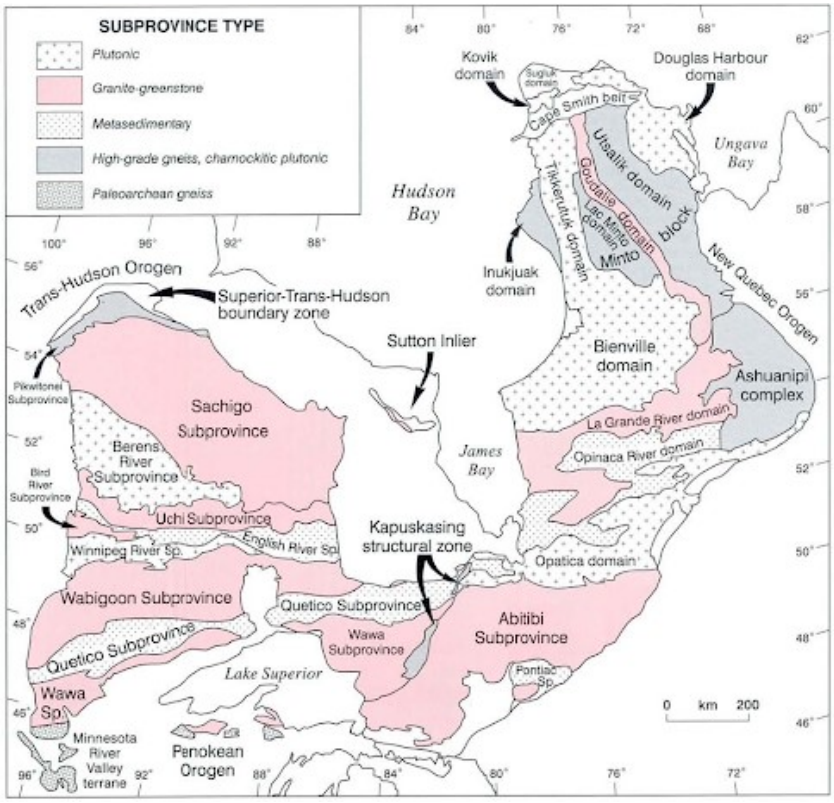

Figure 1.1: Subprovince map of Superior Province, modified from Card (1990)

The Red Lake carbonate platform occurs within the Uchi subprovince, which lies between the North Caribou Terrane and the English River subprovince (Sanborn-Barrie et al., 2000, 2001; McIntyre & Fralick, 2017). It is bounded to the south by the English River subprovince via the Sydney Lake Fault and to the north by the Berens River subprovince. In Northwestern Ontario, this subprovince is exposed for about 600 kilometers and stretches into Manitoba for about 90 kilometers until it reaches Lake Winnipeg, where it is situated beneath younger Phanerozoic rocks to the west (Thurston et al., 1991). A series of Neoarchean to Mesoarchean ca. 3000-2700 Ma rocks lie in the northwestern area of this subprovince (Corfu & Wallace, 1986; Fralick & Burton, 2008). Most parts of the Uchi subprovince had undergone greenschist to lower amphibolite facies metamorphism, while higher grade metamorphosed rocks are common at the boundaries of the major plutons and in areas with high degrees of strain (Corfu & Wallace, 1986; Thurston & Breaks, 1978). Supracrustal rocks that formed the greenstone belt of Uchi subprovince include mafic tholeiitic-komatiitic sequences to calc-alkalic and tholeiitic volcanic arc sequences, and chemical and clastic sedimentary rocks, which were deposited within and upon the volcanic assemblages (Card, 1990; Card & Ciesielski, 1986; Hollings et al., 1999).

The Uchi subprovince consists of a number of greenstone belts including the Lang Lake, the Pickle Lake, the Bee Lake, the Lake St. Joseph, the Red Lake, the Birch-Uchi, the Meen-Dempster, the Miminiska-Fort Hope and the Rice Lake greenstone belts (Thurston et al., 1991).

1.3.1 Red Lake Greenstone Belt

The Red Lake Greenstone Belt (RLGB) belongs to the Uchi subprovince of the Archean Superior Province in Northwestern Ontario and it comprises a complex succession of metavolcanic-metasedimentary rocks (Figure 1.2). The RLGB is an east trending structure marked

by steeply dipping strata of metavolcanic and metasedimentary rocks with more shallowly dipping strata present in the central and eastern part of the belt (Sanborn-Barrie et al., 2000).

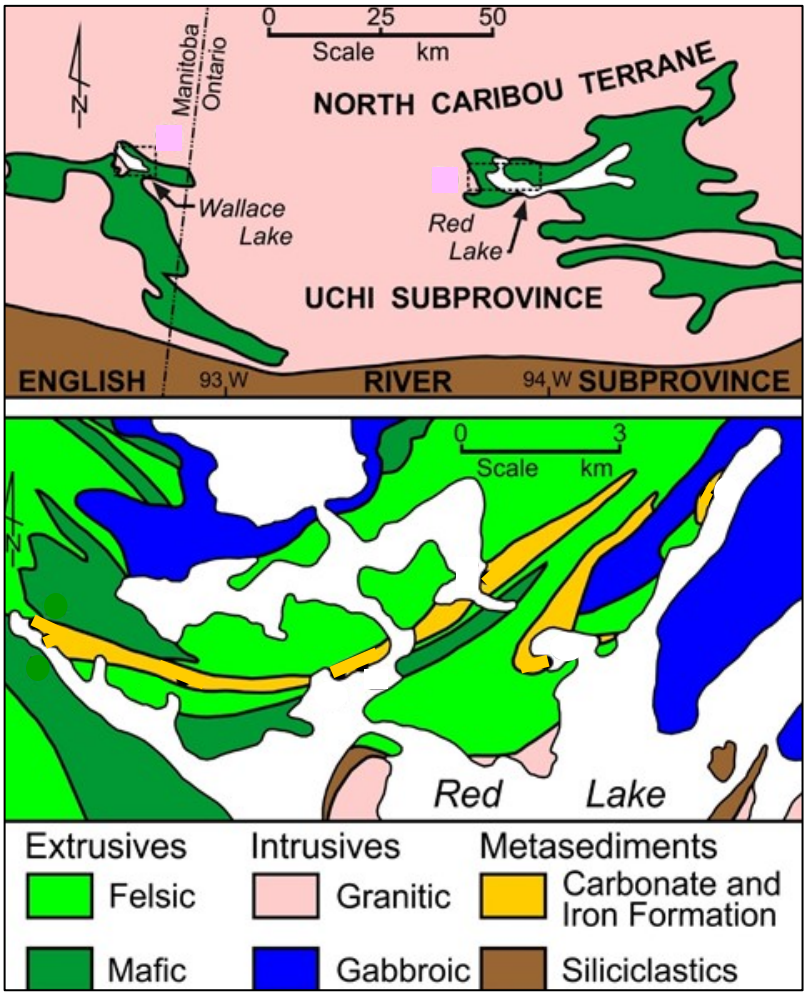

Figure 1.2: The top map shows the location of the Red Lake greenstone belt in the Uchi subprovince, and the bottom map shows different types of rock in the Red Lake greenstone belt (Satkoski et al., 2017).

The Meso-Neoarchean strata of the Red Lake greenstone belt comprise the Balmer, Ball, Slate Bay, Bruce Channel, Trout Bay, Huston, and Confederation assemblages (Figure 1.3). The Balmer assemblage (U-Pb zircon age: 2992-2960 Ma) occurs in the eastern part of the belt, where the tholeiitic to komatiitic sequence comprises tholeiitic basalts, basaltic komatiites, komatiite lava

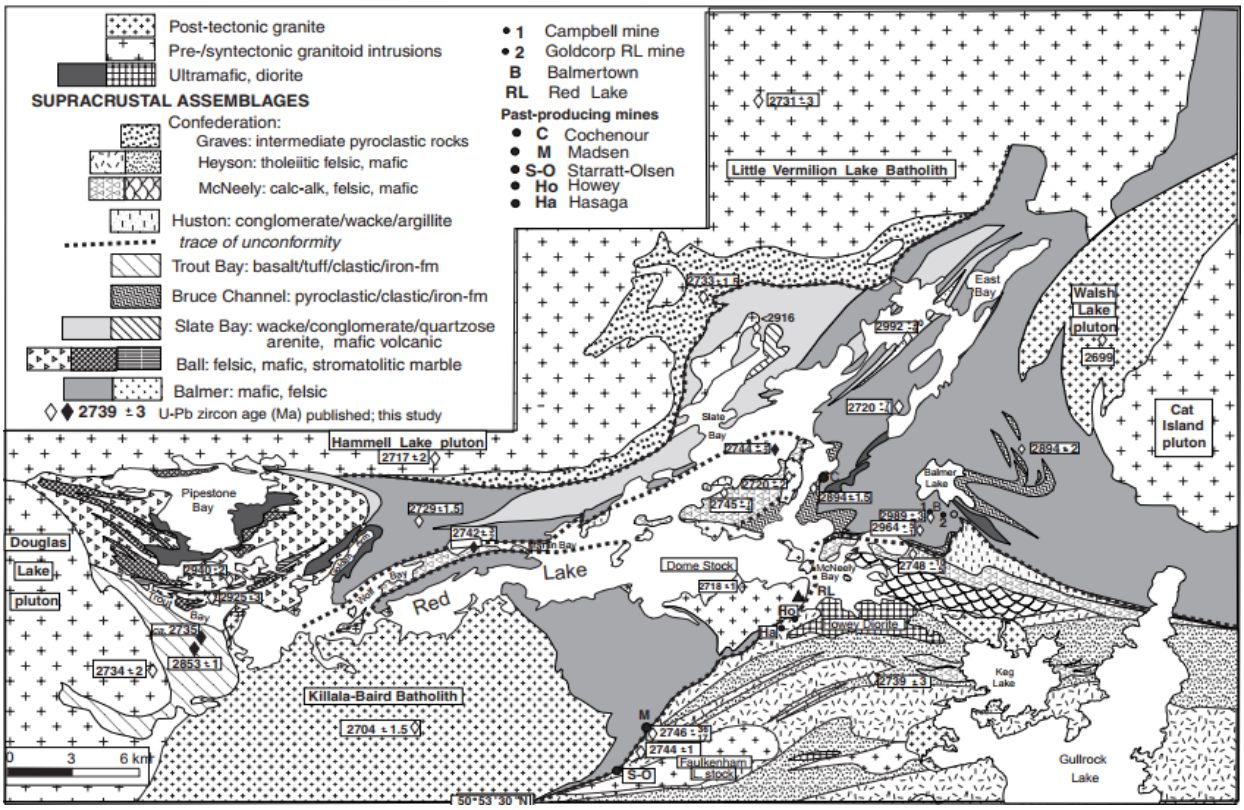

Figure 1.3: Red Lake greenstone belt with different assemblages of rocks and U-Pb ages (modified from Stott et al., 1991; Sanborn-Barrie et al., 2001).

flows, and minor interbedded units of felsic metavolcanic rocks and metasedimentary rocks (Corfu & Andrews, 1987; Hollings et al., 1999). The felsic volcanic rocks are mainly pyroclastic, with local flows and metasedimentary rocks that include argillites, cherts, banded iron formations, and ferruginous marbles as well as wacke-mudstone, with polymictic conglomerates occurring near the top of the sequence (Corfu & Wallace, 1986; Pirie, 1981; Sanborn-Barrie et al., 2000, 2001). The Ball assemblage lies in the western part of the belt, comprises ultramafic and mafic flows intercalated with volcanic rocks of intermediate and felsic composition. (Hollings et al., 1999). This assemblage predominantly consists of tholeiitic basalt flows, felsic calc-alkalic flows, pyroclastic rocks, chemical sediments, e.g. magnetite-chert, dolomite-chert, sulfides and metasedimentary siliciclastic rocks (Pirie, 1981; Hofmann et al., 1985; Corfu & Wallace, 1986;

Hollings et al., 1999; Sanborn-Barrie et al., 2000, 2001). The U-Pb zircon ages of the two rhyolitic units lies directly above and below the stromatolitic sequence are 2940-2925 Ma, respectively (Corfu & Wallace, 1986; Sanborn-Barrie et al., 2000, 2001). The Slate Bay assemblage is clastic sediment dominated unit derived from erosion of the Balmer and Ball assemblages (Sanborn-Barrie et al., 2000, 2001). It unconformably overlies the Balmer assemblage to the north. The maximum depositional age of this assemblage is ca. 2916 Ma from detrital zircon analysis, and it consists of feldspathic wacke interbedded with lithic wacke, argillite, pebble conglomerate and quartzose arenite (Sanborn-Barrie et al., 2000, 2001). The U-Pb zircon age of Bruce Channel assemblage is 2894 Ga which is found in the eastern part of the belt and comprises intermediate pyroclastic rocks, pebble conglomerate, siltstone, cross-bedded wacke and magnetite iron formation (Sanborn-Barrie et al., 2000). Calc-alkalic volcanic sequences include dacitic to rhyodacitic pyroclastic rocks (Pirie, 1981; Corfu & Wallace, 1986). The Trout Bay assemblage represents Neoarchean volcano-sedimentary sequences of 2853 Ma (U-Pb zircon age) which consist of basalt, tholeiitic basalt, intermediate tuff, chert-magnetite iron formation and clastic rocks (Sanborn-Barrie et al., 2001). To the north of the Slate Bay assemblage is the Huston assemblage, which is made up of a polymictic conglomerate deposited between 2890-2740 Ma determined by the U-Pb zircon ages (Sanborn-Barrie et al., 2001). This sedimentary assemblage marks an angular unconformity between Mesoarchean and Neoarchean strata (Sanborn-Barrie et al., 2001; McIntyre & Fralick, 2017). The Confederation assemblage is the youngest assemblage (U-Pb zircon ages 2750-2730 Ma), and it represents several volcanic sequences (Sanborn-Barrie et al., 2000, 2001). It is dominated by felsic to mafic volcanic flows and felsic to intermediate pyroclastic breccia with both calc-alkaline and tholeiitic compositions (Sanborn-Barrie et al., 2000, 2001; McIntyre & Fralick, 2017).

The current study examined the chemical and siliciclastic sediments which are interlayered in the upper portion of the Ball Assemblage. The age of the platform was determined by Corfu and Wallace (1986) by U-Pb zircon age dating of the rhyolitic lapilli tuff below the carbonates and a rhyolitic flow above the carbonates which show the age ranges from 2.94 $\pm$ 2 Ga to 2.92 $\pm$ 3 Ga (Thurston et al., 1991). This defines a general younging direction to the south, which corresponds to the up direction of the numerous stromatolites. In the Red Lake area, the Mesoarchean carbonate platform comprises various chemical sediments, i.e., chert, magnetite iron formation, sulfide iron formation, stromatolitic and other forms of carbonate, as well as siliciclastic sediments, i.e., black shale, siltstone, sandstone, and conglomerate. The sedimentary assemblage is overlain and underlain by mafic to felsic volcanic rocks. The stromatolitic unit is present in an east-west trending southwardly dipping band under Pipestone Bay and is bounded by a rhyolitic pyroclastic unit on Galena Island of Red Lake (McIntyre & Fralick, 2017). The carbonates are associated with oxide iron formation, sulfide iron formation, and carbonaceous mudstone. The oxide iron formation is considered Algoma-type as it was deposited in close association with volcanic activity. In older literature, Algoma-type iron formation was believed to have generally precipitated from hydrothermal plumes and been deposited closer to the venting sites (Gross, 1980; Gross & Zajac; 1983) . However, more modern interpretations consider Algoma-type iron formation to have been precipitated from Archean ocean bottom waters in general (Fralick, 1987; Danielson et al., 1992). The volcanic unit overlying the carbonate succession to the north is composed of calc-alkaline to tholeiitic mafic flows, komatiitic flows, and felsic pyroclastic rocks.

Chapter 2: Methodology

2.1 Fieldwork

Fieldwork was carried out for a week in the Red Lake area in August 2017. It was conducted along the shorelines of Bridget Lake, Trout Bay and Hall Bay to describe and sample the 2.94 Ga - 2.92 Ga (Corfu & Wallace, 1986; Sanborn-Barrie et al., 2001) Ball Assemblage sedimentary rocks of the Red Lake Greenstone Belt. Samples were collected from different lithofacies for geochemical analysis, petrographic analysis, and for slabbing and polishing. Outcrop locations, lithofacies, and bed orientations were documented, and numerous photographs were taken of fieldwork sites.

Figure 2.1: Drill hole and outcrop sites in the Red Lake area.

2.2 Drill Hole Locations

Drill core data were obtained from 11 different holes from the Red Lake area (Table 2.1). The drill hole and outcrop sites of the Red Lake area is presented in a google map in Figure 2.1. In 2010, Halo Resources Ltd. drilled four holes, three to the east of Bridget Lake and another to the north shore of Trout Bay, directly across from Galena Island (Figure 2.2). They conducted

further drilling of seven holes in 2012, five in the Pancake Bay area and two in the Bridget Lake area (Figure 2.3).

Table 2.1: Summary of Red Lake drill-hole information compiled by Halo Resources Ltd.

Hole	Easting	Northing	Azimuth	Dip	Drilling depth (m)	True vertical depth (m)
PB12-32	412950	5654540	210º	42º	301	272
PB12-33	413225	5654560	216º	43º	250	138
PB12-34	413128	5654391	210º	44º	250	123
PB12-35	412845	5654352	214º	40º	286	236
PB12-36	413035	5654273	255º	45º	208	154
BL12-37	414405	5653996	120º	45º	330	206
BL12-38	414250	5653980	261º	45º	50	21
EBL10-27	415838	5653986	216º	48º	396	174
EBL10-28	415727	5653936	230º	48º	453	204
EBL10-29	415473	5653970	215º	47º	180	61
NGI10-31	416319	5653970	180º	51º	372	142

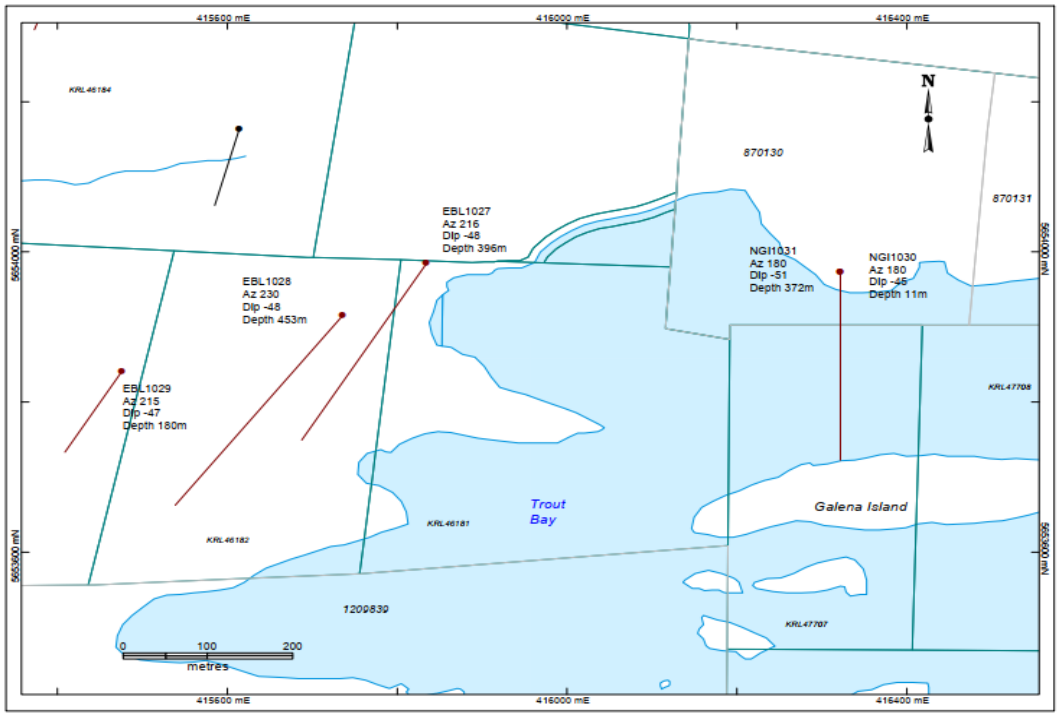

Figure 2.2: 2010 drilled-hole locations at east Bridget Lake and north Galena Island (Timpa, 2011).

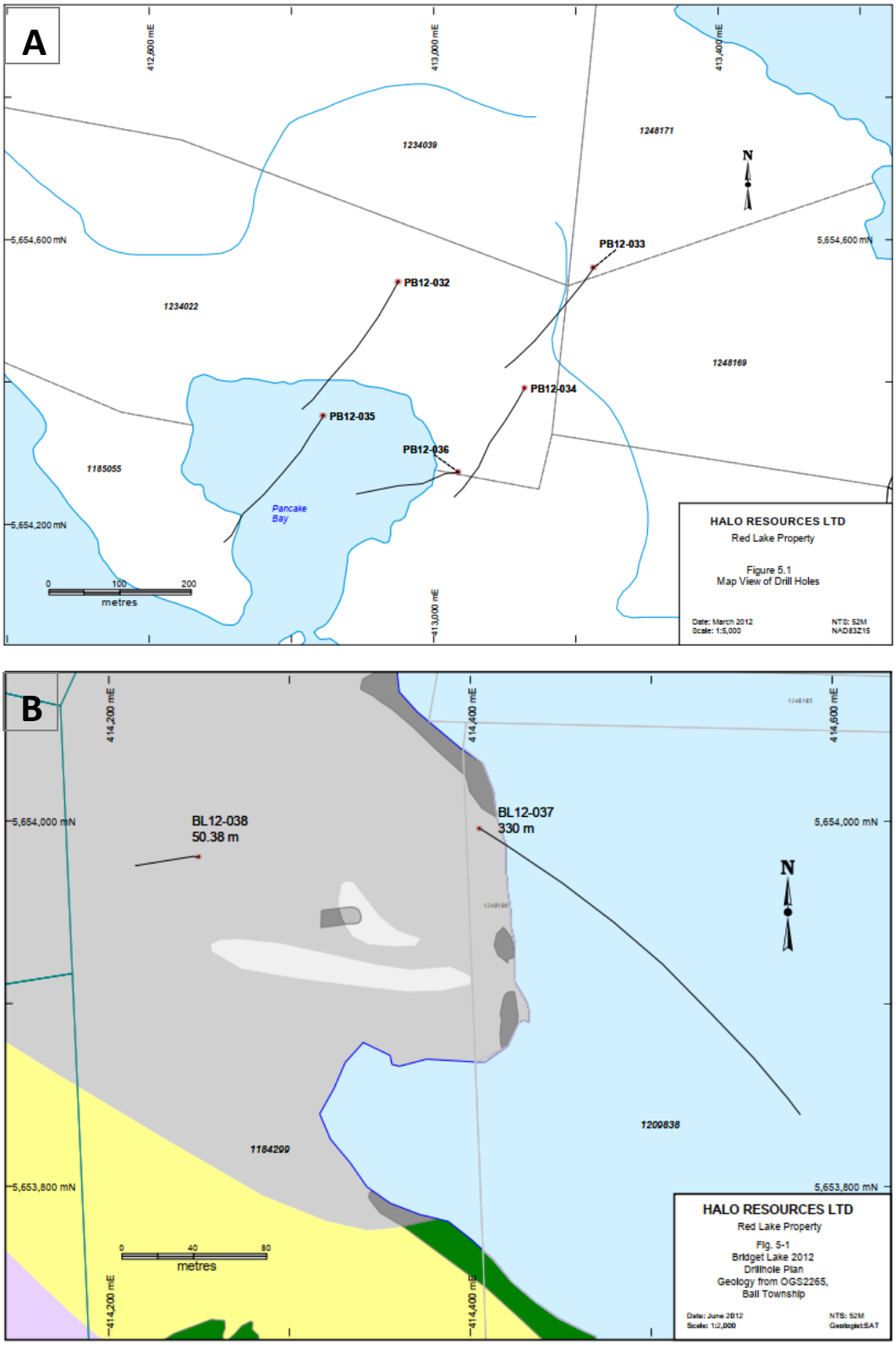

Figure 2.3: Drill-hole locations for holes drilled in 2012 in the (A) Pancake Bay area and (B) Bridget Lake area (Timpa, 2012a, 2012b).

2.3 Core Logging

Approximately 400 m of core of chemical and siliciclastic sedimentary rocks associated with the carbonate from 11 drill-holes were logged in the summer of 2017. Each unit in the cores was thoroughly described and measured. Samples were taken commonly at 2 m intervals for geochemical analysis, thin sectioning, slabbing, and polishing.

2.4 Whole Rock Geochemical Analysis

Rock samples of various lithologies were collected in the Red Lake area from both field work and drill-hole cores. A total of 200 samples were selected from different lithofacies including chert, oxide iron formations, sulfide ion formations, black slates, carbonates, siliciclastics, and volcanic rocks. These samples were analyzed at Lakehead University Instrumentation Laboratory (LUIL), Thunder Bay, Ontario for whole-rock major, minor and rare earth elements.

The sample preparation was started by cutting core, and field samples with a rock saw, crushing a selected fresh piece with a hammer, and finally milling the fragments in an agate ring mill at the lapidary facility in the Department of Geology at Lakehead University. To prevent cross-contamination between samples, the agate mill was cleaned with acetone after the pulverizing of each sample. Additionally, by using a magnet, the magnetite samples were separated from the associated rocks, and 7 samples were washed to get rid of fine-grained siliciclastics. An electric micro-drill was also used to obtain pure pyrite and pyrrhotite samples. The powdered samples were preserved in plastic vials.

Whole Rock Dissolution

In the analysis, 0.5 g of powdered samples were put into Teflon beakers, and 10 ml of double distilled water (DDW) and 5 ml of nitric acid (HNO_3) were added to the beakers along with three blanks and three standards. The three standards include Hawaiian basaltic rock (BHVO-2), quartz latite (QLO-1) (samples from United States Geological Survey, USGS) and a carbonate standard (8-44A) from Fralick & Riding (2015). The beakers were placed on a hot plate at 90˚C and left overnight to remove effervescence from the samples and evaporate the liquids. The next day, 5 ml of hydrofluoric acid (HF) and 10 ml of nitric acid were added and left overnight on the hot plate at 90˚C. The same process was repeated for the next two days. This four-day process allowed silica (SiO_2) to digest completely and remove CO_2 from the samples. On day five, 2 ml of nitric acid was added to the samples and simmered for 10 minutes at 90˚C. Then the beakers were filled to ¾ with DDW and simmered for another 20 minutes. After that, the samples were transferred to a 100 ml volumetric flask by adding DDW to fill it partially. Finally, the flasks were placed on the hot plate for two hours until the solution became transparent. After cooling, the flasks were filled with DDW to make 100 ml solutions of each sample which gave 200 times dilutions of the measured samples. For the ICP-AES analysis, 50 ml of each sample was transferred to plastic vials. However, for ICP-MS analysis 1000 dilution is required, which is obtained with 10 ml of the sample solution and 40 ml of DDW with 2% nitric acid solution in a 50 ml vial.

Partial Dissolution Geochemistry

A partial dissolution process was applied to leach the carbonates from any siliciclastic contamination and to separate magnetite from associated carbonate samples. 0.2 g of powdered sample was used in the sample preparation process. Samples were placed into Teflon vials, and 10

ml of 5% acetic acid was added and allowed to digest overnight. The next day, the clear liquids were siphoned off from the beakers and placed into new Teflon beakers for drying. After drying, the samples were weighed. The samples were then added to 2% nitric acid and DDW to make 100 ml solutions. Finally, samples were poured into 50 ml plastic vials for analysis by ICP-AES and ICP-MS. The empty Teflon vials were reweighed to determine the sample weights during dissolution.

Analyses

Inductively Coupled Plasma-Atomic Emission Spectrometer (ICP-AES) was used for whole rock major and minor elements analysis while Inductively Coupled Plasma-Mass Spectrometer (ICP-MS) was used to determine the elemental concentration of rare earth elements. Selected samples were analyzed in the Lakehead university instrumentation laboratory by a Varian Vista Pro Radial (CETAC ASX-510 Auto Sampler) and a Perkin-Elmer Elan DRC-e analyzer for ICP-AES and ICP-MS respectively.

Analysis Accuracy

Geochemistry samples were analyzed in five batches along with standards and blanks. A total of 138 samples were prepared for the analysis. Table 2.2 is the sample analysis list of various lithologies.

The accuracy of the analysis was determined using the equation below:

$$\text{Analysis Accuracy} = [(\text{Sample}_{\text{This study}} - \text{Sample}_{\text{Standard}}) / \text{Sample}_{\text{Standard}}] \times 100\%$$

Table 2.2: Geochemistry sample analysis list

Geochemistry sample analysis list: ICP-AES and ICP-MS	
Sample type	No. of samples
Carbonate	38
Magnetite	42
Chert	7
Pyrite	7
Pyrrhotite	6
Black slate	19
Sandstone	12
Volcanic rocks	4

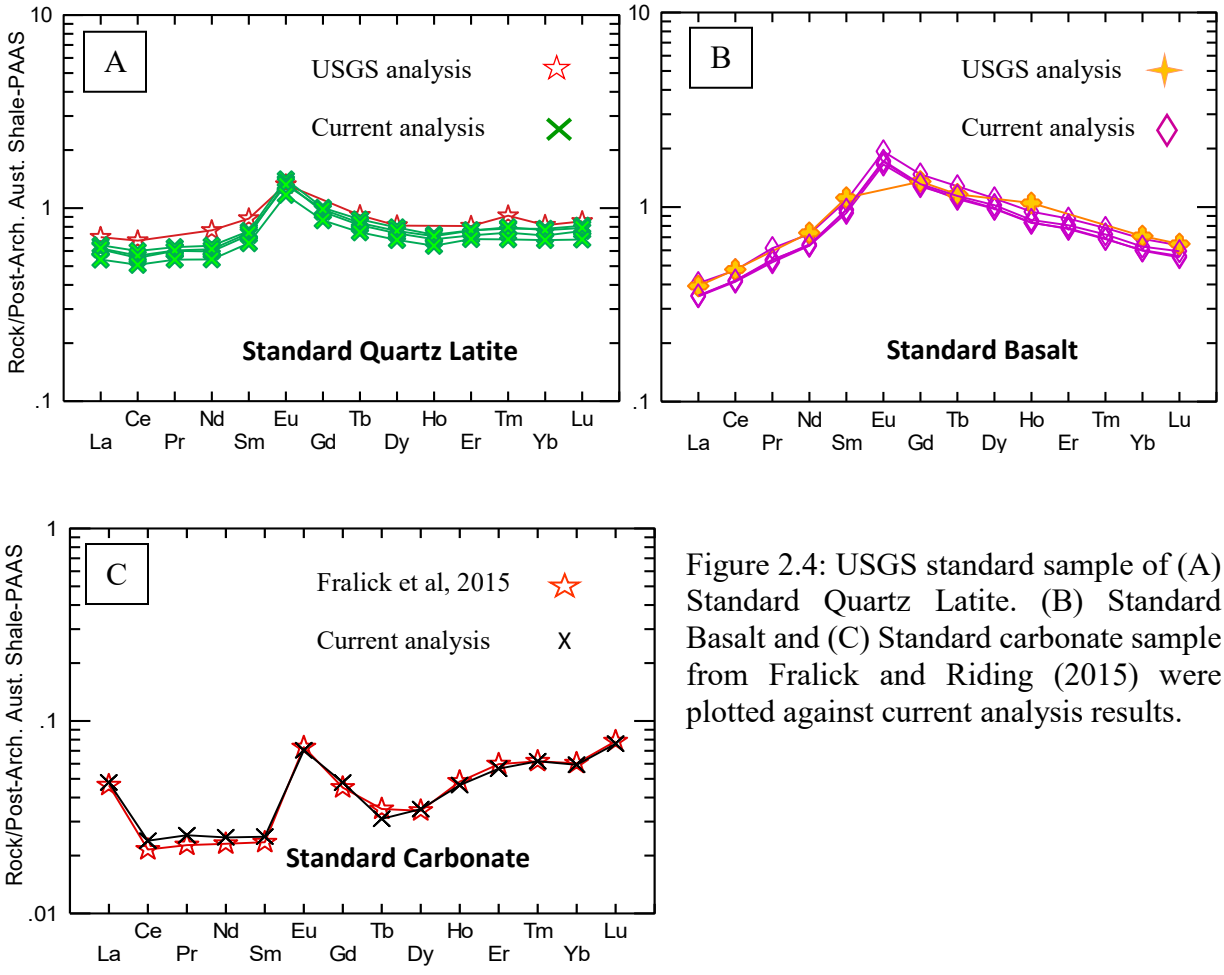

Figure 2.4: USGS standard sample of (A) Standard Quartz Latite. (B) Standard Basalt and (C) Standard carbonate sample from Fralick and Riding (2015) were plotted against current analysis results.

In Figure 2.4 (A) and 2.4 (B), standard quartz latite and Hawaiian basalt results for rare earth elements obtained from this study were plotted against the USGS results, and in Figure 2.4 (C) standard carbonate REE analysis results from this study were plotted with Fralick and Riding (2015) results. Carbonate samples were analyzed in one batch, which is why Figure 2.4 (C) represents a single analysis of a standard along with the given standard results. From the plots, it is clear that the analysis results of REEs in the standard samples of this study are similar to the USGS results. The analytical accuracy for ICP-AES analysis is ±10 % and for ICP-MS is ±3 %.

2.5 Carbon, Oxygen, and Sulfur Isotope Analysis

Carbon, oxygen, and sulfur isotope analyses were completed at the European Institute for Marine Studies, Brest, France, and G.G. Hatch Stable Isotope Laboratory at Ottawa. Powdered samples, which were prepared for geochemical analysis, were sent to France and Ottawa for the C and S analysis. $\delta^{13}C$ isotope analysis of both organic carbon and inorganic carbonate were performed in the French lab in Brest, whereas only limited inorganic carbonate $\delta^{13}C$ isotope analysis was conducted in Ottawa. $\delta^{34}S$ isotope analysis was done at the G.G. Hatch Stable Isotope Laboratory at the University of Ottawa, while multiple S isotope analysis, $\delta^{32}S$, $\delta^{33}S$, $\delta^{34}S$, and $\delta^{36}S$, were determined at laboratory in Paris, France.

Isotope Analysis Procedure at the European Institute for Marine Studies, France:

$\delta^{13}C$ Isotope Analysis for Organic Carbon

In a fume hood, 6 N HCl was added to the powdered sample and left for 12 hours then warmed for 2 hours at 80°C. This process allows samples to be de-carbonated and the residues were washed with Milli-Q water. The residues were centrifuged three to four times to obtain a neutral pH. Then 10-15 mg of the de-carbonated samples were placed into tin capsule to analyze

carbon isotopic composition using a Thermo Scientific Delta V plus mass spectrometer coupled to a Flash 2000 elemental analyzer. Carbon isotope ratios are reported in conventional delta notation with respect to VPDB-standard (Vienna Pee Dee Belemnite). Precision (2σ) for $\delta\ ^{13}C_{org}$ is ± 0.1 ‰.

$\delta^{13}C$ and $\delta^{18}O$ Isotope Analysis for Inorganic Carbon

$\delta^{13}C$ and $\delta^{18}O$ isotope composition of carbonate samples were determined by a Kiel IV automated carbonate preparation device. Powdered samples react with 100 % H_3PO_4 at 72ºC and release CO_2 which was analyzed using a Finnigan MAT 253 mass spectrometer for isotope compositions of C, and O. $^{13}C/^{12}C$ and $^{18}O/^{16}O$ ratios were reported in delta notation relative to the VPDB-standard. Precision of $\delta^{13}C_{carb}$ and $\delta^{18}O$ was 0.1‰ (2σ) and 0.2‰ (2σ), respectively.

Multiple Sulfur Isotope Analysis

Conventional wet chemical extraction was used to retrieve sulfur from sulfide, and to extract mono-sulfides and primary pyrite acid volatile sulfide (AVS) and chromium reducible sulfur (CRS) were deployed respectively. By using cold concentrated hydrochloric (HCl) for 2 hours, AVS was released and resulting hydrogen sulfide (H_2S) was precipitated as silver sulfide (Ag_2S) with a 0.3 M silver nitrate ($AgNO_3$) solution. On the other hand, CRS was released after using hot and acidic 1.0 M chromium chloride ($CrCl_2$) solution (Canfield et al.,1986), and the resulting H_2S was precipitated as Ag_2S. After centrifugation, the precipitated Ag_2S was washed several times with deionized distilled water and dried at 50°C for 48 hours in an oven and weighted to calculate the amount of AVS and CRS. It was then fluorinated to produce SF_6 and analyzed for their multiple sulfur ($\delta^{32}S$, $\Delta^{33}S$, $\Delta^{36}S$, and $\delta^{34}S$) isotope compositions. The isotope compositions were determined by using a dual-inlet Thermo Scientific MAT 253 gas source mass spectrometer

and monitoring ion beams at 127, 128, 129, and 131 m/z (Labidi et al., 2012). Sulfur isotope ratios are reported in conventional delta notation with respect to VCDT (Vienna-Canyon Diablo Troilite) as Eq. (1):

$$\delta^{3a}S = \left[\frac{(^{3a}S/^{32}S)_{sample}}{(^{3a}S/^{32}S)_{VCDT}} \right] -1 \times 1000 \quad (1)$$

where a is either 3, 4 or 6;

and as equations. (2) and (3) for capital delta notation (following Johnston et al., 2008):

$$\Delta^{33}S = \delta^{33}S - 1000 \times \left[\left(1 + \delta^{34}S/1000\right)^{0.515} - 1 \right] \quad (2)$$

$$\Delta^{36}S = \delta^{36}S - 1000 \times \left[\left(1 + \delta^{34}S/1000\right)^{1.9} - 1 \right] \quad (3)$$

International standards IAEA-S-1, IAEA-S-2, and IAEA-S-3 were used for calibration assuming $\delta^{34}S_{VCDT}$ values of -0.3 ‰, +22.7 ‰ and -32.3 ‰ respectively and for normalization IAEA-S-2 standard sample was used which has +5.224 ‰, +0.030 ‰ and -0.203 ‰ of $\delta^{34}S$, $\Delta^{33}S$, and $\Delta^{36}S$, respectively (Thomazo et al., 2018). Analytical precision is ±0.3 ‰.

Isotope Analysis Procedure at G.G. Hatch Stable Isotope Laboratory, Ottawa

$\delta^{13}C$ and $\delta^{18}O$ Isotope Analysis for Inorganic Carbon

About 0.5-0.7 mg of sample was measured into clean Exetainer vials. In another vial, about 10 mL of anhydrous phosphoric acid was poured and then capped, heated and evacuated on a vacuum line for at least 1 hour to degas the acid. Samples vials were placed in a rack with standard samples and 0.1 mL of the prepared acid was carefully added to the samples. Next, the prepared vials were tilted straight and directly placed in the heated block of the Gas-Bench and left for 24

hours to react at 25°C for calcite and at 50°C for dolomite. Afterward, vials were flushed and filled with UHP helium off-line for 4 minutes at a rate of 60-70 mL/min into a Thermo Finnigan Delta-Plus XP IRMS mass spectrometer for $\delta^{13}C$ and $\delta^{18}O$ analysis. Carbon and oxygen isotopes were normalized using international standards NBS-18, NBS-19, and LSVEC (C only). The analytical precision is ±0.15 ‰ and ±0.3 ‰ for $\delta^{13}C$ and $\delta^{18}O$ respectively.

$\delta^{34}S$ Isotope Analysis

The powdered sulfide samples processed at the Hatch Lab in Ottawa were weighed into tin capsules with at least twice the sample weight of tungstic oxide (WO_3) for inorganic and organic sulfur. Samples were placed into an isotope cube elemental analyzer to be flash combusted at 1800ºC with the addition of oxygen. Released gases were carried by ultrapure helium through the elemental analyzer to be cleaned, then separated. SO_2 gas was separated for analysis by the chemical adsorption method and then carried by helium into a Thermo Finnigan Delta-Plus XP IR mass spectrometer, via a conflo IV interface for ^{34}S determination. International standards IAEA-S1, IAEA-S2, and AG-2 were used for calibration assuming $\delta^{34}S_{VCDT}$ values of -0.3 ‰, +22.7 ‰ and -0.71 ‰ respectively. Analytical precision is ±0.2 ‰.

2.6 X-Ray Fluorescence (XRF) Scanning

Nine slabbed core and outcrop samples were scanned to obtain elemental mapping using a high resolution XRF scanner at the European oceanographic institution, IFREMER, Brest.

2.7 CNS Analysis

This analysis was done in the Lakehead University Instrumentation Laboratory. Selected 39 sulfide iron and black slate samples were run via standard TCD detector on a CHNS [Cl] Elementar vario EL analyzer to determine the carbon, nitrogen and sulfur % in these samples.

2.8 Petrographic and FE-SEM-EDS Analysis

Polished thin sections were prepared from selected lithofacies samples. Initially, thin sections were examined under reflected and transmitted light. Photographs were taken to obtain images under plane polarized light (PPL) and cross-polarized light (XPL) with an Olympus DP-70 petrographic microscope.

After analyzing the thin sections with a petrographic microscope, they were coated with carbon in order to be scanned under a scanning electron microscope (SEM). The carbon-coated slides were analyzed with a Hitachi SU-70 Schottky Field Emission SEM with a working distance of 15 mm and an acceleration voltage of 20 kV. Backscattered electron images were taken to compare with petrographic images. EDS (energy dispersive x-ray spectroscopy) mineral mapping was done to ascertain the elemental composition in different lithofacies. Point analysis was accomplished to determine the major element geochemistry of minerals within the carbonate sequence.

Chapter 3: Lithofacies

3.1 Sedimentary Lithofacies Associated with the Red Lake Carbonate Platform

This chapter includes a description of lithofacies observed in the field and drill-core. Each lithofacies present in the deeper water areas of the platform, as defined by McIntyre and Fralick (2017), is discussed with respect to their lithology, bedding characteristics, abundance, and association with other lithologies. The description of the lithofacies is followed by a discussion of the geochemistry of the lithofacies employing XRF elemental mapping of slabs, SEM-EDS investigations of entities smaller than the XRF mapping could resolve, and ICP-AES and ICP-MS whole rock and mineral separate geochemistry. The geochemical analysis of major, minor and rare earth elements of the different lithofacies samples is presented in Appendix 1.1 and 1.2. Isotope geochemistry including sulfur, carbon, and oxygen isotope analysis are presented in Appendix 1.3, 1.4, and 1.5.

3.1.1 Carbonate

Carbonate is common in the study area although in some places it is highly silicified. It generally appears dark gray to orangey brown on the weathered surface and white to grayish on the fresh surface. Carbonates of both organic and inorganic origin occur in outcrop as well as drill core. Microbialites present in the shallow water portion of the platform include stromatolitic carbonates (McIntyre and Fralick, 2017) that are now largely silicified and react very weakly with 10% HCl. They are identified by features such as dome-shaped structures with wavy to flat laminae (Figure 3.1). Deeper water carbonaceous slate, chert, and iron formation underlie, overlie and are intercalated with the 200 m thick shallow water carbonate succession. The deeper water carbonate

rocks observed in outcrops are classified here base on their sedimentary features and mode of occurrence.

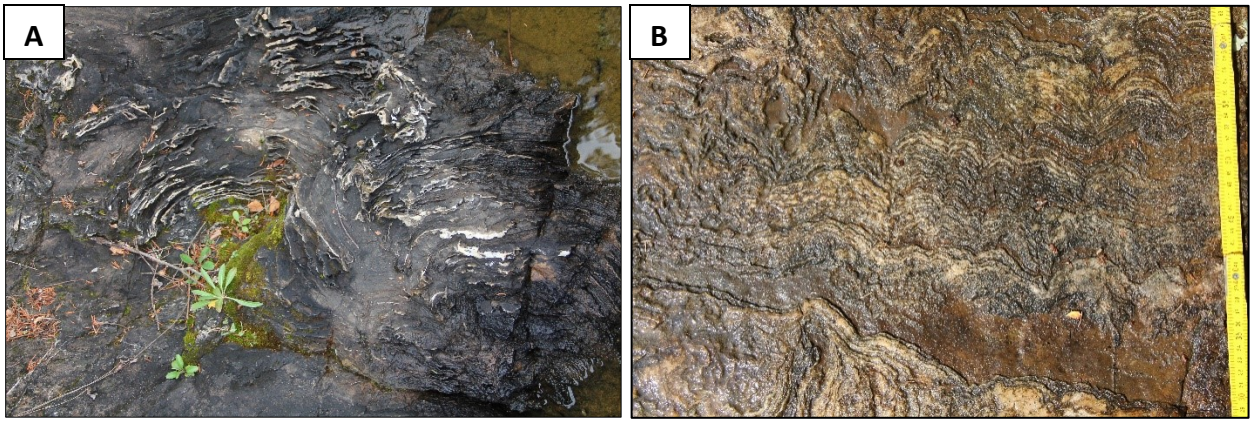

Figure 3.1: (A) Well-preserved domal-stratiform stromatolites and (B) wavy laminated stromatolitic carbonates are common in outcrops and represent shallow water carbonate.

Carbonate Associated with Oxide Facies Iron Formation

Carbonate associated with oxide facies iron formation consists of millimeter-scale magnetite-rich laminae interlayered with ~ 1cm thick calcite layers. The calcite bands are white but orangish on weathered surfaces. Magnetite laminae are thin, straight to wavy and black to dark grey. Contacts between the carbonate and magnetite layers are mostly sharp with little magnetite in the carbonate layers, and the carbonate present in the magnetite layers serves as a matrix to the recrystallized magnetite. At the base of the polished slab section in Figure 3.2-B, magnetite laminae are mm-thick and separated by 0.5 cm thick calcite layers and grade up through a more diffuse mixture of magnetite and calcite to purer calcite while others are sharp sided (see especially 3.2-C). Thin section analysis of carbonate associated with oxide facies iron formation shows, under cross polarized light, recrystallized calcite with obliterated primary textures with the magnetite also recrystallized forming large euhedral crystals. This facies is exposed next to the stromatolitic

carbonate unit on the NW shoreline of the Hall Bay area. However, this facies is probably rare in the Red Lake area, and no drill core sections exhibiting this type of facies were observed.

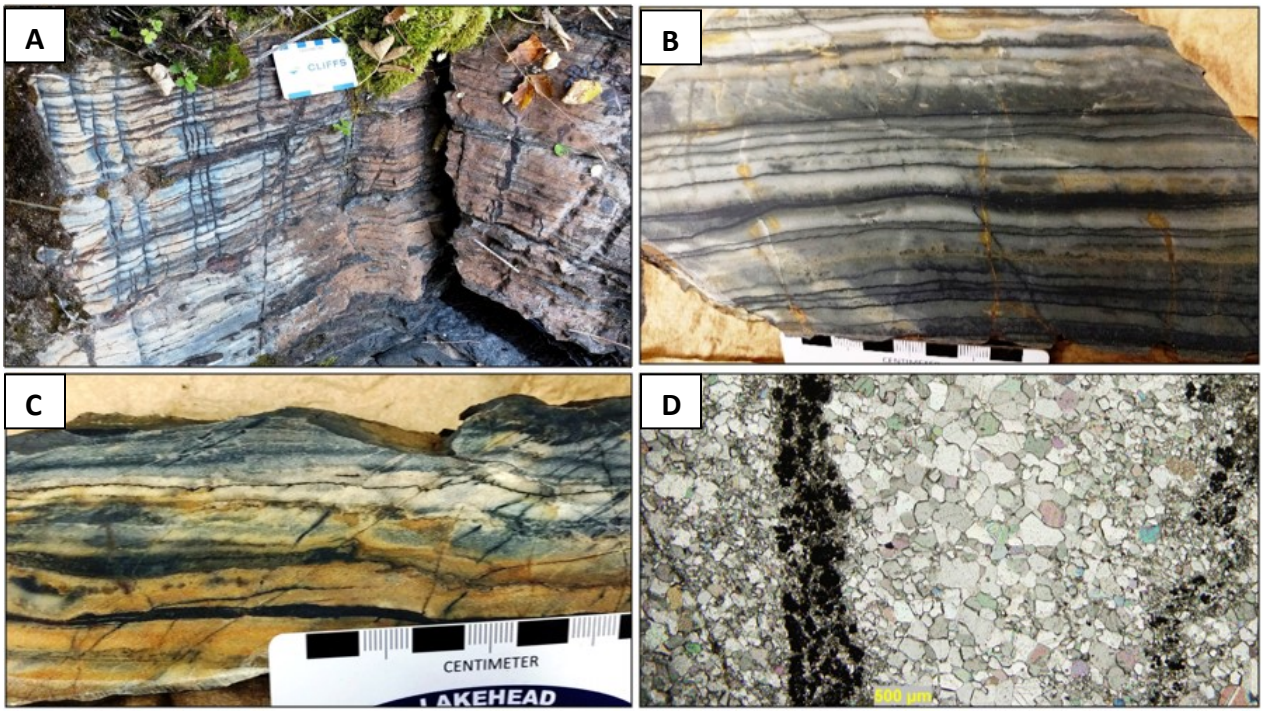

Figure 3.2: Carbonate associated with oxide facies iron formation in A) Outcrop at the shoreline of Hall Bay. Approximately 1 cm thick, white calcite layers alternate with mm-scale magnetite layers. The majority of contacts are sharp with little magnetite in the carbonate layers. (B) and (C) are polished slabs showing some layers in B have a mm-thick magnetite-rich lamina at their base and grade up through a more diffuse mixture of magnetite and calcite to more pure calcite (see especially B), whereas others are sharp sided (see especially C). (D) Thin section under XPL. Note the recrystallized nature of the calcite obliterating primary textures. The carbonate in the magnetite layers serves as a matrix to the recrystallized magnetite which has large euhedral crystals.

Slumped Carbonate

Carbonate-containing slump features are present in association with iron formations and/or siliciclastic sediments on the shoreline of the Hall Bay area in Red Lake. The carbonate clasts/broken layers are contorted, different in size and shape, white to orange in color, and composed of calcite which reacts very strongly with 10% HCl (Figure 3.3). The carbonate clasts/broken layers are hosted in fine-grained, dark gray to black siliciclastic mudstone,

magnetite-rich iron formation or an assemblage of both. The siliciclastic matrix in places reacts with HCl acid and/or contains magnetite, which indicates slumping possibly occur before lithification so that calcite and magnetite were mixed with mudstone. The upper part of the section contains elongated, flat to curvy, 1 mm to 3 mm thick cherty carbonate clasts in a siliciclastic matrix, while the lower portion is matrix dominated with a minor amount of carbonate clasts (Figure 3.3 B). The cherty carbonate clasts also react with HCl, but the matrix does not. The slab in Figure 3.3-C contains slightly magnetic, carbonaceous mudstone matrix with convolute carbonate clasts that are <1 mm to a few mms thick. The carbonate clasts are sub-rounded to sub-angular, a few mm to a cm thick and sprinkled over the carbonaceous mudstone with larger clasts at the center. However, near the bottom carbonate layering is preserved and continuous and has a sharp contact with a ~2.5 cm thick magnetite band (Figure 3.3 D).

The slab in Figure 3.4-A is an example of a slump in carbonate associated with oxide iron formation, where cm-thick broken carbonate layers alternate with mm-scale magnetite layers. These layers are folded and continuous to some extent at the center of the figure but at the bottom carbonate clasts are present in a magnetite-rich matrix. The slumped carbonate sample in the Figure 3.4-B exhibits chaotic association of carbonate, magnetite, and slate, which suggest slumping occur before lithification.

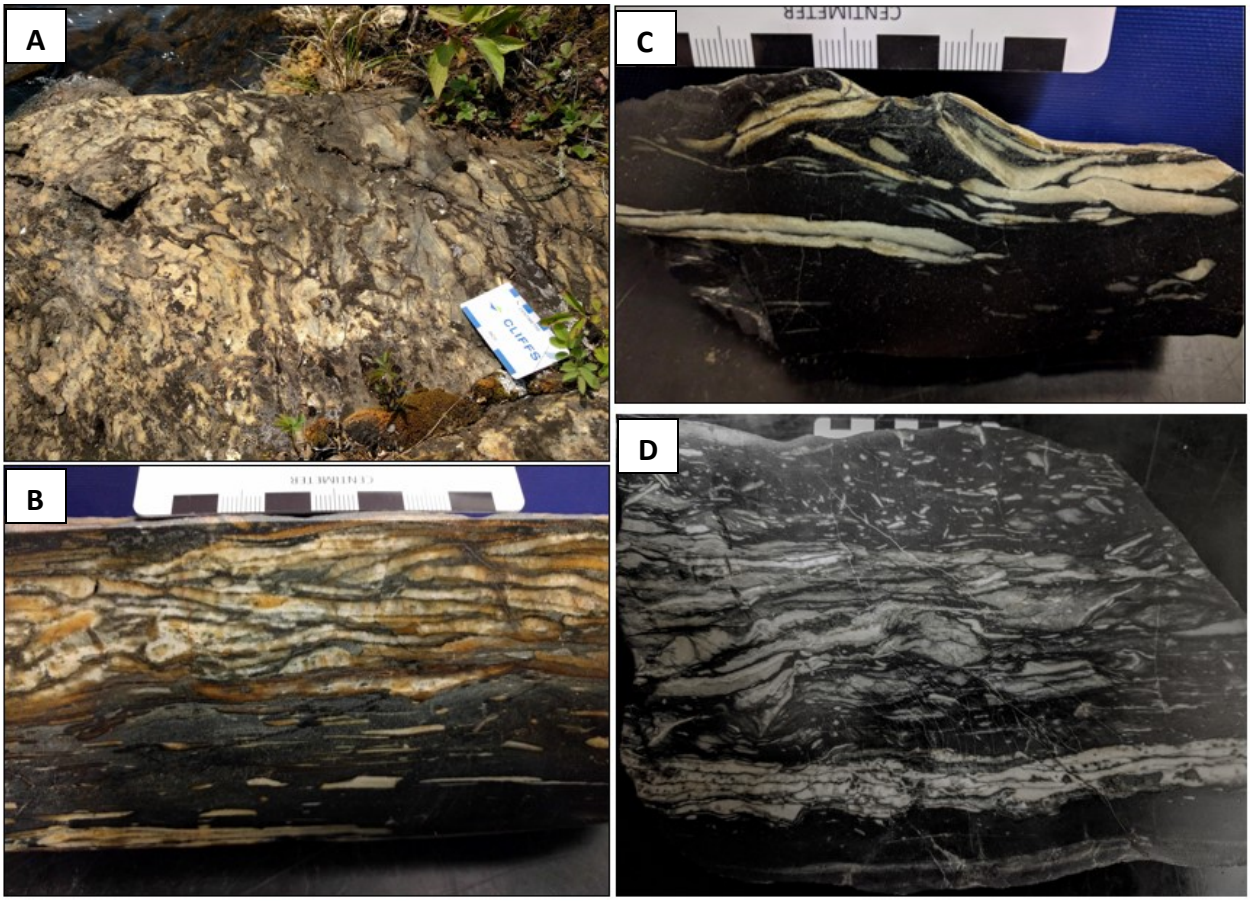

Figure 3.3: (A) Slumped carbonate on the shoreline of Hall Bay. (B) Polished slab of slumped carbonate with the upper part dominated by elongate cherty carbonate clasts/broken convolute layers, while the bottom part is mudstone-rich with a small amount of carbonate clasts. (C) Contorted carbonate clasts scattered in slightly magnetic carbonaceous slate and (D) sub-rounded to sub-angular carbonate clasts sprinkled over the carbonaceous mudstone with larger clasts present at the center. Near the bottom, carbonate layering is somewhat preserved and has a sharp contact with a ~2.5 cm thick magnetite band.

These carbonate slumps are probably caused by soft-sediment deformation rather than a tectonic brecciation process as the tectonic overprint of the rocks is a regional feature, but none of the other lithofacies have any indication of tectonic brecciation. In addition, facies overlying and underlying the contorted units have parallel layering. Also, the broken carbonate layers/clasts are randomly oriented, and they would be expected to have a preferred orientation if post-lithification tectonism were the cause. Finally, the associated slates have no cleavage associated with the

chaotic folding where present. Therefore, it is assumed that this slumped carbonate facies is formed by soft-sediment deformation due to slope instability in the upper slope environment and the slump blocks landed in the mid to lower slope environment and became interbedded with the sediments of those areas.

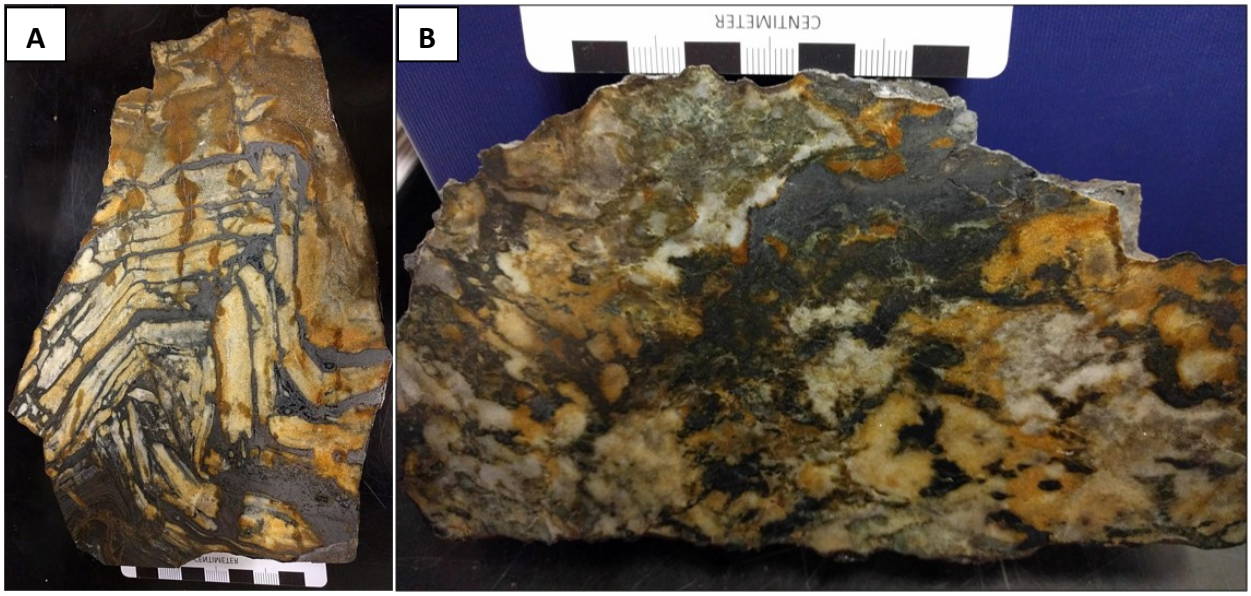

Figure 3.4: (A) Carbonate associated with oxide iron formation slumps where cm-thick broken carbonate layers alternate with mm-scale magnetite layers and suggest slumping occured after lithification of the carbonate. (B) A chaotic association of carbonate and magnetite suggests slumping occur before lithification.

Geochemistry of Carbonate

X-ray Fluorescence (XRF) scanning of laminated carbonate, slumped carbonate, and carbonate associated with oxide iron formation was conducted to visualize the different elemental distributions in these samples. The scanned image of the laminated carbonate in Figure 3.5 reveals that the upper part of the sample is composed of calcite and the lower part is composed of mm-scale thin magnetite laminae and mm size magnetite grains in a siliciclastic matrix. Magnesium content is very low in the upper carbonate portion. Secondary sulfide laminae of mm-scale are also present near the top of the siliciclastic portion.

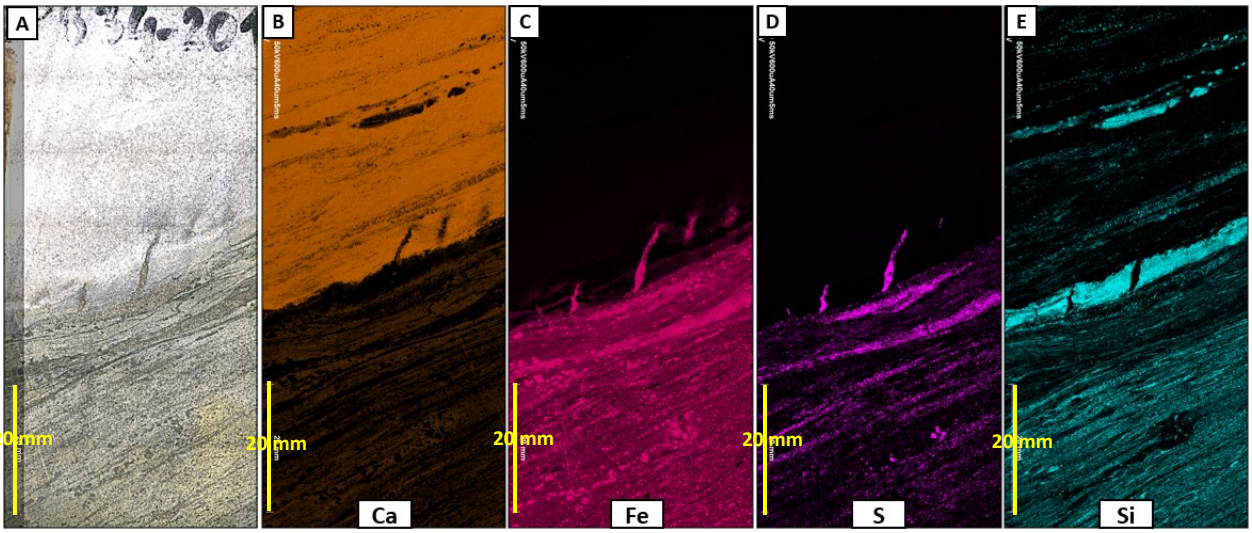

Figure 3.5: XRF scanned image of a laminated carbonate core sample showing the original image (A) and elemental false-color maps of (B) calcium; (C) iron; (D) sulfur and (E) silica. The upper part of the sample is composed of calcite where magnesium content is negligible, and the lower part is composed of mm-scale iron laminae embedded in a siliciclastic matrix. Secondary sulfide is also present in the siliciclastic unit.

The scanned XRF false-color images of slumped carbonate and chert indicate that carbonate layers are composed of calcite and are hosted in a siliciclastic, iron-rich matrix (Figure 3.6). The top photos are of white carbonate clasts in a siliciclastic matrix rich in iron oxides and calcite. At the base of these scans, a >1 cm-thick magnetite band is present. However, in the bottom sample, the white convolute clasts/layers are mostly composed of chert clasts embedded in a calcite matrix. The matrix in the upper part of the slab is mixed with calcite and magnetite.

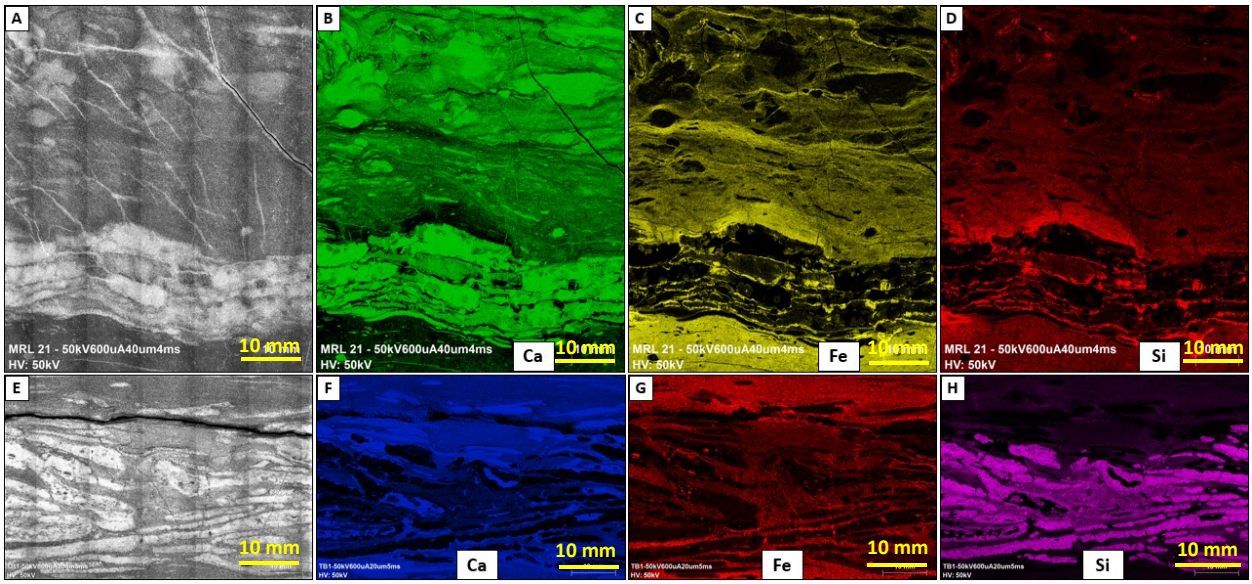

Figure 3.6: XRF scan images of slumped carbonate samples showing original images (A) and (E), and elemental images of calcium in (B) and (F); iron in (C) and (G); silica in (D) and (H). The top photos represent limestone sample where carbonate clasts are aligned near the bottom and the matrix is mixed with calcite and magnetite, with a magnetite band at the base of this slab. The bottom picture shows chert clasts with a matrix of magnetite and calcite.

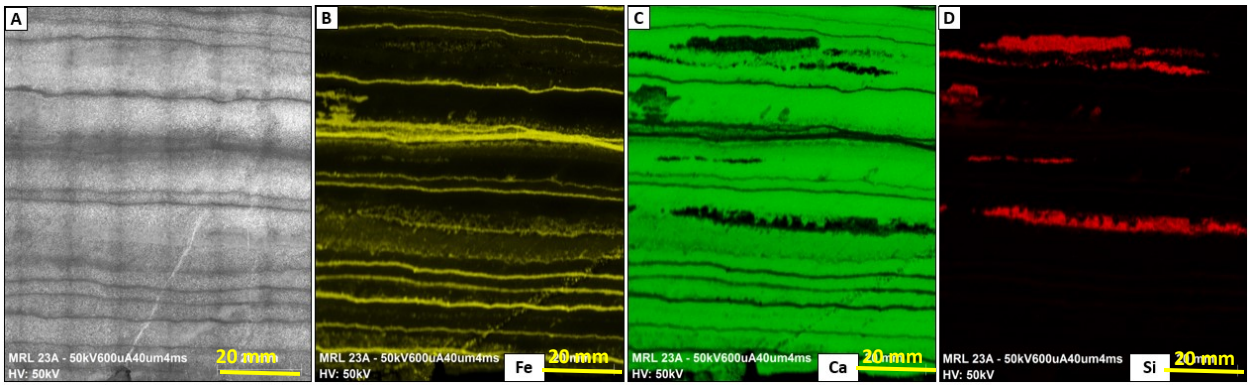

Figure 3.7: XRF scanned false-color images of carbonate associated with oxide iron formation. (A) original image and elemental images of (B) calcium; (C) iron; (D) silica. The images contain mm-scale magnetite layers alternating with cm-scale calcite layers and the stromatactis cavities with pendant calcite cement are filled with secondary silica.

The XRF scanning false-color image of carbonate associated with oxide facies iron formation exhibits mm-scale magnetite laminae interlayered with cm-scale calcite layers (Figure

3.7). The stromatactis cavities between calcite layers are filled by pendant calcite cement on the roofs and secondary silica.

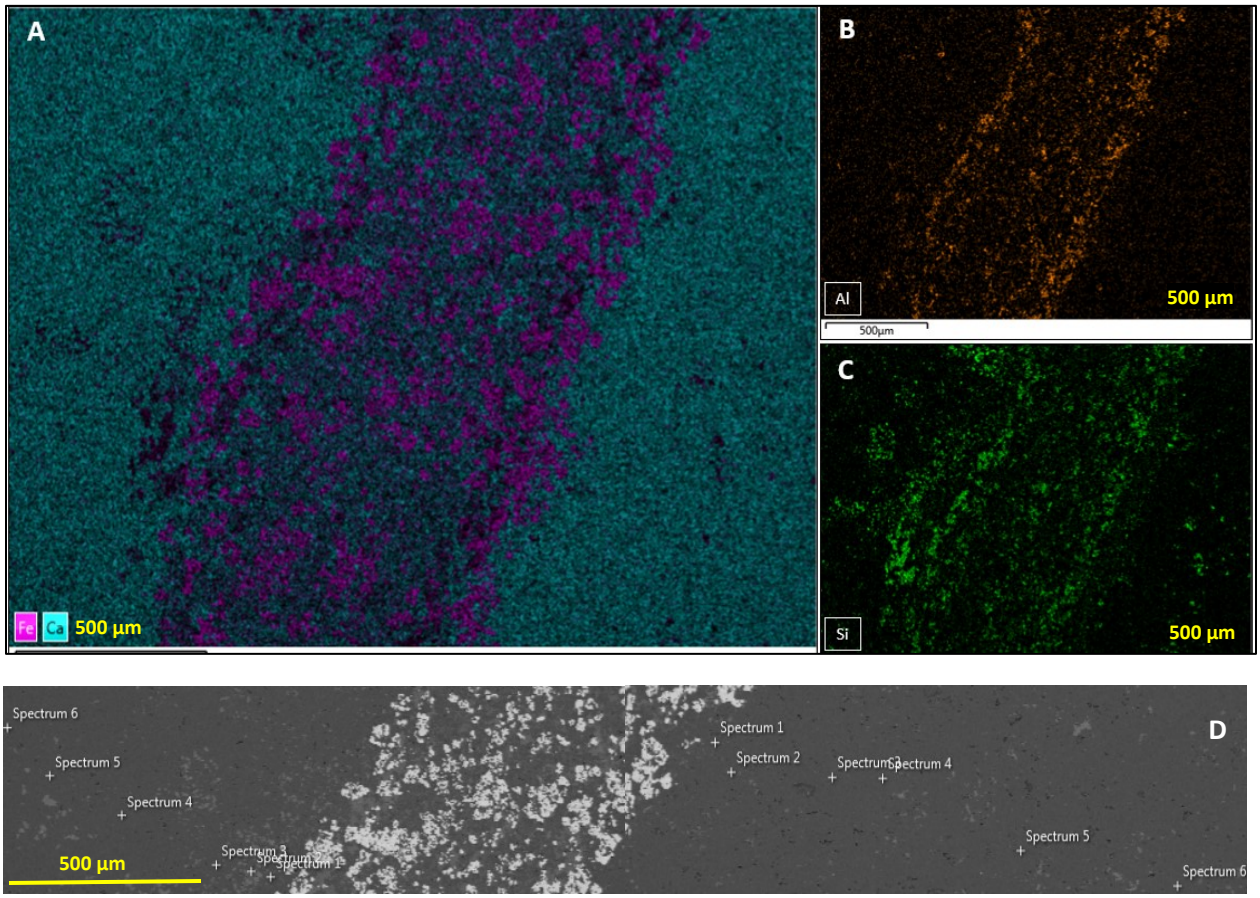

Figure 3.8: A) SEM-EDS layered false-color image of Fe and Ca in the carbonate associated with oxide iron formation. The carbonate band and the iron band are formed by calcite and magnetite respectively. Calcite is also present as a matrix in the magnetite band. B) and C) Elemental map of Al and Si respectively in the same section showing the presence of what was originally mud lining both sides of the magnetite band. D) BSE image and point analysis of carbonate layers on both sides of the magnetite band.

SEM-EDS elemental false-color maps of carbonate associated with oxide facies iron formation also show that carbonate and iron bands were formed by calcite and magnetite respectively. However, calcite is also present as a matrix in the magnetite band. The presence of magnetite associated with calcite is difficult to explain, as to whether the magnetite (Fe_3O_4) was

diagenetically altered from siderite ($FeCO_3$) or altered from iron hydroxide ($Fe(OH)_2$). Multiple point analyses were performed on two carbonate layers, and it was apparent that compositional variation in carbonates is very significant. The Mg, Mn, and Fe content is high close to the magnetite band but gradually decreasing away from it. The data is presented in Table 3.1.

Table 3.1: Composition of carbonate on both side of an iron band

Carbonate compositions in wt. % on the left side of the magnetite band							Carbonate compositions in wt. % on the right side of the magnetite band						
Elements	S-1	S-2	S-3	S-4	S-5	S-6	Elements	S-1	S-2	S-3	S-4	S-5	S-6
MgO	6.68	1.29	1.43	1.08	0.8	0.91	MgO	1.16	1.21	1.15	1.09	0.92	0.83
CaO	37.6	48.6	47.2	47.4	46.5	46.3	CaO	46.9	46.9	48.4	49.5	48.3	45.4
MnO	2.51	1.91	1.98	1.73	1.69	1.47	MnO	1.93	1.78	1.75	1.61	1.63	1.42
FeO	12.43	4.05	4.4	3.21	3.2	2.78	FeO	4.37	4.64	4.43	4.26	3.99	4.1
Al_2O_3		0.25					Al_2O_3						
SiO_2		0.68					SiO_2						
Total	59.2	56.7	55.0	53.4	52.2	51.5	Total	54.3	54.6	55.7	56.5	54.8	51.7

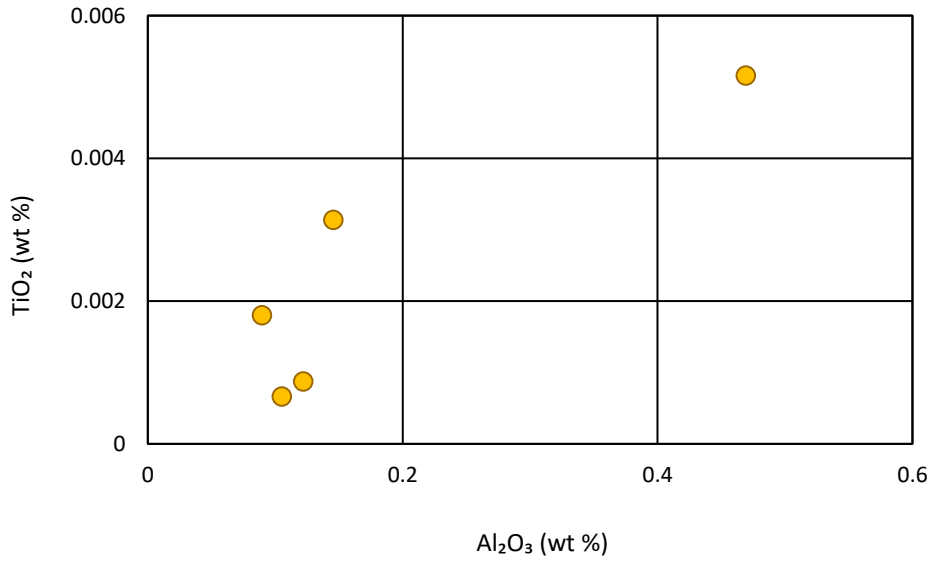

Figure 3.9: Al_2O_3 vs. TiO_2 plot shows that carbonate samples have a negligible amount of siliciclastics (Al_2O_3 content is < 1%).

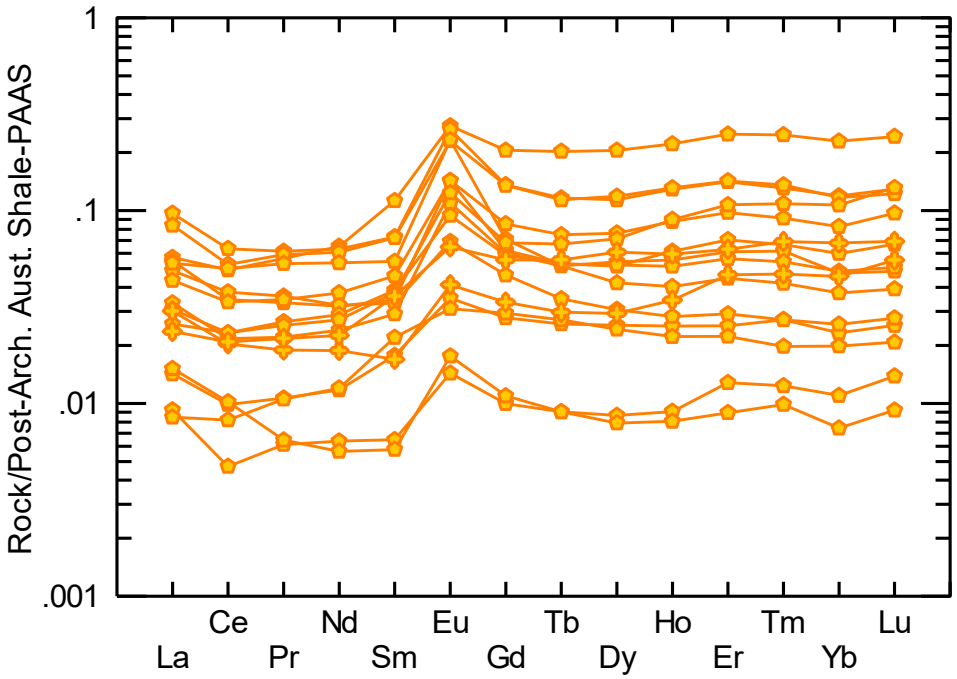

Figure 3.10: PAAS normalized (Taylor & McLennan, 1985) whole rock and partial dissolution of rare earth element patterns of carbonate samples have overall heavy rare earth enrichment, positive Eu anomaly and one sample has a negative Ce anomaly.

The Al_2O_3 vs. TiO_2 plot in Figure 3.9 shows carbonate samples have a very low amount of siliciclastics (Al_2O_3 content is < 1%). The Al_2O_3 content ranges from 0.09 wt % to 0.46 wt %. Similarly, TiO_2 contents range from 0.001 wt % to 0.005 wt %. The rare earth element systematics of carbonate samples is described in Figure 3.10 represents a compilation of this data discussed in detail in Chapter Four. In summary, the PAAS normalized REE patterns of carbonate samples have heavy rare earth element enrichment, positive Eu anomalies, and no negative Ce anomaly except for one sample (Figure 3.10).

3.1.2 Chert

Chert in the Red Lake carbonate platform occurs mostly either interbedded with magnetite or as massive chert. It also occurs as secondary in origin replacing carbonate throughout the

stratigraphy. Pure chert tends to be white while the variation of color depends on the degree of contamination or addition of other minerals, for example, chlorite gives a greenish appearance, iron oxides give reddish coloration, organic carbon and/or carbonaceous mud gives a grayish color, and pure mud gives a cream color. Chert is common in most of the drill holes either as massive chert or as an associate of the oxide iron formation (Figure 3.30). There is an approximately 10 m thick chert bed present beneath the deeper water chemical sedimentary rocks near the top of the PB-32 hole (stratigraphic top) while the deeper water assemblage itself is about 45 m thick. This chert bed is overlain by black slate and underlain by sandstone. There are a few thin chert layers associated with carbonate, sandstone, and oxide iron formation in this hole. The EBL-27 hole has an approximately 130 m thick package of chemical sedimentary rocks where a number of 0.5 m to 8 m thick chert beds are interlayered with black slate, sulfide iron formation, and oxide iron formation. The EBL-28 hole contains a few approximately 5 m thick chert beds in association with sandstone and siltstone. The other drill holes have a somewhat less occurrences of massive chert. The presence of chert interbedded with magnetite is mentioned in the oxide iron formation section. The description of different types of chert in the Red Lake area is discussed below.

Chert Interbedded with Oxide Iron Formation

Chert is mainly interbedded with magnetite in the Red Lake area. The chert bands are 1 cm to 4 cm-thick and alternate with magnetite. Layering is parallel, mostly straight to slightly wavy and white to grey (Figure 3.11 A). The color variation from white to grey is due to an increase in the amount of siliciclastics and incorporation of carbonaceous materials into the chert. Contacts between the chert and magnetite layers are sharp. The chert interbedded with oxide iron formation is laterally continuous in the shoreline of the Bridget Lake area. The core sample in Figure 3.11-B is chert dominated and exhibits 2 cm to 4 cm-thick, slightly fractured white to greyish chert layers

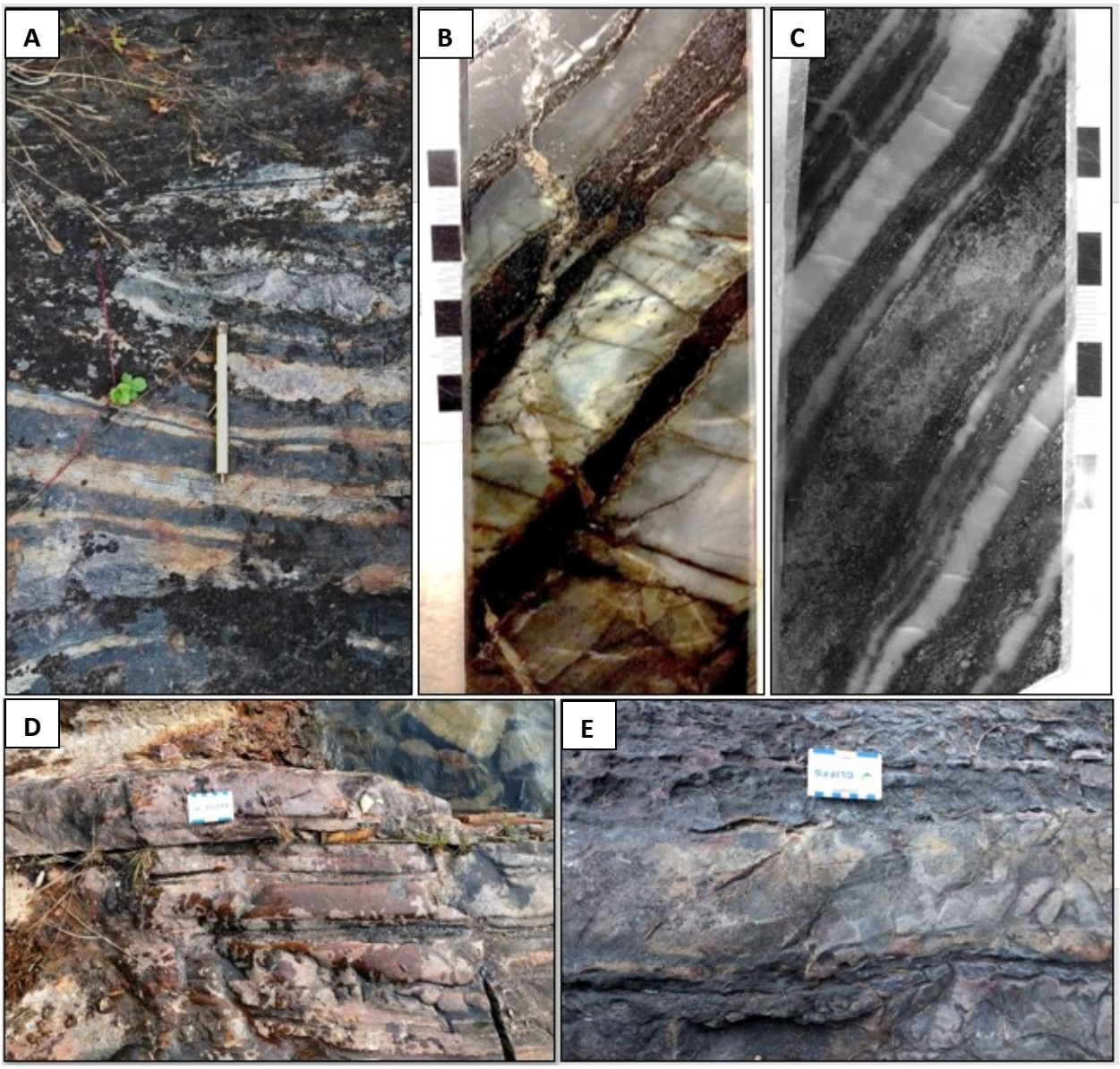

Figure 3.11: Primary Chert in the Red Lake area. (A) 1 cm to 4 cm-thick chert interbedded with magnetite, layering is straight to slightly wavy, parallel and laterally continuous. This is exposed on the shoreline of Briget Lake (outcrop -1). (B) Polished core section showing variable thickness of slightly fractured, white to grey chert laminae interlayered with relatively thin magnetite where grunerite is present along the contact of chert and iron oxide; and in (C) mm to cm-thick chert layers are separated by thick magnetite layers which are rich in secondary iron sulfide. Layering is straight and parallel in both sections. (D) 15 cm to 20 cm-thick chert interbedded with thin magnetite. This is exposed at outcrop - 3. (E) Approximately 15 cm thick massive chert bed interlayered with magnetite at Bridget Lake.

separated by 1 cm- to 2 cm-thick magnetite layers, layering is parallel and straight, and contacts are sharp. The lining along the contacts of magnetite and chert are formed by grunerite. The fractures in the chert layers are filled with secondary sulfides. The core sample in Figure 3.11-C has mm to cm-thick chert layers that are separated by thick, parallel magnetite layers with sharp contacts. The magnetite bands are rich in secondary sulfides.

Massive Chert

The thickness of massive chert beds in outcrops varies from 10 cm to 15 cm. A 30 cm thick massive chert bed is present in outcrop -3. Sometimes massive chert beds are heavily stained with a rusty color due to the oxidation of adjacent sulfide-bearing rocks, which has obscured the original appearance of the chert in the outcrop. Internal lamination may be present in massive chert layers but are not obvious in outcrop sections. In core data, massive cherts are white to gray and sometimes have a fractured appearance. Massive 10 to 20 cm thick, parallel chert beds are commonly interbedded with relatively thin (2 to 4 cm) (Figure 3.11 D) to very thin (0.5 to 1 cm) (Figure 3.11 E) magnetite bands and have sharp contacts with adjacent magnetite and sulfidic slate layers. In outcrop, massive chert beds are present at the shoreline of Bridget Lake (outcrop-1) and along the shoreline of outcrop -3 (see map in Figure 2.1).

Laminated Chert

The laminations in the chert are more conspicuous in slabbed sections than outcrop sections. Generally, the laminations are parallel, a few mm to 1 to 2 cm thick. The chert in Figure 3.12 A has 2 mm to 5 mm thick parallel laminations, which alternate between white and grey chert, and has a sharp contact with thin magnetite layer at its top. The variation of light to dark grey color is due to the difference in mud and/or organic carbon content. However, some laminations are

stained with a rusty color. This is due to the weathering of pyrite inclusions. In Figure 3.12 B, the laminated chert band has sharp upper and lower contacts with magnetite. The chert band is ~10 cm thick with mm to cm-scale internal laminations. The laminations are greenish at the top and cream to orange in color at the center and dark grey near the bottom. Laminated chert was observed along the NE shoreline of Hall Bay (outcrop – 2).

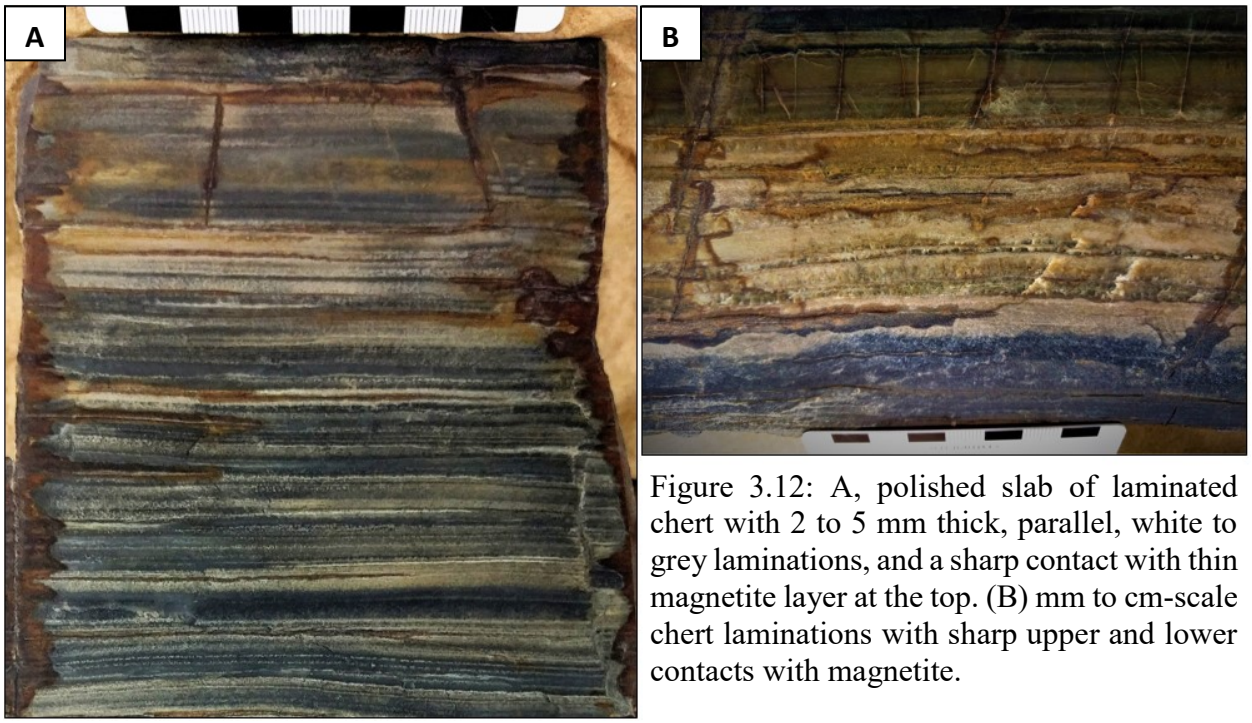

Figure 3.12: A, polished slab of laminated chert with 2 to 5 mm thick, parallel, white to grey laminations, and a sharp contact with thin magnetite layer at the top. (B) mm to cm-scale chert laminations with sharp upper and lower contacts with magnetite.

Geochemistry of Chert

An XRF scanned false-color image of a core slab of chert interlayered with oxide iron formation confirms the presence of iron and silica in the sample. The thickness of both chert and magnetite layers varies from a few mms to cms in scale. The scanned image displays the chert and magnetite layers as parallel and straight with sharp contacts, though there are examples of magnetite grading to chert and chert grading to magnetite. An approximately 2 cm thick white chert layer is present in the middle of the slab that is vaguely divided by wispy magnetite laminae.

The 2.5 cm thick grey chert layer above the white chert layer is not as bright as the white chert layer in the XRF silica map, and there is a trace of iron which indicates this is a ferruginous chert layer. The magnetite laminae thickness gradually increases towards the top and at the top an approximately 1 cm thick magnetite layer that has a yellowish gray lining on both sides is present. This yellowish gray lining at the contact of chert and magnetite is probably grunerite, which is a common iron silicate mineral found in regionally metamorphosed terrains.

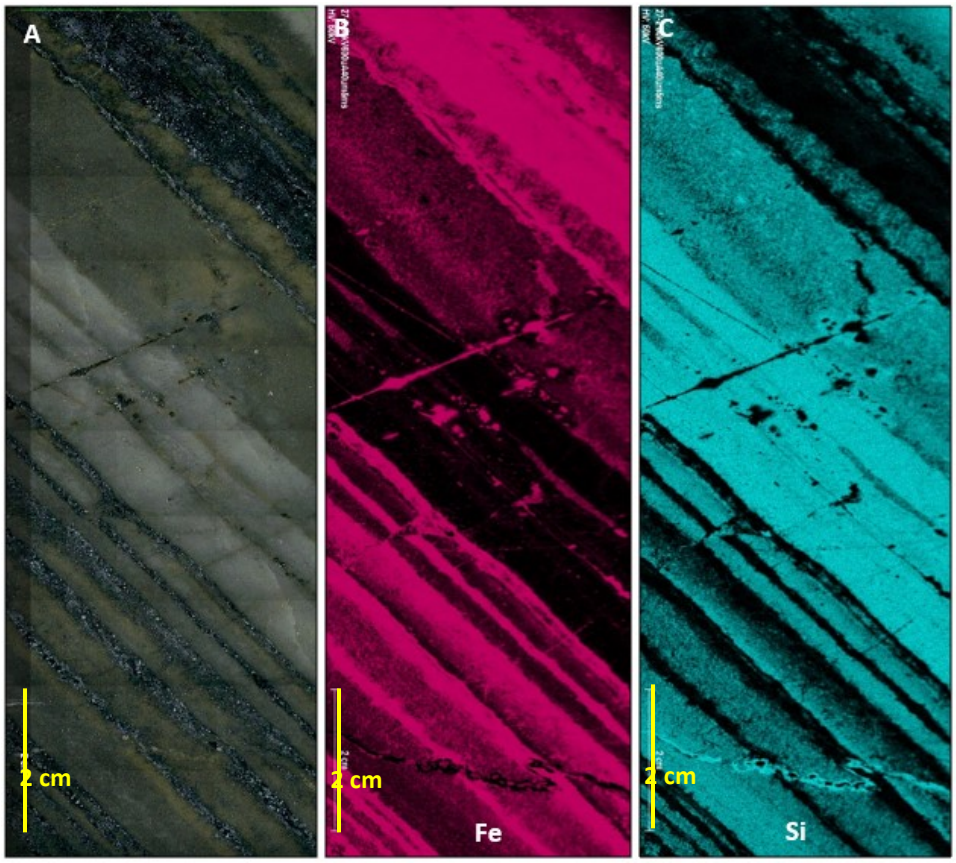

Figure 3.13: XRF scanned image of chert interbedded with magnetite. Elemental mapping shows the distribution of iron and silica. Both chert and magnetite layers have variable thicknesses. Most contacts between the iron and silica-rich bands are sharp but some are gradational.

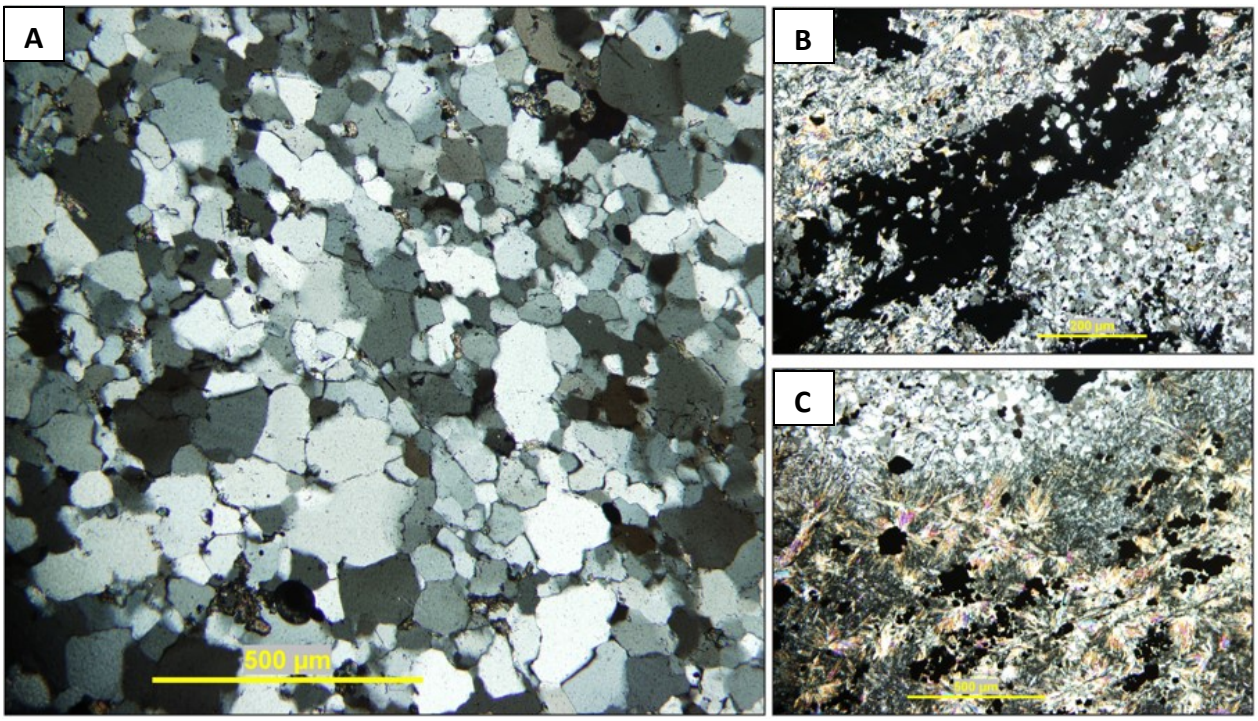

Figure 3.14: Photomicrographs of chert thin sections under cross polarized light using a petrographic microscope. (A) Massive chert composed of mainly quartz. (B) Chert interbedded with magnetite. (C) Chert in association with grunerite and magnetite.

In banded iron formation, chert occurs with magnetite (Figure 3.14 B) and sometimes with magnetite and grunerite (Figure 3.14 C). The cross polarized light image shows radiating, acicular crystals of grunerite, which is a characteristic mineral of metamorphosed iron-rich siliceous sediments with low concentrations of aluminum. In a regionally metamorphosed terrain, the typical assemblage is magnetite-grunerite-quartz (Stevens et al., 2002).

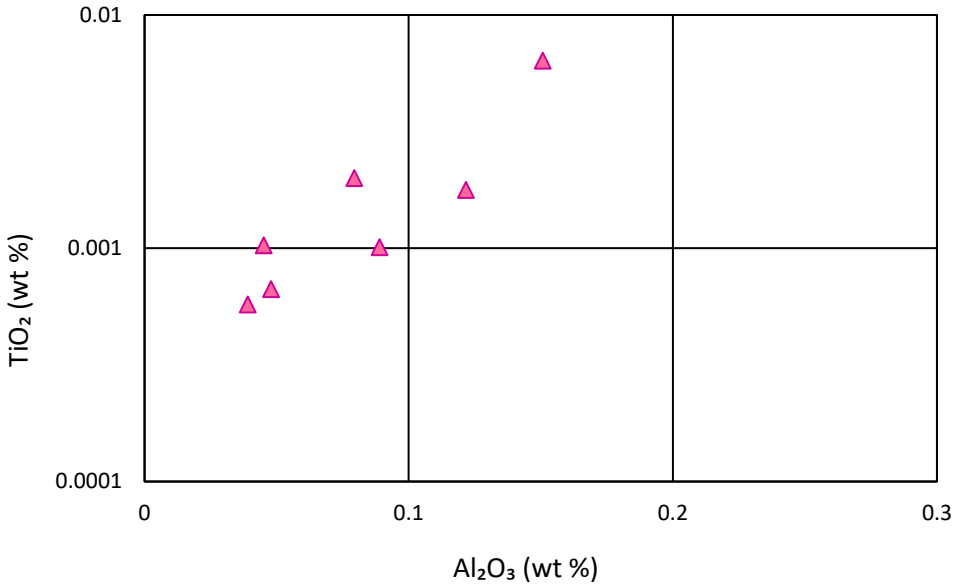

Figure 3.15: Al_2O_3 vs. TiO_2 plot shows siliciclastic contamination in chert samples is negligible except one sample that has >1 wt % Al_2O_3 content.

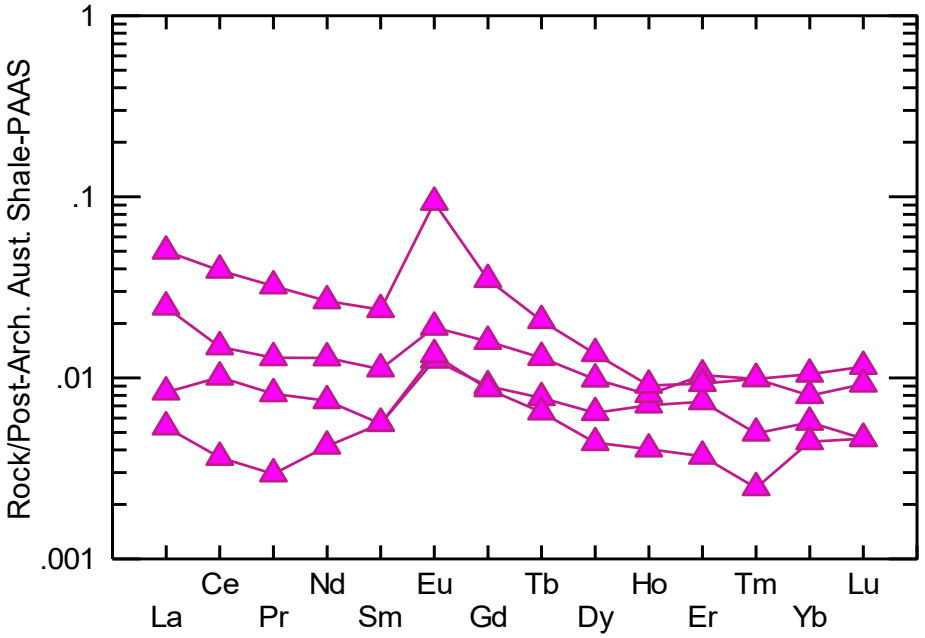

Figure 3.16: PAAS normalized (Taylor & McLennan, 1985) REE patterns of chert with positive Eu anomalies on a somewhat heavy rare earth element depleted pattern.

To determine the siliciclastic contamination in chert samples an Al_2O_3 vs. TiO_2 plot was used. The Al_2O_3 and TiO_2 contents range from 0.039 wt % to 0.15 wt % and 0.001 wt % to 0.006 wt % respectively (Figure 3.15), except for one sample which has 1.8 wt % Al_2O_3 and 0.025 wt % TiO_2. The low concentrations of Al_2O_3 and TiO_2 indicate siliciclastic contamination in most chert samples is negligible. The spider diagram of chert samples is presented in Figure 3.16 and an explanation of the REE systematics is described in Chapter Four. In brief, PAAS normalized REE trends of chert samples show positive Eu anomalies and somewhat heavy rare earth element depleted patterns. Some chert samples could not be plotted on the spider diagram due to their being below the detection limit of REEs. It must also be noted that the REEs are not structurally in the chert but must reside in mineral and fluid inclusions.

3.1.3 Oxide Iron Formation

The oxide iron formation in the Red Lake carbonate platform is characterized by magnetite interbedded with chert. Hematite is uncommon in the Red Lake stratigraphy. Magnetite bands are black, 1-5 cm thick and commonly have sharp contacts with the chert bands (Figure 3.17). Layering is straight to slightly wavy, parallel, and laterally continuous.

Oxide iron formation is abundant in EBL-27 and NGI-31 holes whereas EBL-29, BL-37, BL-38, and PB-32 holes have less of this lithology. In the EBL -27 hole, oxide iron formation of 1 m to 5 m in thickness alternates with sulfide iron formation of 0.5 m to 10 m thickness at approximately 35 m from the stratigraphic base of the drill hole. In the NGI-31 hole, the oxide iron formation is abundant in the ~65 m thick deeper water assemblage where it is overlain and underlain by carbonates. In addition, the oxide iron formation here is of variable thickness (1 m to 10 m) and is interlayered with carbonaceous slate. The oxide iron formations in the EBL-27 and

NGI-31 holes are magnetite dominated and strongly magnetic while oxide iron formations in the BL-37 and BL-38 holes are chert dominated. A 5 m thick oxide iron formation is bracketed with carbonates in the EBL-29 hole. The BL-37 and BL-38 holes have poorly developed oxide iron formation (< 0.5 m thickness) which is associated with chert and carbonate in BL-37 and black slate and chert in BL-38. The PB-32 hole has limited occurrence of oxide iron formation of only 1 m to 5 m thick and it is embedded in a ~175 m thick carbonate succession.

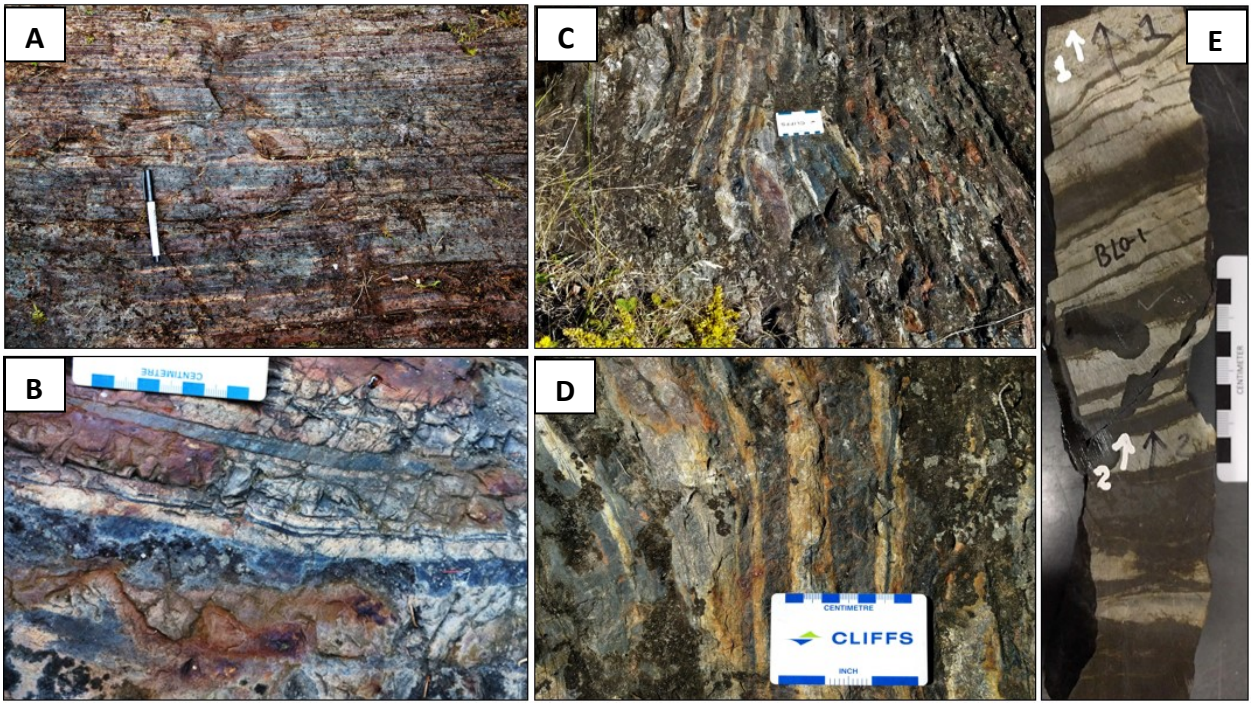

Figure 3.17: Oxide facies iron formation in different locations in the Bridget Lake area. (A), (B), (C) and (D) Magnetite interbedded with chert where magnetite band thickness varies from 1 cm to 5 cm, bands are parallel, mostly straight with sharp contacts with chert. (E) Rock saw cut sample of oxide iron formation. The bottom part of the slab is magnetite dominated. Near the top thin magnetite laminae are separated by 0.5 cm to 1 cm thick chert layers.

On a smaller scale the upper part of the slab of iron formation in Figure 3.17 E contains mm-scale magnetite laminae in the chert bands, but the bottom part of the slab is magnetite dominated. The magnetite band thickness varies from 0.5 cm to 3 cm and alternates with chert bands. Contacts are sharp. A core sample of oxide iron formation was already described in the chert section.

Geochemistry of Oxide Iron Formation

XRF scanned false-color images of oxide facies iron formation are discussed in the previous section. The SEM mineral mapping of oxide iron formation depicts it as mainly magnetite-rich, but it occasionally contains grunerite and Figures 3.18 A-B show the presence of acicular grunerite with magnetite and quartz.

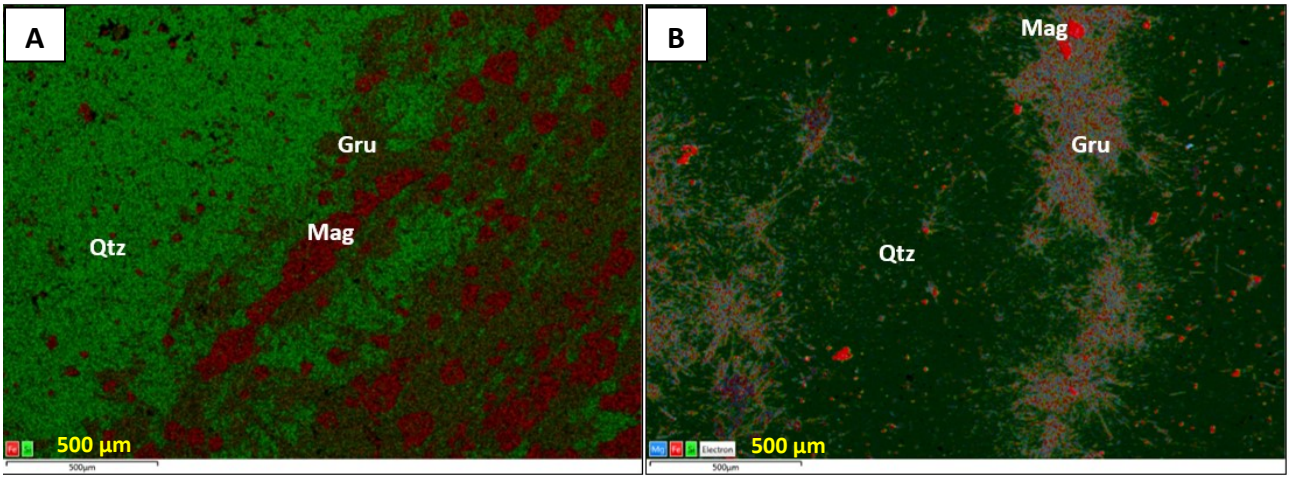

Figure 3.18: SEM-EDS false-color elemental map of oxide iron formation showing magnetite (Mag), quartz (Qtz), and grunerite (Gru) in (A) and (B). Grunerite has typical acicular crystals shape.

The magnetite samples were plotted on an Al_2O_3 vs. TiO_2 diagram to estimate the siliciclastic influence (Figure 3.19). The graph shows Al_2O_3 and TiO_2 content range from 0.032 wt % to 1.4 wt % and 0.002 wt % to 0.094 wt % respectively. Most of the samples have <1 wt % Al_2O_3 content, which indicates the siliciclastic influence in these magnetite samples is insignificant. But a few magnetite samples have >1 wt % Al_2O_3 content which suggest these samples are somewhat contaminated by siliciclastics, which will influence the shape of their REE patterns.

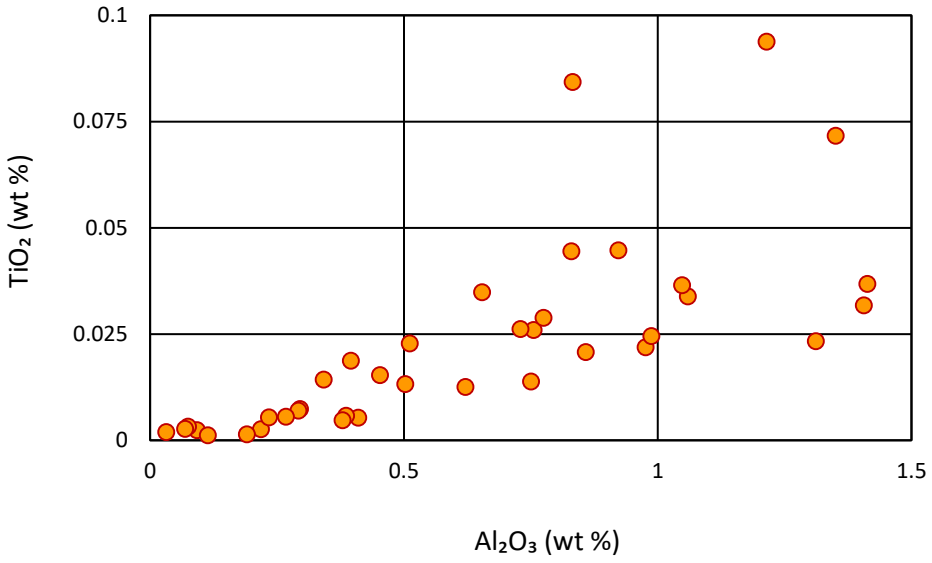

Figure 3.19: Al_2O_3 vs. TiO_2 plot showing most of the samples have < 1 wt % Al_2O_3 content. This indicates the siliciclastic influence in most magnetite samples is insignificant. A few magnetite samples have >1 wt % Al_2O_3 content which suggests these samples are somewhat contaminated by siliciclastics, which will influence their REE patterns by flattening them.

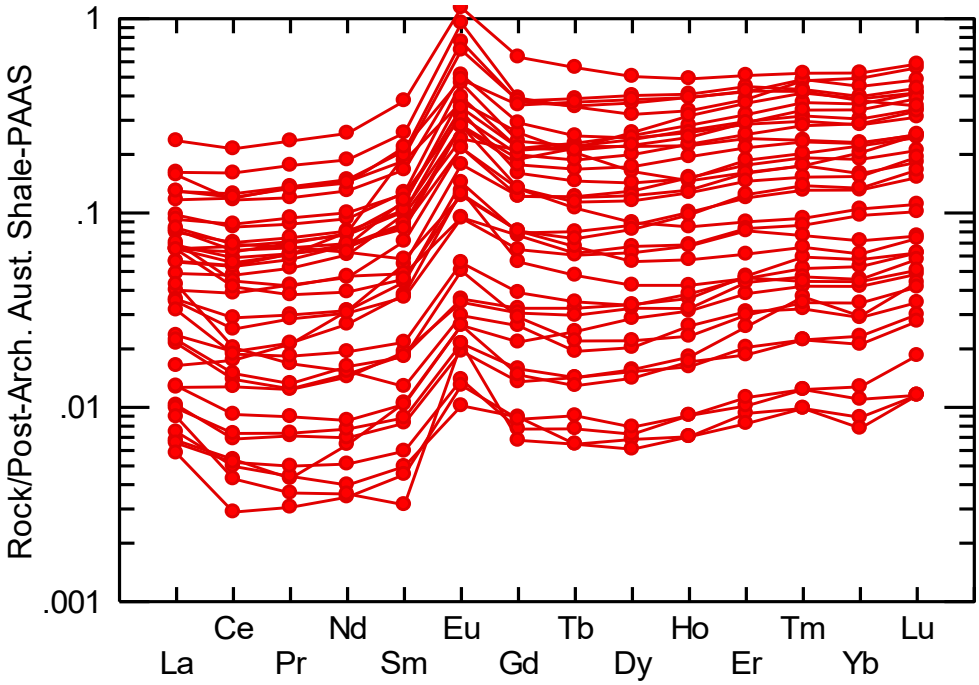

Figure 3.20: PAAS normalized (Taylor & McLennan, 1985) rare earth element patterns of oxide iron formation showing positive Eu* anomalies and heavy rare earth element enrichment.

The PAAS normalized REE systematics of magnetite samples is displayed in the spider diagram of Figure 3.20 and the description of REE systematics is discussed in Chapter Four. In short, the REE pattern of oxide facies iron formation is characterized by positive Eu anomalies and heavy rare earth element enrichment.

3.1.4 Sulfide Iron Formation

The sulfide iron formation at Red Lake is composed of either pyrite or pyrrhotite or both in the same sample and is commonly associated with carbonaceous black slate. This type of deposit is readily identified in the field by oxidation of iron sulfide minerals, the presence of white sulfate salts and sometimes by pyrite nodules. It is often ambiguous to differentiate the sulfide iron formation from carbonaceous shale because black shale usually contains iron sulfide minerals. However, sedimentary rock with more than 20% iron minerals is considered as iron formation (James, 1954).

Sulfide iron formation is plentiful in the EBL-27, NGI-31, and PB-32 holes but limited in the PB-33 hole (Figure 3.30). A deeper water assemblage of approximately 130 m thickness is contained in the EBL-27 hole where sulfide iron formation occurs near the bottom of the hole. Additionally, a 13 m thick sulfide iron formation is interlayered with black slate and oxide iron formation in the deeper water chemical sedimentary package. At the top of EBL-27, a few 0.5 m to 1.5 m thick iron sulfide layers are underlain by carbonate units and interlayered with 0.5 m to 4.5 m thick chert beds. A ~65 m thick interval in the deeper water succession, bracketed within carbonate units, exists near the top of the NGL-31 hole. This succession contains sulfide iron formations of variable thickness (0.5 m to 5 m) which are interbedded with carbonaceous slate and oxide iron formation. On the other hand, sulfide iron formation (~15 m thick) is interlayered with carbonaceous slate and occurs near the top of the PB-32 hole where it is underlain by carbonate

and overlain by chert. Furthermore, the core sections where they are sulfides interlayered with black slate or disseminated as cubes show their textures better in the drill-core than in outcrops. The slabbed core samples with sulfide minerals in black slates contain pyrite as thick to thin layers and as blobs of dull golden to brass yellow colour. The layering is composed of laminae of variable thickness ranging from a few mms to cms. In core samples, pyrrhotite occurs primarily as dark bronze coloured patches to well-layered laminae.

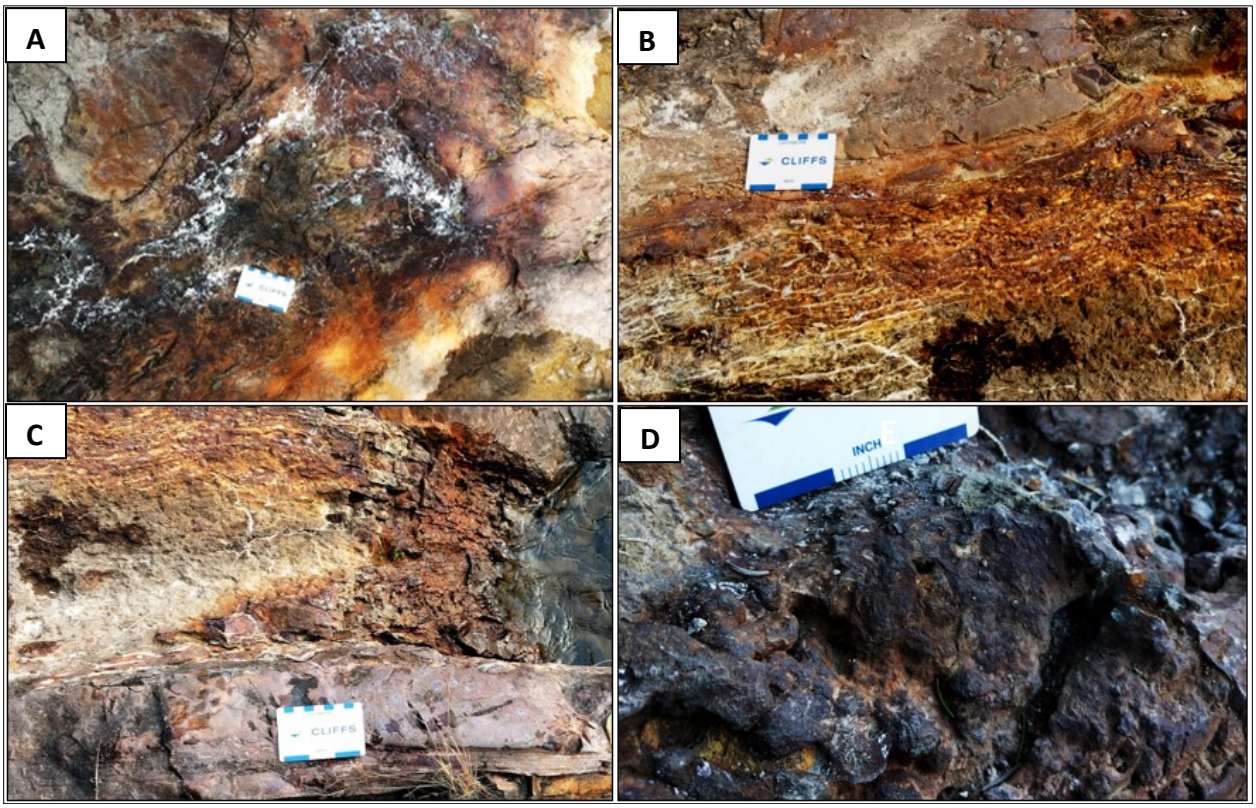

Figure 3.21: Sulfide iron formation in outcrops. (A) Rusty weathered iron sulfide with white sulfosalts in outcrop -1 in the Bridget Lake area. (B) and (C) Highly weathered iron sulfide in contact with massive chert in outcrop - 3. (D) 0.5 cm to 1 cm diameter pyrite nodules present in sulfide iron formation in outcrop - 1 in the Bridget Lake area.

Highly weathered sulfide iron formations were observed occurring with massive chert and oxide iron formation in two outcrop locations. The sulfide iron formations look massive, but it is

difficult to see any textures because of weathering. However, pyrite nodules of roughly 0.5 cm to 1 cm diameter are present in the weathered sulfidic iron bed of outcrop - 1 at Bridget Lake. The thickness of this sulfide iron formation is from 22 cm to 50 cm, and it has sharp contacts with adjacent oxide iron formation and chert. Four sets of highly weathered sulfide iron formations of variable thickness from 15 cm to 80 cm were observed in outcrop – 3, which is ~ 600 m east of the Bow Narrows fishing lodge. They are interbedded with oxide iron formation and chert and have sharp upper and lower contacts with them.

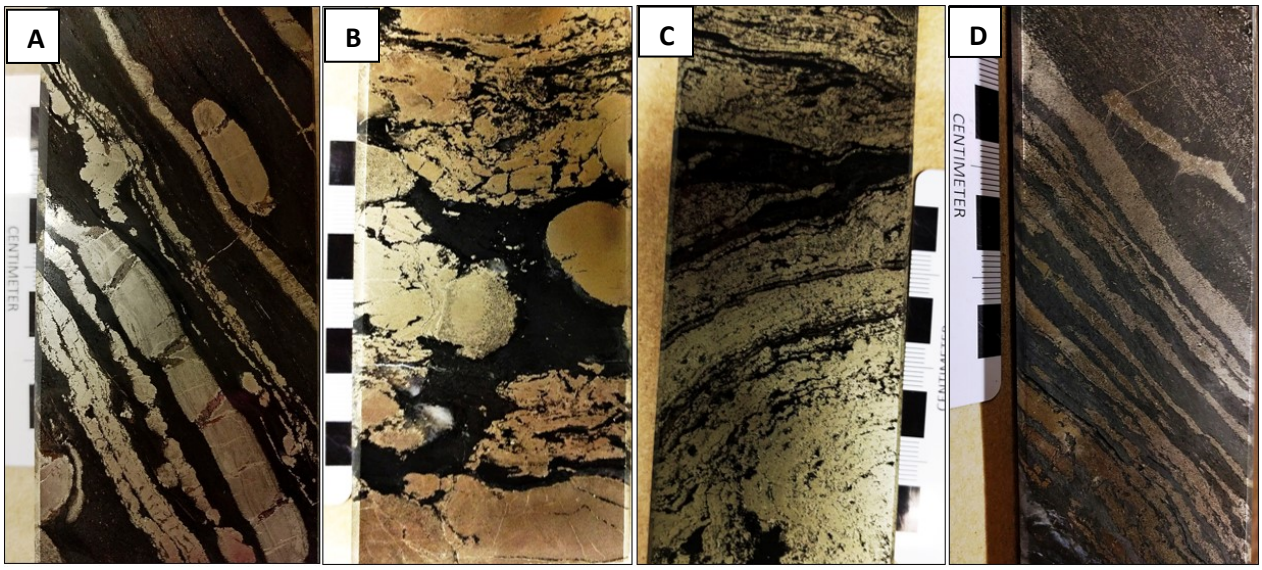

Figure 3.22: Sulfide iron formation in polished core slabs showing in (A) mm- to cm-scale pyrite layers separated by carbonaceous mudstone, in (B) >1 cm diameter pyrite nodules disseminated in black slate, in (C) coalesced mm-scale crenulated pyrite lamination, and in (D) mm- to cm-scale pyrrhotite layers separated by carbon-rich mudstone layers that abruptly changes in abundance upward.

The polished core slabs show the occurrence of thin sulfide layers with black slate. However, massive pyrite layers of 5 cm to 10 cm thick are also present in core samples. The pyrite and pyrrhotite layers are parallel, almost straight to slightly wavy, with sharp contacts with the carbonaceous slate (Figure 3.22-A, D). Lamination thickness of pyrite varies from a few mm to 1

cm and are separated by mm- to cm-scale layers of carbonaceous mudstone (Figure 3.22-A). Pyrite nodules of sub-rounded to rounded shape and > 1 cm in diameter are scattered throughout some areas of the black slate unit (Figure 3.22-B). Some nodules are fractured, and some appear to coalesce. In Figure 3.22-C the mm-scale crenulated, coalesced pyrite laminations alternate with black slate and the proportion of pyrite is greater than siliciclastics. In Figure 3.22-D this pyrrhotite-rich sample contains 1 mm to 0.5 cm thick pyrrhotite laminations separated by carbon-rich mudstone, and the upper part has mm-scale delicate laminae of pyrrhotite.

Geochemistry of Sulfide Iron Formation

XRF scanned false-color images of sulfide iron formation samples show the elemental zonation created by the interlayering of pyrite or pyrrhotite layers with carbonaceous slate layers (Figure 3.23). However, the bottom left corner of the pyrrhotite sample (top photos) is cherty which is conspicuous from the Si image in Figure 3.23-D. Similarly, the Si map of the pyrite sample shows that chert content increases toward the top right side of the sample (Figure 3.23-I).

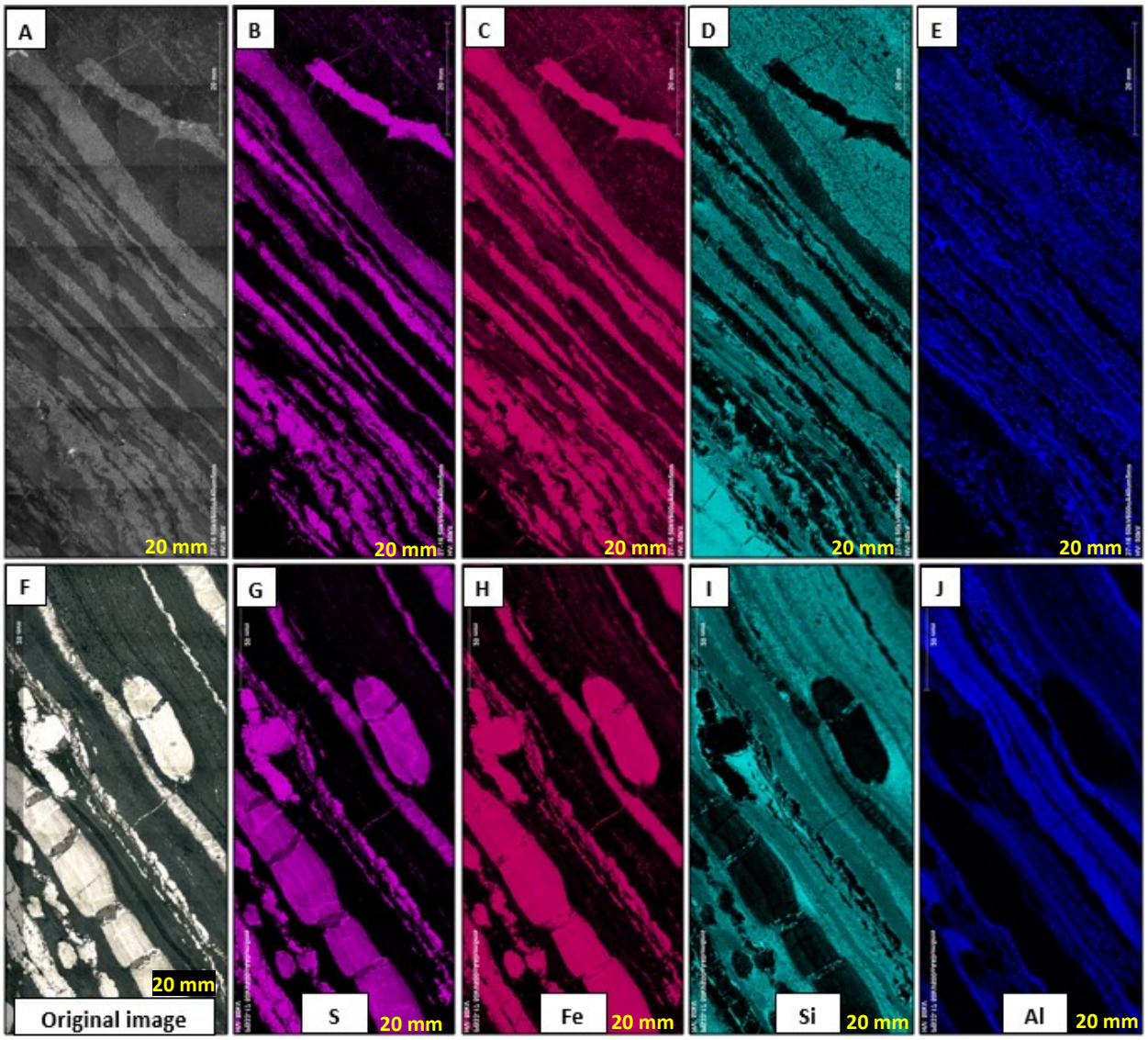

Figure 3.23: XRF scanned false-color images of core slabs of sulfide iron formation. The top five photos represent the elemental composition of a pyrrhotite sample while the bottom five pictures represent the elemental composition of a pyrite sample.

One sulfide iron formation present in the bottom portion of EBL-27 drill-hole contained small amounts of sphalerite (ZnS) and chalcopyrite ($CuFeS_2$) (Figure 3.24-A, B, C). These are anhedral in shape, < 0.2 mm in size and are intergrown with pyrite. Backscattered electrons false-color images and SEM elemental mapping also highlights the co-occurrence of pyrite and pyrrhotite (Figure 3.24-D, E). These images display large euhedral pyrite recrystallized over

anhedral pyrrhotite and the recrystallized pyrite exhibits typical polygranular texture. Such co-occurrences indicate the iron sulfides have undergone replacement reactions making original phases difficult to ascertain.

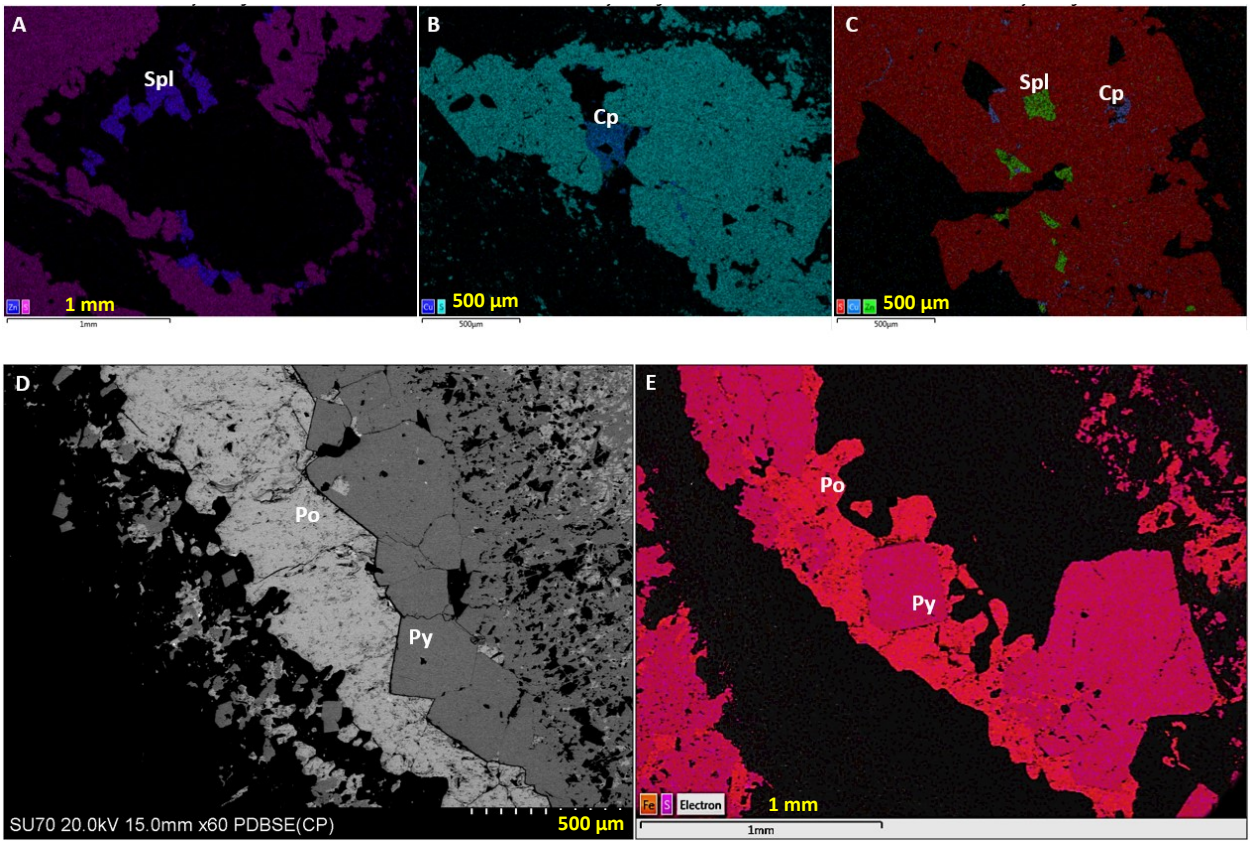

Figure 3.24: (A), (B), and (C) SEM-EDS mineral map of iron sulfides showing the presence of sphalerite (spl) and chalcopyrite (cp). BSE image of iron sulfide sample showing (D) co-occurrence of pyrite (Py) and pyrrhotite (Po). (E) SEM-EDS mineral map depicts recrystallized euhedral pyrite (Py) over an anhedral pyrrhotite (Po) layer.

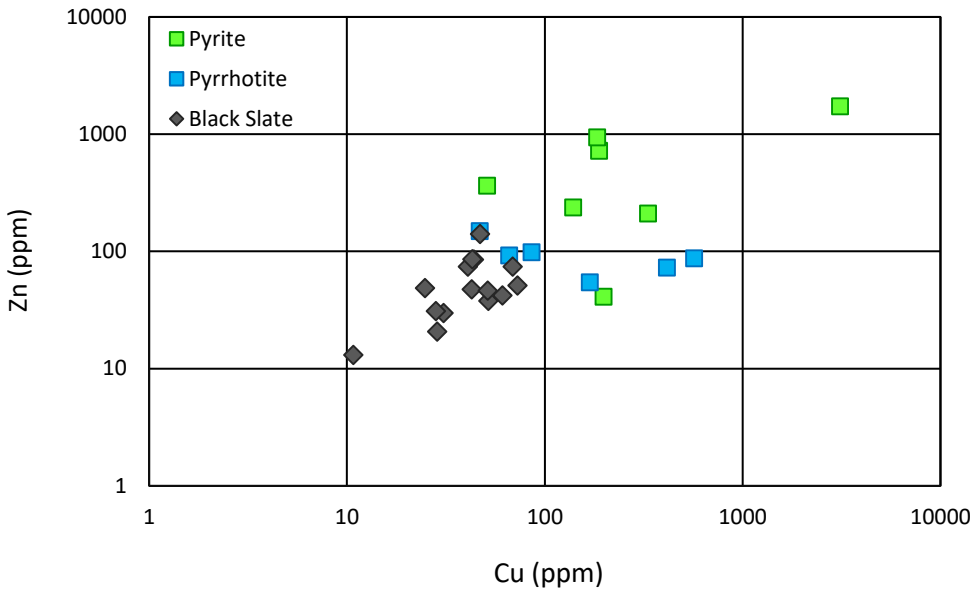

Figure 3.25: Cu vs. Zn plot of iron sulfides, and black slate samples showing most of the pyrite samples have higher presence of Zn and Cu whereas the pyrrhotite samples have low Zn, but some have high Cu content. Increased presence of these elements is an indication of the influence of high-temperature hydrothermal fluid.

Figure 3.25 illustrates the Cu and Zn content present in the pyrite and pyrrhotite rich samples and black slate samples. The graph shows that most pyrite samples have higher copper and zinc values than the pyrrhotite samples. Pyrrhotite samples have low Zn content but a higher amount of Cu. Siliciclastic black slate has both lower Cu and Zn content than most of the sulfide iron formation samples. As sphalerite and chalcopyrite minerals usually form close to the chimney or vent sites due to high-temperature hydrothermal venting, their elevated presence in sulfide samples is possibly an indication of high-temperature hydrothermal input (Hekinian et al., 1985).

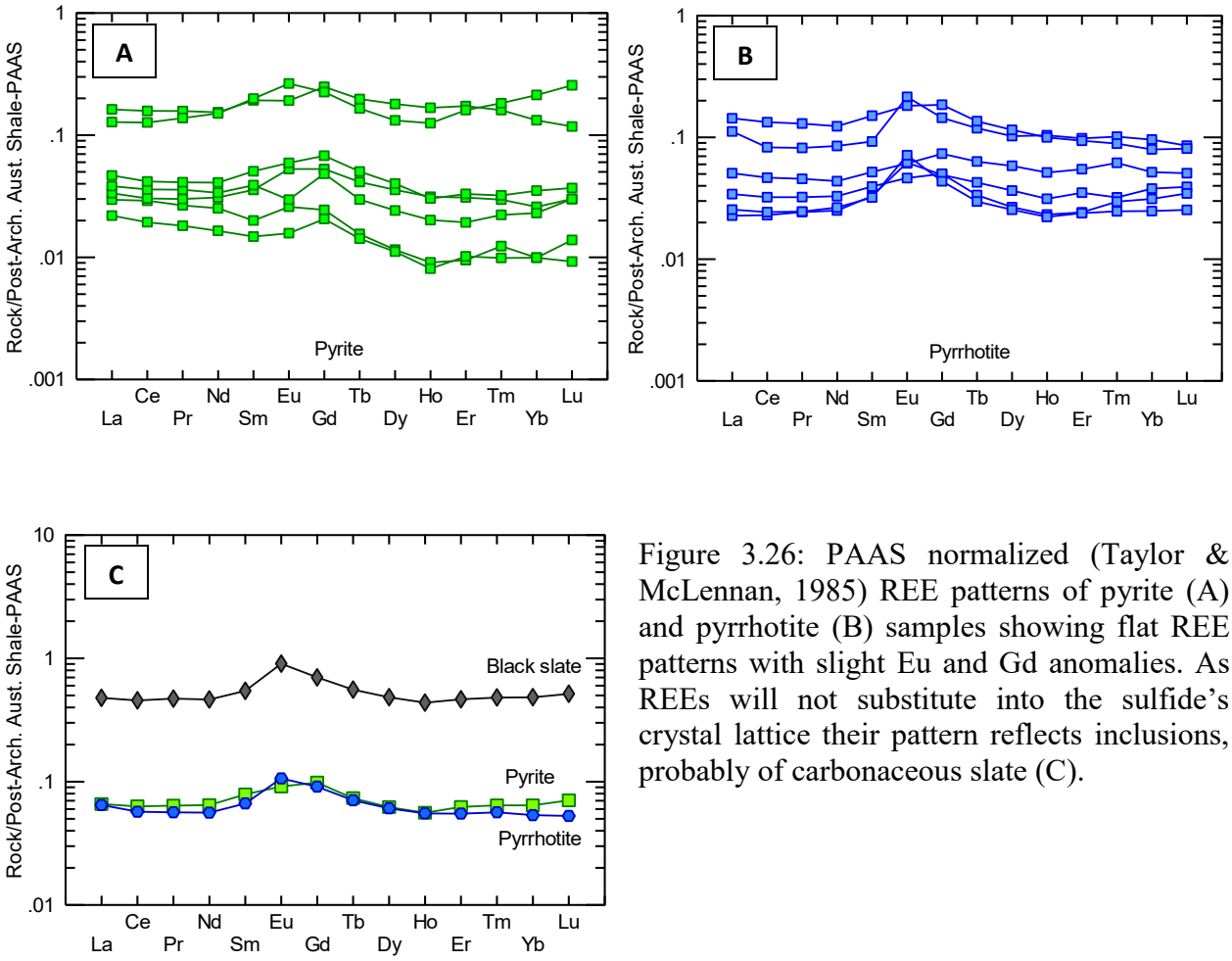

Figure 3.26: PAAS normalized (Taylor & McLennan, 1985) REE patterns of pyrite (A) and pyrrhotite (B) samples showing flat REE patterns with slight Eu and Gd anomalies. As REEs will not substitute into the sulfide's crystal lattice their pattern reflects inclusions, probably of carbonaceous slate (C).

The Al_2O_3 vs. TiO_2 plot is not used here because sulfide iron formations occur in intimate association with black slate and samples are more or less influenced by these siliciclastics. The REE systematics of sulfide iron formation is discussed in Chapter Four. Briefly, sulfide iron formation displays flat REE patterns like the black slate. The REEs cannot substitute into the pyrite or pyrrhotite lattices, thus they must be contained in inclusions in the sulfides. This explains the similarity between the REE patterns of carbonaceous slate and the sulfides (Figure 3.26 C), as the inclusions donating REEs to the sulfides are most likely siliciclastic- and carbon-rich.

3.1.5 Carbonaceous Slate

Carbonaceous slates are organic carbon-rich (TOC up to 5 %) metamorphosed carbonaceous black shale that has developed cleavage and is rare in outcrop due to weathering of the soft rock. Red Lake black slates are mainly composed of muscovite, feldspar, and quartz. Pyrite is more or less commonly associated with carbonaceous slate. Pyrite occurs in black slates as thin laminae, as disseminated small cubes, and as irregular aggregates. Some samples contain spessartine, a Mn-rich garnet.

Black slate is common in drill holes and is mostly massive (i.e., no preserved sedimentary structure inside layers) (Figure 3.30). Near the bottom the EBL-27 hole has a 10 m thick black slate layer that is in association with sulfide iron formation and chert. Moreover, there are several black slate layers of variable thickness (0.5 m to 3 m) present throughout the ~130 m thick deeper water assemblage. Near the top of the PB-32 hole, there is a 40 m thick deeper water chemical sedimentary package which contains a ~10 m thick black slate unit. Carbonaceous slate of approximately 25 m thickness is present in the upper part of the PB-33 hole where it is underlain and overlain by carbonates. In the PB-34 hole, there is a deeper water assemblage of ~90 m thickness in which a number of thin (< 1 m) black slate layers are interbedded throughout the succession, with a ~8 m thick black slate layer occurring at the top of the assemblage. This 8 m thick black slate layer is underlain by sandstone and overlain by carbonate. Unlike PB-34, the PB-35 hole contains several 5 m to 10 m thick black slate units alternating with siltstone and this whole succession is overlain and underlain by carbonates. The other drill holes have a somewhat meagre abundance of carbonaceous slate.

Black slate is common in drill core samples and is mostly massive (Figure 3.27 A). In Figure 3.27 B, the pyritic laminations in black slate are very thin, parallel, slightly wavy, commonly discontinuous and mm size pyrite cubes are sprinkled near the top.

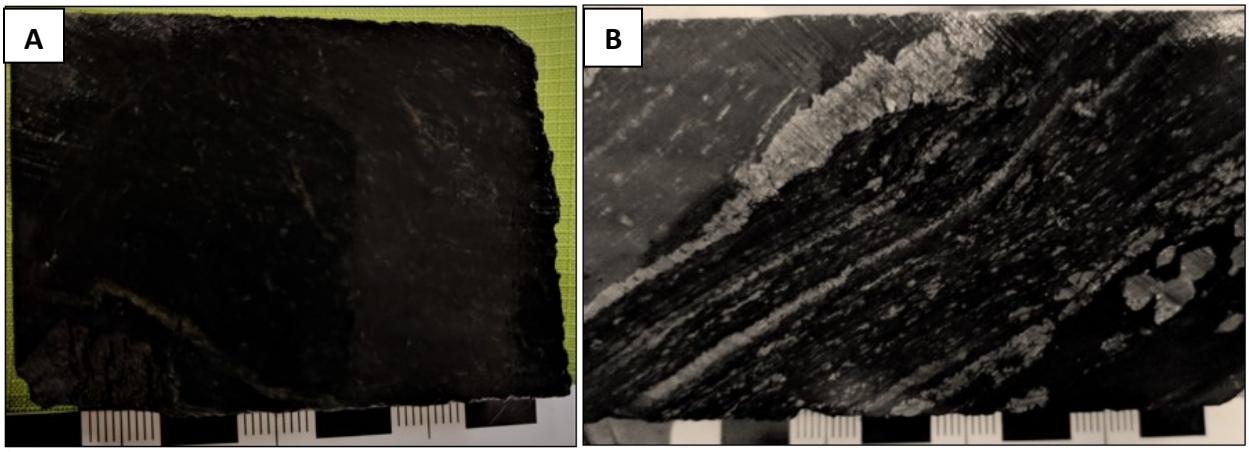

Figure 3.27: (A) Slabbed massive black slate core section and (B) polished core of black slate with thin pyrite laminae.

Geochemistry of Black Slates

SEM elemental false color mapping and spot analyses were conducted in order to determine the composition of black slates. Spot analysis shows the presence of quartz, plagioclase feldspar, muscovite, and pyrite minerals in the black slate. Some samples have an occurrence of spessartine, a manganese-rich garnet.

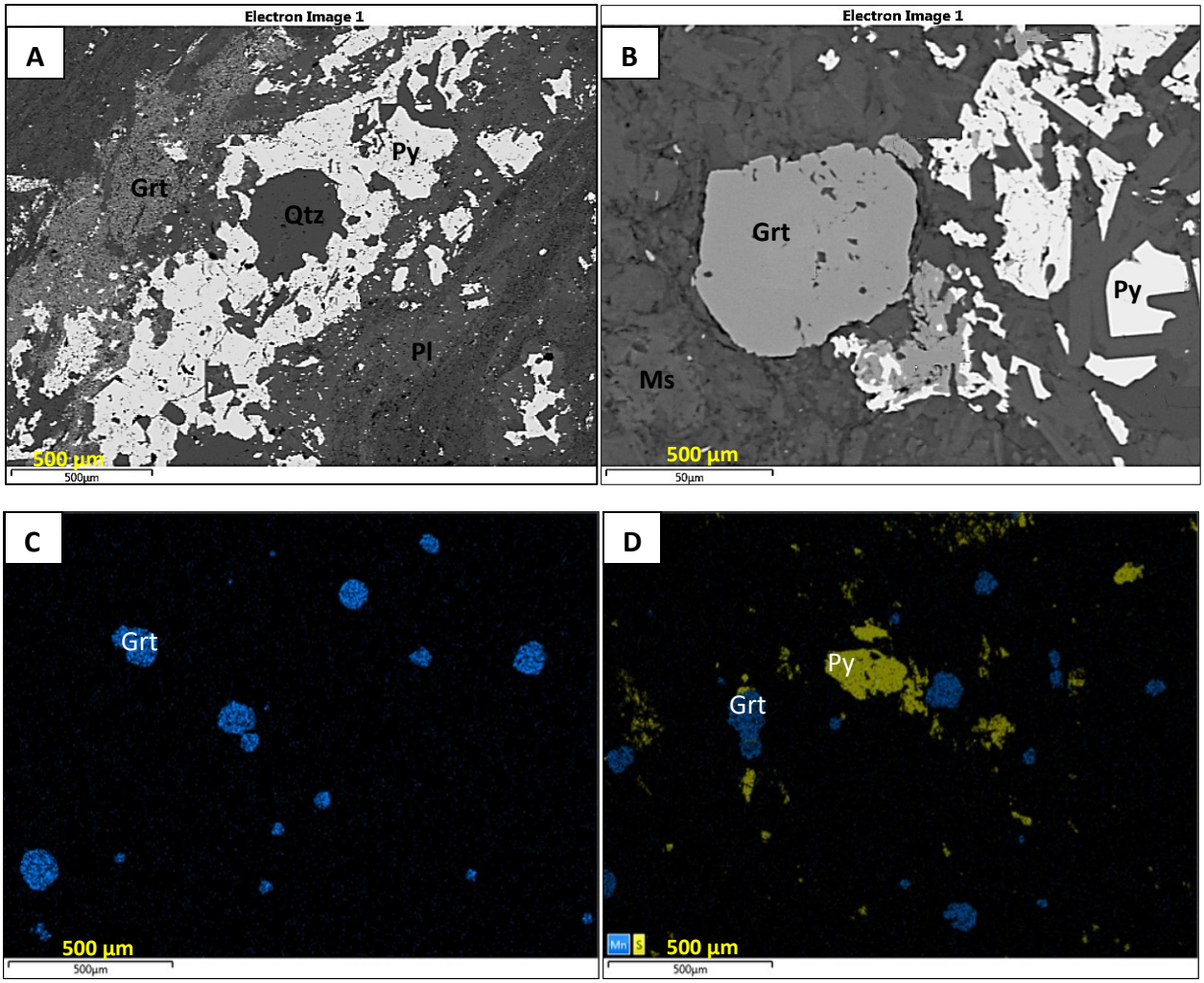

Figure 3.28: (A) and (B) SEM spot analysis showing the presence of quartz (Qtz), plagioclase feldspar (Pl), muscovite (Ms), pyrite (Py), and garnet (Grt). (C) and (D) SEM-EDS elemental mapping of black slate showing the presence of garnet and pyrite.

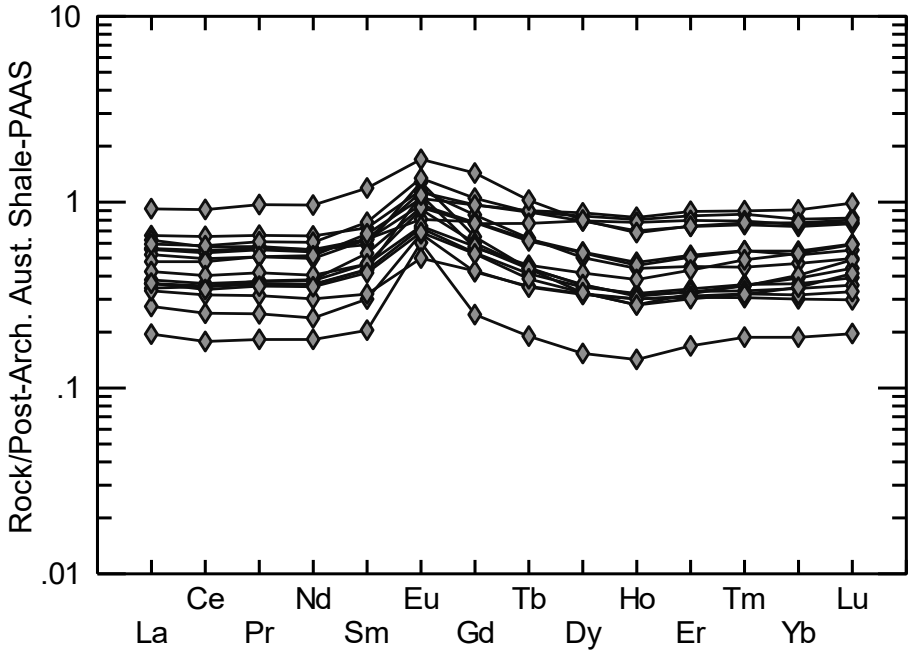

Figure 3.29: PAAS normalized (Taylor & McLennan, 1985) black slate samples have flat REE patterns with slight positive Eu and Gd anomalies.

PAAS normalized REE systematics of black slate samples show relatively flat REE patterns with slight positive Eu anomalies and common Gd anomalies. The systematics of REEs of black slate is discussed in Chapter Four.

3.2 Lithofacies Association

As mentioned earlier in the methodology section continuous core from eleven drill-holes was described and based on the core descriptions lithofacies columns were made. The lithofacies correlation panel (Figure 3.30) displays the 200 m thick, shallow water carbonate succession underlain, overlain, and intercalated with the deeper water chert, oxide iron formation, sulfide iron formation, and carbonaceous slate. Oxide iron formation and sulfide iron formation are prominent in EBL-27 and NGI-31 holes but are rare in EBL-29, Bl-37, BL-38, PB-32, PB-33, PB-34, and PB-35 holes and are absent in EBL-28 and PB-36 holes. Black slates are ubiquitous in all the drill

doles. Lastly, there are several sandstones and conglomerates, and volcanic units both below and above the Red Lake carbonate platform.

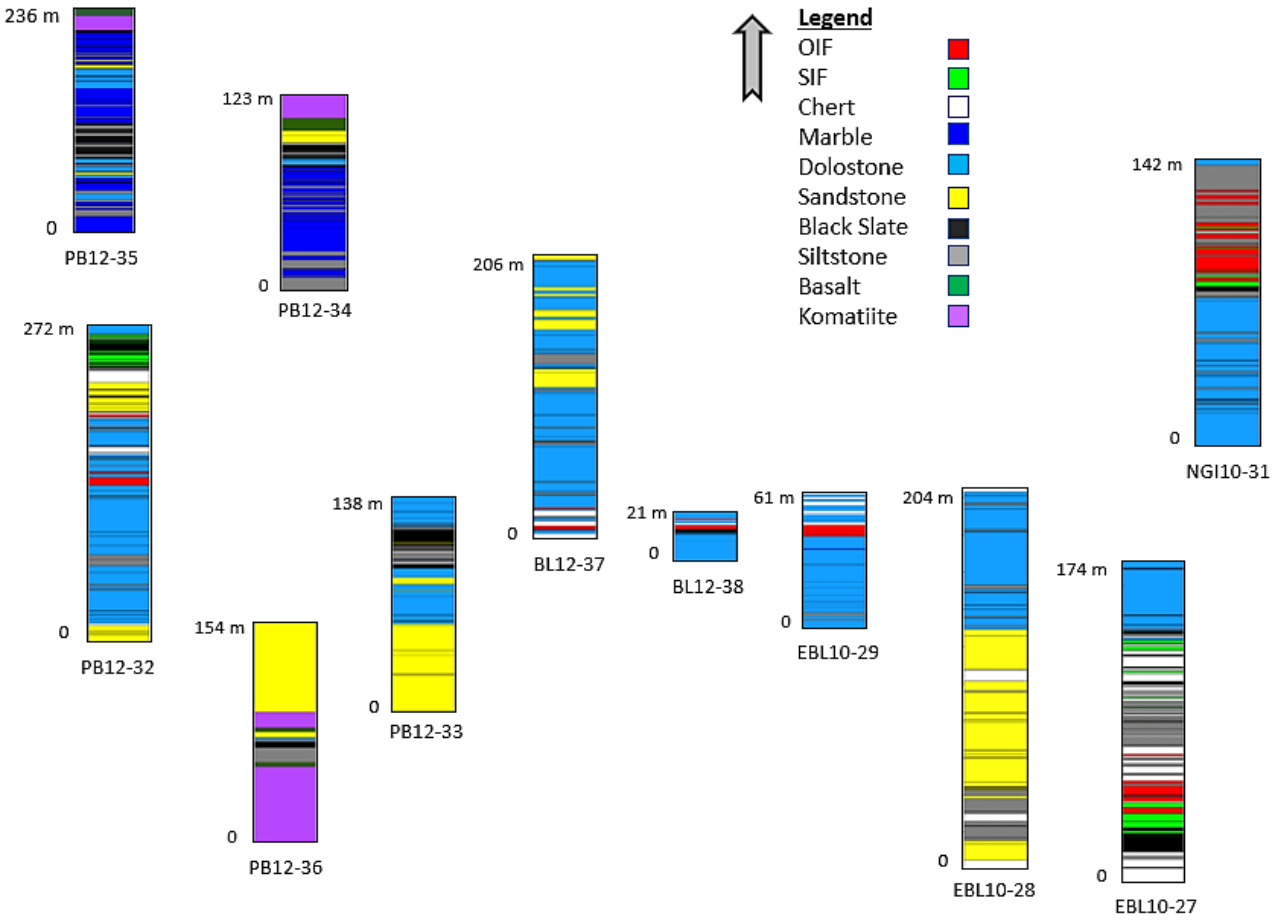

Figure 3.30: Lithofacies correlation panel of the drill holes in Pancake Bay, Bridget Lake, East Bridget Lake and North Galena Island of the western Red Lake area. The stratigraphic columns show that shallow and deep water chemical sediments are associated with siliciclastics and bracketed by volcanic events.

Chapter 4: Results and Discussion

In this chapter, the geochemistry of different types of chemical sedimentary rock and black slate are discussed, and the depositional environment of these sedimentary rocks are described based on field observation, core data, and geochemistry.

4.1 Rare Earth Element Systematics

Rare earth element (REE) chemistry is commonly used as a proxy in geochemical studies of chemical sediments to decipher ancient and modern ocean chemistry due to their stable, immobile nature and resistance to diagenetic change (McConchie, 1987). Rare earth elements include the fifteen elements of the lanthanide series as well as scandium (Sc) and yttrium (Y). The latter two elements are considered REEs because their chemical properties are similar to the lanthanides and they tend to occur together in ore deposits with the lanthanides. These elements have trivalent charges, their ionic radius decrease systematically with consecutive atomic numbers, and usually occur together in nature. These properties make them useful indicator for geochemical processes in oceans, rivers, estuaries, lakes and groundwater (Johannesson & Zhou, 1999; Shields & Stille, 2001; Kamber et al., 2004; Bolhar et al., 2005; Bolhar & Van Kranendonk, 2007; Allwood et al., 2010; Planavsky et al., 2010; Fralick & Riding, 2015). The lanthanide series elements are often divided into two groups: light rare earth elements (LREEs), which comprise La, Ce, Pr, Nd, Sm, Eu and Gd, and heavy rare earth elements (HREEs), which include Tb, Dy, Ho, Er, Tm, Yb, and Lu. Sometime Sm, Eu, Gd, Tb and Dy are included in a third group called middle rare earth elements (MREEs) (Stosch, 2002). In modern seawater, heavy rare earth element influx is relatively greater than light (Elderfield et al., 1990), while middle rare earth element enrichment is common in organic-rich areas (Hannigan & Sholkovitz, 2001).

Chemical sediments precipitated from seawater provide significant information about ocean chemistry. In particular, REE composition of precipitates reflects the water chemistry from which they precipitated (Barrett et al., 1987; Bau & Dulski, 1996b; Bau & Möller, 1993; Bekker et al., 2010; Bolhar et al., 2004; Danielson et al., 1992; Derry & Jacobsen, 1990; Kamber & Webb, 2001; Planavsky et al., 2010; Van Kranendonk et al., 2003). Rare earth element concentrations in seawater reflect their occurrence in a combination of river runoff, hydrothermal input and aeolian transport (Elderfield, 1988). In modern seawater, continental weathering input via river runoff and aeolian action dominates over the hydrothermal input of the primitive ocean (Danielson et al., 1992; Kamber & Webb, 2001). Rare earth element systematics of marine precipitates reflect ocean chemistry because their deposition is largely controlled by ocean water chemistry. Hence, marine sediments are used as a proxy for modern and ancient ocean water as they can provide important clues to the ocean water chemistry and the environmental changes related to the precipitation of sediment. Modern seawater has a shale normalized positive La anomaly, negative Ce anomaly, slightly positive Gd anomaly, slight negative Eu anomaly, depletion of LREEs relative to HREEs, and super-chondritic Y/Ho ratios greater than ~44 (Shields & Stille, 2001; Bolhar et al., 2005; Bolhar & Van Kranendonk, 2007; Planavsky et al., 2010). Many of these properties are similar to the ancient chemical precipitates and used for delineating a marine origin. However, in the Archean ocean, hydrothermal activity was the major source and control of REE abundances (Danielson et al., 1992; Bau & Dulski, 1995; Bolhar et al., 2004).

It is common to use shale normalized spider diagrams to display REE compositions of ancient ocean precipitates relative to the average composition of Post Archean Australian Shale (PAAS) (Nance & Taylor, 1976; Taylor & McLlnnan, 1988; Planavsky et al., 2010). Normalizing the REEs to PAAS allows a spider diagram to deviate from a flat pattern caused by siliciclastic

contamination and display anomalies. PAAS normalized REE data were plotted (Figure 4.1) for magnetite, chert, pyrite, pyrrhotite, and carbonate samples. These show values <1, indicating that REE concentrations in the Archean oceans were depleted relative to PASS. The REE patterns of these chemical sediments and siliciclastic black slate and their anomalies are described below.

4.1.1 Eu Anomaly

Iron formation older than 2.5 Ga shows significant Europium (Eu) enrichment, but the trend decreases towards the early Proterozoic (Danielson et al., 1992). In modern seawater, the Eu/Eu* ratio has a slightly negative anomaly (Kamber et al., 2004). Eu* anomalies occur when Eu^{+3} is partially reduced to Eu^{+2}, and this redox potential is strongly dependent on temperature. Eu changes its state from Eu^{+3} to Eu^{+2} with increasing temperature, and no positive Eu anomaly arises in low temperature (< 250ºC) hydrothermal fluid (Danielson et al., 1992; Peter, 2003). High-temperature hydrothermal fluids circulating through the oceanic crust leach Eu^{+2}, replacing Ca^{+2}, from plagioclase feldspar (Fowler & Doig, 1983). Thus, a positive Eu anomaly is indicative of high-temperature hydrothermal inputs into the ocean. In Archean iron formations, Eu anomalies normally range from 1.0 to 4.29, and average 2.1 (Planavsky et al., 2010). Eu anomaly (Eu/Eu*) is calculated by the formula: $Eu/Eu^* = Eu_{(SN)}/[0.67Sm_{(SN)} + 0.33\ Tb_{(SN)}]$, where SN means shale normalized, which uses Post Archean Australian Shale (PAAS) (Bau & Dulski, 1996b; McLennan, 1989).

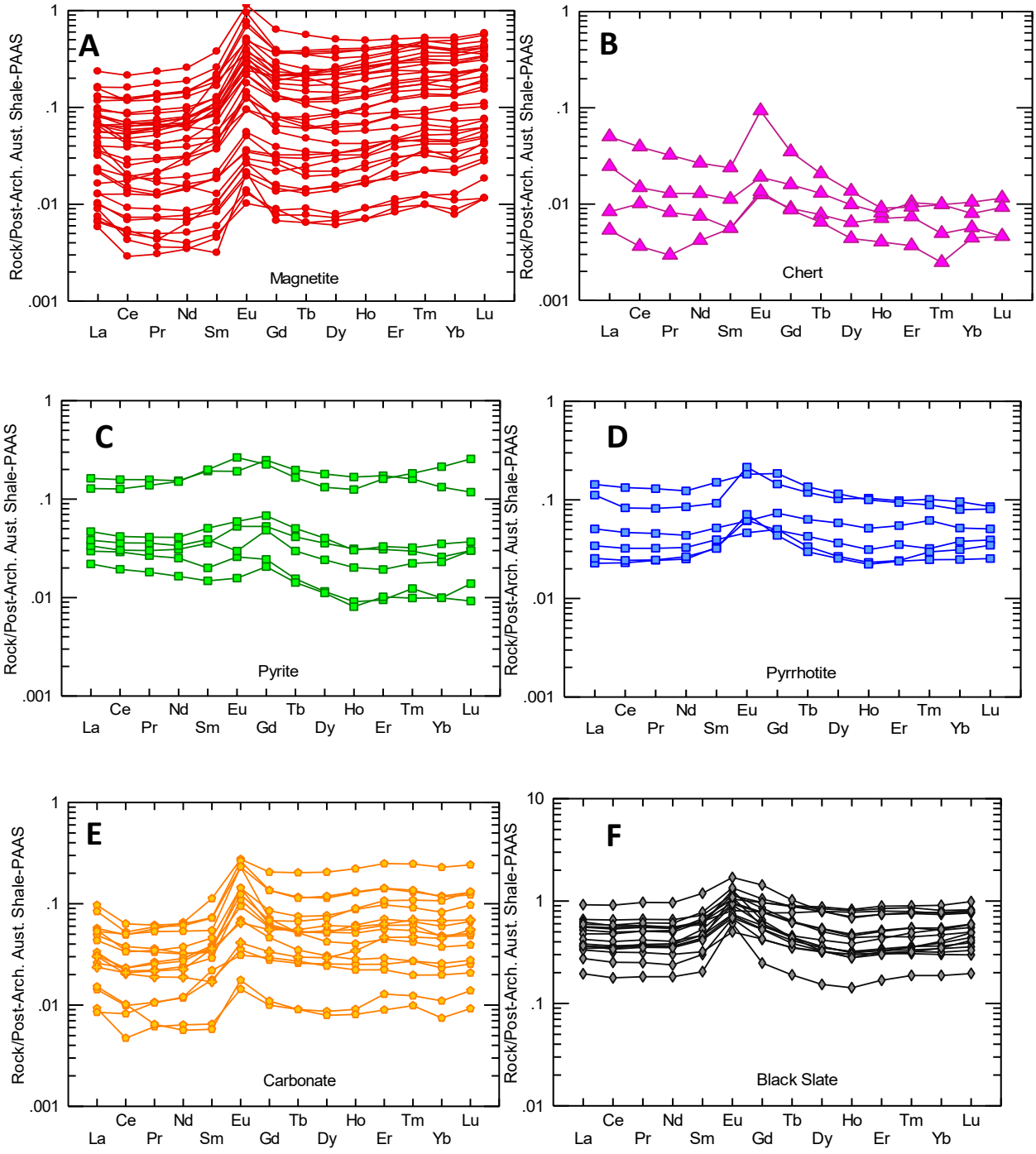

Figure 4.1: PASS normalized (Taylor & McLennan, 1985) spider diagrams of Red Lake chemical sediments and siliciclastic black slate showing the REE patterns of (A) Magnetite, (B) Chert, (C) Pyrite, (D) Pyrrhotite, (E) Carbonate, and (F) Black Slate.

Among the Red Lake chemical sediments, the magnetite samples have Eu anomalies between 1.0 and 3.24, with an average of 2.2, which is similar to the average Archean iron

formations' Eu anomaly of 2.1 (Planavsky et al., 2010). The Red Lake iron formation's positive Eu anomalies are similar to typical Archean iron deposits, e.g. Geraldton and Terrace Bay areas, north of Lake Superior, Canada; Kuruman iron formation, South Africa and banded iron formation in the Warrawoona Group, Pilbara Craton, Australia (Barrett et al., 1987; Bau & Dulski, 1995; Bolhar et al., 2005). This implies that the fluids in the depositional environment of the iron formation had this anomaly and therefore, it may be concluded based on the ubiquitous presence of Eu anomalies that the Archean ocean had a positive Eu anomaly produced by high-temperature Eu^{+2} leaching from plagioclase feldspar in ocean crust basalts and komatiites by circulating fluids due to the influence of direct hydrothermal inputs (Barrett et al., 1987; Danielson et al., 1992). Likewise, sediments derived from this process show positive Eu anomalies as the Archean ocean was being enriched in Eu compared to other rare earth elements (Danielson et al., 1992; Bau & Dulski, 1996). Hence, the presence of positive Eu anomalies in carbonate and siliciclastic black slate indicates that they inherited the seawater composition of the Archean ocean (Danielson et al., 1992; Bau & Dulski, 1996; Planavsky et al., 2010). However, pure chert does not contain REEs because they will not fit into the lattice framework. The REE concentration in pure chert falls typically below the detection limit. A few of the Red Lake chert sample could not be plotted in the spider diagram because of this reason. Thus, the REE patterns found in chert are not derived from the chert, instead, they come from other accompanying materials in the chert.

Surprisingly, among the sulfide iron samples, a few of the pyrrhotite samples have typical Eu anomalies expected of the Archean ocean while most of the pyrite samples have low Eu anomalies associated with Gd anomalies (Figure 4.1-C). As iron sulfides are similar to chert in that they cannot contain REEs in their crystal lattice these signatures must originate by other means. The absence of REEs in pyrite and pyrrhotite mean that the REE patterns in Figures 4.1 C

and D probably originate from fluid inclusions and crystal defects (Zhao & Jiang, 2007). More important is the sulfides' association with black slate, thus, the presence of any little amount of siliciclastics can form a REE pattern similar to the black slate samples (Figure 3.26 C).

Oxide iron formation and carbonate rocks show an overall positive slope of their patterns (Figure 4.1-A and 4.1-E). Moreover, LREE depletion compared to the HREEs is typical in Archean iron formations (Bohlar et al. 2005, Allwood et al. 2010) and a similar trend is observed in the REE plots of the magnetite samples in the Red Lake area. However, the opposite trend (i.e., HREE depletion) is observed in the chert, pyrite and pyrrhotite samples (Figure 4.1-B, 4.1-C and 4.1-D) which, as stated earlier, must be the result of inclusions and/or crystal defects in the chert and iron sulfides.

4.1.2 La and Ce Anomaly

As La and Ce anomalies are related, it is better to plot them together to distinguish the anomalies (Fig. 4.2). Bau and Dulski (1996) described that anomalous concentrations of Lanthanum (La) in seawater could produce false negative Ce anomalies in chemical sedimentary rocks. They introduced a new set of equations to determine whether the chemical sediments are displaying a Ce anomaly or not. The following equations were used to differentiate La and Ce anomalies in chemical sediments: La anomaly $(Ce/Ce^*) = Ce^*/(0.5La_{SN})+(0.5Pr_{SN})$

$$\text{Ce anomaly } (Pr/Pr^*) = Pr^*/(0.5Ce_{SN})+(0.5Nd_{SN})$$

where Ce/Ce^* is the La anomaly, Pr/Pr^* is the Ce anomaly and La_{SN}, Ce_{SN}, Pr_{SN} and Nd_{SN} are the geochemical analysis values divided by the PAAS value.

If $(Pr/Pr^*)_{SN} > 1.05$, then it indicates a prominent negative Ce anomaly similar to modern shallow seawater. A negative Ce anomaly is a common characteristic of modern oxic seawater where Ce^{3+} is oxidized to Ce^{4+} (Goldberg et al., 1963; Elderfield & Greaves, 1982; Peter, 2003) which results in precipitation of CeO_2 or adherence to iron oxyhydroxide (Elderfield & Greaves, 1981; Peter, 2003; McIntyre & Fralick, 2017). However, if there is an enrichment of La relative to Ce then $(Ce/Ce^*)_{SN} < 0.95$ and it indicates a positive La anomaly. The presence of a positive La anomaly is suggestive of uncontaminated marine REE signatures for shale-normalized REE patterns (Bau & Dulski, 1996; Kamber & Webb, 2001).

Shale normalized Ce anomalies are widely used to deduce ancient redox conditions of the oceans (Shields & Stille, 2001; Bohlar et al., 2005; Allwood et al., 2010; Planavsky et al., 2010). A negative Ce anomaly occurs in an environment where Ce^{+3} is oxidized to Ce^{+4}, which is highly insoluble in seawater, therefore, it is preferentially scavenged and absorbed onto Fe-Mn oxyhydroxide surfaces, or it can partition into octahedral sites of precipitates (Sholkovitz et al., 1994; Bau & Dulski, 1996b; Bolhar et al., 2004; Planavsky et al., 2010; Tostevin et al., 2016). The fluid is then left with a negative Ce anomaly which will be inherited by any precipitates that later form from it.

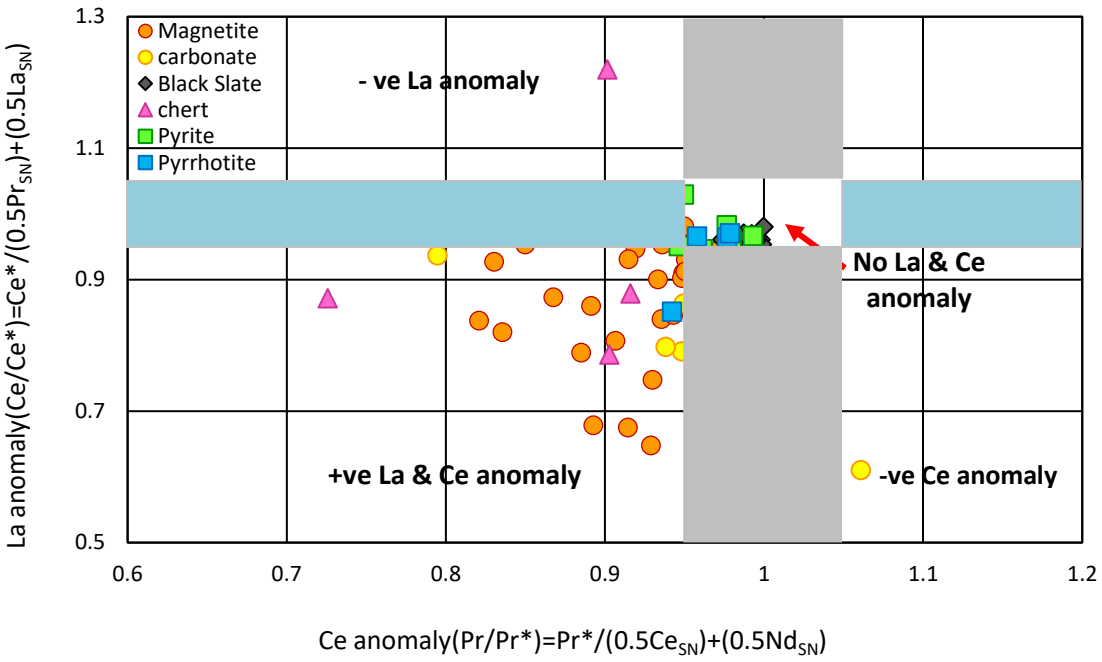

Figure 4.2: PAAS-normalized Ce anomaly (Pr/Pr*) versus La anomaly (Ce/Ce*) plot (modified after Bau & Dulski, 1996). This plot differentiates between La and Ce anomalies. The shaded area represents no La and Ce anomaly as defined by Planavsky et al., (2010).

In Figure 4.2, some of the magnetite and chert samples and a few of the carbonate samples plot in the positive La and positive Ce anomaly field suggestive of precipitation from a Ce present anoxic water column. The presence of a positive Ce anomaly in oxide iron formation indicates that the iron hydroxide formed in an environment where Ce found O_2 to form CeO_2 and preferentially co-precipitated with the iron hydroxide (de Baar et al., 1988; Tostevin et al., 2016). Almost all the sulfide iron formation and black slate samples plot in the middle white area representing no La and no Ce anomaly. One chert sample has a negative La anomaly. In contrast, most of the carbonate and some of the magnetite samples fall in the no Ce anomaly field and some magnetite and a few iron sulfide plots in the no La anomaly field. Negative Ce anomaly is uncommon in this plot, but one carbonate sample derived from the topmost part of the carbonate platform plots in the negative Ce anomaly field, which indicates that this sample precipitated from a Ce depleted water column.

However, due to the presence of a positive Ce anomaly in the Red Lake oxide iron formations, it is assumed that there was a presence of some oxygen in the Mesoarchean off-shore deeper ocean during the deposition of Red Lake iron hydroxides.

4.1.3 Gd Anomaly

Gadolinium (Gd) anomalies are calculated using the equation described by Bau and Dulski (1996). They showed that the size of the Gd anomaly in modern seawater is relatively small ($Gd_{SN}/Gd^*_{SN} < 1.21$). Gadolinium anomalies are generally used to determine the ligand types that control surface complexation of REEs on marine particles (Lee & Byrne, 1993; Bau & Dulski, 1996a).

$$Gd_{PAAS}/Gd^*_{PAAS} = Gd_{PAAS}/(0.33Sm_{PAAS} + 0.67Tb_{PAAS})$$

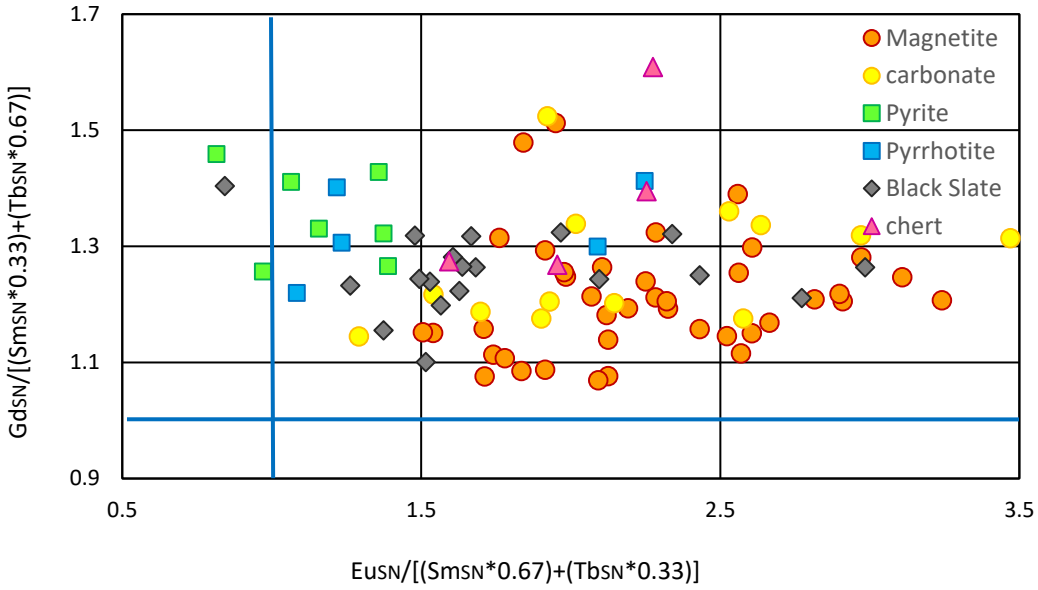

Figure 4.3: PAAS-normalized Gd anomaly versus Eu anomaly plot (modified after Bau and Dulski, 1996). This plot discriminates between Gd and Eu anomalies. The blue line represents the Eu and Gd anomalies zones where $(Eu)_{SN} > 1$ and $(Gd)_{SN} > 1$ are indicative of positive Eu and Gd anomalies respectively. Only two of the sulfide iron samples and one black slate sample have negative Eu anomalies.

A Gd and Eu anomaly plot of the Red Lake chemical sediments is shown in Figure 4.3. If $(Eu)_{SN} > 1$, then it indicates a positive Eu anomalies while $(Gd)_{SN} > 1$ indicates positive Gd anomalies. All chemical sediments (i.e., oxide iron formation, chert, and carbonate) cluster in the field of positive Eu anomalies except a few sulfide iron formations and one black slate sample. Among the sulfide iron samples, all pyrrhotite plots on the positive Eu anomaly field like the other chemical sediments whereas two pyrite samples and one black slate sample plot on the negative Eu anomaly field. Similarly, all chemical sediments and siliciclastic black slate has some degree of positive Gd anomaly. However, most of the magnetite samples have slight positive Gd anomalies, while pyrite, pyrrhotite and black slate samples have high Gd anomalies. The reason for scavenging of Gd in marine sediments is uncertain.

It is still unknown if positive Gd anomalies are created completely within the marine environment or sourced somewhat from continental run-off (Bau & Dulski, 1996a). However, Bau and Dulski (1996) analyzed river and stream water samples and defined that pristine rivers do not show Gd anomalies. But the rivers which are used for draining wastewater from industrial and populated areas are characterized by pronounced positive Gd anomalies, and Bau and Dulski (1996) identified this as an anthropogenic origin of Gd anomalies. Though the detail of this explanation is irrelevant for Gd anomalies present in Archean marine precipitates, there may be a relation with Gd scavenging by organic matter complexation, which can be predicted from Gd anomalies found in modern wastewater.

4.1.4 Y/Ho Plot

The Y/Ho ratio, a useful indicator of the purity of marine sediments, is used to monitor the siliciclastic contamination of REE patterns. Siliciclastic influence can reduce the primary seawater

signature such as La, Ce, Eu, and Gd anomalies and flattens the REE patterns (Webb & Kamber, 2000; Peter, 2003). The Y/Ho weight ratio for crustal rocks ranges from 26 to 28 (Kamber & Webb, 2001). The Y/Ho ratio of modern seawater varies between 44 and 120 and can shift towards chondritic compositions (~28) by addition of siliciclastics and volcanic ash (Nozaki et al., 1997; Webb & Kamber, 2000; Bolhar et al., 2004). Generally, the Y/Ho ratio of Archean carbonates is >44 (Kamber & Webb, 2001), and Red Lake carbonates have Y/Ho ratios of ~ 51. Archean iron formations are characterized by higher than chondritic (>40) Y/Ho ratios (Planavsky et al., 2010), and Red Lake magnetite samples have Y/Ho ratios of ~ 42. The Y/Ho ratios of carbonate (~51), iron formation (~42) and chert (~42) are noticeably higher than the PAAS shale ratio of 26. In contrast, the black slates' Y/Ho ratio is ~27, and the sulfide iron samples have Y/Ho ratios of ~25, which is reasonable as sulfide iron formation is associated with black slate and probably inherits it's REE signature from inclusions of this material. Thus, any siliciclastic contamination will lower the Y/Ho ratio in chemical sediments. It is a common practice to plot Y/Ho ratio against immobile elements such as Al_2O_3. A linear trend should indicate contamination by siliciclastic (Kamber & Webb, 2001; Bolhar et al., 2004). Plots of Y/Ho and Al_2O_3 in Figure 4.4 display no correlation between them, except at high Al values). However, the blue line in the graph is the PASS composite value, and most of the samples are above the line, which indicates siliciclastic contamination is minimal. Some of the sulfide iron formation samples are plotted on/near the line, which indicates that these samples have a siliciclastic influence to some extent.

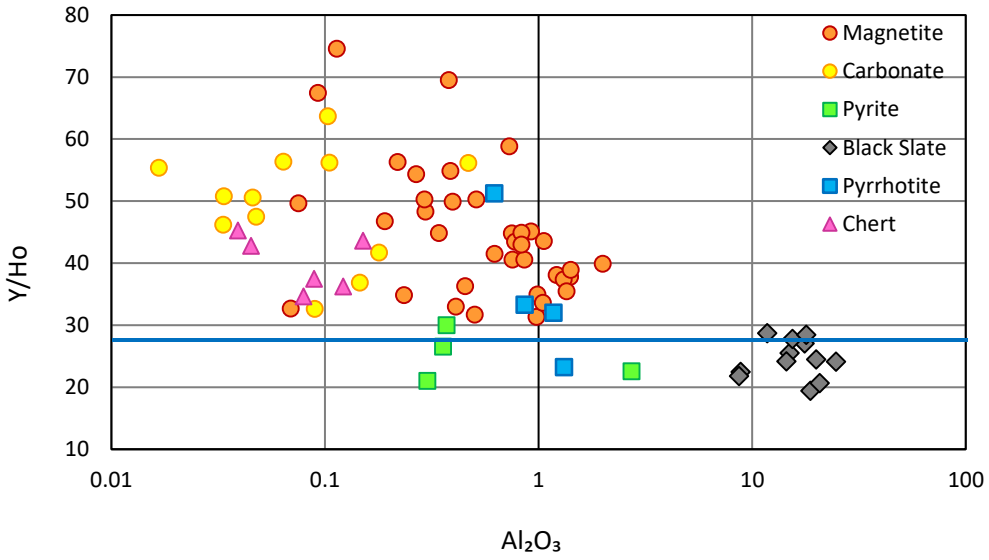

Figure 4.4: Plot of the Y/Ho ratio against the immobile element Al_2O_3. The blue line represents the average PAAS composition (27). Samples with less than 1 wt. % Al_2O_3 are scattered, plotting mostly above the average shale indicating lower degrees of siliciclastic contamination. A few pyrite and pyrrhotite samples plot near the average shale line indicating siliciclastic influence.

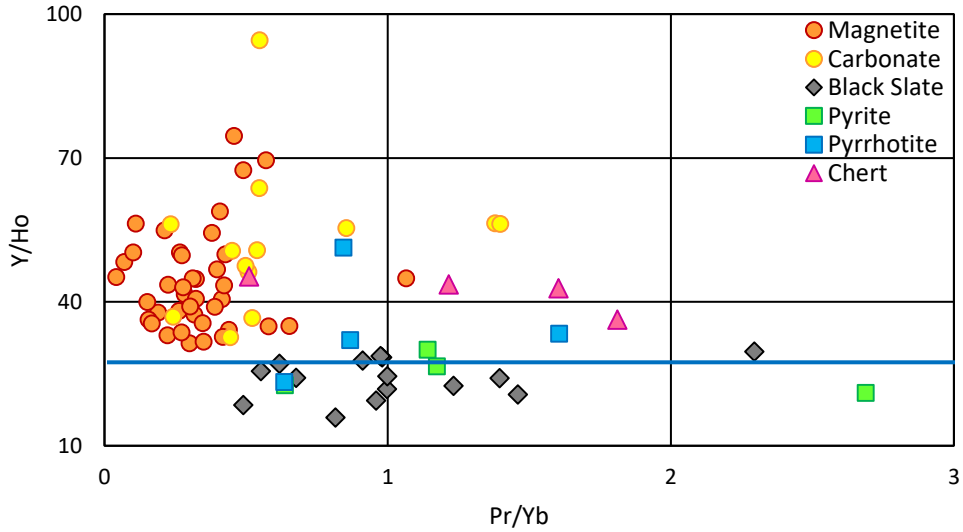

Figure 4.5: Plot of PAAS-normalized REE slope against Y/Ho ratio. The blue line is the average PAAS composition (27). Samples with slope values < 1 are scattered, plotting mostly above the average shale line and are HREE enriched. Samples with slope values > 1 are also scattered, plotting mostly above the average shale line are LREE enriched.

A plot of the PAAS-normalized light to heavy REE slope against Y/Ho ratios (Figure 4.5) shows that magnetite and carbonate samples have higher Y/Ho ratios and lower Pr/Yb ratios, which is similar to the modern seawater REE trend. This indicates that complexation and scavenging of REEs in the 2.93 Ga ocean was broadly similar to todays ocean. Siliciclastic black slate and sulfide iron formation samples have Y/Ho ratios close to the average PAAS value. This, plus their variable Pr/Yb ratios, probably resulted from mineral inclusions in the iron sulfides. Chert samples have both high Y/Ho and Pr/Yb ratios; however, the REEs present in the chert samples are not scavenged by chert; rather they are derived from mineral and fluid inclusions.

4.1.5 REE Pattern Slope

To calculate the slope of the REE curves, PAAS normalized ratios between light and heavy REEs (Pr/Yb) and medium and heavy REEs (Gd/Yb) was plotted in Figure 4.6 (Planavsky et al., 2010). The plot of these ratios is useful to determine if there is a correlation between the light to heavy rare earth elements.

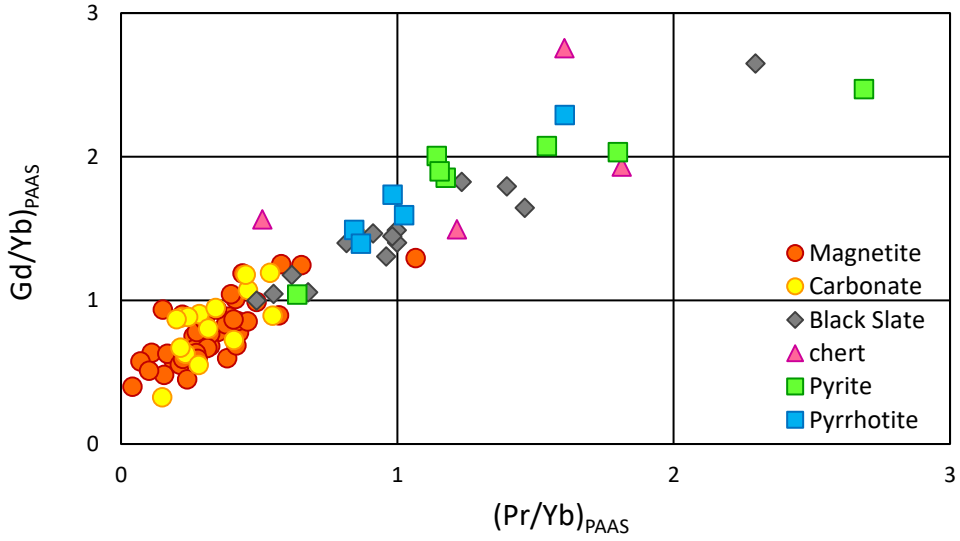

Figure 4.6: PAAS normalized Gd/Yb and Pr/Yb ratios plot showing a positive correlation between light to heavy REE and medium to heavy REE slopes.

The light to heavy REE (Pr/Yb) slopes versus medium to heavy REE (Gd/Yb) slopes can differentiate between the enrichment or depletion trends of LREEs or HREEs. Pr/Yb ratio >1 means samples are HREE-depleted and/or LREE-enriched, while a Pr/Yb ratio <1 indicates samples are HREE-enriched and/or LREE-depleted. Archean chemical precipitates derived from seawater are typically HREE enriched. The Red Lake chemical sediments show a strong positive correlation between Pr/Yb and Gd/Yb ratios. It is obvious that magnetite samples are the most LREE depleted, and next to them are carbonate samples. Alternatively, chert and most of the pyrite samples are HREE depleted. The pyrrhotite samples have a variable degree of LREE and HREE depletion/enrichment. The HREE-enriched and LREE-depleted patterns in the oxide iron formation and carbonate samples suggest that the ancient ocean had similar LREE and HREE fractionation trends as the modern ocean (Kamber & Webb, 2001).

In summary, the chemical sediments consisting of carbonate and magnetite from both shallow and deeper water environments have high positive Eu anomalies, higher Y/Ho ratios, and lower Pr/Yb ratios. These attributes suggest that the ocean was heavily influenced by hydrothermal activity and enriched in HREEs, the later is similar to the modern ocean. The positive Ce anomalies in the iron formation samples suggest that Ce was preferentially precipitating from seawater compared to the other rare earth elements. Therefore, it indicates the presence of some oxygen in deeper water during iron hydroxide precipitation events.

4.2 Redox-sensitive Elements and their Implications

Elements such as chromium (Cr), molybdenum (Mo), vanadium (V), and uranium (U) are generally derived in solution from oxidative weathering and behave similarly in the surface environment (Voegelin et al., 2010; Wille et al., 2013). The geochemical behavior of these

elements is highly sensitive to the redox condition of the ambient environment where they change valence state and act differently depending on whether or not oxygen is present (Calvert & Pedersen, 1993; Morford et al., 2001). Therefore, enrichment of redox-sensitive metals and their stable isotope variations in ancient marine sediments are used as powerful proxies, which provide implications for oxygenation of the atmosphere at, and before, the Great Oxidation Event (Anbar, 2007; Wille et al., 2013). Chemical weathering of crustal rocks and transport via river runoff is the main source of dissolved Mo into the ocean, and its precipitation from seawater occurs in both oxic and anoxic environments (McManus et al., 2002; Voegelin et al., 2010). The increase in Mo concentration in Archean sediments was interpreted as a gradual rise of atmospheric O_2 levels (Voegelin et al. 2010). Uranium rich minerals are dominantly derived from felsic igneous rocks, such as granites or pegmatites (Grandstaff 1976). Zircon, apatite, allanite, and monazite are also important accessory sources of U (Partin et al. 2013). However, riverine delivery is the main input of dissolved U into the seawater, which essentially reflects oxidative weathering of continental crust and release of rock-hosted U(IV) to soluble U(VI). Similarly, chromium (Cr) and vanadium (V) are also derived from oxidative weathering of crustal rocks and reach the ocean by river runoff. Under oxidative weathering conditions, Cr, Mo, V, and U are oxidized and transported into the ocean as soluble oxyanions (Wille et al. 2013).

To understand the atmospheric redox conditions during the deposition of 2.93 Ga old chemical sediments at Red Lake, redox-sensitive trace metal concentrations were studied. Elemental concentrations of Cr, Mo, V, and U were plotted against Al_2O_3 and TiO_2 content to determine whether they were derived from the siliciclastic phase or not. Figures 4.7 to 4.14 are logarithmic bivariate plots of Al_2O_3, and TiO_2 with Cr, Mo, V, and U respectively. Bivariate plots of geochemical elements are useful to differentiate between mobile and immobile elements in

metamorphosed sedimentary rock (McLennan, 1989; Fralick & Kronberg, 1997). The idea behind these bivariate plots is that the concentration of immobile elements will increase or decrease at a constant rate depending on the mass gain or loss of the mobile elements to/from the system, respectively. Therefore, samples containing immobile elements will form a linear array that goes through the origin (McLennan, 1989; Mclennan et al., 1993; Fralick & Kronberg, 1997).

Element pairs of Al_2O_3 vs. Cr (Figure 4.7) and TiO_2 vs. Cr (Figure 4.8) show a positive, linear correlation, which indicates Cr was immobile and derived from the siliciclastic phase in the samples. It is noticeable that the carbonate samples have very low Al_2O_3 and TiO_2, but they have a slight enrichment of Cr. The enrichment of Cr in carbonate samples in these graphs is not significant enough to use it as evidence of oxidative weathering; however, it can be a trivial indication. In Figure 4.9 and 4.10 Al_2O_3 vs. Mo and TiO_2 vs. Mo were plotted respectively. Both plots have a somewhat linear correlation, and data are scattered at a lower concentration. The correlation of Mo with Al_2O_3 and TiO_2 suggest that Mo was derived from the siliciclastic phase. Some of the pyrite and pyrrhotite samples are showing Mo enrichment, which indicates sulfidic porewaters allowed to scavenge some Mo into pyrite and pyrrhotite. The plots of Al_2O_3 vs. V (Figure 4.11) and the TiO_2 vs. V (Figure 4.12) have a somewhat linear, positive slope. Carbonate samples have below detection level concentrations of V hence, these samples are ignored in these graphs. Thus, the source of V is derived from the siliciclastic input. The U vs. Al_2O_3 graph (Figure 4.13) shows poor correlation whereas the U vs. TiO_2 graph (Figure 4.14) has a better linear trend. The linear relationship indicates that U was immobile and derived from the siliciclastic phase. Similar to Cr enrichment, the carbonate samples have slight U enrichment. Again, in these graphs, this does not appear as a strong U enrichment to support oxidative weathering of U from crustal rocks.

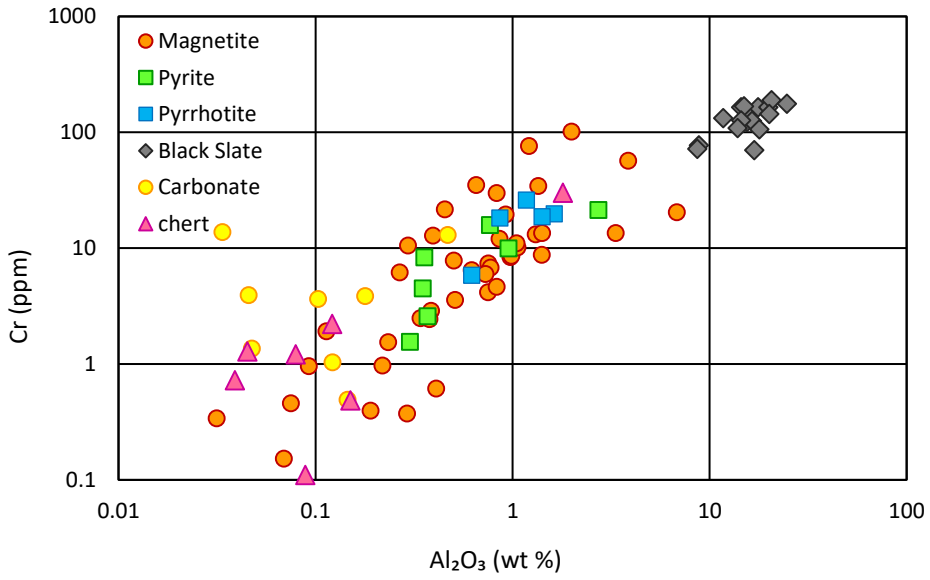

Figure 4.7: A logarithmic bivariate plot of Al_2O_3 vs Cr, which shows a positive linear correlation between Al_2O_3 and Cr. The linear relationship indicates that Cr was immobile and derived from siliciclastics.

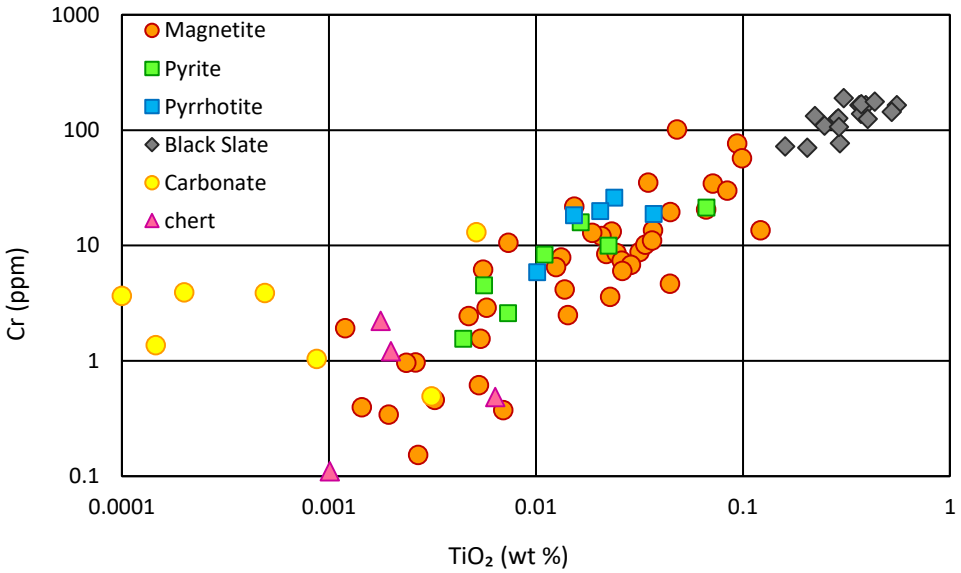

Figure 4.8: A logarithmic bivariate plot of TiO_2 vs Cr. This graph shows a somewhat positive linear correlation between TiO_2 and Cr, but at lower concentrations the data becomes more scattered. The linear correlation indicates that Cr was immobile and derived from the siliciclastic phase.

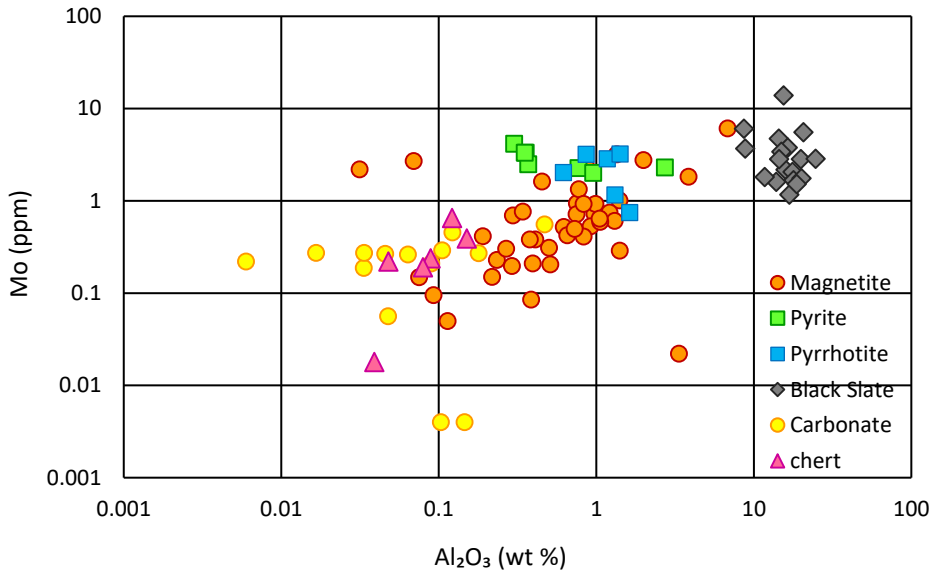

Figure 4.9: A logarithmic bivariate plot of Al_2O_3 vs Mo, where the magnetite, pyrite, and pyrrhotite samples are mostly scattered. The lack of linear correlation between Al_2O_3 and Mo suggests that Mo was derived from a non-siliciclastic phase.

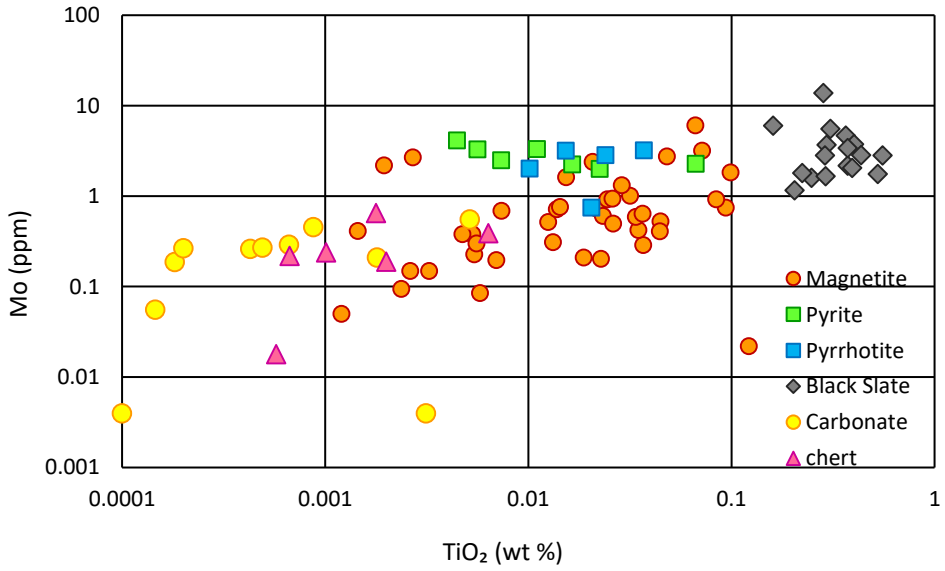

Figure 4.10: A logarithmic bivariate plot of TiO_2 vs Mo. The magnetite, pyrite, and pyrrhotite samples are mostly scattered. The lack of linear correlation between TiO_2 and Mo suggests that molybdenum was derived from a non-siliciclastic phase.

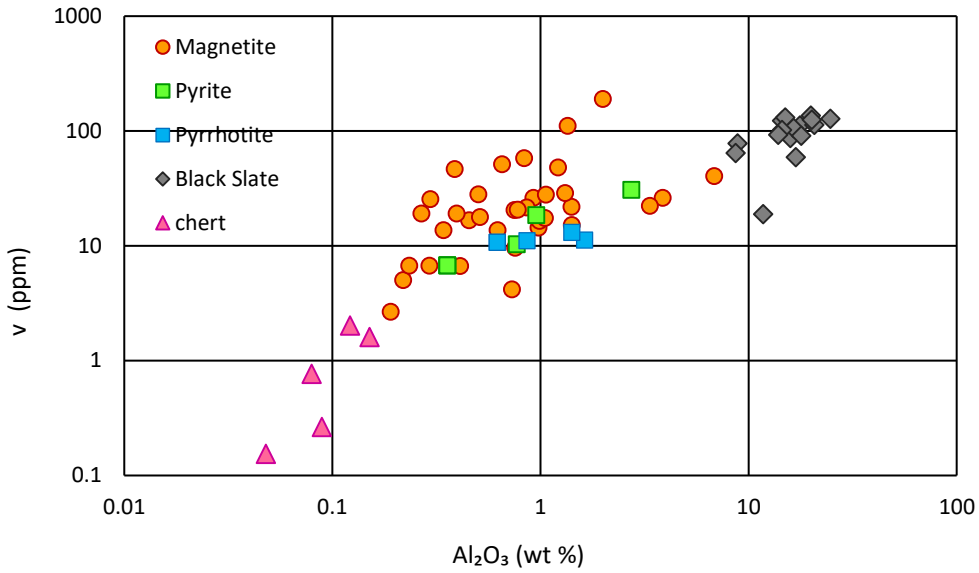

Figure 4.11: A logarithmic bivariate plot of Al_2O_3 vs V. This graph shows a linear correlation between Al_2O_3 and V but some of the magnetite samples are scattered. However, the linear trend indicates a siliciclastic influence.

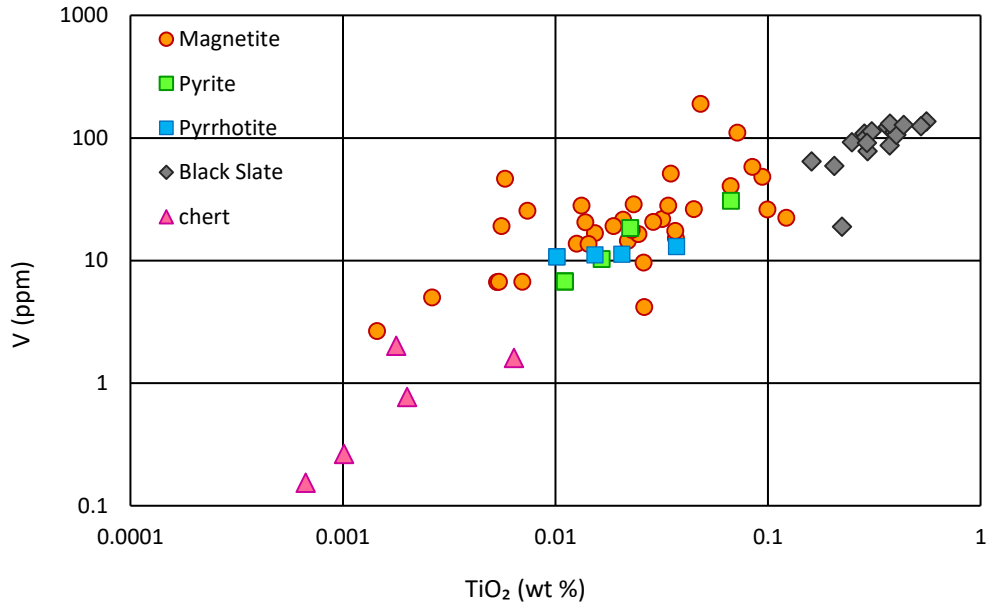

Figure 4.12: A logarithmic bivariate plot of TiO_2 vs V, which has a positive linear correlation between TiO_2 and V. However, some magnetite data are scattered, and the linear trend indicates a siliciclastic influence.

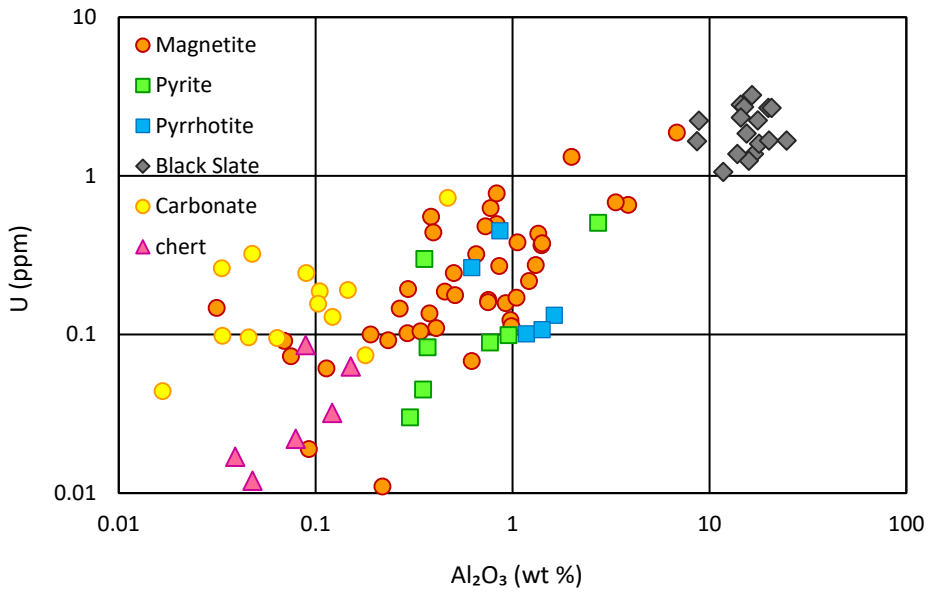

Figure 4.13: A logarithmic bivariate plot of Al_2O_3 vs U. This graph shows a somewhat positive scattered linear correlation and indicates U was partially derived from the siliciclastic phase.

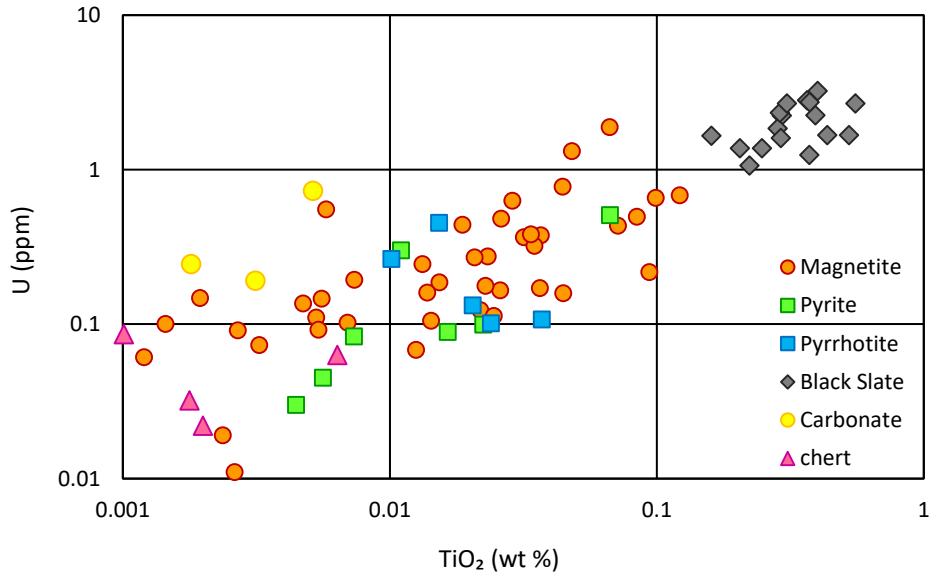

Figure 4.14: A logarithmic bivariate plot of TiO_2 vs U. This graph shows a somewhat positive scattered linear correlation between TiO_2 and U. The linear relationship indicates that U was somewhat immobile and at least partially derived from the siliciclastic phase.

In an attempt to further understand the enrichment of these elements in Red Lake chemical sediments, Cr/TiO_2 vs. V/TiO_2 ratios (Figure 4.15) and Mo/TiO_2 vs. U/TiO_2 (Figure 4.16) ratios were plotted. Both plots show that the majority of chemical sediments fall above and to the right of the siliciclastic black slate cluster, which indicates that the abundance of these elements is higher in the chemical sediments than would be expected if they were only derived from the siliciclastic phase contained in the samples of chemical sediment.

In addition, redox-sensitive element concentrations in sedimentary rocks can be expressed in terms of enrichment factors (Wedepohl 1971, 1995; Tribovillard et al. 2008). The original formula is TM/Al EF = (TM/Al sample) ÷(TM/Al average shale), where Al-normalized trace metal (TM) concentration is compared to the average shale value defined by Wedepohl (1971 and 1991). When EF >1, it indicates trace metal enrichment relative to average shale (Wedepohl 1971, 1995). Hence, to assess the relative enrichment of Cr, Mo, V, and U in Red Lake chemical sedimentary rocks compared to the siliciclastic black slate, enrichment factors of Cr, Mo, V, and U are plotted in Figure 4.17. The enrichment factor plot of Cr (Figure 4.17-A) shows that most of the carbonate samples have Cr concentrations higher than the black slate. The Mo enrichment factor graph (Figure 4.17-B) reveals that almost all chemical sedimentary rocks have EF>1. The V and U enrichment plots (Figure 4.17-C and 4.17-D) show that most of the magnetite and pyrite-pyrrhotite samples are rich in V, whereas carbonate samples are highly enriched in U along with most of the magnetite, pyrite-pyrrhotite and chert samples. Thus, the enrichment factors of these redox-sensitive elements might be an indication of slight oxidative weathering.

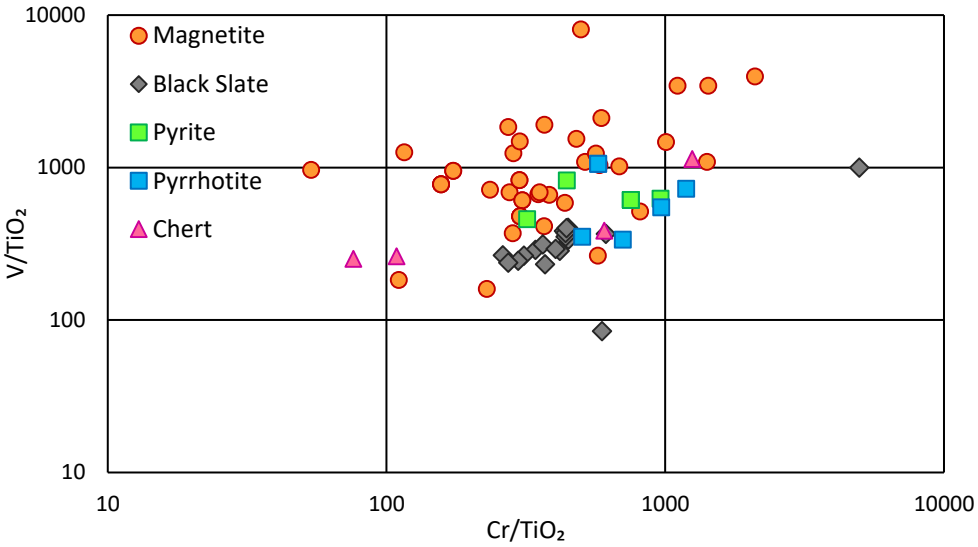

Figure 4.15: A logarithmic bivariate ratio plot of Cr/TiO_2 vs. V/TiO_2. If all elements are chemically immobile the samples will plot as a tight cluster (Fralick & Kronberg, 1997; Fralick, 2003), as most of the black slates do. However, if they have been chemically mobile, they will scatter. This type of ratio graph is more sensitive than those in Figures 4.7 to 4.14. The graph shows chemical sediments fall above the siliciclastic black slate cluster. This indicates that most magnetite, pyrite, and pyrrhotite samples contain more V than can be accounted for by their siliciclastic phase. Those plotting to the right of the slate cluster also contain more Cr than that present in their siliciclastic phase.

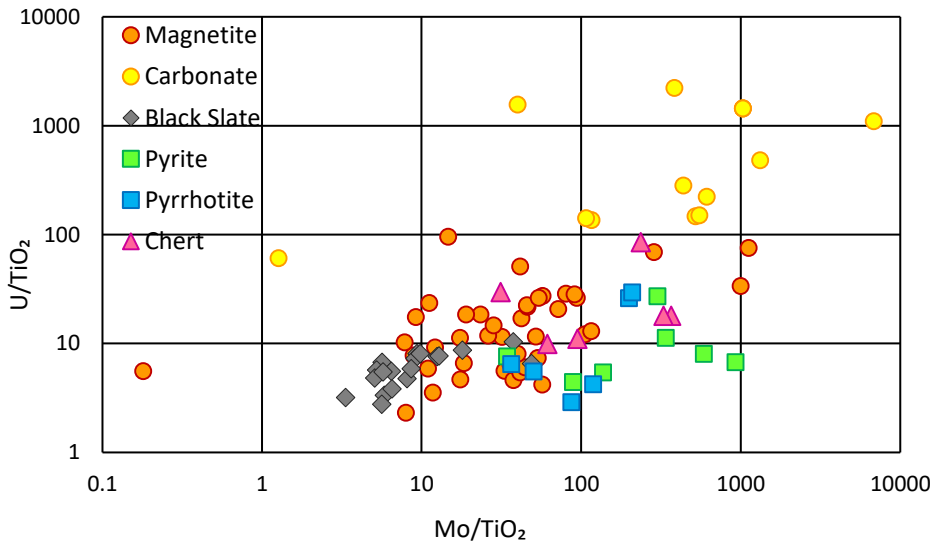

Figure 4.16: A logarithmic bivariate ratio plot of Mo/TiO_2 vs. U/TiO_2. The graph shows chemical sediments mostly fall above and to the right of the siliciclastic black slate cluster. This indicates that the majority of magnetite, carbonate, pyrite, and pyrrhotite samples have excess Mo and U not in their siliciclastic phases.

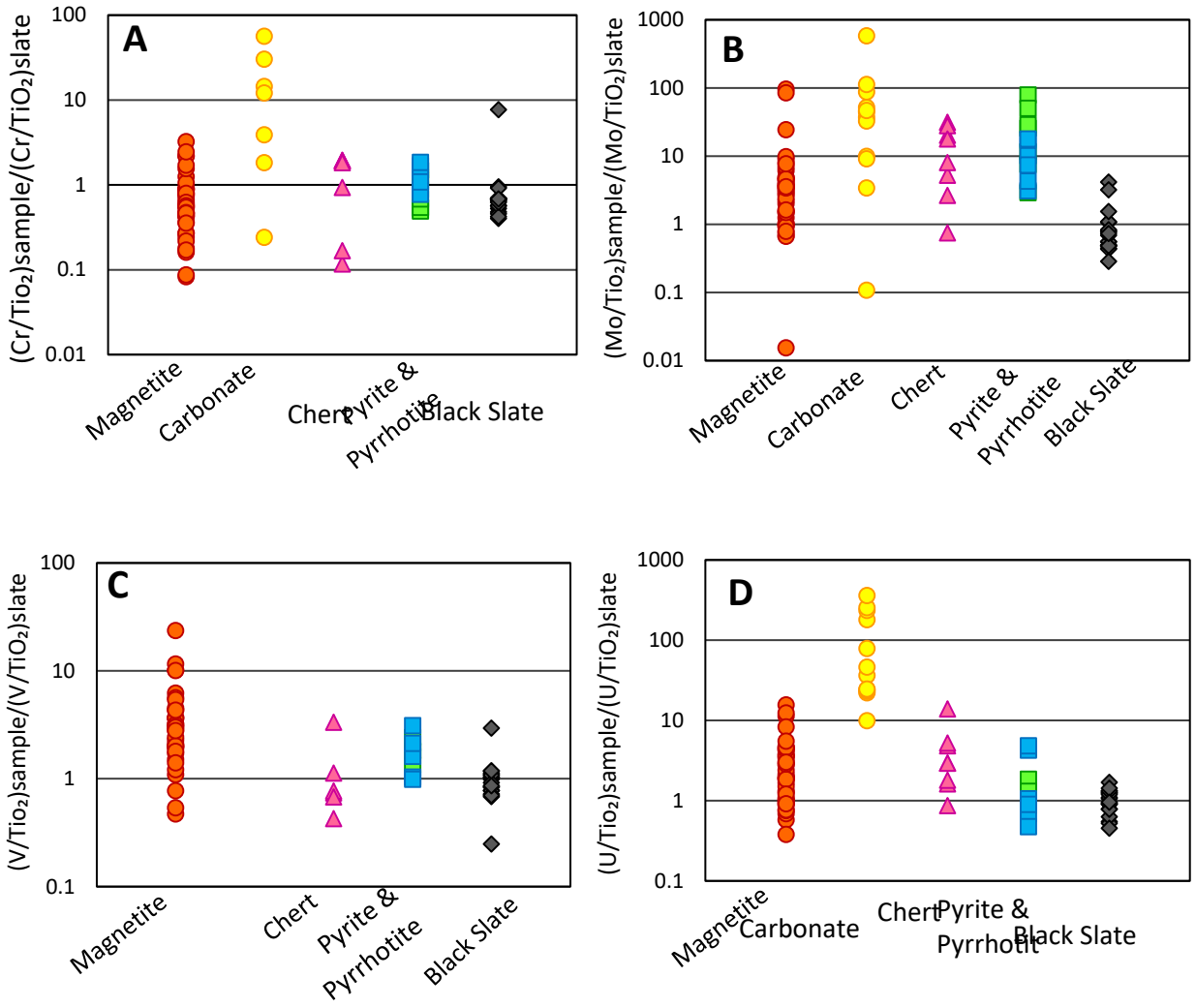

Figure 4.17: Enrichment factors of Cr, Mo, V, and U were plotted for different chemical sediments. (A) The logarithmic plot of enrichment factors of Cr shows that some magnetite, and iron sulfide samples and most of the carbonate samples have Cr concentration >1. (B) The Mo enrichment factors plot shows most of the chemical sediments have a greater abundance of Mo than the black slate. (C) The enrichment factors plot of V indicates that most of the magnetite and sulfidic iron formation samples are enriched in V. (D) The U enrichment factors graph displays a higher abundance of U in carbonate samples. Most of the magnetite and chert samples have U enrichment.

In conclusion, the redox-sensitive element graphs show that at least a portion of the V, Cr, Mo and U resides in the siliciclastic phases present in the samples. However, the ratio plots of Cr, Mo, V, and U show that the majority of Red Lake chemical sediments fall above and to the right

of the siliciclastic black slate cluster. The enrichment factors (EF) of Cr, Mo, V and U of different chemical sedimentary rocks clearly defines that if EF > 1, then it is enriched relative to siliciclastic black slate. Therefore, based on the above graphs it is suggested that chemical sedimentary rocks have enrichment of these elements to some degree beyond the siliciclastics they contain. The input of these elements was probably seawater, but the question is how did they reach the seawater. There are two possibilities, either they were derived from a high-temperature hydrothermal fluid, or they came from fluvial discharge due to mild oxidative weathering.

4.3 Manganese Enrichment in the Offshore Deeper Water Chemical and Siliciclastic Deposits

Sedimentary rock records from Precambrian to Recent indicate that manganese (Mn) minerals commonly precipitated from various sources (e.g., hydrothermal and hydro-genetic) (Ingri & Pontér, 1986; Beukes & Gutzmer, 1996; Gutzmer & Beukes, 1996; Gauthier-Lafaye & Weber, 2003). Manganese minerals associated with the iron formations of the Archean ocean generally precipitated from seawater where submarine volcanism induced hydrothermal venting was the major supplier of the Mn and Fe into the ocean (Roy, 1992; Holland, 2005). In contrast, significant deposition of Mn was initiated by the introduction of O_2 after the Great Oxidation Event (GOE) which resulted in changes in the redox condition of the ancient ocean (Anbar & Holland, 1992; Gauthier-Lafaye & Weber, 2003; Roy, 2006; Tsikos et al., 2010; Ossa et al., 2016). It is assumed that Mn and Fe emanated from high-temperature hydrothermal fluids and were retained in the anoxic seawater in dissolved form until they combined with free O_2 to form Fe-Mn-oxyhydroxide, hydroxides and oxides (Holland, 2005; Roy, 2006). In the Archean ocean, high-temperature hydrothermal plumes were the main sources of Mn and Fe, and they remained dissolved in the anoxic seawater for lengthy time periods (Roy, 1992; Holland, 2005). Typically,

Mn does not form sulfides like iron, rather remains dissolved until it oxidizes (Van Cappellen et al., 1998; Maynard, 2010; Johnson et al., 2016).

To be deposited in sedimentary rocks, Mn is oxidized from the Mn^{+2} state to either Mn^{+3} or Mn^{+4} and forms an oxyhydroxide (Calvert & Pedersen, 1993; Armstrong, 2008; Johnson et al., 2016). Presence of free O_2, therefore, is the key to the precipitation of Mn oxide. Hence, manganese oxidation indicates the presence of free oxygen(O_2) in the depositional environment, which is very significant evidence of partial or restricted oxygenation in the anoxic Archean world. In the Archean environment, the photosynthetic activity of cyanobacteria near the shoreline photic zones was the factory of O_2 production (Kasting, 1993). Thus, Mn enrichment in the geologic record of the Archean provides insight into ancient oxygen availability and the paleo-ocean redox chemistry (Maynard, 2010).

There are two hypotheses regarding Mn precipitation in the Archean which can be considered. According to Kasting (1993), free O_2 derived from localized photosynthetic activity in the basin-margin photic zones was responsible for the precipitation of Mn. In this case, oxidation of aqueous Mn^{+2} to Mn^{+3} or Mn^{+4} happened. The other hypothesis, proposed by Johnson et al. (2013), focuses on Mn-based photosynthesis. It describes photo-oxidation of Mn^{2+} where anoxygenic photobiology used Mn as an electron donor. However, this hypothesis has very little substantive evidence.

In the Red Lake carbonate platform, various degrees of Mn enrichment have been observed throughout the successions. Figure 4.18 illustrates the Mn and Fe oxide plots for different types of sedimentary rocks. As mentioned earlier, Mn and Fe can coexist from hydrothermal venting, which may explain in part the higher Mn enrichment observed in the magnetite (0.23-6.44% MnO)

samples. The carbonate samples overall have moderate Mn concentration (0.17-0.71% MnO). The variable concentration of Mn in these samples possibly indicates the inconstant availability of Mn in the carbonate depositional environment. Sulfide iron formation (0.02-0.84% MnO) and black slate (0.01-0.98% MnO) samples have very low to moderate Mn concentrations. Two of the black slate and sulfide samples with an elevated concentration of Mn were analyzed in the SEM to determine the detailed mineralogy of these samples. The black slate samples have spessartine, which is a Mn-bearing garnet. Similarly, the Mn-rich sulfide samples show the presence of Mn-rich grunerite.

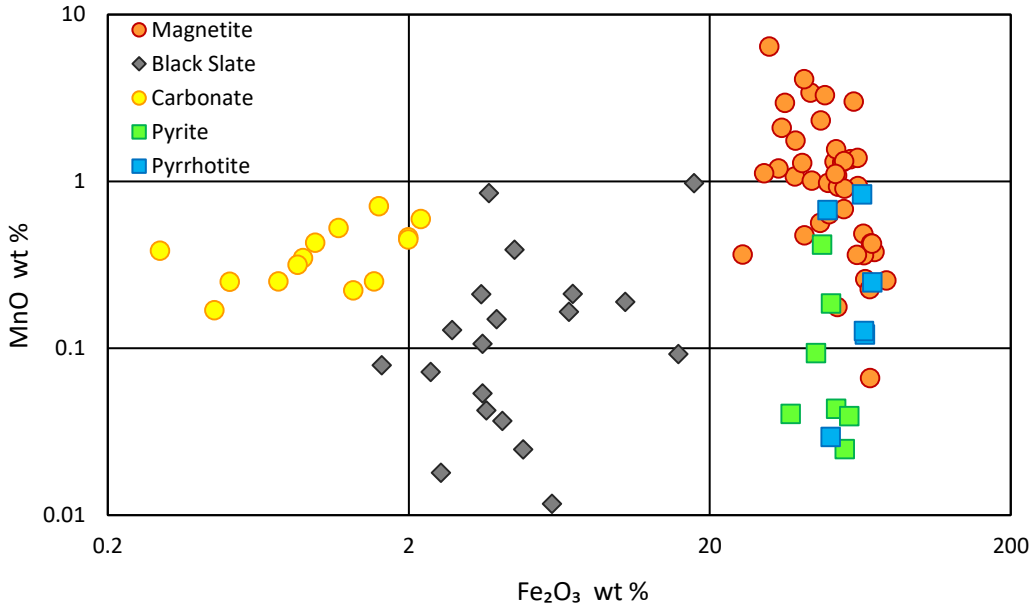

Figure 4.18: MnO wt % vs Fe_2O_3 wt. % plot of magnetite-black slate-carbonate-sulfide samples showing higher Mn concentration in some magnetite samples.

It is perplexing how Mn can occur in the black slate and the sulfide iron formations, which were the product of a pure anoxic environment. In an anoxic basin, dissolved Mn^{+2} can accumulate in the sulfidic bottom waters due to the reduction of Mn^{+4}-oxide which forms in the oxic water column above the redox boundary (Spencer & Brewer, 1971; Calvert & Pedersen, 1993). This

reaction should produce manganese sulfide (MnS), but in the Red Lake samples, the presence of MnS was not identified. However, higher Mn enrichments can denote short-term oxic and/or suboxic conditions in the depositional basin (Calvert & Pedersen, 1993; Dellwig et al., 2010; Planavsky et al., 2018). Thus, the hypothesis presumed here is that Mn was initially precipitated in a slightly oxygenated upper water level environment and then settled on top of the sediments deposited under reducing conditions in the bottom environment. The presence of spessartine, in the black shale sample, may align with this hypothesis and it can be said Mn was originally precipitated as Mn-oxyhydroxide from further up in the water column, landed on the anoxic bottom, and during metamorphism, it transformed into garnet or grunerite depending on the surrounding mineralogy.

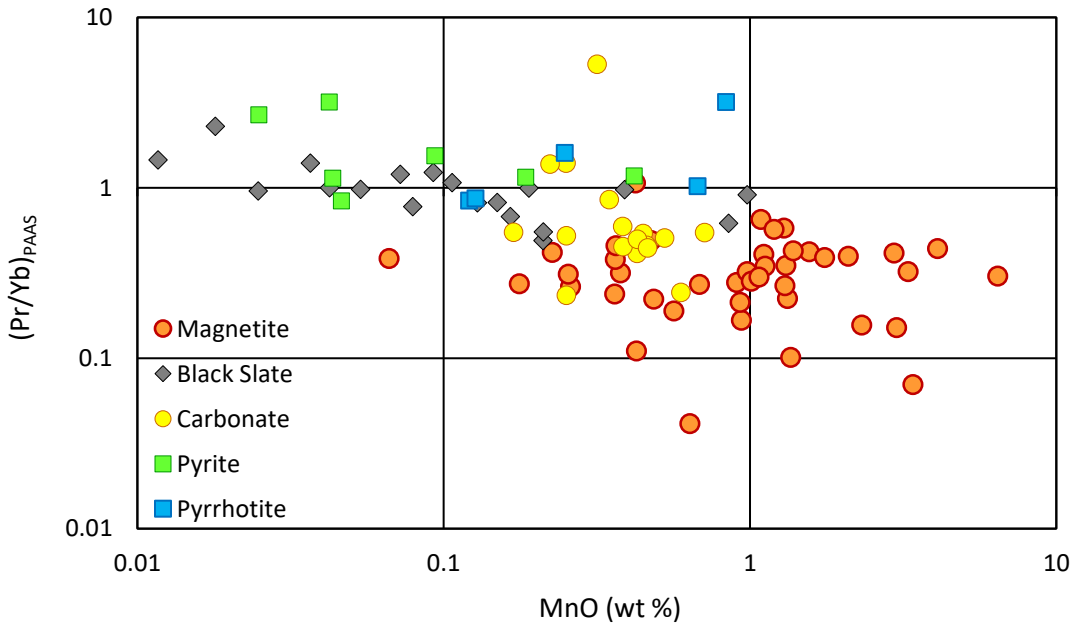

Figure 4.19: PAAS normalized ratios of Pr/Yb vs MnO, representing the slope of the REE pattern against MnO in magnetite-black slate-carbonate-sulfide facies.

In Figure 4.19, REE slopes vs MnO of black shale, sulfide iron formation, carbonate and, oxide iron formation facies are shown. Both the black shale and sulfide facies show a roughly flat negative trend, whereas the magnetite facies have positive slopes. The carbonate facies have slightly negative to positive slopes. This Figure indicates most HREE enriched magnetite samples have high Mn, while black shale and sulfide iron samples have low Mn and are HREE depleted. Most of the carbonate samples are HREE enriched although some are LREE enriched, and all have moderate concentrations of Mn.

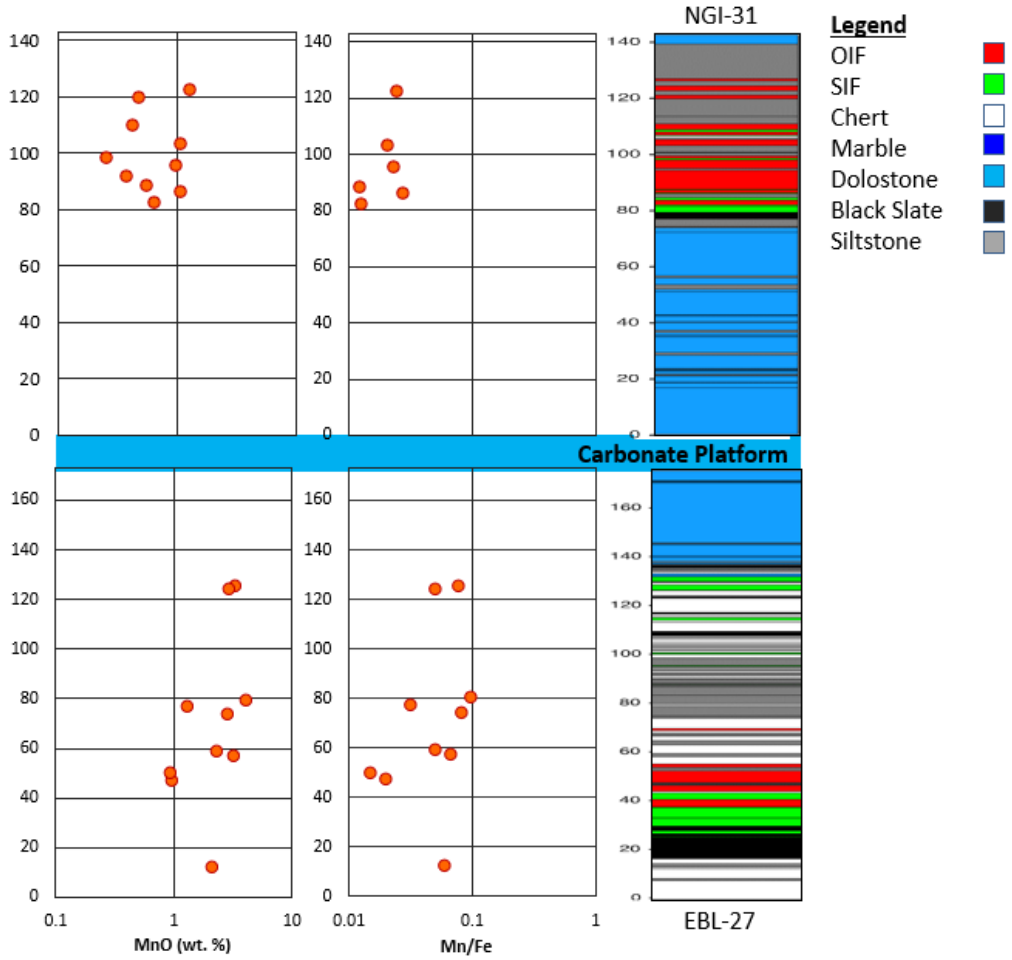

Figure 4.20: MnO and Mn/Fe ratio plots over the stratigraphic depth showing Mn concentration slightly increases towards the carbonate platform in the EBL-27 hole and Mn is more common in the oxide facies iron formation directly under the carbonate platform than that above it.

In Figure 4.20, EBL-27 and NGI-31 holes represent the MnO and Mn/Fe ratios of the oxide iron formation in successions above and below the carbonate platform. Magnetite samples have higher MnO (0.94 - 4.10) and Mn/Fe ratio (0.015 - 0.099). In the EBL-27 hole, it is possible that Mn enrichment in iron formation increased towards the carbonate platform, which is reasonable because near the shoreline O_2 abundance should be higher if oxygenic photosynthesis was occurring. In the NGI-31-hole, iron formations overlie the carbonate platform where the Mn enrichment trend in the magnetite samples is low and chaotic. Such a stratigraphic position probably indicates a relative sea level change which inundated the carbonate platform and caused the shifting of the shoreline. Based on this assumption, it can be said that the precipitation of iron hydroxide post platform flooding occurred in a deeper water environment where O_2 supply was very limited and probably Fe captured almost all the free O_2 as it is more reactive with O_2 than Mn. Another possible reason for having this irregular trend could be due to the inconsistent supply of Mn ions during the precipitation of iron oxyhydroxide.

Overall, the Mn concentration in the Red Lake successions reveals the gradual enrichment of Mn towards the carbonate platform where O_2 was possibly supplied by shoreline cyanobacteria. The anomalously high Mn enrichments in some samples probably indicate the short-term oxic and/or suboxic conditions of the depositional environment.

4.4 Zr-Hf-Nb Systematics in the Archean Ocean

Elements such as Al, Ti, Zr, and Nb are derived primarily from igneous rocks. They tend to be very resistant during weathering and diagenesis and do not go into solution; therefore, they are considered chemically immobile and insoluble (Sugitani et al., 1996). Hence, these elements can only be found in the siliciclastic phases of the sedimentary rocks and ideally should be absent

in pure chemical sediments. However, the dilemma arises when a significant concentration of a minor element like Zr is observed in pure iron formation. The concentrations of Zr, Hf, and Nb, Ta in pure iron formation are not well established yet, and what controls the distribution of these elements in iron formation is not clear. Not much study has been done so far to understand the source of these elements. However, Bau and Alexander (2009) attempted to figure out the dynamics of these elements in their work on 2.73 Ga old Temagami iron formation. In their study, they described the source of Zr, Hf, and Ta in magnetite as being significantly from seawater instead of a detrital origin.

A similar approach has been taken in this study to understand the dynamics of these elements in the 2.93 Ga IF of Red Lake. Instead of using Ta data, Nb, which has similar chemical behaviur the geochemical twin of Ta, has been used here because the geochemical data of Ta was not reliable.

Bivariate plots of Zr have been used here to find a correlation with other immobile elements such as Al and Ti (Figure 4.21 A & B) to determine whether they are sourced from a detrital origin, but no linear trend is present in these plots. Fe_2O_3/Al_2O_3 vs. Zr/Al_2O_3 ratios and Fe_2O_3/Al_2O_3 vs. Hf/Al_2O_3 ratios were plotted (Figure 4.21-C & D) to see whether Zr and Hf were co-precipitated with iron oxyhydroxides, and the data shows that iron oxyhydroxides have considerably higher ratios than the slates. Also, bivariate plots of Zr/Al_2O_3 vs. Hf/Al_2O_3, and Nb/Al_2O_3 vs. Hf/Al_2O_3 (Figure 4.21 E & F) show magnetite samples have higher Zr, Hf, and Nb vs Al_2O_3 ratios than siliciclastic black slate, which may indicate that their association is related to the precipitation of iron formation.

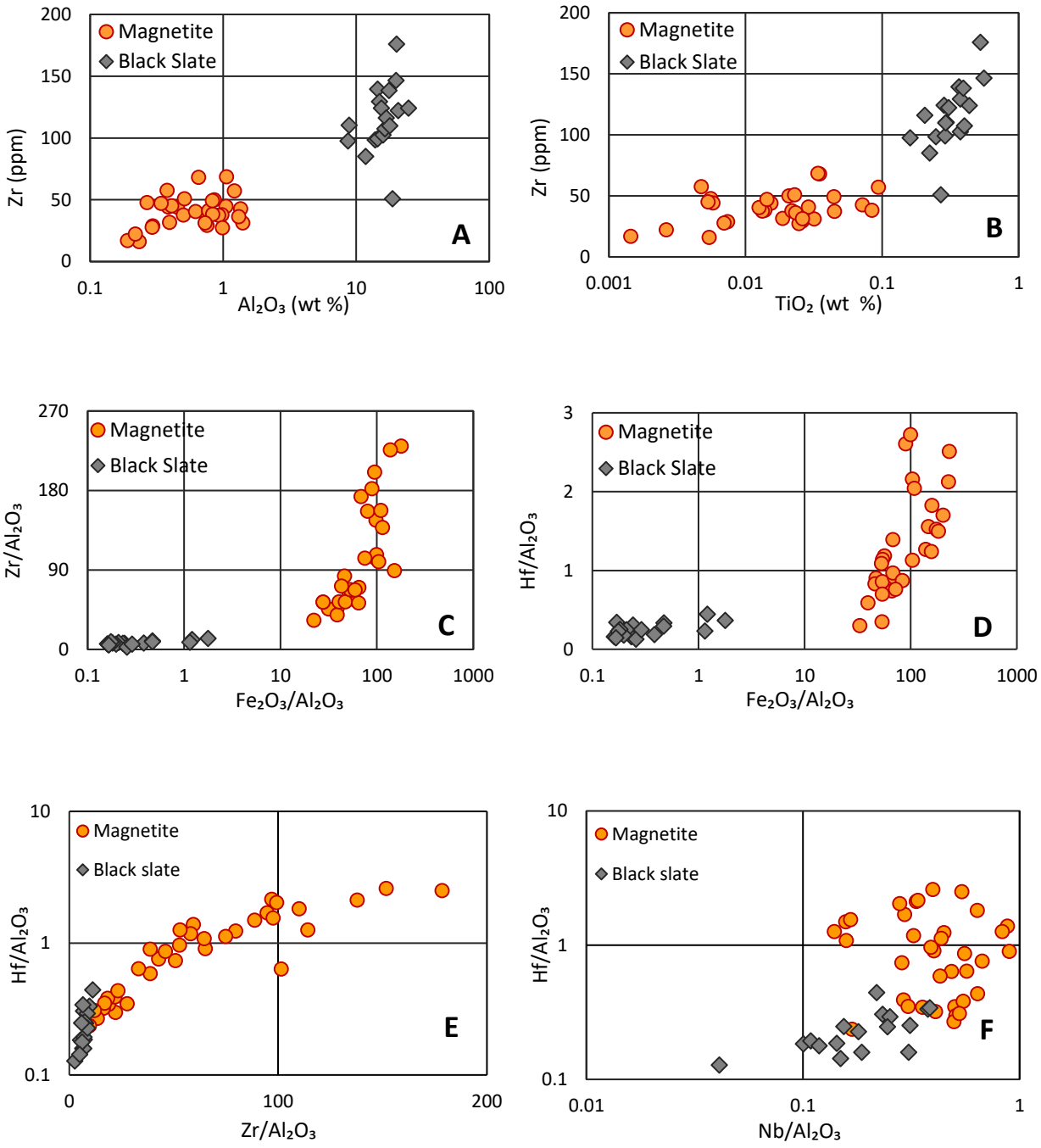

Figure 4.21: Bivariate plots of A) Zr vs. Al_2O_3. B) Zr vs. TiO_2. C) Fe_2O_3/Al_2O_3 vs. Zr/Al_2O_3. D) Fe_2O_3/Al_2O_3 vs. Hf/Al_2O_3. E) Hf/Al_2O_3 vs. Zr/Al_2O_3. F) Hf/Al_2O_3 vs. Nb/Al_2O_3. of Red Lake magnetite and black slate samples indicate that the source of Zr, Hf, and Nb in the magnetite is not entirely from their detrital component.

The behavior of Zr, Hf, and Nb in pure iron formation can be examined by the analysis of ratios of the geochemical twins Zr-Hf (Goldschmidt, 1937; Bau & Alexander, 2009). The Zr/Hf ratios of igneous rocks and clastic sedimentary rocks group close to chondritic (Zr/Hf: 38) and upper continental crust (Zr/Hf: 41) ratios (Anders & Grevesse, 1989; Wedepohl, 1995). The Zr and Hf ratios in Red Lake iron formation are between 38 and 90, which, for the most part, is far more than the chondritic and upper continental crust ratios. The Red Lake black shale shows Zr/Hf ratios between 19 and 43, which is within the range of chondritic and upper continental crust ratios. If the Zr and Hf in the Red Lake iron formation samples were derived significantly from detrital sources, they should cluster close to the chondritic and upper continental crust ratios. In modern seawater, the Zr/Hf ratio is 147 to 370 (Firdaus et al., 2008), which tells us that it is highly fractionated compare with the chondrite ratios. Thus, the non-chondritic Zr/Hf ratios of Red Lake iron formation suggest that there is a considerable role of nondetrital Zr and Hf, which was probably derived from seawater, although the Archean seawater Zr/Hf ratio is not known. Furthermore, in modern oceans and estuaries, preferential scavenging of Zr and Hf is observed where Hf is scavenged over Zr and drives the seawater Zr/Hf ratio towards the superchondritic values (Firdaus et al., 2008).

A similar scenario is found when Nb is considered. In modern seawater, the Hf/Nb ratio is 0.07 to 0.16 (Firdaus et al., 2008), whereas the Red Lake oxide iron formation samples shows a Hf/Nb ratio of 0.58 to 9.5, which is much higher than modern seawater. Also, the Hf/Nb ratios of chondrite and upper continental crust are 0.43 and 0.22 respectively, lower than the oxide iron formation of Red Lake. There is still uncertainty concerning the Archean seawater Hf/Nb ratio, but an assumption like that in the previous discussion can be adopted here, and it can be assumed

that Nb was preferentially scavenged from seawater rather than Hf during iron formation precipitation.

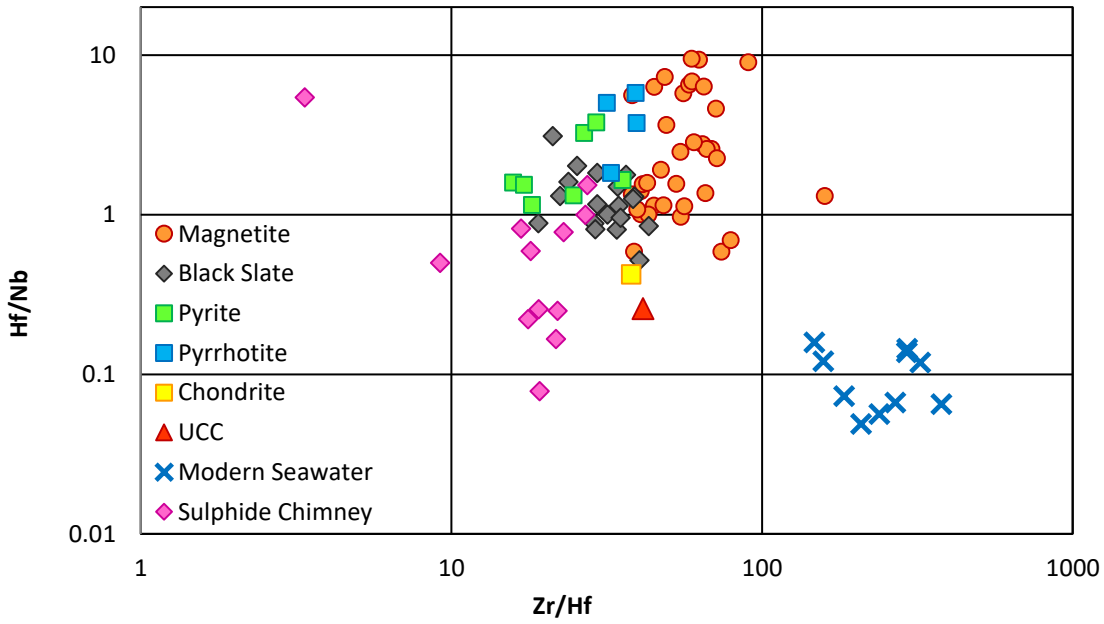

Figure 4.22: Ratio plots of Zr/Hf and Hf/Nb showing magnetite samples plot above the upper continental crust, chondrite, and black slate. This indicates that Zr, Hf, and Nb were dissolved in seawater and preferentially absorbed by iron oxyhydroxide with adsorption being Zr>Hf>Nb.

Figure 4.22 is a ratio plot of Hf/Nb vs. Zr/Hf of Red Lake iron formation and black shale with chondrite, upper continental crust, modern seawater and modern sulfide chimney data to illustrate the above discussion (Anders & Grevesse, 1989; Wedepohl, 1995; Firdaus et al., 2008; Paropkari et al., 2010). From this graph, it can be seen that the sulfide chimney samples have relatively low Zr/Hf and Hf/Nb ratios although some samples have plots close to the Red Lake black shale and sulfide iron formation samples, which indicates that those chimney samples are contaminated by siliciclastics. The plot of pure iron formation samples of Red Lake shows Zr/Hf and Hf/Nb ratios significantly higher than the chondrite and upper continental crust plots. A few detritus-mixed IF have their vicinity close to the black shale, and one sample plots near chondrite.

Detritus-poor sulfide iron samples show a trend similar to that of the iron formation samples, whereas the detritus-rich samples cluster around the black shale samples. The modern seawater samples have a higher Zr/Hf ratio but a lower Hf/Nb ratio.

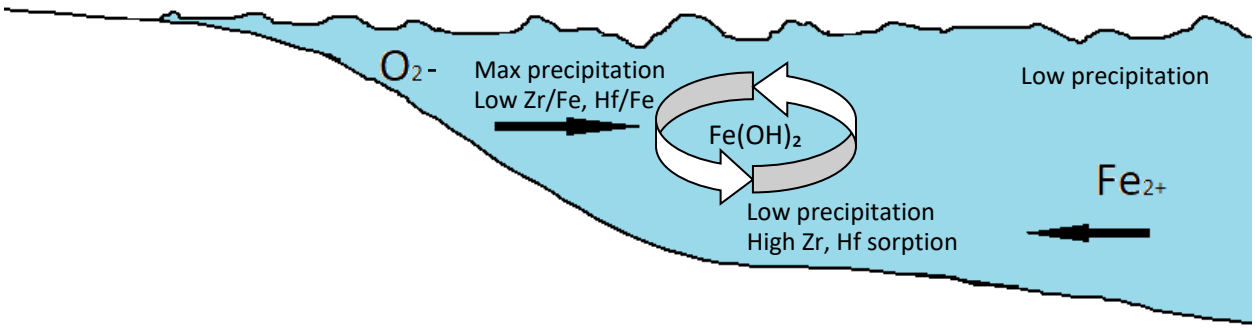

Figure 4.23: Schematic diagram of Zr, Hf sorption relative to the precipitation rate of iron oxyhydroxide. The slower the iron precipitation, the higher the Zr absorption.

To explain the dynamics which are responsible for the scavenging of these elements, it is assumed that the slower the precipitation of iron hydroxide, the higher the Zr, Hf and Nb sorption and the lower Zr/Hf and Hf/Nb ratios (Schmidt et al., 2014). The precipitation of iron hydroxide depends on the availability of a ferruginous water mass and the supply of an oxygenated water mass. A hypothetical scenario is illustrated in Figure 4.23, where the deeper part of the ocean is a representation of an anoxic ferruginous ocean, while the shallower part represents an oxygen-rich environment. The iron hydroxide precipitation occurs predominantly near the boundary of an oxygenated water mass and an anoxic Fe^{+2} rich water mass. This boundary can shift on either side depending on the supply of both water masses and fluctuation of the water level. Rapid precipitation results mainly from the delivery of O_2-rich water. On the other hand, slow deposition is caused by either insufficient supply of oxygenated water or iron deficiency in the water mass. The sorption of Zr, Hf, and Nd from seawater to iron hydroxide depends on the progress of precipitation (i.e., more rapid precipitation gives lower sorption and vice versa).

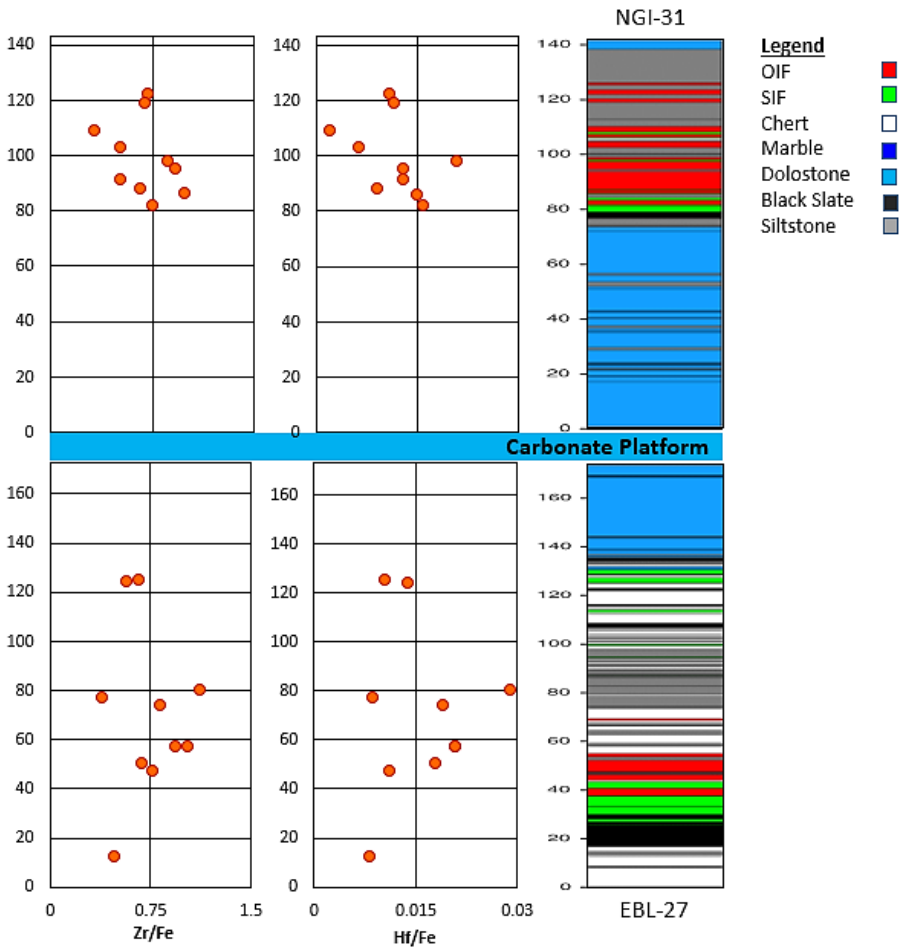

Figure 4.24: Ratio plots of Zr/Fe and Hf/Fe with depth showing a slight correlation with distance from the carbonate platform.

Zr/Fe and Hf/Fe ratios of Red Lake magnetite samples (Figure 4.24) was plotted against depth to visualize if there is any depositional trend of Zr and Hf with depth. From the depth curve vs. ratio plot and stratigraphy of the EBL-27 and NGI-31 drill holes, it is somewhat evident that towards the carbonate platform the Zr/Fe and Hf/Fe ratios change. In the EBL-27 hole, from the approximately 10 m to 80 m interval the ratios of both Zr/Fe and Hf/Fe gradually increase, which indicates a slower growth rate of iron hydroxides. Close to the carbonate platform, about 125 m in depth in the drill-hole, both ratios decrease (i.e., faster growth rate), which is reasonable because near the shoreline O_2 influx would have accelerated the precipitation of iron hydroxides if O_2 was

produced in the shallows. The slight scattering of a few samples denotes the fluctuation of the rate of precipitation that causes the ratio shifts back and forth. In the NGI-31 hole, the ratio of Zr/Fe and Hf/Fe is higher near the contact with the carbonate platform but decreases away from it. Data that deviated from the linear trend represent an occasional change in the deposition rates. Thus, it can be said that in the NGI-31 hole, the precipitation rate of iron hydroxide was higher near the carbonate contact.

In summary, it is hard to validate the results of the analysis with others' work as there is so little information available to help us understand the relation among Zr, Hf, and Nb in the iron formations of the Archean Eon. However, the distribution of Zr, Hf, and Nb in 2.93 Ga Red Lake oxide iron formation yields Zr/Hf and Hf/Nb ratios that differ from chondrite, upper continental crust, modern seawater, and Red Lake black shale. This probably indicates these elements in oxide facies iron formation are derived significantly from seawater rather than totally from detrital sources. The sorption of these elements is interrelated with the growth rate of iron hydroxides, and slower precipitation favors higher sorption of these elements (Bau and Alexander, 2009).

4.5 Sulfur and carbon isotopes

In this study, sulfide iron formation and black slate samples from five drill holes were used for organic carbon and sulfur isotope analysis. For inorganic carbon (carbonate) isotope analysis, outcrop data and drill core data were used. Four of these drill holes, namely PB-32, PB-33, PB-34, and PB-35 are from the Pancake Bay area, and EBL-27 is located in the East Bridget Lake area.

4.5.1 Sulfur isotopes

Sulfur is the 10th most abundant element in the Earth's crust and has five isotopes. Among the five isotopes, four are naturally occurring sulfur isotopes and stable (^{32}S, ^{33}S, ^{34}S, and ^{36}S)

while one (^{35}S) is unstable, or radiogenic. The approximate terrestrial abundances of these stable isotopes are ^{32}S: ~95.02, ^{33}S: ~0.75, ^{34}S: ~4.21, and ^{36}S: ~0.02 % (Macnamara & Thode, 1950). Isotopic fractionation happens due to the variations in thermodynamic properties of molecules which is dependent on mass. However, non-mass-dependent fractionation or mass-independent fractionation (MIF) refers to the processes that cause variations in the abundances of isotopes that are independent of their masses. MIF of sulfur isotopes is noted for deposits older than 2.3 Ga while deposits younger than 2.0 Ga have no significant MIF in $\Delta^{33}S$ values (Farquhar et al., 2000; Pavlov & Kasting, 2002; Farquhar & Wing, 2003; Mojzsis et al., 2003; Ono et al., 2003; Bekker et al., 2004). This isotopic fractionation shift in the rock record indicates an important change in the Archean sulfur chemistry and/or cycling after the Neoarchean. Therefore, it can be said that the 2.93 Ga old Red Lake sulfides should show MIF of sulfur.

Isotopic fractionation of elements is dependent on chemical variables such as oxidation state, atomic mass, electronic configuration of the isotopic elements and the elements to which they are bound (O'Neil, 1986). The oxidation state of sulfur is particularly important because the heavier isotopes of sulfur are enriched in the higher oxidation states relative to lower oxidation states and the ^{34}S enrichment follows the trend $SO_4^{2-} > SO_3^{2-} > S_x^0 > S^{2-}$ (Sakai, 1968; Bachinski, 1969; Seal, 2006). Mass-independent fractionation of sulfur indicates an anomalous enrichment or depletion of $^{33}S/^{32}S$ and $^{36}S/^{32}S$ isotope ratios compare to the associated $^{34}S/^{32}S$ ratios. According to Farquhar et al. (2001), photodissociation of sulfur dioxide ($SO_{2)}$ gas results in MIF of sulfur. Under ultraviolet radiation, the SO_2 molecule dissociates to sulfur monoxide (SO) which ultimately produces elemental sulfur by the following reaction. Due to this reaction, the end product, elemental sulfur becomes anomalously enriched in ^{33}S, and depleted in ^{36}S, while vice versa for the residual SO_2 (Farquhar et al., 2001).

$SO_2 \xrightarrow{uv} SO + O,$

$SO \xrightarrow{uv} S + O$

The multiple sulfur isotope analysis of Red Lake sulfides shows $\delta^{34}S_{VCDT}$ values ranging from -8.83 ‰ to +3.85 ‰, the $\Delta^{33}S_{VCDT}$ values ranging from -0.65 ‰ to +1.2 ‰ and the $\Delta^{36}S_{VCDT}$ values ranging from -2.44 ‰ to +0.22 ‰. The $\Delta^{33}S$ vs. $\Delta^{36}S$ plot (Figure 4.25) has a slope of -1 which is typical for Archean mass-independent fractionation of sulfur and is similar to other Archean data (Farquhar et al., 2001, 2007; Ono et al., 2006). Since the slope is consistent with other Archean slopes, this trend infers similar mass-independent fractionation of sulfur was taking place during formation of the Mesoarchean Red Lake sulfides and is interpreted as evidence of mass-independent isotopic fractionations initiated in a gas-phase reaction (Farquhar et al., 2001, 2007; Ono et al., 2006; Rodzinyak, 2012).

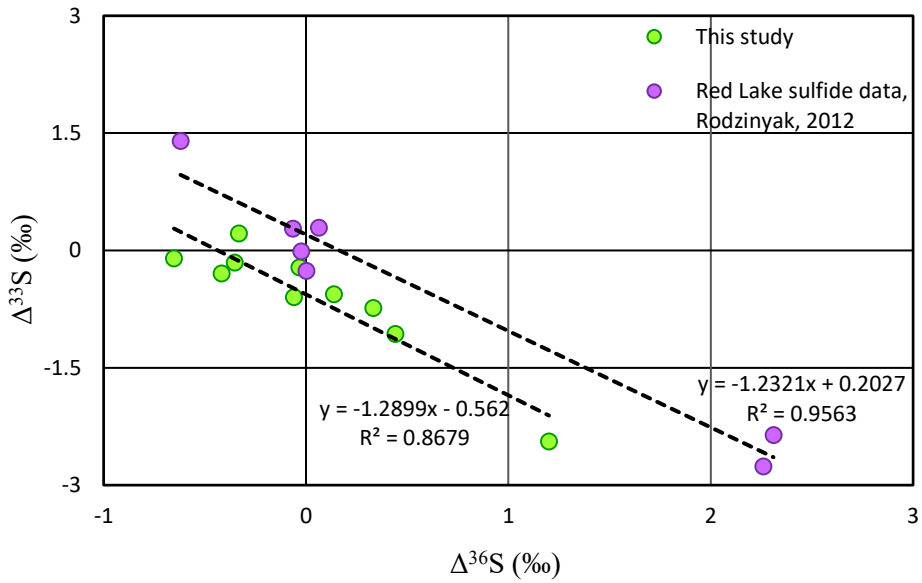

Figure 4.25: Plot of $\Delta^{33}S$ vs. $\Delta^{36}S$ for mass independent data for 2.93 Ga. old Red Lake sulfide samples. The correlation between $\Delta^{33}S$ and $\Delta^{36}S$ is interpreted as evidence of mass-independent isotopic fractionations which has a characteristic slope of -1

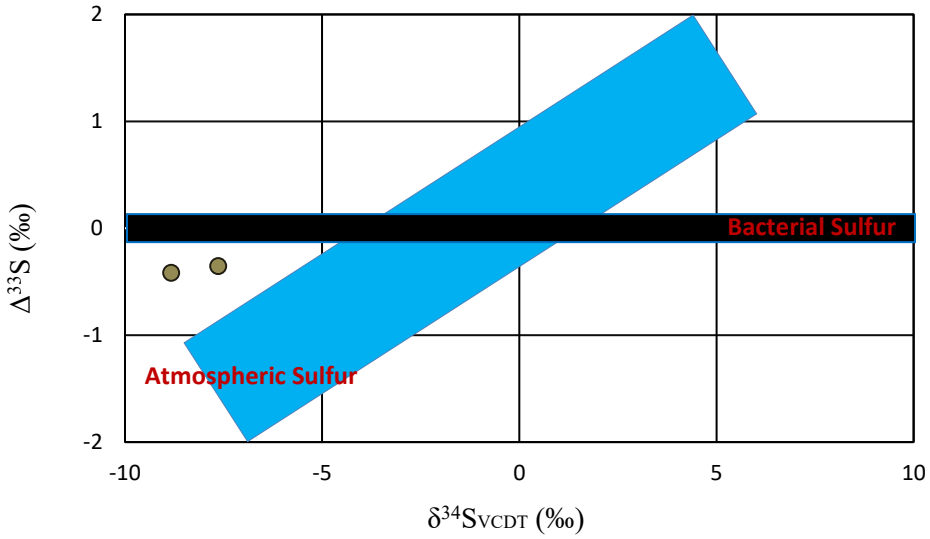

Figure 4.26: Plot of $\delta^{34}S$ vs. $\Delta^{33}S$ for Red Lake sulfide samples. The diagonal array is interpreted as atmospheric reactions that produced mass independent fractionation. The horizontal distribution along the x-axis is attributed to microbial processes.

In the $\delta^{34}S$ vs. $\Delta^{33}S$ plot of Figure 4.26, the diagonal array of samples is interpreted as the product of atmospheric photolysis reactions of mass-independent fractionation of sulfur whereas the horizontal trend of samples is suggestive of microbial processing (Ono et al., 2003; Rodzinyak, 2012). Likewise, the $\delta^{34}S$ vs. $\Delta^{33}S$ plot (Figure 4.27) with literature data shows Red Lake data are compatible with other Archean deposits and follow the Archean array proposed by Ono et al. (2003), but also have similarities with samples from the 2.45 to 2.2 time period.

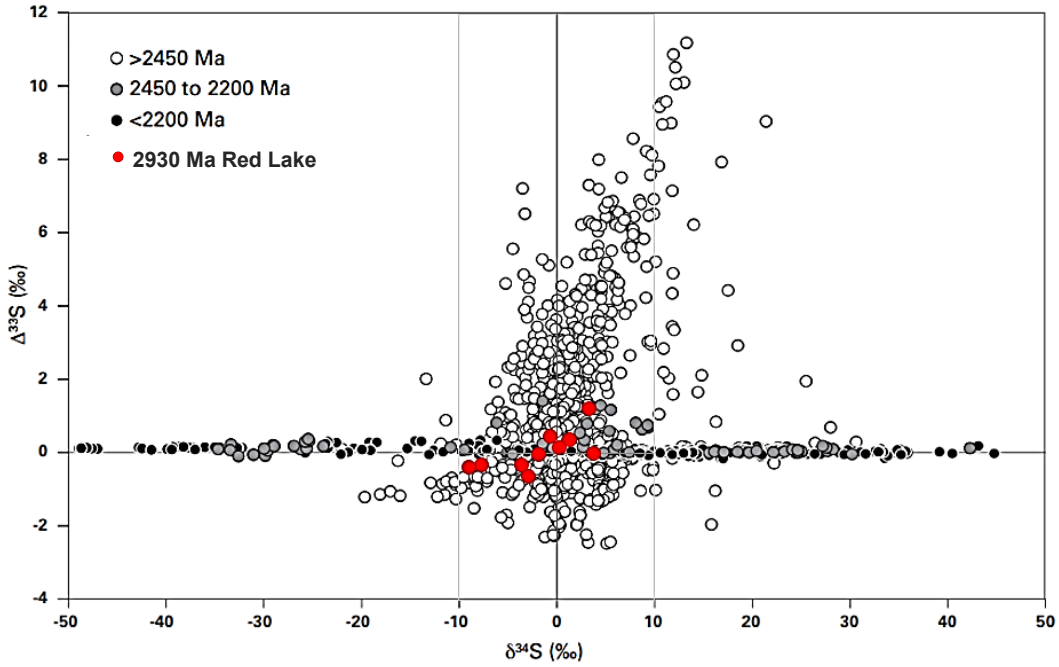

Figure 4.27: $\delta^{34}S$ vs. $\Delta^{33}S$ plot of Red Lake (~2.93 Ga) samples (red circle) along with data from the literature where white circles are samples older than 2.45 Ga, gray circles are samples younger than 2.45 Ga but older than 2.2 Ga, and black circles are samples younger than 2.2 Ga. The broad positive correlation between $\delta^{34}S$ values and $\Delta^{33}S$ values in samples older than 2.45 Ga is known as the 'Archean Array' (Ono et al., 2003). The Red Lake samples tend to follow this array, but also are similar to the samples from the 2.45 to 2.2 Ga time period (Modified after Johnston, 2011).

Furthermore, the $\delta^{34}S$ isotope analysis of Red lake sulfides and pyritiferous, organic-rich black slate samples show the isotopic abundance of ^{34}S ranges from -8.83 ‰ to +7.29 ‰. The PB-32 hole has $\delta^{34}S$ values ranging from -1.38 ‰ to +2.81 ‰ for sulfides samples and +1.47 ‰ to +4.29 ‰ for pyritiferous black slate samples. The PB-33 hole has -8.83 ‰ to +0.1 ‰ values for sulfide samples, and one black slate sample is +0.11 ‰. The PB-34 drill-hole has pyritiferous black slate samples only which gave positive $\delta^{34}S$ values ranging from +1.24 ‰ to +5.43 ‰. In the PB-35 hole, sulfides samples gave +1.03 ‰ to +6.24 ‰, and pyritiferous black slate samples gave +3.75 ‰ to +7.29 ‰. The EBL-27 hole sulfide samples have -7.63 ‰ to +3.45 ‰ values and black slate samples

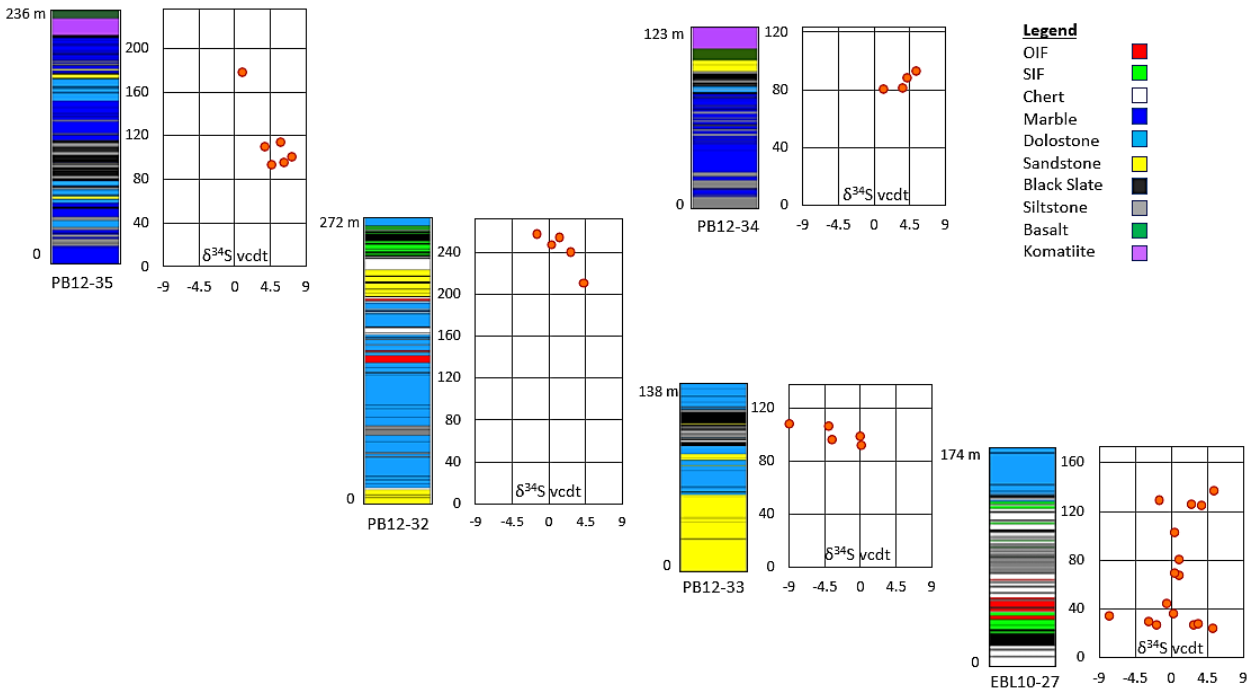

Figure 4.28: Plot of $\delta^{34}S$ ‰ VCDT vs. depth of the Red Lake sulfides and pyritiferous black slate samples from PB-32, PB-33, PB-34, PB-35, and EBL-27 holes. The plot shows sulfur isotope variability throughout the core log.

have isotopic values from -1.47 ‰ to +5.41 ‰. The $\delta^{34}S$ values of these samples were plotted against depth and displayed according to stratigraphic position in Figure 4.28. The deepest sulfidic deposits have S isotopic values that are quite variable, but above this zone, they cluster close to 0. Then as the carbonate platform is approached, they become positive. Further up stratigraphy sulfide-rich units interbedded with the carbonate platform have negative isotopic values, whereas pyritiferous shales and sulfide layers immediately above the platform have positive values.

According to the previous studies of VMS deposits and their modern seafloor equivalents, the possible sources of sulfur can come from: (1) leaching of sulphur from igneous, and/or metamorphic rock; (2) bacterial sulphate reduction of seawater sulphate; or (3) seawater sulphate reduction due to thermochemical reaction (Shanks et al., 1995; Watanabe et al., 1997; Hoefs,

1997; Seal, 2006; Alt & Shanks, 2006; Brueckner et al., 2015). The typical values of $\delta^{34}S$ obtained from their studies are: (1) sulfur leached from igneous rocks and/or direct contributions from magmatic fluids are $\delta^{34}S\approx$ -5 ‰ to +5 ‰; (2) sulfur from bacterial sulfate reduction due to microbial activity in reduced sediments are $\delta^{34}S\approx$ -50 ‰ to +20 ‰ (Shanks et al., 1995; Goodfellow & Peter, 1996; Watanabe et al., 1997; Gemmell & Sharpe, 1998; Shanks III, 2001; Canfield, 2001; Seal, 2006) and (3) seawater sulfate present in sulfate minerals or reduced by thermochemical processes are $\delta^{34}S\approx$ 4 ‰ to 33 ‰ (Claypool et al., 1980; Kampschulte & Strauss, 2004; Paytan & Gray, 2012). However, according to Canfield and Poulton (1998, 2011), for a limited sulfate ocean like the Archean due to the lack of oxygen, the biological fractionation of sulfur would have a less fractionated ratio, i.e., the isotopic value would be close to the seawater value. Hence, sulfur derived from bacterial sulfate reduction could have a heavier $\delta^{34}S$ value indicating a sulfate deficient environment while a lighter value of $\delta^{34}S$ is an indication of biologically fractionated sulfur derived from a more extensive S pool (Shanks et al., 1995; Goodfellow & Peter, 1996; Watanabe et al., 1997; Canfield, 2001; Seal, 2006; Canfield 1998; Poulton & Canfield, 2011).

The $\delta^{34}S$ isotopic composition of Red Lake sulfides and black slates of different drill holes are compared in Figure 4.29, with the following: (1) and (2) a modern vent system of the Juan de Fuca Ridge (Shanks & Seyfried, 1987); Archean VMS deposits of (3) Kidd Creek (Jamieson et al, 2006) and (4) Noranda camp (Sharman, 2011). It is known that sulfur of primary origin (i.e., meteorites and igneous rocks) have $\delta^{34}S$ values close to zero (Thode et al., 1961; Ryznar et al., 1967; Grinenko & Thode, 1970; Schwarcz & Burnie, 1973; Mitchell & Krouse, 1975; Thode et al., 1991). In addition to this, Ono et al. (2003) estimated that the $\delta^{34}S$ of Archaean seawater sulfate ranged from 6 to 16 ‰ with a $\Delta^{33}S$ of approximately -2 ‰.

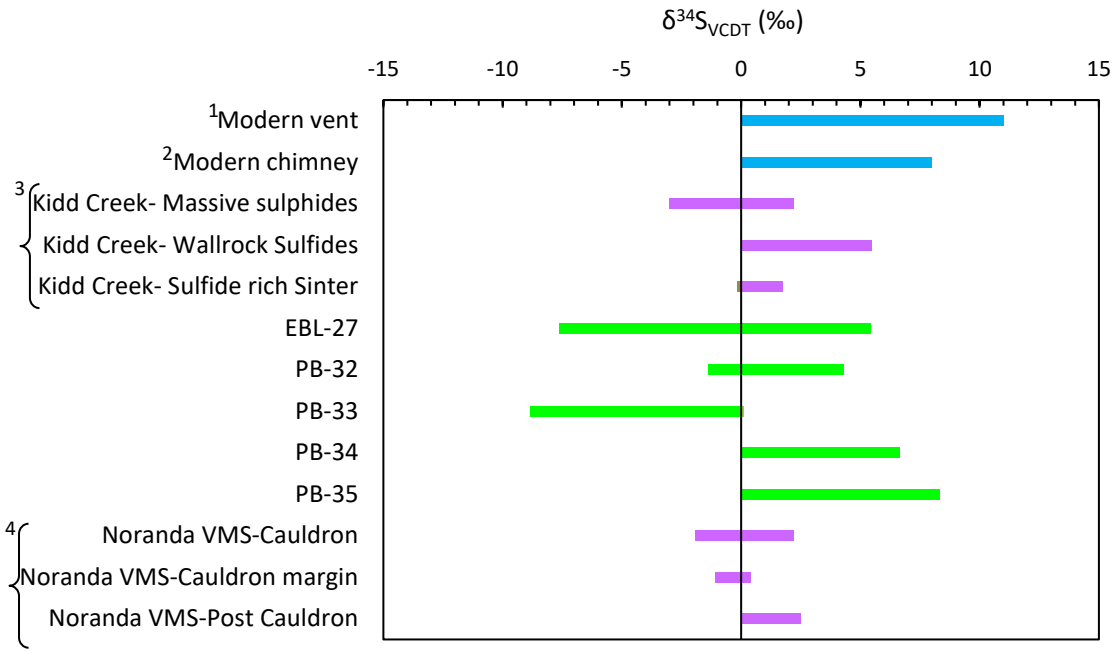

Figure 4.29: Plot of $\delta^{34}S$ ‰ VCDT data from different sulfur sources. EBL-27, PB-32, PB-33, PB-34, and Pb-35 are sulfides and black slate data from this study; data in (1) and (2) are from Shanks and Seyfried (1987); (3) Jamieson (2006); (4) Sharman (2011).

Based on the above information, it is presumed that the sulfur in the Red Lake sulfides and black slates were derived from multiple sources. $\delta^{34}S$ values close to zero represents sulfur that was probably leached from igneous sources due to high-temperature hydrothermal fluids and vented on the seafloor. However, some of the Red Lake $\delta^{34}S$ values (+5.43 ‰ to +7.29 ‰) roughly fall within the range of Archean seawater sulfate proposed by Ono et al., (2003). Additionally, the higher negative values (-8.83 ‰ to -7.63 ‰) are indicative of bacterial sulfate reduction in sediments.

4.5.2 Carbon isotopes in the organic matter

Carbon is the essential element to form life, and it has three naturally occurring isotopes ^{12}C, ^{13}C, and ^{14}C. The ^{12}C is lighter, ^{13}C is heavier, and ^{14}C is radiogenic. In nature, the proportion of ^{12}C and ^{13}C is approximately 93:1. Carbon isotope composition of the substance is expressed as

$\delta^{13}C_{PDB}$ which gives the deviation of the $^{13}C/^{12}C$ ratio of a sample relative to the conventional standard PDB. A positive value of $\delta^{13}C$ in a sample indicates a higher $^{13}C/^{12}C$ ratio or ^{13}C enrichment and a negative value represents a lower $^{13}C/^{12}C$ ratio with corresponding ^{13}C depletion. Organic matter is preferentially composed of ^{12}C and is removed from the hydrosphere-atmosphere system after burial, that subsequently causes the carbon on the surface to become heavier or enriched in ^{13}C. Hence, the carbon isotopic composition of the organic matter can provide information about the biological activity and carbon intake by microorganism within a sedimentary basin.

The carbonaceous black slates and sulfide iron formations of Red Lake contain organic carbon or kerogen as remnants of ancient organic matter representing life at that early stage of Earth history. The measured total organic carbon (TOC) content ranges from 0.1 to 5.4 wt. % in these sediments. The analysed $\delta^{13}C$ values of PB-32, PB-33, PB-34, PB-35 and EBL-27 holes range from -27.61 ‰ to -21.20 ‰, -27.99 ‰ to -21.70 ‰, -21.41 ‰ to -18.98 ‰, -24.90 ‰ to -22.64 ‰ and -30.15 ‰ to -17.76 ‰ respectively.

A sedimentary profile with carbon isotopic compositions is given in Figure 4.30 that displays the isotopic change with elevation in the stratigraphic column. The Pancake Bay holes, except for PB-33, show $\delta^{13}C$ gradually decreases away from the carbonate platform towards the overlying volcanics. Surprisingly, the EBL-27 hole has two distinct trends of $\delta^{13}C$: a clustering of

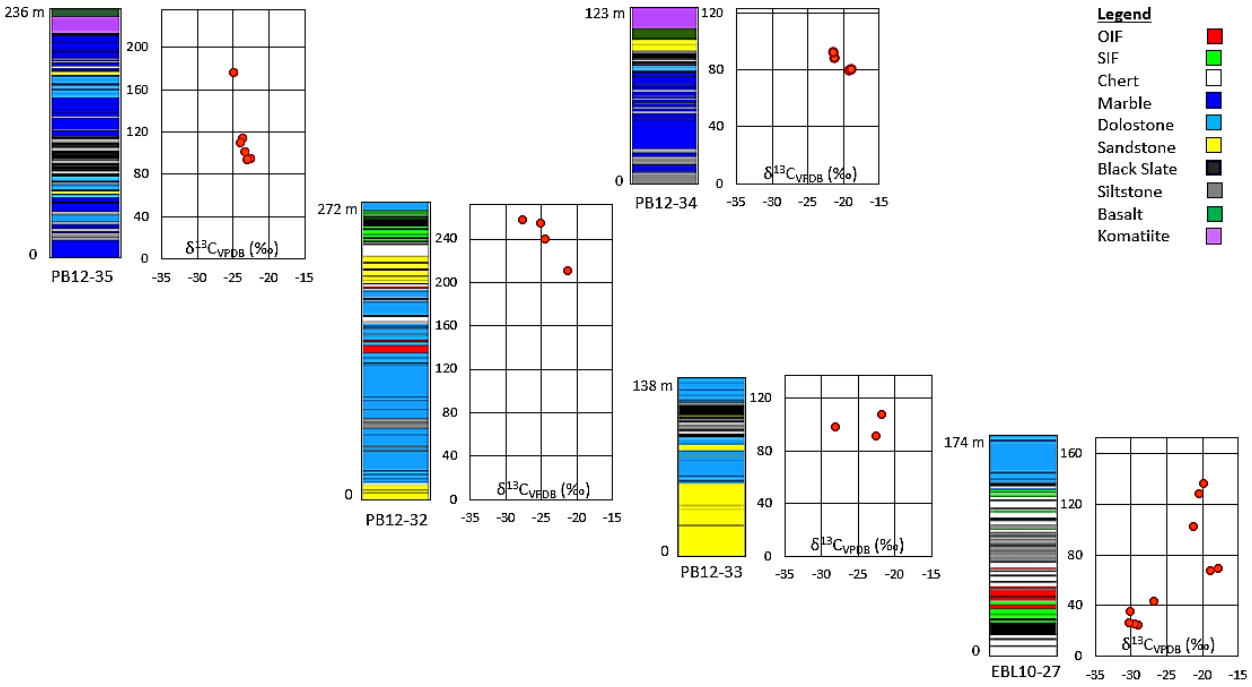

Figure 4.30: Plot of δ^{13}Corg ‰ VPDB vs. depth of the Red Lake sulfides and black slates from PB-32, PB-33, PB-34, PB-35, and EBL-27 holes. This plot depicts the changes in organic δ^{13}C through the core log.

low δ^{13}C values around -30 ‰ near the bottom of the hole and higher δ^{13}C values of about -17 ‰ in the middle of the hole. The high negative δ^{13}C value of organic matter implies a greater depletion of ^{13}C or conversely an enrichment of ^{12}C. Therefore, the bottom part of the hole has ^{12}C enriched signature while the upper part of the hole has ^{13}C enriched signature. However, Posth et al. (2017) documented that purple sulfur bacteria (PSB) and green sulfur bacteria (GSB) follow different enzymatic pathways to fix carbon and fractionate carbon isotopes differently. Thus, the dissimilar δ^{13}C isotopic trend present in Red Lake organic matter might be indicative of different microbial communities living in the depositional basin.

The δ^{13}Corg VPDB isotopic ratios of organic matter in Red Lake samples are between -30 to -17 ‰ which is similar to the values reported by Schidlowski et al. (1983). Their study revealed

that the average range of organic carbon $\delta^{13}C$ variations through Earth's history is between -35 and -20 ‰. In addition, organic carbon $\delta^{13}C$ values from the Sturgeon and Savant Lake Greenstone Terranes of Northwest Ontario, Wabigoon Belt of Superior Province of Canada, as well as other Archean deposits from different parts of the world, e.g., Fortescue Group of Western Australia and the Ventersdorp Supergroup of South Africa, indicate that the samples were characterized by ^{13}C depleted organic matter and thus, might be suggestive of a global feature for the Archean (Shegelski, 1978; Schoell & Wellmer, 1981; Strauss, 1986; Hayes et al., 1989).

4.5.3 Carbon isotopes in the carbonate rocks

In Archean seawater, the isotopic composition of $\delta^{13}C_{VPDB}$ carbon is +1.5 ‰ ± 1.5‰ (Veizer et al., 1989a; Veizer et al., 1989b and references therein). The $\delta^{13}C$ values of bulk Precambrian carbonates are around 0‰, which is similar to the marine carbonate values for the Phanerozoic (Schidlowski et al., 1983). Primary isotope compositions of carbon and oxygen of carbonate rocks may change due to post-depositional alteration. Different diagenetic processes (e.g., meteoric diagenesis or metamorphism) may reduce both the $\delta^{13}C$ and $\delta^{18}O$ composition of carbonate rocks and dolomitization can also lower the $\delta^{18}O$ value (Quinn & Matthews, 1990; Kaufman & Knoll, 1995; Singh et al., 1998; Melezhik et al., 2003; Fairchild & Kennedy, 2007; Bristow & Kennedy, 2008).

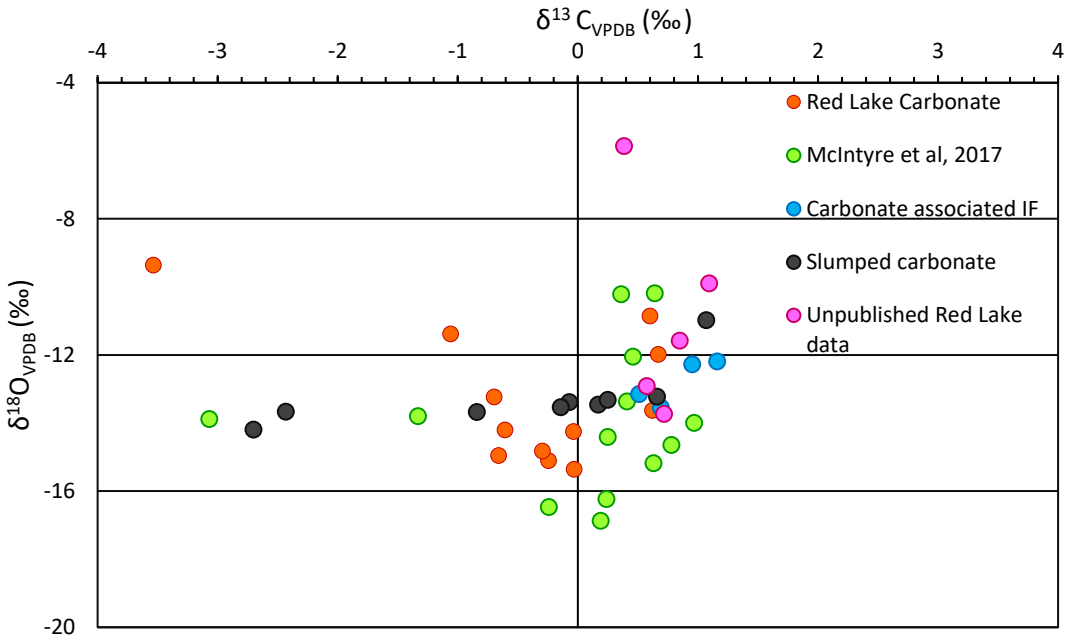

Figure 4.31: Plot of $\delta^{13}C_{VPDB}$‰ vs. $\delta^{18}O_{VPDB}$‰ of the Red Lake carbonate samples show most carbon and oxygen isotope values are within the range commonly recorded for Archean shallow-water carbonates.

The $\delta^{l3}C$ values for Red Lake carbonate range from -3.53 ‰ to +1.16 ‰ and are somewhat compatible with Archean seawater. The dolomite, calcite, and calcite-rich dolostone samples show $\delta^{l3}C$ values of -0.66 ‰ to +0.62 ‰, -2.7 ‰ to +1.07 ‰, and -3.53 ‰ to -1.06 ‰ respectively (Figure 4.31). The carbonate associated with oxide iron formation has values of +0.51 ‰ and +1.16 ‰. The shale-hosted slumped carbonate samples, and magnetite hosted slumped carbonate samples have $\delta^{l3}C$ values of -2.7 ‰ to -0.07 ‰ and +1.07 ‰ to +0.25 ‰ respectively.

With the exception of one of McIntyre and Fralick's (2017) samples, the carbonate associated with oxide facies iron formation has positive $\delta^{l3}C$ values, whereas the $\delta^{l3}C$ values of shale-hosted carbonate slumped material change gradually from positive to negative (Figure 4.32). Low $\delta^{l3}C$ values of samples from the shale-hosted carbonate slump facies indicates the presence of CO_2 derived from organic carbon as it's high TOC content with substantial negative isotopic

ratios can alter the slumped in carbonate. Hence, post-depositional alteration played a role here. Moreover, lower $\delta^{13}C$ values were identified for deeper water carbonates in other Archean carbonate platforms such as the Hamersley (Becker & Clayton, 1972; Kaufman et al., 1990), Transvaal Supergroup (Beukes et al., 1990; Schneiderhan et al., 2006; Fischer et al., 2009) and Steep Rock (Fralick & Riding, 2015). According to Kaufman et al. (1990), deep Archean seawater had a $\delta^{13}C$ value of -5‰ but during diagenesis, organic carbon reacted with iron oxyhydroxide and further lowered the $\delta^{13}C$ values. Fralick and Riding (2015) also observed a lower -5.5‰ $\delta^{13}C$ value for deeper seawater siderite. Therefore, the more negative $\delta^{13}C$ values of Mesoarchean Red Lake carbonates represent an enrichment of $\delta^{12}C$ or depletion of $\delta^{13}C$, which probably resulted from deposition in a setting where CO_2 was derived from the recycling of organic matter enriched in ^{12}C (Thode & Goodwin, 1983; Schidlowski et al., 1983; Schidlowski, 1988; Baur et al., 1985).

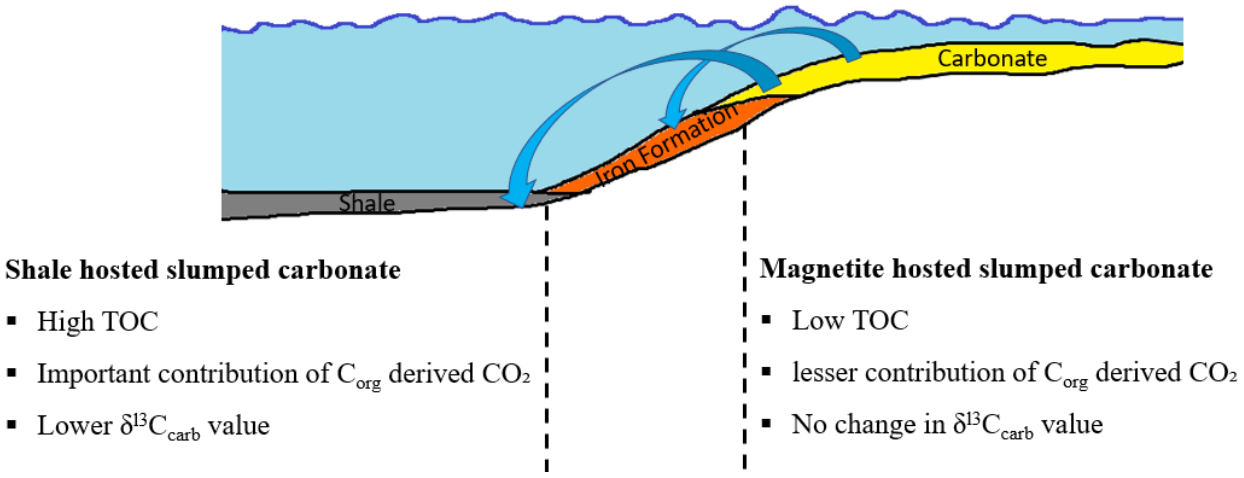

Figure 4.32: A hypothetical scenario of $\delta^{13}C$ isotope distribution in slumped carbonate. Slate hosted carbonate slumps have low $\delta^{13}C$ values relative to magnetite hosted carbonate slumps because of biological recycling of CO_2 in areas of high TOC.

The $\delta^{18}O_{VPDB}$ ‰ value of Red Lake carbonates is -9.3 ‰ to -15.4 ‰, which is similar to the $\delta^{18}O$ value of Archean carbonates ranging from -9 ‰ to -15 ‰ (Kaufman et al., 1990; Beukes et al., 1990; Fischer et al., 2009 and Heimann et al., 2010). McIntyre and Fralick, (2017) reported

that Red Lake calcite samples have $\delta^{18}O$ isotope values similar to other Archean carbonate samples, but dolomite samples have a lower $\delta^{18}O$ value compare with other Archean carbonate samples. Furthermore, Mg/Ca ratio verses $\delta^{18}O$ plots depict dolomite content increasing with decreasing $\delta^{18}O$ value (Figure 4.33), which is opposite to data from Phanerozoic carbonates (Jaffrés et al., 2007). The Red Lake dolomite samples have low $\delta^{18}O$ values ranging from -15.4‰ to -13.6‰. Negative oxygen isotope ratios in dolomites are often referred to as the presence of isotopically light waters during dolomitization (Wright & Tucker, 1990). Dolomite commonly forms in restricted settings, giving higher $\delta^{18}O$ values. Nevertheless, dolomitization can happen in many different ways in nature. It is often associated with hypersaline, evaporative settings (Friedman, 1980), which give an elevated $\delta^{18}O$ composition (i.e., enriched with the heavier O_2 isotope). Alternatively, increased influx of meteoric water into evaporite basins or mixing of marine and meteoric waters can lower the $\delta^{18}O$ composition during dolomitization. Due to this process, dolomites become enriched in the lighter oxygen isotope (i.e., depleted $\delta^{18}O$ composition). It is likely that dolomitization of Red Lake carbonates was caused by the mixing of saline water and meteoric water, thus, a lighter ^{16}O or depleted ^{18}O signature was preserved. The isotopic signature of $\delta^{18}O$ in dolomite is different than the isotopic signature of calcite, which further suggests diagenetic alteration of the composition of $\delta^{18}O$ in dolomite. Red Lake calcite and dolomite occur together, and they were metamorphosed simultaneously thus alteration during metamorphism resetting the oxygen isotopic signature in case of dolomite is ruled out.

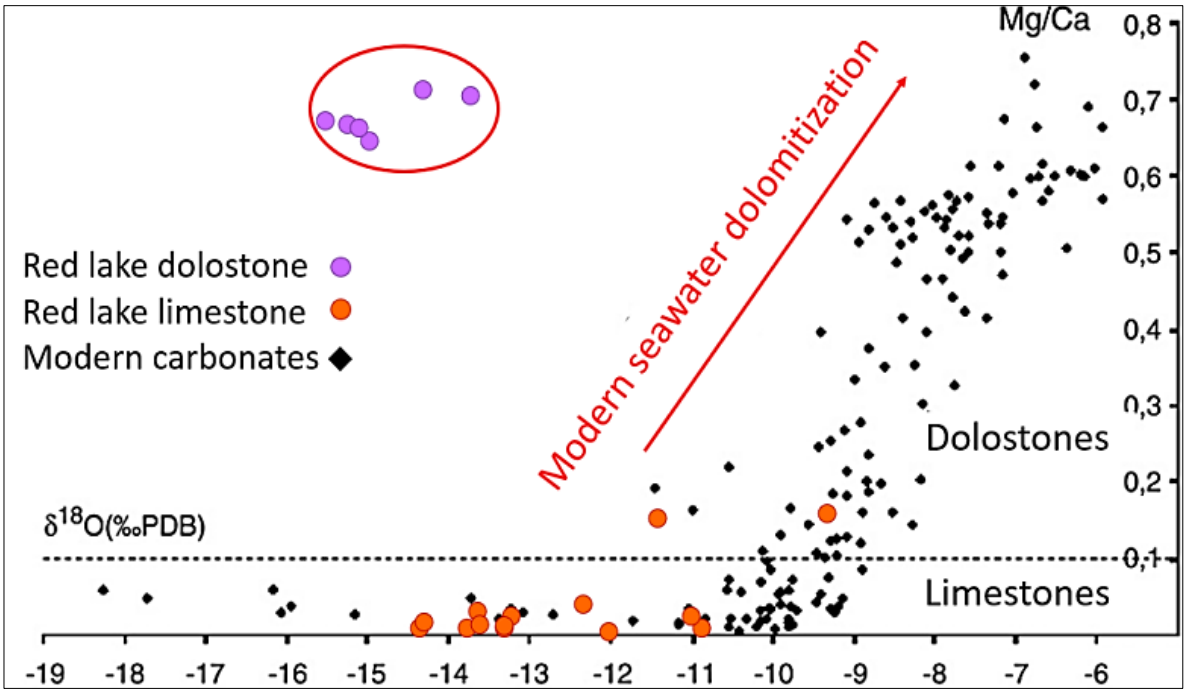

Figure 4.33: Mg/Ca vs. $\delta^{18}O$ plots showing dolomite content increasing with decreasing the $\delta^{18}O$ value in Red Lake area but literature data has an opposite trend (Jaffrés et al., 2007). This trend suggests dolomite in the Red Lake area were formed differently.

Regarding the behavior of strontium (Sr) isotopes in Red Lake carbonates, Satkoski et al., (2017) mentioned that Red Lake dolomite did not preserve the primary Sr signature of seawater due to diagenesis, but calcite samples preserved the seawater Sr isotopic composition. Generally, seawater Sr is enriched in the light isotope while Sr derived from the radiogenic decay of rubidium (Rb) is enriched in the heavy isotopic composition. The calcite samples have lower $^{87}Sr/^{86}Sr$ ratios, whereas the dolomite samples have higher $^{87}Sr/^{86}Sr$ ratios, suggesting that during diagenesis dolomite was enriched in the heavier Sr isotope (Satkoski et al., 2017). Multiple lines of evidence suggest that Red Lake dolomites were modified diagenetically while the limestone has an unaltered seawater composition.

Chapter 5: Depositional Environment of Lithofacies

Chemical sedimentary rocks are chemical precipitates, which settle from the water column and reflect the composition of seawater. Any variability in the composition of water chemistry is related to different physicochemical factors including fluctuations in ionic concentrations, Eh, pH, and temperature. All these are key controls of the variety of chemical sedimentary rocks. Therefore, to delineate the depositional environment of Red Lake chemical and siliciclastic sedimentary rocks, observation from outcrop, core data, and geochemical analysis of various lithofacies must be considered. The order described here is similar to that used in Chapter 3.

Carbonate

In the Archean ocean, there are many examples where carbonate was deposited in shallow water while chert, magnetite, and sulfide were deposited in the deeper water of the basin (Fischer et al., 2009; Heimann et al., 2010; Fralick & Riding, 2015). In the Red Lake carbonate platform, carbonates deposited in the peritidal environment are composed of ferronian dolomite while carbonates deposited in the deep subtidal to upper slope settings are composed of calcite (McIntyre & Fralick, 2017). The geochemical analysis of carbonate samples shows calcite-rich carbonate present above and below the peritidal ferronian dolomite which indicates probable relative sea level change. The REE patterns of carbonate samples have no La and Ce anomalies, but they have high Eu anomalies, high Y/Ho ratios, and HREE enrichment. The lack of negative Ce anomalies in all but two samples indicates that the water column was not oxic and high Eu anomalies suggest deposition occurred in a marine environment with good interchange with the world ocean.

The depositional environment of carbonate associated with magnetite and slumped carbonate are described below.

Carbonate associated with oxide facies IF

In the Red Lake carbonate platform, other than normal oxide iron formation, carbonate associated oxide iron formation has been observed in outcrop. The alternating deposition of carbonate and magnetite layers is certainly interesting. However, to explain the deposition of alternating iron and carbonate layers, it is hypothesized that upwelling of Fe^{+2}-rich deeper water to the shallow ocean caused precipitation of iron oxyhydroxides when carbonate precipitation was dormant. The formation of thin laminae of magnetite was probably due to very dilute hydrothermal input, or intermittent supply of Fe^{+2}-rich water, or intermittent supply of oxygen. After the deposition of iron hydroxides, when the seawater became supersaturated with bicarbonate ions the next phase of carbonate deposition occurred. The SEM-EDS analysis of carbonate associated with magnetite shows a very thin layer of mud accumulated between carbonate and magnetite layers, which indicates the depositional time gap between carbonate and magnetite precipitation was longer. It's presence also indicates that carbonate precipitation was not simply overwhelmed periodically by short bursts of iron hydroxide precipitation but must have been shut off to allow the clay to accumulate. The carbonate associated oxide iron formation is present stratigraphically below the stromatolitic carbonate, which confirms their presence near the shallow water environment. Therefore, it is very likely a transitional facies between deeper water oxide iron formation and shallow water carbonate facies.

Slumped carbonate

The carbonate slump facies is present stratigraphically below the laminated carbonate facies. The laminated carbonate facies was deposited in peritidal settings (McIntyre & Fralick, 2017). Two types of carbonate slumps occur in the Red Lake carbonate platform: magnetite hosted

slumps and shale-hosted slumps. The carbonate slump landed below the photic zone where no carbonate was being deposited and the settling of slumped carbonate was variable depending on the condition of in situ environments, e.g., they were deposited when chert and Fe oxide precipitation were shut off, and mud accumulation was active as background sediment or vice versa. Furthermore, the inorganic $\delta^{13}C$ carbon isotope analysis suggests that shale-hosted carbonate slumps have a range of values from positive to negative $\delta^{13}C$. The low $\delta^{l3}C$ values result from the biological recycling of CO_2 in areas of high TOC. In contrast, magnetite hosted slumps have positive $\delta^{13}C$ values.

The REE signature of both magnetite and shale-hosted slumps have REE patterns similar to the shallow water carbonate, although they were deposited in the upper slope environment.

Chert

Biologically mediated silica precipitation is common in the modern ocean, but for the Archean ocean, the origin of silica is controversial due to the lack of silica-secreting organisms (Cloud, 1973; Holland, 1974; Delvigne et al., 2012). In the modern ocean, silicon concentrations in hydrothermal fluids range from ~450 to ~650 ppm, whereas in the Archaean ocean, silicon concentrations in hydrothermal fluids were probably ~1680 ppm to ~3000 ppm, which is 4 to 7 times greater than modern hydrothermal fluids (Mortlock et al., 1993; Van den Boorn, 2008; Shibuya et al., 2010; Wang et al., 2011). For ancient oceans, therefore, the generally accepted source of silica is hydrothermal, and the ancient ocean was saturated with silicic acid (H_4SiO_4), which caused the deposition of silica (Siever, 1957; Cloud, 1973; Holland, 1973; Barrett, 1982; Gross & Zajac, 1983; Barrett et al., 1987; Siever, 1992; Maliva et al., 2005; Van den Boorn, 2008). However, there are several hypotheses regarding the formation of Archean chert including: (1)

cherts formed by direct precipitation of hydrothermal fluids and/or silica-saturated seawater, (2) silicification of precursor rock by interaction with hydrothermal-fluid and/or silica-saturated seawater, and (3) post-depositional alteration by diagenetic or metamorphic-metasomatic processes (Delvigne et al., 2012; Van den Boorn, 2008).

In the Red Lake carbonate platform, primary chert mostly occurs interbedded with magnetite, and as massive to laminated chert. In other examples, primary chert tends to occur associated with oxide iron formation in a deep-water setting, rather than that in a shallow water setting (Fralick & Burton, 2008). At Red Lake, massive chert and laminated chert also occur in association with oxide iron formation. Thus, Red Lake chert is considered a deeper water facies due to its occurrence with deeper water iron formation. Massive chert deposition may result from rapid precipitation of low-temperature silica-rich hydrothermal fluids while the regular, flat, laterally continuous chert laminae are probably indicative of precipitation in a low energy environment from silica-saturated seawater. Chert associated with oxide iron formation represents variable ocean chemistry from a silica-saturated water mass to a ferruginous water mass. The alternating accumulation of chert and magnetite layers denotes periods of inactive hydrothermal input and Fe-poor sedimentation and vice versa (Morris, 1993; Steinhoefel et al., 2009).

Even though the crystal structure of chert cannot accept REEs inclusions contained within it give PAAS normalized REE patterns that include positive La and Eu anomalies and high Y/Ho ratio reflecting the Archean seawater-like REE signature. Particularly, the positive Eu anomaly is suggestive of precipitation from Archean seawater.

Oxide Iron Formation

There is a lack of a well-accepted theory for banded iron formation deposition in the

Archean ocean, and the depositional mechanism of iron formation is still controversial due to the absence of good modern analogs (Fralick, 1995; Delvigne et al., 2012). Factors responsible for the deposition of iron formation are iron and silica sources, transport mechanisms, and depositional controls. Additionally, clastic influx should be minimal for the accumulation of iron formation, so that chemical sediments can dominate in the depositional environment. Possible sources of iron in the Archean ocean were subaerial or subaqueous weathering of iron-bearing rocks and iron-rich hydrothermal input (Goodwin, 1956; Huber, 1959; Drever, 1974; Garrels et al., 1973; Barrett et al., 1987; Fralick, 1995). However, it is generally accepted that hydrothermal alteration of oceanic crust was the primary source of iron in the Archean ocean (Jacobsen & Pimentel-Klose, 1988; Derry & Jacobsen, 1990; Bau & Möller, 1993). Several models have been proposed for the depositional mechanism of banded iron formation. The oxidation of ferrous iron (Fe^{+2}) by oxygen model states mixing of upwelled Fe^{+2} rich, high-temperature hydrothermal plumes or reduced iron-rich deep water with the near-shore cyanobacterial produced O_2-rich shallow water causes the oxidation of Fe^{+2} (Cloud, 1973; Klein & Beukes, 1989; Beukes et al., 1990; Beukes & Klein, 1990; Isley, 1995; Hamade et al., 2003; Beukes & Gutzmer, 2008; Steinhoefel et al., 2009). The oxidized ferric iron is insoluble in seawater and sinks to the bottom as ferric oxyhydroxide or hydroxide. Alternatively, according to Konhauser et al. (2002) anoxygenic bacterial iron oxidation was responsible for the deposition of iron formation. The UV induced photo-oxidation of ferrous iron is another model for the deposition of iron formation (Cairns-Smith, 1978; Braterman et al, 1983).

The oxide facies iron formation in the Red Lake area is characterized by mm to cm-scale magnetite bands alternating with chert bands. The overall flat, regular, laterally continuous magnetite bands in oxide iron formation indicate that precipitation occurred in a low energy environment. The absence of carbonate, slumped rock and presence of volcanic rocks above the

iron formations in the NGI-31 hole suggest that Red Lake iron formation formed distal from the carbonate platform, possibly, in the deep water of an upper slope setting. Thickness variations in magnetite and chert bands were probably caused by the effect of changes in discrete hydrothermal venting as well as the composition and temperature of hydrothermal fluids (Barrett et al., 1987; Fralick et al., 1989). Chemical sedimentation and controlling physical factors on outer shelves and slope environments are not well described in the literature. However, quiescence of siliciclastic supply is undoubtedly a significant control, which in other examples was triggered by sea-level rise (Fralick, 1995). Hydrothermal venting probably created a zone of saturation and precipitation may have occurred away from the vents, even up to tens to hundreds of kilometers (Barrett et al., 1987).

The ferrous iron-rich water mass was probably reacting with a somewhat oxygenated water mass along a redox boundary in the water column with the result that ferric oxyhydroxides or hydroxides settled to the bottom and eventually altered to magnetite during diagenesis. The mixing of an anoxic ferruginous water column and a somewhat oxic water column was possibly due to intense upwelling of hydrothermal plumes or storm surge induced shuttle of oxygenated water, or both.

The geochemistry of REEs in Red Lake oxide iron formation samples reflects mostly no La anomaly to a positive La anomaly in some samples. Most samples have weak positive Ce anomalies and all samples have positive Gd anomalies. They also have pronounced Eu anomalies and high Y/Ho ratios. The Pr/Yb ratio is <1 which indicated that iron formations are HREE enriched. However, significant Eu anomalies are suggestive of precipitation from seawater influenced by high-temperature hydrothermal fluids.

Sulfide Iron Formation

Sulfide iron formation formed in a completely anoxic environment. Proximity to the source of hydrothermal venting often controls the formation of iron facies. The deposition of sulfide iron formation facies commonly occurs close to the vent site in a reducing environment (Goodwin, 1973). Black smokers may transform into white smokers with cooling of magma chambers or the country rock through which the fluid passes, and vice versa with recharge of the magma chamber or gradual heating of the country rock to the vein system (Haymon et al., 1991; Wilcock & Delaney, 1996). With low Eh conditions, sulfide iron formation deposition occurs near vents, or in low relief areas nearby on the ocean floor.

The occurrence of fine-grained carbonaceous shales with sulfide iron formation represents slow deposition below storm wave-base (Fralick et al., 1989). Each pyritic lamination probably reflects an individual hydrothermal pulse. However, the thick massive pyrite layers are indicative of rapid precipitation near the vent site. It is assumed that the Red Lake sulfides were precipitated from a bottom anoxic water layer in a deeper part of the platform environment. Some of the sulfide-facies iron formations are characterized by irregularly laminated to nodular pyrite associated with carbonaceous shale. This co-occurrence reflects the presence of microbial communities and therefore proximity to a relatively low-temperature diffuse hydrothermal venting. Moreover, sulfur isotope analysis confirms the presence of bacterial sulfate reduction. Intermittent emanations of iron-rich solutions into a euxinic bottom water layer is directly or indirectly related to the mm- to cm-scale banding in the pyrite and pyrrhotite.

The shale normalized REE patterns of sulfide iron formation show no La and Ce anomalies. Interestingly, pyrite samples mostly have low to no Eu anomalies and high Gd anomalies while

some pyrrhotite samples have typical Archean seawater Eu anomalies with smaller Gd anomalies. However, REEs do not fit into the iron sulfide lattice; therefore, the REE concentration in pure pyrite and pyrrhotite samples should be insignificant, and the REE pattern present in iron sulfides must come from either fluid and mineral inclusions or other materials associated with these rocks.

Black slates

Organic-rich mud deposition, ideally, occurs in a low energy environment and indicates a slow rate of sedimentation. As mentioned earlier, black slates are metamorphosed carbon-rich shale, which is fine-grained, massive, and often contains different sulfidic minerals. The carbon content in black slates varies from 1.34 to 5.12 %. This carbon content indicates that there was a high supply of organic materials in the depositional basin. Rain-out deposition of mud would have occurred as background sedimentation in deeper water environments when the seawater composition remained undisturbed for long intervals of time. The deposition of Red Lake slate possibly begun with cessation of volcanic activity, less venting of hydrothermal fluids, and no coarse-grained clastic sedimentation.

The Red Lake black slate has crustal Y/Ho ratios of ~25 which confirms their siliciclastic origin. The black slate has an overall flat REE pattern with moderate Eu anomaly. As the Archean ocean was heavily influenced by hydrothermal activity, therefore, during deposition of organic-rich mud it gradually absorbed Eu and inherited the anomaly.

Chapter 6: Conclusion

The Red Lake carbonate platform is part of the Red Lake Greenstone Belt which belongs to the Uchi Subprovince of the Archean Superior Province. This is the oldest known carbonate platform on earth and formed sometime between 2.94 Ga to 2.92 Ga (Corfu & Wallace, 1986). The 400 m thick Red Lake carbonate platform contains a variety of chemical sedimentary rocks including, carbonate, chert, oxide iron formation, sulfide iron formation, and siliciclastic black slate. The deeper water chemical sedimentary rocks and black slate were investigated using an array of different types of geochemical techniques, e.g., whole rock geochemical analysis, XRF scanning, SEM-EDS analysis, and isotope analyses, to interpret the depositional environment and sediment-water interaction of the 2.93 Ga Mesoarchean ocean.

Rare earth element analysis outlines that the chemical sediments generally have typical Archean seawater-derived REE patterns, with HREE enrichment (Figure 4.1A and E), and insignificant siliciclastic influence (Figures 3.9, 3.15 and 3.19). The magnetite samples have pronounced positive Eu anomalies, slight Gd anomalies, super-chondritic Y/Ho ratios, HREE enrichment and some of the samples have positive Ce anomalies. Positive Ce anomalies in magnetite samples imply that there was a redox boundary in the depositional settings. Similarly, the carbonate rocks have positive Eu anomalies, slight Gd anomalies, super-chondritic Y/Ho ratios, HREE enriched patterns and no negative Ce anomaly, except one carbonate sample. Conversely, the REE signatures present in the chert and the sulfide iron formation samples do not result from pure chert or iron sulfide since REEs do not fit into the lattice framework of these minerals. Their patterns will reflect the presence of minerals, organic and/or fluid inclusions (Figure 4.1 B, D, and E). Siliciclastic carbonaceous slate has positive Eu anomalies indicating that the siliciclastic sediment inherited the REE seawater composition of the Archean ocean through adsorption,

probably onto the surface of clays. Overall, due to the omnipresence of Eu anomalies in chemical and siliciclastic rocks, it is suggested that the REE composition of the Mesoarchean ocean was influenced by high-temperature hydrothermal inputs (Barrett et al., 1987; Danielson et al., 1992; Bau & Dulski, 1996; Planavsky et al, 2010).

Elemental concentrations in the chemical sediments provide information on the causes of precipitation and its rate. The zirconium and hafnium concentrations in oxide iron formations (Figure 4.20) denote that they were in part derived from a nondetrital source and were mobile in the Archean ocean and preferentially co-precipitated with iron hydroxide (Bau & Alexander, 2009). Slower rates of deposition of iron hydroxide allowed higher sorption of Zr and Hf (Schmidt et al., 2014). Manganese oxide concentration in oxide iron formation increases up stratigraphy towards the shallow water carbonate platform (Figure 4.19), possibly indicating the presence of O_2 produced by cyanobacteria. Redox-sensitive elements such as Cr, Mo, V, and U plotted against Al_2O_3 and TiO_2 (Figures 4.7 to 4.14) and ratio plots of Cr/TiO_2 vs. V/TiO_2 and Mo/TiO_2 vs. U/TiO_2 (Figures 4.15 and 4.16) show that a portion of the element's concentration was derived from siliciclastic material in the chemical sedimentary rocks, but they have enrichment of these elements to some degree beyond the siliciclastics they contain. Either high-temperature hydrothermal fluid or fluvial discharge was the possible source of these elements in the seawater. In the former, the presence of oxygen is not necessary, but in the latter possibility, the presence of O_2 in the weathering environment would promote these elements' mobility. In summary, the presence of positive Ce anomalies and high Mn concentration in some of the oxide iron formation, as well as redox-sensitive element enrichment in the chemical sedimentary rocks, suggest that there was some oxygen present in this depositional setting.

Multiple sulfur isotope analysis (Figures 4.24 to 4.26) infers that bacterial fractionation of sulfur and mass-independent fractionations of sulfur both were active as well as the source of sulfur in the Red Lake sulfides was diverse (Figure 4.28). The organic carbon isotope plot (Figure 4.29) shows two different trends; one group has lighter $\delta^{13}C$ values at approximately - 30 ‰ and the other group has heavier $\delta^{13}C$ values of -17 ‰. Such trends indicate purple sulfur bacteria might be present in the shallow water carbonate platform along with cyanobacteria as different bacteria fractionate carbon isotopes differently, with purple sulfur bacterial fractionating C less than oxygenic phototrophs (Posth et al., 2017). Analysis of inorganic carbon isotopes denotes that their values fall within the range typical of Archean carbonate. However, the carbonate associated with oxide facies iron formation has positive $\delta^{l3}C$ values, whereas the shale-hosted slumped carbonate has gradually changing positive to negative $\delta^{l3}C$ value due to diagenetic modification. In other Archean carbonate platforms such as the Hamersley, the deep Archean seawater had a $\delta^{l3}C$ value of -5‰ (Kaufman et al., 1990), and in the Steep Rock, a lower -5.5‰ $\delta^{l3}C$ value was observed for deeper seawater siderite (Fralick & Riding, 2015). During diagenesis organic carbon derived from the recycling of organic matter (^{12}C enriched) (Schidlowski et al., 1983; Thode & Goodwin 1983; Buaret al, 1985) reacted with iron oxyhydroxide and lowered the $\delta^{l3}C$ values (Kaufman et al., 1990). Additionally, the $\delta^{18}O$ oxygen isotope value indicates that dolomitization of Red Lake dolomites did not occur in a restricted marine environment. The lighter oxygen isotope value in dolomites suggests that dolomitization occurred in an environment where there was an influx of fresh water.

The lithofacies associations of the chemical sedimentary rocks and siliciclastic rocks indicate that ocean chemistry at the depositional sites was not consistent at ~2930 Ma, and also relative sea level fluctuated during deposition. Throughout the accumulation of different chemical

sediments, ocean chemistry changed depending on the intensity of low to high-temperature hydrothermal activity and other factors that are more difficult to identify. However, organic-rich mud was being deposited as background sediment, but the accumulation became prominent during cessation of chemical sedimentation. Carbonate precipitation was active in the shallow part of the platform in a prevailing warm, slightly oxic water environment. The chert and oxide iron had a variable precipitation rate and alternated in the banded iron formation indicating a change in the saturation of seawater caused by Fe^{+2}, or by silicic acid or by O_2. Depending on the presence or absence of O_2, oxide iron formation or sulfide iron formation formed respectively from the ferruginous water column in this area of the Archean ocean. Also, H_2S emission from the venting site and an organic-rich muddy bottom was favorable for maintaining euxinic conditions, which ultimately resulted in the precipitation of sulfide iron formation. In contrast, Fe-rich seawater and/or high-temperature hydrothermal venting fluid combined with O_2 causing the precipitation of iron hydroxide. In summary, Red Lake sulfides were deposited in deeper water anoxic environments, while magnetite and chert were precipitated in suboxic environments and carbonates were deposited in what was probably a slightly oxic shallow water environment.

This study focused mainly on the deep water chemical and siliciclastic rock sequences and these rocks are present above and below the shallow water stromatolitic carbonate unit. It is obvious from the drill-hole core logs that deeper water carbonates, chert, oxide iron formation, sulfide iron formation, and other siliciclastic rocks repeatedly interlayer with the shallow water stromatolitic carbonate successions, which suggest multiple events of carbonate platform flooding. Also, the $\delta^{13}C$ organic carbon isotope value at the bottom of the succession is -30‰, towards the platform it reaches -20‰, through the stromatolitic unit it averages approximately -17‰, and the strata overlying the stromatolitic succession have upwardly decreasing $\delta^{13}C$ values, down to -

25‰. This isotopic trend suggests that deposition of sequences underlying and overlying the stromatolite unit occurred in a similar organic carbon isotopic environment. A somewhat similar pattern was also observed for sulfur isotopes. However, further analysis needs to be done to comprehend the relative sea-level change dynamics through time and its control of degree of isotopic fractionation.

References

Aizawa, K., Ogawa, Y., Ishido, T., Attias, Eric., Rob Evens, Kerry Key, S. N., Bachmann, O., Bergantz, G., … Li, B. (2017). Geochemistry of Zr, Hf, and REE in a wide spectrumof Eh and water composition: The case of Dead Sea Fault system(Israel). *Journal of Geophysical Research: Solid Earth*, *116*(1), 1–12. https://doi.org/10.2113/2.4.476

Allwood, A. C., Kamber, B. S., Walter, M. R., Burch, I. W., & Kanik, I. (2010). Trace elements record depositional history of an Early Archean stromatolitic carbonate platform. *Chemical Geology*, *270*(1–4), 148–163. https://doi.org/10.1016/j.chemgeo.2009.11.013

Alt, J. C., & Shanks, W. C. (2006). Stable isotope compositions of serpentinite seamounts in the Mariana forearc: Serpentinization processes, fluid sources and sulfur metasomatism. *Earth and Planetary Science Letters*, *242*(3), 272–285. https://doi.org/https://doi.org/10.1016/j.epsl.2005.11.063

Anbar, A. D. (2007). A Whiff of Oxygen Before the Great Oxidation Event? *Science*, *307*(5706), 111–113.

Anbar, A. D., & Holland, H. D. (1992). The photochemistry of manganese and the origin of banded iron formations. *Geochimica et Cosmochimica Acta*, *56*(7), 2595–2603. https://doi.org/10.1016/0016-7037(92)90346-K

Anders, E., & Grevesse, N. (1989). Abundances of the elements: Meteoritic and solar. *Geochimica et Cosmochimica Acta*, *53*(1), 197–214. https://doi.org/https://doi.org/10.1016/0016-7037(89)90286-X

Armstrong, A. . (2008). Why did Nature choose manganese to make oxygen? *Philosophical Transactions of the Royal Society B: Biological Sciences*, *363*(1494), 1263–1270. https://doi.org/10.1098/rstb.2007.2223

Bachinski, D. J. (1969). Bond strength and sulfur isotopic fractionation in coexisting sulfides. *Economic Geology*, *64*(1), 56–65. Retrieved from http://dx.doi.org/10.2113/gsecongeo.64.1.56

Barrett, T. J. (1982). 11_Stratigraphy and sedimentology of Jurassic bedded chert overlying ophiolites in the North Apennines , Italy.

Barrett, T. J., Fralick, P. W., & Jarvis, I. (1987). Rare-earth-element geochemistry of some Archean iron formations north of Lake Superior, Ontario. *Canadian Journal of Earth Sciences*, *25*(4), 570–580. https://doi.org/10.1139/e88-055

Bau, M., & Alexander, B. W. (2009). Distribution of high field strength elements (Y, Zr, REE, Hf, Ta, Th, U) in adjacent magnetite and chert bands and in reference standards FeR-3 and FeR-4 from the Temagami iron-formation, Canada, and the redox level of the Neoarchean ocean. *Precambrian Research*, *174*(3–4), 337–346. https://doi.org/10.1016/j.precamres.2009.08.007

Bau, M., & Dulski, P. (1995). Comparative study of yttrium and rare-earth element behaviours in

fluorine-rich hydrothermal fluids. *Contributions to Mineralogy and Petrology*, *119*(2), 213–223. https://doi.org/10.1007/BF00307282

Bau, M., & Dulski, P. (1996a). Anthropogenic origin of positive gadolinium anomalies in river waters. *Earth and Planetary Science Letters*, *143*(1–4), 245–255. https://doi.org/10.1016/0012-821X(96)00127-6

Bau, M., & Dulski, P. (1996b). Distribution of yttrium and rare-earth elements in the Penge and Kuruman iron-formations, Transvaal Supergroup, South Africa. *Precambrian Research*, *79*(1), 37–55. https://doi.org/https://doi.org/10.1016/0301-9268(95)00087-9

Bau, M., & Möller, P. (1993). Rare earth element systematics of the chemically precipitated component in early precambrian iron formations and the evolution of the terrestrial atmosphere-hydrosphere-lithosphere system. *Geochimica et Cosmochimica Acta*, *57*(10), 2239–2249. https://doi.org/https://doi.org/10.1016/0016-7037(93)90566-F

Baur, M. E., Hayes, J. M., Studley, S. A., & Walter, M. R. (1985). Millimeter-scale variations of stable isotope abundances in carbonates from banded iron-formations in the Hamersley Group of Western Australia. *Economic Geology*, *80*(2), 270–282. Retrieved from http://dx.doi.org/10.2113/gsecongeo.80.2.270

Becker, R. H., & N. Clayton, R. (1972). Carbon isotopic evidence for the origin of a banded iron-formation in Western Australia. *Geochimica et Cosmochimica Acta*, *36*(5), 577–595. https://doi.org/https://doi.org/10.1016/0016-7037(72)90077-4

Bekker, A., Holland, H. D., Wang, P.-L., Rumble III, D., Stein, H. J., Hannah, J. L., Beukes, N. J. (2004). Dating the rise of atmospheric oxygen. *Nature*, *427*, 117. Retrieved from https://doi.org/10.1038/nature02260

Bekker, A., Slack, J. F., Planavsky, N., Krapež, B., Hofmann, A., Konhauser, K. O., & Rouxel, O. J. (2010). Iron formation: The sedimentary product of a complex interplay among mantle, tectonic, oceanic, and biospheric processes. *Economic Geology*, *105*(3), 467–508. https://doi.org/10.2113/gsecongeo.105.3.467

Beukes, N., & Gutzmer, J. (2008). Origin and paleoenvironmental significance of major iron formations at the Archean-Paleoproterozoic boundary. *Society of Economic Geologists Reviews*, *15*(August), 5–47. https://doi.org/10.5382/Rev.15.01

Beukes, N. J., & Gutzmer, J. (1996). A voleanic-exhalative origin for the world ’ s largest (Kalahari) manganese field: A discussion of the paper by D.H. Cornell and S.S. Shütte. *Mineralium Deposita*, *31*, 242–245.

Beukes, N. J., & Klein, C. (1990). Geochemistry and sedimentology of a facies transition from microbanded to granular iron-formation in the early Proterozoic Transvaal Supergroup, South Africa. *Precambrian Research*, *47*(1), 99–139. https://doi.org/https://doi.org/10.1016/0301-9268(90)90033-M

Beukes, N. J., Klein, C., Kaufman, A. J., & Hayes, J. M. (1990). Carbonate petrography, kerogen distribution, and carbon and oxygen isotope variations in an early Proterozoic transition

from limestone to iron-formation deposition, Transvaal Supergroup, South Africa. *Economic Geology*, *85*(4), 663–690. https://doi.org/10.2113/gsecongeo.85.4.663

Bolhar, R., Kamber, B. S., Moorbath, S., Fedo, C. M., & Whitehouse, M. J. (2004). Characterisation of early Archaean chemical sediments by trace element signatures. *Earth and Planetary Science Letters*, *222*(1), 43–60. https://doi.org/10.1016/j.epsl.2004.02.016

Bolhar, R., & Van Kranendonk, M. J. (2007). A non-marine depositional setting for the northern Fortescue Group, Pilbara Craton, inferred from trace element geochemistry of stromatolitic carbonates. *Precambrian Research*, *155*(3–4), 229–250. https://doi.org/10.1016/j.precamres.2007.02.002

Bolhar, R., Van Kranendonk, M. J., & Kamber, B. S. (2005). A trace element study of siderite-jasper banded iron formation in the 3.45 Ga Warrawoona Group, Pilbara Craton - Formation from hydrothermal fluids and shallow seawater. *Precambrian Research*, *137*(1–2), 93–114. https://doi.org/10.1016/j.precamres.2005.02.001

Braterman, P. S., Cairns-Smith, A. G., & Sloper, R. W. (1983). Photo-oxidation of hydrated Fe2+—significance for banded iron formations. *Nature*, *303*, 163. Retrieved from https://doi.org/10.1038/303163a0

Bristow, T. F., & Kennedy, M. J. (2008). Carbon isotope excursions and the oxidant budget of the Ediacaran atmosphere and ocean. *Geology*, *36*(11), 863–866. Retrieved from http://dx.doi.org/10.1130/G24968A.1

Brueckner, S. M., Piercey, S. J., Layne, G. D., Piercey, G., & Sylvester, P. J. (2015). Variations of sulphur isotope signatures in sulphides from the metamorphosed Ming Cu(−Au) volcanogenic massive sulphide deposit, Newfoundland Appalachians, Canada. *Mineralium Deposita*, *50*(5), 619–640. https://doi.org/10.1007/s00126-014-0567-7

Cairns-Smith, A. G. (1978). Precambrian solution photochemistry, inverse segregation, and banded iron formations. *Nature*, *276*, 807. Retrieved from https://doi.org/10.1038/276807a0

Calvert, S. E., & Pedersen, T. F. (1993). Geochemistry of Recent oxic and anoxic marine sediments: Implications for the geological record. *Marine Geology*, *113*(1), 67–88. https://doi.org/https://doi.org/10.1016/0025-3227(93)90150-T

Canfield, D. E. (1998). A new model for Proterozoic ocean chemistry. *Nature*, *396*(6710), 450–453. https://doi.org/10.1038/24839

Canfield, D. E. (2001). Biogeochemistry of sulfur isotopes. *Reviews in Mineralogy and Geochemistry*, *43*(1), 607–636.

Card, K. D. (1990). A review of the Superior Province of the Canadian Shield, a product of Archean accretion. *Precambrian Research*, *48*(1), 99–156. https://doi.org/https://doi.org/10.1016/0301-9268(90)90059-Y

Card, K. D., & Ciesielski, A. (1986). Subdivisions of the Superior Province of the Canadian Shield. *Geoscience Canada*, *13*(1), 5–13. Retrieved from https://journals.lib.unb.ca/index.php/GC/article/view/3439

Claypool, G. E., Holser, W. T., Kaplan, I. R., Sakai, H., & Zak, I. (1980). The age curves of sulfur and oxygen isotopes in marine sulfate and their mutual interpretation. *Chemical Geology*, *28*, 199–260.

Cloud, P. (1973). Paleoecological significance of the banded iron-formation. *Economic Geology*, *68*(7), 1135–1143. https://doi.org/10.2113/gsecongeo.68.7.1135

Corfu, F., & Andrews, A. J. (1987). Geochronological constraints on the timing of magmatism, deformation, and gold mineralization in the Red Lake greenstone belt, northwestern Ontario. *Canadian Journal of Earth Sciences*, *24*(7), 1302–1320.

Corfu, F., & Wallace, H. (1986). U–Pb zircon ages for magmatism in the Red Lake greenstone belt, northwestern Ontario. *Canadian Journal of Earth Sciences*, *23*(1), 27–42. https://doi.org/10.1139/e86-004

Danielson, A., Möller, P., & Dulski, P. (1992). The europium anomalies in banded iron formations and the thermal history of the oceanic crust. *Chemical Geology*, *97*(1), 89–100. https://doi.org/https://doi.org/10.1016/0009-2541(92)90137-T

de Baar, H. J., German, C. R., Elderfield, H., & Van Gaans, P. (1988). Rare earth element distributions in anoxic waters of the Cariaco Trench. *Geochimica et Cosmochimica Acta,* 52(5), 1203-1219.

Dellwig, O., Leipe, T., März, C., Glockzin, M., Pollehne, F., Schnetger, B., Brumsack, H.-J. (2010). A new particulate Mn–Fe–P-shuttle at the redoxcline of anoxic basins. *Geochimica et Cosmochimica Acta*, *74*(24), 7100–7115. https://doi.org/https://doi.org/10.1016/j.gca.2010.09.017

Delvigne, C., Cardinal, D., Hofmann, A., & André, L. (2012). Stratigraphic changes of Ge/Si, REE+ Y and silicon isotopes as insights into the deposition of a Mesoarchaean banded iron formation. *Earth and Planetary Science Letters*, *355*, 109–118.

Derry, L. A., & Jacobsen, S. B. (1990). The chemical evolution of Precambrian seawater: Evidence from REEs in banded iron formations. *Geochimica et Cosmochimica Acta*, *54*(11), 2965–2977. https://doi.org/https://doi.org/10.1016/0016-7037(90)90114-Z

Drever, J. I. (1974). Geochemical model for the origin of precambrian banded iron formations. *Bulletin of the Geological Society of America*, *85*(7), 1099–1106. https://doi.org/10.1130/0016-7606(1974)85<1099:GMFTOO>2.0.CO;2

Elderfield, H. (1988). The oceanic chemistry of the rare-earth elements. *Philosophical Transactions of the Royal Society of London. Series A, Mathematical and Physical Sciences*, *325*(1583), 105–126.

Elderfield, H., & Greaves, M. J. (1981). Negative cerium anomalies in the rare earth element patterns of oceanic ferromanganese nodules. *Earth and Planetary Science Letters*, *55*(1), 163–170. https://doi.org/https://doi.org/10.1016/0012-821X(81)90095-9

Elderfield, H., & Greaves, M. J. (1982). The rare earth elements in seawater. *Nature*, *296*(5854), 214–219. https://doi.org/10.1038/296214a0

Elderfield, H., Upstill-Goddard, R., & Sholkovitz, E. R. (1990). The rare earth elements in rivers, estuaries, and coastal seas and their significance to the composition of ocean waters. *Geochimica et Cosmochimica Acta*, *54*(4), 971–991.

Fairchild, I. J., & Kennedy, M. J. (2007). Neoproterozoic glaciation in the Earth System. *Journal of the Geological Society*, *164*(5), 895–921. Retrieved from http://dx.doi.org/10.1144/0016-76492006-191

Farquhar, J., Bao, H., & Thiemens, M. (2000). Atmospheric Influence of Earth's Earliest Sulfur Cycle. *Science*, *289*(5480), 756 LP-758. https://doi.org/10.1126/science.289.5480.756

Farquhar, J., Peters, M., Johnston, D. T., Strauss, H., Masterson, A., Wiechert, U., & Kaufman, A. J. (2007). Isotopic evidence for Mesoarchaean anoxia and changing atmospheric sulphur chemistry. *Nature*, *449*, 706. Retrieved from https://doi.org/10.1038/nature06202

Farquhar, J., Savarino, J., Airieau, S., & Thiemens, M. H. (2001). Observation of wavelength-sensitive mass-independent sulfur isotope effects during SO2 photolysis: Implications for the early atmosphere. *Journal of Geophysical Research: Planets*, *106*(E12), 32829–32839. https://doi.org/10.1029/2000JE001437

Farquhar, J., & Wing, B. A. (2003). Multiple sulfur isotopes and the evolution of the atmosphere. *Earth and Planetary Science Letters*, *213*(1), 1–13. https://doi.org/https://doi.org/10.1016/S0012-821X(03)00296-6

Firdaus, M. L., Norisuye, K., Nakagawa, Y., Nakatsuka, S., & Sohrin, Y. (2008). Dissolved and labile particulate Zr, Hf, Nb, Ta, Mo and W in the western North Pacific Ocean. *Journal of Oceanography*, *64*(2), 247–257. https://doi.org/10.1007/s10872-008-0019-z

Fischer, W. W., Schroeder, S., Lacassie, J. P., Beukes, N. J., Goldberg, T., Strauss, H., Knoll, A. H. (2009). Isotopic constraints on the Late Archean carbon cycle from the Transvaal Supergroup along the western margin of the Kaapvaal Craton, South Africa. *Precambrian Research*, *169*(1–4), 15–27. https://doi.org/10.1016/j.precamres.2008.10.010

Fowler, A. D., & Doig, R. (1983). The significance of europium anomalies in the REE spectra of granites and pegmatites, Mont Laurier, Quebec. *Geochimica et Cosmochimica Acta*, *47*(6), 1131–1137.

Fralick, P. (1995). Depositional Controls on Iron Formation Associations in Canada. *Special Publication of the International Association of Sedimentologists*, *22*, 384.

Fralick, P. (2003). Geochemistry of clastic sedimentary rocks: ratio techniques. *Geochemistry of Sediments and Sedimentary Rocks: Evolutionary Considerations to Mineral Deposit-Forming Environments: Geological Association of Canada, Geotext*, *4*, 85–103.

Fralick, P., & Burton, J. (2008). Geochemistry of Paleoproterozoic Gunflint Formation carbonate: implications for early hydrosphere-atmosphere evolution. *Geochimica et Cosmochimica Acta*, *72*(12, Supplement 1), A280. https://doi.org/10.1016/j.precamres.2016.12.014

Fralick, P., & Riding, R. (2015). Steep Rock Lake: Sedimentology and geochemistry of an

Archean carbonate platform. *Earth-Science Reviews*, *151*, 132–175. https://doi.org/10.1016/j.earscirev.2015.10.006

Fralick, P. W., Barrett, T. J., Jarvis, K. E., Jarvis, I., Schnieders, B. R., & Kemp, R. Vande. (1989). Sulfide-facies iron formation at the Archean Morley occurrence, northwestern Ontario. Contrasts with oceanic hydrothermal deposits. *Canadian Mineralogist*, *27 pt 4*, 601–616.

Fralick, P. W., & Kronberg, B. I. (1997). Geochemical discrimination of clastic sedimentary rock sources. *Sedimentary Geology*, *113*(1), 111–124. https://doi.org/https://doi.org/10.1016/S0037-0738(97)00049-3

Friedman, G. M. (1980). Dolomite is an evaporite mineral: Evidence from the rock record and from sea marginal ponds of the red sea. *The Society of Economic Paleontologists and Mineralogists*, *SEPM Speci*(28), 69–80.

Garrels, R. M., Perry, E. A., & Mackenzie, F. T. (1973). Genesis of Precambrian Iron-Formations and the Development of Atmospheric Oxygen. *Economic Geology*, *68*(7), 1173–1179. Retrieved from http://dx.doi.org/10.2113/gsecongeo.68.7.1173

Gauthier-Lafaye, F., & Weber, F. (2003). Natural nuclear fission reactors: time constraints for occurrence, and their relation to uranium and manganese deposits and to the evolution of the atmosphere. *Precambrian Research*, *120*(1), 81–100. https://doi.org/https://doi.org/10.1016/S0301-9268(02)00163-8

Gemmell, J. B., & Sharpe, R. (1998). Detailed sulfur-isotope investigation of the TAG hydrothermal mound and stockwork zone, 26 N, Mid-Atlantic Ridge. In *Proceedings-Ocean Drilling Program Scientific Results* (pp. 71–84). National Science Foundation.

Goldberg, E. D., Koide, M., Schmitt, R. A., & Smith, R. H. (1963). Rare-Earth distributions in the marine environment. *Journal of Geophysical Research*, *68*(14), 4209–4217. https://doi.org/10.1029/JZ068i014p04209

Goldschmidt, V. M. (1937). The principles of distribution of chemical elements in minerals and rocks. The seventh Hugo Müller Lecture, delivered before the Chemical Society on March 17th, 1937. *Journal of the Chemical Society (Resumed)*, (0), 655–673. https://doi.org/10.1039/JR9370000655

Goodfellow, W. D., & Peter, J. M. (1996). Sulphur isotope composition of the Brunswick No. 12 massive sulphide deposit, Bathurst Mining Camp, New Brunswick: implications for ambient environment, sulphur source, and ore genesis. *Canadian Journal of Earth Sciences*, *33*(2), 231–251.

Goodwin, A. M. (1956). Facies relations in the Gunflint iron formation [Ontario]. *Economic Geology*, *51*(6), 565–595. Retrieved from http://dx.doi.org/10.2113/gsecongeo.51.6.565

Goodwin, A. M. (1973). Archean Iron-Formations and Tectonic basins of the Canadian Shield. *Economic Geology*, *68*(7), 915–933. Retrieved from http://dx.doi.org/10.2113/gsecongeo.68.7.915

Grandstaff, D. E. (1976). A kinetic study of the dissolution of uraninite. *Economic Geology*, *71*(8), 1493–1506.

Grinenko, V. A., & Thode, H. G. (1970). Sulfur isotope effects in volcanic gas mixtures. *Canadian Journal of Earth Sciences*, *7*(6), 1402–1409.

Gross, G. A. (1980). A classification of iron formations based on depositional environments. *The Canadian Mineralogist*, *18*(2), 215–222. Retrieved from http://dx.doi.org/

Gross, G. A., & Zajac, I. S. (1983). Iron-Formation in Fold Belts Marginal to the Ungava Craton. In A. F. Trendall & R. C. B. T.-D. in P. G. Morris (Eds.), *Iron-Formation Facts and Problems* (Vol. 6, pp. 253–294). Elsevier. https://doi.org/https://doi.org/10.1016/S0166-2635(08)70045-8

Gutzmer, J., & Beukes, N. J. (1996). Mineral paragenesis of the Kalahari managanese field, South Africa. *Ore Geology Reviews*, *11*(6), 405–428. https://doi.org/https://doi.org/10.1016/S0169-1368(96)00011-X

Hamade, T., Konhauser, K. O., Raiswell, R., Goldsmith, S., & Morris, R. C. (2003). Using Ge/Si ratios to decouple iron and silica fluxes in Precambrian banded iron formations. *Geology*, *31*(1), 35–38. Retrieved from http://dx.doi.org/10.1130/0091-7613(2003)031%3C0035:UGSRTD%3E2.0.CO

Hannigan, R. E., & Sholkovitz, E. R. (2001). The development of middle rare earth element enrichments in freshwaters: weathering of phosphate minerals. *Chemical Geology*, *175*(3–4), 495–508.

Hans Wedepohl, K. (1995). The composition of the continental crust. *Geochimica et Cosmochimica Acta*, *59*(7), 1217–1232. https://doi.org/https://doi.org/10.1016/0016-7037(95)00038-2

Hayes, J. M., Popp, B. N., Takigiku, R., & Johnson, M. W. (1989). An isotopic study of biogeochemical relationships between carbonates and organic carbon in the Greenhorn Formation. *Geochimica et Cosmochimica Acta*, *53*(11), 2961–2972.

Haymon, R. M., Fornari, D. J., Edwards, M. H., Carbotte, S., Wright, D., & Macdonald, K. C. (1991). Hydrothermal vent distribution along the East Pacific Rise crest (9 09′–54′ N) and its relationship to magmatic and tectonic processes on fast-spreading mid-ocean ridges. *Earth and Planetary Science Letters,* 104(2-4), 513-534.

Hekinian, A. R., Fevrier, M., Bischoff, J. L., Picot, P., & Shanks, W. C. (1985). Sulfide Deposits from the East Pacific Rise near 21 ° N Published by : American Association for the Advancement of Science Stable URL : http://www.jstor.org/stable/1683348, *207*(4438), 1433–1444.

Hoefs, J. (1997). *Stable isotope geochemistry* (Vol. 201). Springer.

Hofmann, H. J., Thurston, P. C., & Wallace, H. (1985). Archean stromatolites from Uchi greenstone belt, northwestern Ontario. In *Evolution of Archean Supracrustal Sequences* (Vol. 28, pp. 125–132). Geol. Assoc. Can. Spec. Pap.

Holland, H. D. (1973). The Oceans: A possible source of iron in iron-formations. *Economic Geology*, *68*(7), 1169–1172. https://doi.org/10.2113/gsecongeo.68.7.1169

Holland, H. D. (1974). Aspects of the Geologic History of Seawater BT - Cosmochemical Evolution and the Origins of Life. In J. Oró, S. L. Miller, C. Ponnamperuma, & R. S. Young (Eds.) (pp. 87–91). Dordrecht: Springer Netherlands.

Holland, H. D. (2005). Sedimentary Mineral Deposits and the Evolution of Earth's Near-Surface Environments. *Economic Geology*, *100*(8), 1489–1509. Retrieved from http://dx.doi.org/10.2113/gsecongeo.100.8.1489

Holland, H. D. (2006). The Oxygenation of the Atmosphere and Oceans. *Advances in Astrobiology and Biogeophysics*, *361*(1470), 903–315. https://doi.org/10.1007/3-540-33088-7_2

Hollings, P., Wyman, D., & Kerrich, R. (1999). Komatiite–basalt–rhyolite volcanic associations in Northern Superior Province greenstone belts: significance of plume-arc interaction in the generation of the proto continental Superior Province. *Lithos*, *46*(1), 137–161. https://doi.org/http://dx.doi.org/10.1016/S0024-4937(98)00058-9

Huber, N. K. (1959). Some aspects of the origin of the Ironwood iron-formation of Michigan and Wisconsin. *Economic Geology*, *54*(1), 82–118. Retrieved from http://dx.doi.org/10.2113/gsecongeo.54.1.82

Ingri, J., & Pontér, C. (1986). Iron and manganese layering in recent sediments in the Gulf of Bothnia. *Chemical Geology*, *56*(1), 105–116. https://doi.org/https://doi.org/10.1016/0009-2541(86)90114-2

Isley, A. E. (1995). Hydrothermal Plumes and the Delivery of Iron to Banded Iron Formation. *The Journal of Geology*, *103*(2), 169–185. https://doi.org/10.1086/629734

Jacobsen, S. B., & Pimentel-Klose, M. R. (1988). A Nd isotopic study of the Hamersley and Michipicoten banded iron formations: the source of REE and Fe in Archean oceans. *Earth and Planetary Science Letters*, *87*(1), 29–44. https://doi.org/https://doi.org/10.1016/0012-821X(88)90062-3

Jaffrés, J. B. D., Shields, G. A., & Wallmann, K. (2007). The oxygen isotope evolution of seawater: A critical review of a long-standing controversy and an improved geological water cycle model for the past 3.4 billion years. *Earth-Science Reviews*, *83*(1–2), 83–122. https://doi.org/10.1016/j.earscirev.2007.04.002

James, H. L. (1954). Sedimentary facies of iron-formation. *Economic Geology*, *49*(3), 235–293. https://doi.org/10.2113/gsecongeo.49.3.235

Jamieson, J. W., Wing, B. A., Hannington, M. D., & Farquhar, J. (2006). Evaluating isotopic equilibrium among sulfide mineral pairs in Archean ore deposits: case study from the Kidd Creek VMS deposit, Ontario, Canada. *Economic Geology*, *101*(5), 1055–1061.

Johannesson, K. H., & Zhou, X. (1999). Origin of middle rare earth element enrichments in acid waters of a Canadian High Arctic lake. *Geochimica et Cosmochimica Acta*, *63*(1), 153–165.

Johnson, J. E., Webb, S. M., Ma, C., & Fischer, W. W. (2016). Manganese mineralogy and diagenesis in the sedimentary rock record. *Geochimica et Cosmochimica Acta*, *173*, 210–231. https://doi.org/10.1016/j.gca.2015.10.027

Johnson, J. E., Webb, S. M., Thomas, K., Ono, S., Kirschvink, J. L., & Fischer, W. W. (2013). Manganese-oxidizing photosynthesis before the rise of cyanobacteria. *Proceedings of the National Academy of Sciences*, *110*(28), 11238 LP-11243. https://doi.org/10.1073/pnas.1305530110

Johnston, D. T. (2011). Multiple sulfur isotopes and the evolution of Earth's surface sulfur cycle. *Earth-Science Reviews*, 106(1-2), 161-183.

Kamber, B. S., Bolhar, R., & Webb, G. E. (2004). Geochemistry of late Archaean stromatolites from Zimbabwe: evidence for microbial life in restricted epicontinental seas. *Precambrian Research*, *132*(4), 379–399. https://doi.org/https://doi.org/10.1016/j.precamres.2004.03.006

Kamber, B. S., & Webb, G. E. (2001). The geochemistry of late Archaean microbial carbonate: Implications for ocean chemistry and continental erosion history. *Geochimica et Cosmochimica Acta*, *65*(15), 2509–2525. https://doi.org/10.1016/S0016-7037(01)00613-5

Kampschulte, A., & Strauss, H. (2004). The sulfur isotopic evolution of Phanerozoic seawater based on the analysis of structurally substituted sulfate in carbonates. *Chemical Geology*, *204*(3–4), 255–286.

Kasting, J. F. (1993). Earth's early atmosphere. *Science*, *259*(5097), 920 LP-926. https://doi.org/10.1126/science.11536547

Kasting, J. F., Pavlov, A. A., & Siefert, J. L. (2001). A coupled ecosystem-climate model for predicting the methane concentration in the Archean atmosphere. *Origins of Life and Evolution of the Biosphere*, *31*(3), 271–285. https://doi.org/10.1023/A:1010600401718

Kaufman, A. J., Hayes, J. M., & Klein, C. (1990). Primary and diagenetic controls of isotopic compositions of iron-formation carbonates. *Geochimica et Cosmochimica Acta*, *54*(12), 3461–3473. https://doi.org/https://doi.org/10.1016/0016-7037(90)90298-Y

Kaufman, A. J., & Knoll, A. H. (1995). Neoproterozoic variations in the C-isotopic composition of seawater: stratigraphic and biogeochemical implications. *Precambrian Research*, *73*(1), 27–49. https://doi.org/https://doi.org/10.1016/0301-9268(94)00070-8

Klein, C., & Beukes, N. J. (1989). Geochemistry and Sedimentology of a Facies Transition from Limestone to Iron-Formation Deposition in the Early Proterozoic Transvaal Supergroup, South-Africa. *Economic Geology*, *84*(7), 1733–1774.

Labidi, J., Cartigny, P., Birck, J. L., Assayag, N., & Bourrand, J. J. (2012). Determination of multiple sulfur isotopes in glasses: A reappraisal of the MORB δ34S. *Chemical Geology*, *334*, 189–198. https://doi.org/https://doi.org/10.1016/j.chemgeo.2012.10.028

Lee, J. H., & Byrne, R. H. (1993). Complexation of trivalent rare earth elements (Ce, Eu, Gd, Tb, Yb) by carbonate ions. *Geochimica et Cosmochimica Acta*, *57*(2), 295–302. https://doi.org/https://doi.org/10.1016/0016-7037(93)90432-V

Macnamara, J., & Thode, H. G. (1950). Comparison of the Isotopic Constitution of Terrestrial and Meteoritic Sulfur. *Physical Review*, *78*(3), 307–308. https://doi.org/10.1103/PhysRev.78.307

Maliva, R. G., Knoll, A. H., & Simonson, B. M. (2005). Secular change in the Precambrian silica cycle: Insights from chert petrology. *GSA Bulletin*, *117*(7–8), 835–845. Retrieved from http://dx.doi.org/10.1130/B25555.1

Maynard, J. B. (2010). The Chemistry of Manganese Ores through Time: A Signal of Increasing Diversity of Earth-Surface Environments. *Economic Geology*, *105*(3), 535–552. Retrieved from http://dx.doi.org/10.2113/gsecongeo.105.3.535

McConchie, D. M. (1987). *The geology and geochemistry of the Joffre and Whaleback shale members of the Brockman Iron Formation. Unpublished PhD thesis. University of Western Australia.*

McIntyre, T., & Fralick, P. (2017). Sedimentology and Geochemistry of the 2930 Ma Red Lake-Wallace Lake Carbonate Platform, Western Superior Province, Canada. *The Depositional Record*, *3*(2), 258–287. https://doi.org/10.1002/dep2.36

McLennan, S. M. (1989). Rare earth elements in sedimentary rocks; influence of provenance and sedimentary processes. *Reviews in Mineralogy and Geochemistry*, *21*(1), 169–200. Retrieved from http://dx.doi.org/

McLennan, S. M., Hemming, S., Mcdaniel, D. K., & Hanson, G. N. (1993). Geochemical approaches to sedimentation, provenance, and tectonics. *Geological Society of America*, *Special pa*(284), 21–40.

McManus, J., Nägler, T. F., Siebert, C., Wheat, C. G., & Hammond, D. E. (2002). Oceanic molybdenum isotope fractionation: Diagenesis and hydrothermal ridge-flank alteration. *Geochemistry, Geophysics, Geosystems*, *3*(12), 1–9. https://doi.org/10.1029/2002GC000356

Melezhik, V. A., Fallick, A. E., Smirnov, Y. P., & Yakovlev, Y. N. (2003). Fractionation of carbon and oxygen isotopes in 13C-rich Palaeoproterozoic dolostones in the transition from medium-grade to high-grade greenschist facies: a case study from the Kola Superdeep Drillhole. *Journal of the Geological Society*, *160*(1), 71 LP-82. https://doi.org/10.1144/0016-764902-008

Mitchell, R. H., & Krouse, H. R. (1975). Sulphur isotope geochemistry of carbonatites. *Geochimica et Cosmochimica Acta*, *39*(11), 1505–1513.

Mojzsis, S. J., Coath, C. D., Greenwood, J. P., McKeegan, K. D., & Harrison, T. M. (2003). Mass-independent isotope effects in Archean (2.5 to 3.8 Ga) sedimentary sulfides determined by ion microprobe analysis. *Geochimica et Cosmochimica Acta*, *67*(9), 1635–1658. https://doi.org/https://doi.org/10.1016/S0016-7037(03)00059-0

Morford, J. L., Russell, A. D., & Emerson, S. (2001). Trace metal evidence for changes in the redox environment associated with the transition from terrigenous clay to diatomaceous sediment, Saanich Inlet, BC. *Marine Geology*, *174*(1), 355–369.

https://doi.org/https://doi.org/10.1016/S0025-3227(00)00160-2

Morris, R. C. (1993). Genetic modelling for banded iron-formation of the Hamersley Group, Pilbara Craton, Western Australia. *Precambrian Research*, *60*(1), 243–286. https://doi.org/https://doi.org/10.1016/0301-9268(93)90051-3

Mortlock, R. A., Froelich, P. N., Feely, R. A., Massoth, G. J., Butterfield, D. A., & Lupton, J. E. (1993). Silica and germanium in Pacific Ocean hydrothermal vents and plumes. *Earth and Planetary Science Letters*, *119*(3), 365–378. https://doi.org/https://doi.org/10.1016/0012-821X(93)90144-X

Nance, W. B., & Taylor, S. R. (1976). Rare earth element patterns and crustal evolution—I. Australian post-Archean sedimentary rocks. *Geochimica et Cosmochimica Acta*, *40*(12), 1539–1551.

Nozaki, Y., Zhang, J., & Amakawa, H. (1997). The fractionation between Y and Ho in the marine environment. *Earth and Planetary Science Letters*, *148*, 329–340. https://doi.org/10.1016/S0012-821X(97)00034-4

O'Neil, J. . (1986). THEORETICAL AND EXPERIMENTAL ASPECTS OF ISOTOPIC FRACTIONATION. *Reviews in Mineralogy*, *16*, 1–40. Retrieved from http://pubs.er.usgs.gov/publication/70014508

Ono, S., Eigenbrode, J. L., Pavlov, A. A., Kharecha, P., Rumble, D., Kasting, J. F., & Freeman, K. H. (2003). New insights into Archean sulfur cycle from mass-independent sulfur isotope records from the Hamersley Basin, Australia. *Earth and Planetary Science Letters*, *213*(1), 15–30. https://doi.org/https://doi.org/10.1016/S0012-821X(03)00295-4

Ono, S., Wing, B., Johnston, D., Farquhar, J., & Rumble, D. (2006). Mass-dependent fractionation of quadruple stable sulfur isotope system as a new tracer of sulfur biogeochemical cycles. *Geochimica et Cosmochimica Acta*, *70*(9), 2238–2252. https://doi.org/https://doi.org/10.1016/j.gca.2006.01.022

Ossa, F., Hofmann, A., Vidal, O., Kramers, J. D., Belyanin, G., & Cavalazzi, B. (2016). Unusual manganese enrichment in the Mesoarchean Mozaan Group, Pongola Supergroup, South Africa. *Precambrian Research*, *281*, 414–433. https://doi.org/https://doi.org/10.1016/j.precamres.2016.06.009

Paropkari, A. L., Ray, D., Balaram, V., Surya Prakash, L., Mirza, I. H., Satyanarayana, M., Kaisary, S. (2010). Formation of hydrothermal deposits at Kings Triple Junction, northern Lau back-arc basin, SW Pacific: The geochemical perspectives. *Journal of Asian Earth Sciences*, *38*(3–4), 121–130. https://doi.org/10.1016/j.jseaes.2009.12.003

Partin, C. A., Lalonde, S. V, Planavsky, N. J., Bekker, A., Rouxel, O. J., Lyons, T. W., & Konhauser, K. O. (2013). Uranium in iron formations and the rise of atmospheric oxygen. *Chemical Geology*, *362*, 82–90.

Pavlov, A. A., & Kasting, J. F. (2002). Mass-Independent Fractionation of Sulfur Isotopes in Archean Sediments: Strong Evidence for an Anoxic Archean Atmosphere. *Astrobiology*,

2(1), 27–41. https://doi.org/10.1089/153110702753621321

Paytan, A., & Gray, E. T. (2012). Sulfur isotope stratigraphy. In *The geologic time scale* (pp. 167–180). Elsevier.

Peter, J. (2003). Ancient iron-rich metalliferous sediments (iron formations): their genesis and use in the exploration for stratiform base metal sulphide deposits, with examples from the Bathurst Mining Camp. *Geochemistry of Sediment and Sedimentary Rocks*, (4), 1145–1176.

Pirie, J. (1981). Regional setting of gold deposits in the Red Lake area, northwestern Ontario; in genesis of Archean volcanic-hosted gold deposits. *Ontario Geological Survey,* miscellaneous paper 97, 71-93.

Planavsky, N., Bekker, A., Rouxel, O. J., Kamber, B., Hofmann, A., Knudsen, A., & Lyons, T. W. (2010). Rare Earth Element and yttrium compositions of Archean and Paleoproterozoic Fe formations revisited: New perspectives on the significance and mechanisms of deposition. *Geochimica et Cosmochimica Acta*, *74*(22), 6387–6405. https://doi.org/10.1016/j.gca.2010.07.021

Planavsky, N. J., Slack, J. F., Cannon, W. F., O'Connell, B., Isson, T. T., Asael, D., Bekker, A. (2018). Evidence for episodic oxygenation in a weakly redox-buffered deep mid-Proterozoic ocean. *Chemical Geology*, *483*(August 2017), 581–594. https://doi.org/10.1016/j.chemgeo.2018.03.028

Posth, N. R., Bristow, L. A., Cox, R. P., Habicht, K. S., Danza, F., Tonolla, M., Canfield, D. E. (2017). Carbon isotope fractionation by anoxygenic phototrophic bacteria in euxinic Lake Cadagno. *Geobiology*, *15*(6), 798–816. https://doi.org/10.1111/gbi.12254

Poulton, S. W. (2011). *Ferruginous Conditions: A Dominant Feature of the Ocean through Earth's History* (Vol. 7).

Quinn, T. M., & Matthews, R. K. (1990). Post-Miocene diagenetic and eustatic history of Enewetak Atoll: Model and data comparison. *Geology*, *18*(10), 942–945. Retrieved from http://dx.doi.org/10.1130/0091-7613(1990)018%3C0942:PMDAEH%3E2.3.CO

Rodzinyak, K. J. (2012). *An Astrobiological Exploration of Mass Dependent and Mass Independent Sulfur Isotope Fractionation*. Unpublished M.Sc. Thesis . McGill University, Montreal, Quebec.

Roy, S. (1992). Environments and processes of manganese deposition. *Economic Geology*, *87*(5), 1218–1236. Retrieved from http://dx.doi.org/10.2113/gsecongeo.87.5.1218

Roy, S. (2006). Sedimentary manganese metallogenesis in response to the evolution of the Earth system. *Earth-Science Reviews*, *77*(4), 273–305. https://doi.org/https://doi.org/10.1016/j.earscirev.2006.03.004

Ryznar, G., Campbell, F. A., & Krouse, H. R. (1967). Sulfur isotopes and the origin of the Quemont ore body. *Economic Geology*, *62*(5), 664–678.

Sakai, H. (1968). Isotopic properties of sulfur compounds in hydrothermal processes.

GEOCHEMICAL JOURNAL, *2*(1), 29–49. https://doi.org/10.2343/geochemj.2.29

Sanborn-Barrie, M., Skulski, T., Parker, J., & Dubé, B. (2000). Integrated regional analysis of the Red Lake greenstone belt and its mineral deposits , western Superior Province , Ontario. *Geological Survey of Canada*, *Current Re*(C18), 14.

Sanborn-Barrie, M., Skulski, T., & Parker, J. R. (2001). Three hundred million years of tectonic history recorded by the Red Lake greenstone belt, Ontario. *Geological Survey of Canada*, *Current Re*(June), 14. https://doi.org/10.4095/212109

Satkoski, A. M., Fralick, P., Beard, B. L., & Johnson, C. M. (2017). Initiation of modern-style plate tectonics recorded in Mesoarchean marine chemical sediments. *Geochimica et Cosmochimica Acta*, *209*, 216–232.

Schidlowski, M., Hayes, J. M., & Kaplan, I. R. (1983). Isotopic inferences of ancient biochemistries-Carbon, sulfur, hydrogen, and nitrogen.

Schmidt, K., Bau, M., Hein, J. R., & Koschinsky, A. (2014). Fractionation of the geochemical twins Zr-Hf and Nb-Ta during scavenging from seawater by hydrogenetic ferromanganese crusts. *Geochimica et Cosmochimica Acta*, *140*, 468–487. https://doi.org/10.1016/j.gca.2014.05.036

Schoell, M., & Wellmer, F.-W. (1981). Anomalous 13C depletion in early Precambrian graphites from Superior Province, Canada. *Nature*, *290*, 696. Retrieved from http://dx.doi.org/10.1038/290696a0

Schwarcz, H. P., & Burnie, S. W. (1973). Influence of sedimentary environments on sulfur isotope ratios in clastic rocks: a review. *Mineralium Deposita*, *8*(3), 264–277.

Seal, R. R. (2006). Sulfur Isotope Geochemistry of Sulfide Minerals. *Reviews in Mineralogy and Geochemistry*, *61*(1), 633–677. https://doi.org/10.2138/rmg.2006.61.12

Shanks, W. C. (2001). Stable isotopes in seafloor hydrothermal systems: vent fluids, hydrothermal deposits, hydrothermal alteration, and microbial processes. *Reviews in Mineralogy and Geochemistry*, *43*(1), 469–525.

Shanks, W. C., Boehlke, J. K., Seal, R. R., & Humphris, S. E. (1995). Stable isotopes in mid-ocean ridge hydrothermal systems: Interactions between fluids, minerals, and organisms. *Geophysical Monograph-American Geophysical Union*, *91*, 194.

Shanks, W. C., & Seyfried, W. E. (1987). Stable isotope studies of vent fluids and chimney minerals, southern Juan de Fuca Ridge: Sodium metasomatism and seawater sulfate reduction. *Journal of Geophysical Research: Solid Earth*, *92*(B11), 11387–11399.

Sharman, E. R. (2011). Application of multiple sulfur isotope analysis to Archean ore-forming processes: Unpublished PhD Thesis, Montréal, Canada, McGill Univesity.

Shegelski, R. J. (1978). Stratigraphy and Geochemistry of Archean Iron Formations in the Sturgeon Lake–Savant Lake Greenstone Terrain. In *Unpublished Ph. D. Thesis* (p. 251). University of Toronto.

Shibuya, T., Komiya, T., Nakamura, K., Takai, K., & Maruyama, S. (2010). Highly alkaline, high-temperature hydrothermal fluids in the early Archean ocean. *Precambrian Research*, *182*(3), 230–238. https://doi.org/https://doi.org/10.1016/j.precamres.2010.08.011

Shields, G., & Stille, P. (2001). Diagenetic constraints on the use of cerium anomalies as palaeoseawater redox proxies: an isotopic and REE study of Cambrian phosphorites. *Chemical Geology*, *175*(1), 29–48. https://doi.org/https://doi.org/10.1016/S0009-2541(00)00362-4

Sholkovitz, E. R., Landing, W. M., & Lewis, B. L. (1994). Ocean particle chemistry: The fractionation of rare earth elements between suspended particles and seawater. *Geochimica et Cosmochimica Acta*, *58*(6), 1567–1579. https://doi.org/https://doi.org/10.1016/0016-7037(94)90559-2

Siever, R. (1957). The Silica Budget in the Sedimentary Cycle. *American Mineralogist*, *42*(11–12), 821–841. Retrieved from http://dx.doi.org/

Siever, R. (1992). The silica cycle in the Precambrian. *Geochimica et Cosmochimica Acta*, *56*(8), 3265–3272. https://doi.org/https://doi.org/10.1016/0016-7037(92)90303-Z

Singh, S. K., Trivedi, J. R., Pande, K., Ramesh, R., & Krishnaswami, S. (1998). Chemical and Strontium, Oxygen, and Carbon Isotopic Compositions of Carbonates from the Lesser Himalaya: Implications to the Strontium Isotope Composition of the Source Waters of the Ganga, Ghaghara, and the Indus Rivers. *Geochimica et Cosmochimica Acta*, *62*(5), 743–755. https://doi.org/https://doi.org/10.1016/S0016-7037(97)00381-5

Spencer, D. W., & Brewer, P. G. (1971). Vertical advection diffusion and redox potentials as controls on the distribution of manganese and other trace metals Dissolved in waters of the Black Sea. *Journal of Geophysical Research*, *76*(24), 5877–5892. https://doi.org/10.1029/JC076i024p05877

Steinhoefel, G., Horn, I., & von Blanckenburg, F. (2009). Micro-scale tracing of Fe and Si isotope signatures in banded iron formation using femtosecond laser ablation. *Geochimica et Cosmochimica Acta*, *73*(18), 5343–5360. https://doi.org/https://doi.org/10.1016/j.gca.2009.05.037

Stevens, G., Droop, G. T. R., Armstrong, R. A., & Anhaeusser, C. R. (2002). Amphibolite facies metamorphism in the Schapenburg schist belt: A record of the mid-crustal response to~ 3.23 Ga terrane accretion in the Barberton greenstone belt. *South African Journal of Geology*, *105*(3), 271–284.

Stosch, H. G. (2002). Geochemie der Seltenen Erden: Skript zur Vorlesung am Mineralogisch-Petrographischen Institut der Universität zu Köln, 1988–1993, Skript mit Ergänzungen von 1998 und Sommer 2000.

Stott, G. M., Corfu, F., Thurston, P. C., Williams, H. R., & Sutcliffe, R. H. (1991). Uchi subprovince. *Geology of Ontario. Edited by PC Thurston, HR Williams, RH Sutcliffe, and GM Stott. Ontario Geological Survey, Special*, *4*(Part 1), 145–238.

Strauss, H. (1986). Carbon and sulfur isotopes in Precambrian sediments from the Canadian Shield. *Geochimica et Cosmochimica Acta*, *50*(12), 2653–2662.

Sugitani, K., Horiuchi, Y., Adachi, M., & Sugisaki, R. (1996). Anomalously low Al2O3/TiO2 values for Archean cherts from the Pilbara Block, Western Australia—possible evidence for extensive chemical weathering on the early earth. *Precambrian Research*, *80*(1), 49–76. https://doi.org/https://doi.org/10.1016/S0301-9268(96)00005-8

Taylor, S. R., & McLennan, S. M. (1985). *The continental crust: its composition and evolution*. Blackwell Scientific Pub., Palo Alto, CA.

Taylor, S. R., & McLennan, S. M. (1988). The significance of the rare earths in geochemistry and cosmochemistry. *Handbook on the Physics and Chemistry of Rare Earths*, *11*, 485–578.

Thode, H. G., Ding, T., & Crocket, J. H. (1991). Sulphur-isotope and elemental geochemistry studies of the Hemlo gold mineralization, Ontario: sources of sulphur and implications for the mineralization process. *Canadian Journal of Earth Sciences*, *28*(1), 13–25.

Thode, H. G., & Goodwin, A. M. (1983). Further sulfur and carbon isotope studies of late Archean iron-formations of the Canadian shield and rise of sulfate reducing bacteria. *Prec*, *20*(132), 337–356.

Thode, H. G., Monster, J., & Dunford, H. B. (1961). Sulphur isotope geochemistry. *Geochimica et Cosmochimica Acta*, *25*(3), 159–174.

Thomazo, C., Brayard, A., Elmeknassi, S., Vennin, E., Olivier, N., Caravaca, G., Jenks, J. F. (2018). Multiple sulfur isotope signals associated with the late Smithian event and the Smithian/Spathian boundary. *Earth-Science Reviews*.

Thurston, P. C., & Breaks, F. W. (1978). Metamorphic and tectonic evolution of the Uchi-English River Subprovince. In *Metamorphism in the Canadian Shield* (pp. 49–62).

Thurston, P. C., Osmani, I. A., Stone, D., Williams, H. R., Sutcliffe, R. H., & Stott, G. M. (1991). Northwestern Superior Province: review and terrane analysis. *Geology of Ontario. Edited by PC Thurston, HR Williams, RH Sutcliffe, and GM Stott. Ontario Geological Survey, Special*, *4*(Part 1), 81–144.

Timpa, S. (2011). *Report On Drilling Performed on Red Lake Gold Mines – Halo Resources Ltd . Joint Venture West Red Lake Property , Northern Ontario , Canada*.

Timpa, S. (2012a). *Bridget Lake Winter 2012 Drill Report. Halo Resources Ltd . Joint Venture West Red Lake Property , Northern Ontario , Canada*.

Timpa, S. (2012b). *Pancake Bay Winter 2012 Drill Report. Halo Resources Ltd . Joint Venture West Red Lake Property , Northern Ontario , Canada*.

Tostevin, R., Shields, G. A., Tarbuck, G. M., He, T., Clarkson, M. O., & Wood, R. A. (2016). Effective use of cerium anomalies as a redox proxy in carbonate-dominated marine settings. *Chemical Geology*, *438*, 146–162. https://doi.org/https://doi.org/10.1016/j.chemgeo.2016.06.027

Tribovillard N, Lyons TW, Riboulleau A, Bout-Roumazeilles V (2008) A possible capture of molybdenum during early diagenesis of dysoxic sediments. Bull la Société géologique Fr 179:3–12

Tsikos, H., Matthews, A., Erel, Y., & Moore, J. M. (2010). Iron isotopes constrain biogeochemical redox cycling of iron and manganese in a Palaeoproterozoic stratified basin. *Earth and Planetary Science Letters*, *298*(1), 125–134. https://doi.org/https://doi.org/10.1016/j.epsl.2010.07.032

Van Cappellen, P., Viollier, E., Roychoudhury, A., Clark, L., Ingall, E., Lowe, K., & Dichristina, T. (1998). Biogeochemical Cycles of Manganese and Iron at the Oxic−Anoxic Transition of a Stratified Marine Basin (Orca Basin, Gulf of Mexico). *Environmental Science & Technology*, *32*(19), 2931–2939. https://doi.org/10.1021/es980307m

Van den Boorn, S. (2008). *Silicon isotopes and the origin of the Archaean cherts. Unpublished PhD thesis. Geologica Ultraiectina (293)*. Departement Aardwetenschappen. Universiteit Utrecht.

Van Kranendonk, M. J., Webb, G. E., & Kamber, B. S. (2003). Geological and trace element evidence for a marine sedimentary environment of deposition and biogenicity of 3.45 Ga stromatolitic carbonates in the Pilbara Craton, and support for a reducing Archaean ocean. *Geobiology*, *1*(2), 91–108.

Veizer, J., Hoefs, J., Lowe, D. R., & Thurston, P. C. (1989). Geochemistry of Precambrian carbonates: II. Archean greenstone belts and Archean sea water. *Geochimica et Cosmochimica Acta*, *53*(4), 859–871. https://doi.org/https://doi.org/10.1016/0016-7037(89)90031-8

Veizer, J., Hoefs, J., Ridler, R. H., Jensen, L. S., & Lowe, D. R. (1989). Geochemistry of Precambrian carbonates: I. Archean hydrothermal systems. *Geochimica et Cosmochimica Acta*, *53*(4), 845–857. https://doi.org/https://doi.org/10.1016/0016-7037(89)90030-6

Voegelin, A. R., Nägler, T. F., Beukes, N. J., & Lacassie, J. P. (2010). Molybdenum isotopes in late Archean carbonate rocks: Implications for early Earth oxygenation. *Precambrian Research*, *182*(1), 70–82. https://doi.org/https://doi.org/10.1016/j.precamres.2010.07.001

Wang, J., Chen, D., Wand, D., Yan, D., Zhou, X., & Wang, Q. (2011). Petrology and geochemistry of chert on the marginal zone of Yangtze Platform, western Hunan, South China, during the Ediacaran–Cambrian transition. *Sedimentology*, *59*(3), 809–829. https://doi.org/10.1111/j.1365-3091.2011.01280.x

Watanabe, Y., Naraoka, H., Wronkiewicz, D. J., Condie, K. C., & Ohmoto, H. (1997). Carbon, nitrogen, and sulfur geochemistry of Archean and Proterozoic shales from the Kaapvaal Craton, South Africa. *Geochimica et Cosmochimica Acta*, *61*(16), 3441–3459.

Wedepohl, K.H (1971) Environmental influences on the chemical composition of shales and clays. Phys Chem Earth 8:307–333

Wedepohl, K.H. (1991). The composition of the primitive upper earth's mantle. International

Kimberlite Conference: Extended Abstracts (Vol. 5, pp. 451-453).

Webb, G. E., & Kamber, B. S. (2000). Rare earth elements in Holocene reefal microbialites: A new shallow seawater proxy. *Geochimica et Cosmochimica Acta*, *64*(9), 1557–1565. https://doi.org/10.1016/S0016-7037(99)00400-7

Wilcock, W. S., & Delaney, J. R. (1996). Mid-ocean ridge sulfide deposits: Evidence for heat extraction from magma chambers or cracking fronts?. *Earth and Planetary Science Letters, 145(1-4), 49-64.*

Wille, M., Nebel, O., Van Kranendonk, M. J., Schoenberg, R., Kleinhanns, I. C., & Ellwood, M. J. (2013). Mo-Cr isotope evidence for a reducing Archean atmosphere in 3.46-2.76Ga black shales from the Pilbara, Western Australia. *Chemical Geology*, *340*, 68–76. https://doi.org/10.1016/j.chemgeo.2012.12.018

Wright, V. P., & Tucker, M. E. (1990). *Carbonate sedimentology*. Blackwell scientific publications.

Zhao, K. D., & Jiang, S. Y. (2007). Rare earth element and yttrium analyses of sulfides from the Dachang Sn-polymetallic ore field, Guangxi Province, China: Implication for ore genesis. *Geochemical Journal*, *41*(2), 121–134. https://doi.org/10.2343/geochemj.41.121

Appendix 1: Geochemistry

Appendix 1.1: Whole-rock major & trace element geochemical data (bd=below detection)

Carbonate																
Sample		NGI 31-34	NGI 31-15	BL 38-1	BL 37-3	PB 32-1	PB 34-13	PB 34-27	PB 35-4	PB 36-8B	PB 36-11	RL-18A-C	RL-18B-C	RL-23-C	RL-24-C	HB-5	LK-11
Depth (m)		11	71	20	198	269	48	75	209	74	78	O/C	O/C	O/C	O/C	O/C	O/C
Al_2O_3	Wt. %	0.01	0.03	0.04	0.05	0.02	0.47	0.11	0.12	0.18	0.05	0.05	0.03	0.15	0.10	0.06	0.09
CaO		8.78	13.01	14.12	13.51	10.30	7.99	15.93	43.22	15.80	27.61	23.92	26.22	27.10	23.31	21.17	16.80
MgO		5.85	8.09	8.84	8.51	6.25	1.12	0.10	0.34	2.34	0.22	0.22	0.23	0.43	0.51	0.25	0.33
Na_2O		0.01	0.03	0.06	0.04	bd	0.01	0.05	0.21	0.03	0.05	0.06	0.02	0.05	0.13	0.07	0.04
K_2O		bd	bd	bd	bd	bd	0.11	bd	bd	0.03	bd	bd	bd	0.01	bd	bd	bd
Fe_2O_3		0.74	1.99	2.46	2.65	0.89	1.53	0.51	0.45	0.85	0.30	0.98	1.17	2.19	1.59	1.31	1.99
MnO		0.25	0.45	0.46	0.43	0.35	0.25	0.25	0.17	0.32	0.38	0.43	0.53	0.60	0.71	0.22	0.46
P_2O_5		bd	bd	bd	bd	bd	bd	bd	0.01	0.01	0.02	bd	bd	bd	bd	0.02	bd
TiO_2		bd	bd	0.000	0.000	0.000	0.005	0.001	0.001	0.000	0.000	0.000	0.000	0.003	0.000	0.000	0.002
Ba	ppm	0.22	0.60	1.04	2.02	1.58	53.52	1.91	20.71	9.43	16.40	2.23	2.94	bd	16.19	4.31	3.60
Cr		0.33	13.73	3.43	bd	bd	13.03	bd	1.04	3.87	3.92	1.36	bd	0.49	3.65	0.00	bd
Cu		1.11	bd	bd	bd	bd	bd	bd	bd	bd	bd	bd	bd	1.59	bd	bd	bd
Li		bd	bd	bd	bd	bd	bd	bd	bd	bd	bd	bd	bd	bd	bd	bd	bd
Sr		5.34	17.33	13.19	17.28	14.93	19.08	39.68	186.01	64.42	185.14	35.75	36.68	58.15	57.33	68.02	39.62
V		bd	bd	bd	bd	bd	bd	bd	bd	bd	bd	bd	bd	bd	bd	bd	bd
Y		0.81	2.59	2.94	4.20	0.44	5.00	2.25	0.85	2.13	1.27	6.18	5.91	8.11	3.89	1.58	12.43
Zn		7.5	9.8	9.8	12.0	6.6	6.7	1.6	3.1	21.2	1.6	4.3	1.1	5.2	10.7	3.1	3.4
Zr		bd	bd	bd	bd	bd	bd	bd	bd	bd	bd	bd	bd	bd	bd	bd	bd
As		bd	125.02	bd	bd	bd	bd	bd	bd	bd	bd	bd	bd	bd	bd	bd	bd
B		127	338	667	464	16	11	488	2184	26	554	631	296	487	1255	706	434
Be		bd	bd	bd	bd	bd	bd	bd	bd	bd	bd	bd	bd	bd	bd	bd	bd
Co		5.50	bd	bd	bd	bd	6.92	bd	bd	5.56	bd	bd	bd	bd	bd	bd	bd
Mo		0.22	0.27	0.38	0.44	0.27	0.56	0.29	0.46	0.27	0.27	0.06	0.19	0.00	0.00	0.26	0.21
Nb		0.03	0.06	0.04	0.04	0.04	0.13	0.08	0.07	0.03	0.04	0.04	0.03	0.09	0.10	0.06	0.11
Ni		6.16	15.64	bd	6.92	bd	8.07	bd	bd	bd	7.74	bd	bd	bd	6.49	bd	bd
S		bd	bd	bd	2632	183	1864	152	467	100	284	bd	bd	91	bd	bd	132
Sb		0.18	0.32	0.18	1.04	1.11	0.45	1.08	0.60	0.47	0.61	0.11	0.24	0.46	0.35	0.37	0.36
Sc		bd	bd	bd	bd	bd	bd	bd	bd	bd	bd	bd	bd	bd	bd	bd	bd
Si		1632	3761	6665	4871	802	360	5221	22329	1652	6431	6529	3817	5554	12208	7303	4701
Sn		0.84	0.88	0.89	0.91	0.94	0.91	1.13	0.78	0.79	0.90	0.95	1.35	0.86	0.89	1.15	1.31
Cd		0.16	0.29	0.32	0.37	0.16	0.20	0.51	0.22	0.98	0.17	0.17	0.18	0.17	0.27	0.17	0.32
Cs		0.01	0.03	0.03	0.06	0.06	0.52	0.11	0.03	0.05	0.04	0.44	0.45	0.16	0.28	0.36	0.40

Carbonate																	
Sample		NGI 31-34	NGI 31-15	BL 38-1	BL 37-3	PB 32-1	PB 34-13	PB 34-27	PB 35-4	PB 36-8B	PB 36-11	RL-18A-C	RL-18B-C	RL-23-C	RL-24-C	HB-5	LK-11
Pb	ppm	3.42	4.10	4.87	6.49	3.54	3.61	10.70	5.17	5.88	210.41	4.35	5.51	1.65	3.13	5.32	5.25
Hf		0.07	0.17	0.19	0.27	0.03	0.24	0.39	0.20	0.07	0.11	0.25	0.12	0.17	0.50	0.33	0.57
Rb		0.11	0.18	0.37	0.79	0.69	10.42	1.59	1.01	1.59	0.62	0.50	0.48	1.09	0.90	1.09	1.01
Ta		0.04	0.08	0.05	0.08	0.15	0.07	0.07	0.20	0.45	0.08	0.04	0.06	0.04	0.11	0.05	0.07
Th		0.01	0.04	0.07	0.07	0.03	0.48	0.19	bd	0.18	0.07	0.03	0.03	0.14	0.04	0.13	0.16
U		0.04	0.10	0.07	0.56	0.04	0.73	0.19	0.13	0.07	0.10	0.32	0.26	0.19	0.16	0.10	0.24
W		62.25	34.51	33.88	17.41	54.04	92.75	48.59	8.11	86.63	15.62	bd	bd	0.12	3.23	5.54	6.10

Chert								
Sample		NGI 31-14	EBL 27-88	EBL 28-1	EBL 28-7	EBL 28-28	EBL 28-31	EBL 28-44
Depth (m)		73	17	4	26	97	107	137
Al_2O_3	Wt. %	0.04	0.15	0.08	0.12	1.80	0.09	0.05
CaO		2.49	0.01	0.07	0.50	0.39	0.18	0.04
MgO		1.57	0.06	0.11	0.34	0.37	0.09	0.04
Na_2O		0.00	bd	0.00	0.00	0.07	0.00	bd
K_2O		0.00	0.00	0.01	0.00	0.02	0.02	0.01
Fe_2O_3		0.77	0.60	1.07	0.46	0.45	0.25	0.32
MnO		0.06	0.02	0.18	0.04	0.01	0.01	0.00
P_2O_5		bd	0.00	bd	0.00	0.00	bd	0.00
TiO_2		0.001	0.006	0.002	0.002	0.025	0.001	0.001
Ba	ppm	0.18	0.20	1.19	0.40	2.53	3.67	1.69
Cr		0.73	0.48	1.21	2.22	30.07	0.11	bd
Cu		1.06	2.35	2.79	1.45	6.84	1.83	0.31
Li		0.22	1.41	0.29	0.51	25.41	0.13	0.26
Sr		3.12	0.22	0.97	0.84	15.62	1.08	0.18
V		bd	1.61	0.77	2.02	3.70	0.26	0.15
Y		0.32	0.35	0.10	0.15	0.30	0.08	0.04
Zn		3.2	1.9	5.3	2.7	4.3	0.4	0.8
Zr		1.87	2.31	0.44	1.10	17.34	1.03	0.68
As		2.64	2.97	bd	bd	8.87	bd	3.23
B		54	9	9	3	40	15	8
Be		bd	bd	bd	bd	bd	bd	bd
Co		bd	bd	bd	bd	bd	bd	bd
Mo		0.02	0.39	0.19	0.65	0.22	0.24	0.22
Nb		0.02	0.08	0.01	0.03	0.36	0.16	0.02
Ni		3.65	2.22	3.52	5.57	67.58	5.90	13.18
S		258	254	225	271	264	1206	79

Chert								
Sample		NGI 31-14	EBL 27-88	EBL 28-1	EBL 28-7	EBL 28-28	EBL 28-31	EBL 28-44
Sb	ppm	0.25	0.11	0.15	0.10	0.09	0.52	0.13
Sc		0.09	0.20	0.02	0.20	0.90	bd	0.07
Si		591	105	156	103	543	143	308
Sn		0.18	0.58	bd	0.02	0.18	0.02	0.15
Cd		bd	bd	0.22	0.21	bd	0.19	bd
Cs		0.01	0.03	0.01	0.03	0.12	0.02	0.05
Pb		bd	bd	bd	bd	0.36	bd	bd
Hf		bd	0.03	bd	bd	0.42	bd	bd
Rb		0.10	0.22	0.30	0.08	0.97	0.34	0.52
Ta		3.48	2.57	1.17	2.38	6.62	1.85	2.41
Th		bd	0.02	bd	bd	0.84	bd	bd
U		0.02	0.06	0.02	0.03	0.13	0.09	0.01
W		58.26	156.89	88.78	164.74	112.96	202.69	120.14

Magnetite																						
Sample		EBL 27-89	NGI 31-12	NGI 31-11	NGI 31-10	NGI 31-7	NGI 31-9	NGI 31-8	NGI 31-6	NGI 31-4	NGI 31-3	NGI 31-2	EBL 27-80	EBL 27-79	EBL 27-78	EBL 27-77	EBL 27-75	EBL 27-74	EBL 27-22	EBL 27-62	EBL 27-30	EBL 29-44
Depth (m)		12	82	86	88	98	91	95	103	109	119	122	47	50	57	59	74	77	80	124	125	45
Al_2O_3	Wt. %	0.19	0.92	0.98	1.41	1.21	1.31	0.62	0.99	0.22	0.41	0.50	0.75	1.35	0.86	0.45	0.76	0.23	3.86	1.99	0.30	0.29
CaO		1.50	1.62	8.76	3.72	1.18	1.37	4.15	4.31	0.32	0.40	0.38	1.73	0.44	1.35	0.96	2.37	0.70	0.48	1.86	0.30	0.27
MgO		4.61	2.71	7.71	6.34	2.50	2.09	6.49	6.97	3.91	2.68	4.82	6.04	1.64	5.56	4.99	5.36	3.21	4.53	0.99	4.75	4.23
Na_2O		0.30	0.42	0.30	0.48	0.34	0.52	0.41	0.25	0.25	0.42	0.30	0.39	0.46	0.34	0.32	0.37	0.19	0.23	0.23	0.22	0.24
K_2O		0.01	0.04	0.09	0.12	0.19	0.15	0.04	0.01	0.01	0.10	0.04	0.08	0.07	0.01	0.03	0.02	0.02	0.01	0.00	0.01	0.01
Fe_2O_3		34.68	49.76	38.35	46.49	65.69	70.44	43.66	52.91	68.62	64.66	51.95	49.48	62.10	48.30	46.75	35.53	40.55	41.18	60.19	43.23	58.63
MnO		2.09	0.64	1.07	0.57	0.26	0.38	1.01	1.09	0.43	0.49	1.31	0.98	0.94	3.28	2.32	2.96	1.29	4.10	3.01	3.41	1.36
P_2O_5		0.01	0.02	0.13	0.06	0.04	0.03	0.11	0.14	0.21	0.20	0.13	0.06	0.01	0.03	0.02	0.04	0.06	0.13	0.01	0.01	0.01
TiO_2		0.001	0.045	0.022	0.032	0.094	0.023	0.013	0.025	0.003	0.005	0.013	0.014	0.072	0.021	0.015	0.026	0.005	0.099	0.048	0.007	0.007
Ba	ppm	3.17	22.99	28.47	31.59	53.79	117.00	7.04	5.61	24.49	34.56	14.04	20.92	55.79	2.93	19.69	7.11	11.18	4.84	5.65	3.14	7.33
Cr		0.40	19.52	8.40	8.78	76.22	13.17	6.47	8.60	0.97	0.62	7.83	4.16	34.42	12.08	21.65	7.37	1.55	56.89	101.26	10.53	0.37
Cu		3.98	51.81	28.80	37.53	46.07	25.76	23.65	48.00	0.44	3.61	2.97	14.92	15.42	7.88	23.59	29.41	7.96	68.84	27.94	20.23	1.41
Li		0.84	0.00	6.91	9.88	9.90	5.41	4.38	2.62	1.28	2.07	2.00	4.18	2.68	2.13	bd	3.74	bd	4.22	2.44	bd	1.65
Sr		7.52	8.93	81.38	22.53	12.10	15.84	16.61	24.51	7.28	6.53	6.36	16.19	5.08	8.69	19.12	21.96	24.11	4.11	8.07	2.31	6.49
V		2.66	26.21	14.45	21.87	48.22	28.84	13.71	16.46	5.02	6.69	28.01	20.53	110.66	21.58	16.70	9.64	6.71	26.18	190.34	25.44	6.71
Y		1.96	8.17	12.23	10.58	4.95	5.57	10.96	5.07	8.50	7.26	10.55	8.64	8.62	9.09	11.40	10.43	2.93	16.60	16.17	3.43	1.56

Magnetite																						
Sample		EBL 27-89	NGI 31-12	NGI 31-11	NGI 31-10	NGI 31-7	NGI 31-9	NGI 31-8	NGI 31-6	NGI 31-4	NGI 31-3	NGI 31-2	EBL 27-80	EBL 27-79	EBL 27-78	EBL 27-77	EBL 27-75	EBL 27-74	EBL 27-22	EBL 27-62	EBL 27-30	EBL 29-44
Zn	ppm	57.2	69.0	273.1	136.9	179.2	93.1	436.8	124.6	153.4	153.3	182.9	196.6	103.8	137.9	169.3	108.0	80.1	186.5	95.2	210.7	120.9
Zr		16.92	37.39	37.88	31.11	57.09	36.28	40.46	27.32	22.18	45.14	37.66	38.21	42.61	49.92	43.97	29.30	15.98	46.40	34.43	28.82	27.70
As		99.11	0.00	13.75	55.79	26.00	17.95	222.8	33.68	6.82	bd	218.6	52.80	400.8	18.15	116.8	11.97	32.39	47.37	bd	24.26	8.47
B		2901	3910	2635	4113	3039	4740	3845	2426	2511	4788	2850	3603	4212	3262	2916	3552	1916	2214	2006	1989	2349
Be		bd	0.00	bd	bd	0.53	0.92	bd	bd	bd	bd	bd	bd	0.57	bd	bd	bd	bd	bd	bd	bd	bd
Co		bd	21.07	bd	bd	33.29	19.47	bd	bd	bd	bd	bd	bd	22.20	bd	12.99	bd	23.39	bd	51.79	27.93	bd
Mo		0.41	0.53	0.73	1.02	0.75	0.61	0.52	0.93	0.15	0.38	0.31	0.72	3.19	2.41	1.62	0.94	0.23	1.83	2.76	0.69	0.20
Nb		0.03	0.41	0.42	0.72	0.89	0.85	0.25	0.50	0.11	0.26	0.22	0.22	0.83	0.28	0.15	0.68	0.31	2.04	0.84	0.05	0.09
Ni		10.49	32.15	8.54	32.52	48.62	23.80	24.09	13.29	4.33	4.20	9.46	16.06	30.14	11.31	47.68	9.39	3.97	76.23	232.10	59.75	6.91
S		6794	70059	21069	13985	37071	18965	12148	14689	33	1769	1199	7746	22287	3441	15426	10259	5467	79794	101509	28144	1451
Sb		0.44	5.16	7.30	10.53	10.42	9.89	20.76	9.83	6.23	9.70	6.00	3.49	4.21	1.45	2.71	2.49	2.25	3.45	2.33	1.92	3.42
Sc		1.41	0.00	2.82	4.05	0.00	0.00	2.07	2.24	0.35	0.29	4.00	4.47	6.40	5.41	3.14	2.05	bd	4.51	17.09	10.66	0.53
Si		24811	8	24481	37549	6	9	35173	22567	22171	42059	25559	32731	8	30113	26378	31081	17708	20684	4	18242	21621
Sn		0.15	0.25	1.99	0.65	1.73	0.47	0.78	0.60	0.56	0.75	0.48	0.84	0.35	0.45	0.80	0.25	0.31	0.54	0.46	1.80	0.34
Cd		0.01	bd	2.75	0.53	1.07	0.39	0.92	0.62	0.09	0.14	0.02	0.36	0.05	0.43	0.39	0.43	0.09	1.00	0.14	0.35	0.01
Cs		0.09	0.68	0.88	0.94	1.62	1.30	0.35	0.12	0.18	1.28	1.43	1.03	1.59	0.12	0.33	0.07	0.33	0.19	0.15	0.09	0.57
Pb		0.29	15.42	6.90	4.86	26.69	23.03	7.84	4.38	2.84	3.12	bd	1.33	5.11	0.66	3.47	2.56	3.77	5.61	4.06	1.67	bd
Hf		0.29	0.79	0.58	0.42	1.38	0.92	0.56	0.34	0.14	0.75	0.57	0.56	1.12	1.02	0.98	0.68	0.36	1.20	0.84	0.46	0.50
Rb		0.61	3.82	7.15	8.42	17.00	15.81	2.54	0.63	0.75	4.09	4.11	5.98	10.81	0.75	2.22	0.72	1.30	1.48	0.79	0.71	2.41
Ta		2.14	0.04	4.05	3.00	0.14	0.11	2.91	11.63	2.68	2.87	2.57	3.07	0.09	3.05	0.05	2.32	0.14	8.13	0.09	0.16	1.95
Th		0.03	0.33	0.35	0.28	0.73	0.71	0.15	0.27	0.02	0.30	0.30	0.18	0.55	0.30	0.14	0.53	0.18	1.89	0.76	0.03	0.03
U		0.10	0.16	0.12	0.37	0.22	0.27	0.07	0.11	0.01	0.11	0.24	0.16	0.43	0.27	0.19	0.17	0.09	0.66	1.32	0.19	0.10
W		22.98	bd	20.82	9.61	5.73	4.26	7.41	8.54	172.9	14.98	23.06	7.53	5.80	8.14	10.12	9.38	123.0	25.98	13.61	80.09	6.56

Magnetite																					
Sample		EBL 29-45	EBL 29-46	EBL 29-49	PB 32-23	PB 32-18	PB 34-3	PB 34-18	PB 34-21	PB 34-25	PB 34-27A	PB 35-44	PB 35-43	BL 37-41	BL 37-40	BL 38-4	RL 18A-M	RL 18B-M	RL 23-M	RL 24-M	BLO 1	EBL 28-4
Depth (m)		46	48	52	138	168	14	63	66	72	75	32	40	10.5	11	14	O/C	O/C	O/C	O/C	O/C	17
Al_2O_3	Wt. %	0.39	0.40	0.51	0.09	0.38	0.03	1.41	0.78	0.65	1.06	0.34	0.83	0.27	0.07	0.11	0.83	0.07	3.35	0.73	1.05	6.83
CaO		0.06	0.16	0.28	0.71	16.25	0.77	16.19	11.49	3.90	9.14	2.22	5.07	1.67	1.05	7.89	9.14	2.89	19.70	11.75	0.34	0.94
MgO		3.44	4.16	5.80	5.24	9.41	0.12	5.81	3.20	0.84	2.58	0.56	1.19	2.10	0.67	5.20	1.37	0.48	3.13	3.09	4.54	2.95

Magnetite																						
Sample		EBL 29-45	EBL 29-46	EBL 29-49	PB 32-23	PB 32-18	PB 34-3	PB 34-18	PB 34-21	PB 34-25	PB 34-27A	PB 35-44	PB 35-43	BL 37-41	BL 37-40	BL 38-4	RL 18A-M	RL 18B-M	RL 23-M	RL 24-M	BLO 1	EBL 28-4
Na_2O	Wt. %	0.49	0.26	0.49	0.06	0.58	0.02	0.35	0.28	0.42	0.49	0.30	0.36	0.45	0.08	0.17	0.45	0.09	0.61	0.40	0.54	0.22
K_2O		0.02	0.02	0.03	0.02	0.01	0.01	0.37	0.10	0.04	0.07	0.01	0.08	0.01	0.00	0.00	0.03	0.00	0.08	0.03	0.02	0.08
Fe_2O_3		53.39	61.91	55.02	41.23	33.84	68.08	38.55	52.61	64.97	55.88	77.21	69.23	61.62	53.08	25.70	56.04	67.95	30.29	52.27	55.78	31.48
MnO		0.93	1.39	1.30	0.48	1.20	0.07	1.75	1.56	0.36	1.33	0.26	0.42	0.36	0.18	0.37	0.91	0.23	1.12	1.11	0.68	6.44
P_2O_5		0.01	0.02	0.01	0.01	0.01	0.01	0.01	0.01	0.00	0.01	0.01	0.01	0.01	0.01	bd	0.02	bd	0.03	0.02	0.13	0.01
TiO_2		0.006	0.019	0.023	0.002	0.005	0.002	0.037	0.029	0.035	0.034	0.014	0.084	0.006	0.003	0.001	0.044	0.003	0.122	0.026	0.037	0.067
Ba	ppm	6.75	6.53	6.16	7.78	3.60	4.05	33.42	36.10	16.90	15.89	6.93	29.12	10.32	5.49	4.77	16.81	4.91	28.06	41.44	8.93	10.32
Cr		2.88	12.83	3.59	0.96	2.44	0.34	13.54	6.78	35.12	10.16	2.49	29.84	6.16	0.46	1.92	4.64	0.15	13.52	6.00	11.01	20.46
Cu		6.73	0.48	7.33	1.50	9.27	29.74	7.89	38.50	32.69	16.63	5.67	26.90	2.57	4.93	4.01	1.74	58.12	41.83	8.98	42.20	29.85
Li		1.30	1.14	6.40	bd	3.07	bd	5.67	bd	5.02	5.32	bd	bd	2.22	bd	2.81	6.21	bd	11.86	7.30	3.92	5.26
Sr		1.10	4.75	10.56	3.71	25.03	4.16	57.29	73.44	94.16	55.11	8.61	48.88	15.27	107.93	27.47	30.17	12.88	99.08	436.11	7.02	4.42
V		46.60	19.12	17.75	bd	bd	bd	15.22	20.67	51.17	27.99	13.65	57.92	19.12	bd	bd	bd	bd	22.32	4.19	17.47	40.57
Y		1.98	3.39	1.61	0.47	1.81	bd	2.61	5.47	0.00	4.36	0.72	2.56	1.25	0.45	0.52	4.17	0.56	13.82	2.24	8.67	19.34
Zn		96.3	114.8	84.1	43.0	34.6	64.4	98.1	118.1	72.3	73.5	99.2	92.0	65.0	50.5	61.4	54.2	61.1	62.1	118.8	175.6	112.7
Zr		44.15	31.55	50.84	bd	57.62	bd	26.71	40.98	68.11	68.47	47.11	38.35	47.76	bd	bd	49.31	bd	56.53	31.26	44.68	65.98
As		0.26	6.38	3.67	bd	11.53	bd	bd	bd	0.00	bd	bd	bd	4.99	19.45	274.68	bd	bd	bd	bd	120.96	26.73
B		4830	2505	4828	740	5404	279	3171	2236	3646	3773	2875	3573	4300	769	1584	4096	934	4920	3291	4720	2328
Be		bd	bd	bd	bd	bd	bd	0.63	bd	0.00	bd	bd	bd	bd	bd	0.55	bd	bd	bd	bd	0.53	bd
Co		bd	bd	bd	27.73	4.43	13.75	8.87	12.62	61.14	22.61	13.54	35.93	bd	81.29	2.40	7.24	13.49	8.07	6.28	16.10	bd
Mo		0.09	0.21	0.20	0.10	0.38	2.19	0.29	1.33	0.43	0.59	0.77	0.93	0.30	0.15	0.05	0.41	2.70	0.02	0.50	0.64	6.08
Nb		0.05	0.18	0.14	0.03	0.15	0.02	0.50	0.30	0.32	0.17	0.11	0.46	0.15	0.10	0.02	0.73	0.11	1.02	0.49	4.08	1.15
Ni		6.58	13.95	26.77	bd	13.43	417.56	10.97	55.85	138.23	104.33	6.50	20.69	2.51	4.36	bd	3.71	399.16	5.97	6.91	17.09	231.68
S		2600	969	462	1968	32547	336777	9099	47677	89475	68539	6760	16771	2917	4922	1752	368	343568	6791	467	12853	24948
Sb		1.89	5.19	5.62	0.36	1.37	0.36	0.91	0.77	1.87	1.47	1.09	1.12	1.78	1.20	1.15	1.99	0.36	2.01	3.01	2.31	0.70
Sc		10.49	2.62	1.12	bd	bd	0.00	bd	bd	0.00	bd	bd	bd	0.18	bd	bd	bd	bd	3.36	bd	3.28	24.22
Si		39903	22677	42565	6871	47698	1	30128	21440	7	33790	26422	31348	37439	7251	14933	36210	8003	44559	29626	9	24541
Sn		0.23	0.51	0.36	0.15	0.18	0.13	0.57	0.35	0.69	0.48	0.45	0.41	0.22	0.31	0.32	0.66	0.07	0.47	0.40	0.36	0.33
Cd		bd	0.02	0.04	0.04	0.10	bd	0.29	0.81	bd	0.47	0.06	0.12	bd	0.07	0.13	0.08	0.03	0.15	0.12	0.70	0.38
Cs		0.66	0.97	1.68	0.13	0.05	0.01	8.75	0.40	0.20	0.47	0.07	0.14	0.04	0.04	0.02	7.54	0.01	0.70	1.06	0.37	0.72
Pb		bd	bd	0.35	6.74	4.31	12.61	4.09	6.90	3.58	4.02	4.44	6.61	bd	1.07	1.18	2.47	6.97	2.69	5.18	8.00	2.08
Hf		0.49	0.49	1.04	0.11	0.99	0.09	0.49	0.75	1.78	1.15	0.73	0.72	0.67	0.17	0.31	1.16	0.13	1.17	0.56	1.13	1.62

Magnetite																					
Sample		EBL 29-45	EBL 29-46	EBL 29-49	PB 32-23	PB 32-18	PB 34-3	PB 34-18	PB 34-21	PB 34-25	PB 34-27A	PB 35-44	PB 35-43	BL 37-41	BL 37-40	BL 38-4	RL 18A-M	RL 18B-M	RL 23-M	RL 24-M	BLO 1	EBL 28-4
Rb	ppm	2.50	4.49	5.85	0.57	0.32	0.31	88.27	6.38	3.47	3.79	0.92	2.03	0.75	0.40	0.18	5.02	0.12	5.30	2.47	2.32	6.22
Ta		1.39	3.87	2.34	0.09	0.43	0.02	0.09	0.37	0.07	0.05	0.07	0.09	4.30	0.24	0.04	0.14	0.49	0.13	0.06	0.10	9.22
Th		0.03	0.20	0.17	0.13	0.06	0.02	0.09	0.16	0.27	0.13	0.08	0.50	0.01	bd	0.05	0.46	0.07	0.57	0.43	0.54	3.01
U		0.55	0.44	0.18	0.02	0.14	0.15	0.38	0.63	0.32	0.38	0.11	0.50	0.15	0.07	0.06	0.78	0.09	0.68	0.48	0.17	1.88
W		5.13	5.36	6.27	127.89	182.67	31.06	9.59	268.44	56.82	24.15	33.35	63.54	35.90	440.87	3.76	4.62	433.83	bd	8.63	12.40	92.68

		Pyrite							Pyrrhotite					
Sample		EBL 27-8	EBL 27-9	EBL 27-10	EBL 27-11	PB 32-4	PB 32-6	PB 33-17	EBL 27-7	EBL 27-31	PB 32-5	PB 32-5	PB 33-29	PB 33-20
Depth (m)		25.5	26	28	34	254	239	107	25	124	247	247	95	104
Al_2O_3	Wt. %	0.36	0.37	0.30	2.73	0.77	0.96	0.35	1.18	0.62	1.32	1.42	0.86	1.63
CaO		1.58	0.17	0.03	0.03	0.07	0.18	0.05	0.10	0.67	0.56	0.10	2.61	0.20
MgO		2.05	0.11	0.14	0.22	0.94	0.46	0.11	0.39	0.56	0.28	0.18	2.36	0.36
Na_2O		0.06	0.05	0.01	0.56	0.02	0.06	0.01	0.10	0.10	0.19	0.33	0.03	0.21
K_2O		0.02	0.05	0.04	0.07	0.29	0.17	0.05	0.19	0.01	0.03	0.24	0.03	0.15
Fe_2O_3		47.15	52.54	56.22	37.09	45.09	50.56	58.11	65.48	64.15	50.38	65.03	49.24	69.27
MnO		0.42	0.04	0.02	0.04	0.09	0.19	0.04	0.12	0.84	0.03	0.13	0.67	0.25
P_2O_5		0.01	0.01	0.01	0.02	0.01	0.01	0.00	0.01	0.01	0.01	0.01	0.02	0.01
TiO_2		0.011	0.007	0.004	0.067	0.016	0.022	0.006	0.024	0.010	0.023	0.037	0.015	0.020
Ba	ppm	5.74	7.62	10.82	12.48	18.70	17.25	5.15	18.08	3.87	7.18	28.36	4.99	29.29
Cr		8.30	2.59	1.55	21.34	15.87	9.96	4.50	26.01	5.84	16.10	18.69	18.22	19.82
Cu		50.97	3098.72	139.06	198.10	187.97	184.03	332.68	414.52	568.96	168.40	85.65	46.80	66.06
Li		3.10	2.48	2.77	8.76	13.11	7.06	2.44	8.49	bd	4.40	6.71	3.44	9.94
Sr		3.10	3.38	2.29	1.70	1.67	4.91	1.85	5.01	3.37	8.18	6.16	7.39	11.95
V		6.76	0.00	bd	30.66	10.30	18.46	0.00	0.00	10.71	7.68	13.05	11.10	11.23
Y		4.41	0.00	bd	2.80	0.00	0.00	0.00	0.00	5.28	0.72	bd	3.30	0.00
Zn		364.7	1724.2	236.7	41.0	720.3	940.3	210.3	73.0	87.4	54.6	98.7	149.4	92.4
Zr		0.00	0.00	0.00	66.62	0.00	0.00	0.00	0.00	0.00	22.30	30.56	bd	0.00
As		537.57	499.26	754.38	285.20	573.54	893.20	797.72	21.98	0.00	bd	13.24	503.14	2045.71
B		72	32	0	5232	88	0	0	675	814	1529	2150	124	1327
Be		0.00	0.00	0.00	bd	0.00	0.00	0.00	0.00	0.00	bd	0.00	bd	0.00
Co		102.21	81.96	40.44	139.26	265.98	344.08	152.83	374.46	103.29	29.08	13.22	85.94	199.03
Mo		3.33	2.50	4.15	2.30	2.26	2.00	3.32	2.86	2.03	1.15	3.23	3.20	0.75
Nb		0.14	0.09	0.06	0.76	0.05	0.20	0.09	0.14	0.20	0.15	0.30	0.24	0.10

		Pyrite								Pyrrhotite				
Sample		EBL 27-8	EBL 27-9	EBL 27-10	EBL 27-11	PB 32-4	PB 32-6	PB 33-17	EBL 27-7	EBL 27-31	PB 32-5	PB 32-5	PB 33-29	PB 33-20
Ni	ppm	89.88	400.61	327.36	149.02	314.38	405.02	1559.58	1357.06	650.32	503.80	641.52	84.19	669.11
S		450898	496908	535217	287000	371097	461297	473397	336066	327537	277800	325117	447772	349498
Sb		26.19	33.04	35.06	17.43	32.19	57.71	120.74	8.99	0.67	10.65	32.61	17.14	26.50
Sc		0.00	0.00	0.00	3.32	0.00	0.00	0.00	0.00	2.88	2.42	2.20	bd	0.00
Si		0	0	0	46459	0	0	0	1	2	13341	4	647	3
Sn		1.10	2.76	1.19	2.28	0.60	0.63	0.88	0.49	0.55	0.83	1.09	0.82	0.48
Cd		3.56	20.80	1.38	0.24	4.68	3.82	0.98	0.19	0.19	0.13	0.19	1.26	0.15
Cs		0.98	0.95	1.25	0.65	5.17	1.37	0.74	1.54	0.02	0.19	0.83	0.82	0.44
Pb		287.83	297.75	272.75	98.78	165.29	195.00	344.59	88.17	7.38	47.96	106.68	153.40	34.27
Hf		0.19	0.10	0.10	2.49	0.19	0.33	0.13	0.34	0.36	0.56	0.64	0.18	0.35
Rb		2.10	4.43	5.02	5.17	47.41	14.06	3.78	10.84	0.47	2.11	11.65	2.29	6.09
Ta		0.07	0.04	0.00	0.17	0.04	0.05	0.01	0.10	0.06	0.03	0.22	0.08	0.02
Th		0.38	0.25	0.08	1.71	0.19	0.29	0.14	0.28	0.21	0.37	0.32	0.45	0.41
U		0.30	0.08	0.03	0.51	0.09	0.10	0.05	0.10	0.26	0.13	0.11	0.45	0.13
W		86.19	40.71	bd	52.32	bd	bd	bd	123.05	9.20	15.33	14.04	23.36	2.29

		Black slate																	
Sample		EBL 27-6	EBL 27-16	EBL 27-32	EBL 27-33	PB 32-10	PB 32-6	PB 32-5	PB 32-4	PB 33-31	PB 34-29	PB 34-30	PB 34-33	PB 34-34	PB 35-29	PB 35-25	PB 35-21	PB 35-19	PB 36-8A	PB 36-10
Depth (m)		24	43	128	136	210	239	247	254	91	79	80	88	92	93	101	110	114	74	75
Al_2O_3	Wt. %	17.63	8.83	16.86	15.89	14.98	8.67	15.47	14.45	16.46	6.56	14.47	13.89	19.92	20.09	18.72	17.88	20.67	11.75	24.71
CaO		1.13	0.34	3.03	0.15	1.47	2.38	2.21	2.37	1.40	3.13	1.24	0.94	1.42	0.43	1.07	1.37	3.17	12.55	0.13
MgO		2.00	0.78	2.14	1.23	1.59	1.73	1.17	1.23	1.25	0.43	1.54	0.84	1.04	0.80	1.88	1.12	0.66	3.59	1.52
Na_2O		0.88	0.51	1.08	0.39	1.42	1.67	1.59	1.59	1.11	0.96	1.32	1.44	1.82	1.00	0.85	1.56	2.56	3.77	0.31
K_2O		2.96	0.77	1.59	3.17	2.45	0.72	1.67	1.44	2.79	0.51	2.94	3.05	4.72	5.67	4.86	3.89	3.34	1.73	7.46
Fe_2O_3		3.69	15.71	3.91	2.55	7.02	10.46	17.75	6.81	2.78	1.63	3.48	2.36	3.62	3.52	4.80	3.52	5.98	4.49	4.10
MnO		0.85	0.09	0.15	0.02	0.21	0.19	0.98	0.17	0.13	0.08	0.21	0.07	0.04	0.11	0.02	0.05	0.01	0.39	0.04
P_2O_5		0.05	0.04	0.06	0.05	0.05	0.03	0.05	0.06	0.04	0.02	0.04	0.04	0.05	0.07	0.02	0.05	0.03	0.19	0.07
TiO_2		0.393	0.294	0.205	0.373	0.374	0.160	0.284	0.365	0.401	0.085	0.289	0.248	0.556	0.525	0.270	0.291	0.308	0.223	0.435
Ba	ppm	170.94	122.60	99.00	306.77	434.00	66.88	218.37	192.48	446.00	215.20	398.20	385.60	632.60	673.20	947.60	744.20	826.20	131.43	1444.43
Cr		164.66	77.06	70.20	138.47	167.98	71.88	122.82	164.40	124.96	37.78	126.82	108.88	164.76	143.56	1339.80	106.20	188.78	132.29	175.87
Cu		51.80	122.18	24.77	28.53	68.84	122.86	128.47	460.54	30.80	10.76	42.70	28.08	43.74	51.34	47.08	40.86	61.08	43.01	72.75
Li		60.54	33.26	68.20	10.47	59.44	35.30	43.49	84.84	82.84	16.56	53.50	21.46	25.78	44.74	55.70	35.52	31.20	28.03	45.03
Sr		80.96	73.08	123.79	35.24	136.18	83.04	99.45	135.72	125.56	93.26	126.90	221.80	234.40	90.66	144.38	354.60	523.20	243.50	51.96
V		111.62	78.10	59.03	86.68	130.72	64.44	108.72	123.10	106.00	34.24	101.68	92.50	136.16	124.92	269.80	91.10	113.00	18.85	127.56

Black slate																				
Sample		EBL 27-6	EBL 27-16	EBL 27-32	EBL 27-33	PB 32-10	PB 32-6	PB 32-5	PB 32-4	PB 33-31	PB 34-29	PB 34-30	PB 34-33	PB 34-34	PB 35-29	PB 35-25	PB 35-21	PB 35-19	PB 36-8A	PB 36-10
Y	ppm	21.64	15.24	8.96	12.64	20.96	6.04	8.72	9.18	11.04	10.98	14.28	9.30	11.10	14.64	2.74	9.10	5.74	8.55	10.51
Zn		37.8	431.6	48.8	20.7	74.1	873.2	539.4	46.0	29.8	13.1	47.4	30.9	85.2	46.4	141.1	74.2	42.2	85.4	51.0
Zr		138.36	110.26	116.12	102.37	129.38	97.58	124.17	139.42	107.30	35.72	99.20	98.42	146.44	175.86	50.84	109.74	122.20	85.05	124.08
As		bd	28.98	137.74	47.43	39.90	156.30	bd	28.92	97.16	bd	109.50	48.00	42.14	13.58	100.68	bd	14.24	bd	bd
B		2384	1518	1366	4117	2856	4306	921	1835	2010	563	2086	3342	2364	4386	2906	2736	2442	2065	1719
Be		0.00	bd	bd	bd	0.00	bd	bd	bd	0.00	bd	0.00	0.00	0.00	0.00	0.00	0.00	0.00	bd	bd
Co		32.38	43.04	bd	bd	50.36	51.14	8.04	16.08	19.60	12.26	24.34	20.74	33.32	30.16	72.68	22.86	36.90	bd	bd
Mo		2.06	3.69	1.16	2.18	3.41	6.04	13.86	4.70	3.77	0.74	2.83	1.61	2.83	1.76	1.52	1.67	5.56	1.81	2.85
Nb		4.33	4.00	3.15	4.89	3.78	1.90	3.16	5.46	6.35	0.66	3.38	1.51	6.22	3.63	0.77	2.13	3.19	1.69	3.68
Ni		130.82	70.66	69.56	114.38	218.60	190.96	143.23	106.60	109.76	35.48	127.90	107.82	146.78	144.56	323.80	105.24	241.40	78.63	193.64
S		16162	67640	14098	7326	29660	80580	81815	30860	9142	4350	8788	6572	12380	14846	21780	15182	28480	11317	18482
Sb		2.86	45.88	4.58	3.71	1.47	24.03	25.97	7.95	9.93	1.16	2.30	1.05	1.61	1.60	19.93	4.37	5.54	2.17	1.93
Sc		15.12	14.74	10.49	12.39	16.74	12.26	21.97	14.18	13.70	3.42	13.34	12.02	17.36	17.58	52.06	13.50	16.06	6.12	18.15
Si		21279	12907	11559	5990	23259	36559	8177	14643	17145	5323	17543	28979	20039	37659	26419	22979	22539	30877	11763
Sn		1.76	3.65	0.83	1.87	2.28	2.29	5.57	2.66	3.35	1.02	2.24	1.47	2.61	1.41	2.25	1.00	2.22	0.53	2.35
Cd		0.46	2.76	0.86	0.26	0.62	5.84	4.89	0.46	1.68	0.27	1.56	0.56	2.26	1.17	3.62	1.14	1.14	0.78	2.39
Cs		11.41	8.41	3.77	3.19	4.26	7.39	7.09	5.74	10.36	1.69	14.07	5.35	8.35	8.03	14.88	8.30	8.07	4.34	11.79
Pb		21.86	108.24	51.88	15.34	35.42	111.59	72.34	51.12	38.84	18.74	31.82	28.93	42.48	13.59	86.05	31.03	76.09	15.71	13.05
Hf		4.35	3.24	2.69	2.53	4.39	3.84	3.59	4.82	5.62	1.21	4.43	2.69	5.04	4.57	2.40	3.20	5.13	2.19	3.54
Rb		151.18	92.39	78.44	151.73	100.83	84.63	116.56	92.58	194.01	20.75	170.83	104.02	187.79	169.42	307.56	155.79	159.02	66.46	309.05
Ta		0.52	0.45	13.97	20.08	0.50	0.29	0.35	0.64	0.96	0.14	0.45	0.23	0.73	0.46	0.10	0.31	0.43	9.48	14.64
Th		8.42	7.18	5.48	4.74	10.54	6.07	6.42	8.21	11.44	1.79	9.99	5.75	10.89	6.78	2.10	6.13	10.44	3.83	6.89
U		2.24	2.23	1.37	1.25	2.72	1.65	1.85	2.81	3.23	0.50	2.33	1.37	2.68	1.67	0.75	1.60	2.68	1.06	1.67
W		18.46	70.07	39.79	41.00	17.22	8.84	19.36	11.01	26.94	56.09	15.54	17.12	29.14	3.50	4.13	11.44	11.97	24.57	21.80

Siliciclastics – Sandstone and Siltstone													
Sample		EBL 28-6	EBL 28-59	BL 37-2	BL 37-1	PB 32-9	PB 34-1	PB 34-22	PB 34-38	PB 35-35	PB 35-16	PB 36-6	PB 36-12
Depth (m)		22	179	201	203	218	11	68	100	71	128	69	80
Al_2O_3	Wt. %	19.16	16.02	17.93	18.86	16.86	17.06	16.60	3.48	16.27	16.77	10.02	16.40
CaO		0.16	0.92	8.54	5.70	4.52	4.45	2.41	5.45	5.68	1.50	0.11	8.08
MgO		0.90	1.47	6.96	2.11	3.94	2.01	1.09	21.38	3.48	2.27	11.21	6.97
Na_2O		0.86	0.32	1.59	2.13	1.25	2.35	2.58	0.47	2.30	0.29	0.21	3.72
K_2O		3.18	4.14	1.45	2.30	2.20	1.62	3.43	0.01	3.37	4.39	1.60	0.43
Fe_2O_3		3.91	1.54	12.38	4.34	5.36	3.64	2.57	8.31	4.21	2.69	7.34	9.12

Siliciclastics – Sandstone and Siltstone													
Sample		EBL 28-6	EBL 28-59	BL 37-2	BL 37-1	PB 32-9	PB 34-1	PB 34-22	PB 34-38	PB 35-35	PB 35-16	PB 36-6	PB 36-12
MnO	Wt. %	0.15	0.05	0.17	0.06	0.08	0.05	0.05	0.17	0.11	0.07	0.05	0.21
P_2O_5		0.11	0.07	0.06	0.14	0.11	0.10	0.10	bd	0.12	0.10	0.06	0.46
TiO_2		0.486	0.141	0.831	0.353	0.373	0.357	0.235	0.155	0.362	0.179	0.238	0.820
Ba	ppm	176.57	227.17	277.33	674.65	263.91	351.03	1034.57	5.94	748.57	221.23	160.38	191.40
Cr		96.65	5.39	242.64	11.73	19.43	23.96	6.97	2130.46	81.40	10.19	2054.34	89.72
Cu		10.45	5.39	210.10	9.57	19.84	4.95	7.19	10.05	17.95	0.95	0.68	28.78
Li		37.11	15.47	55.73	51.26	75.90	47.83	28.45	5.32	48.11	29.74	56.23	21.19
Sr		133.12	34.36	192.24	492.54	148.54	386.72	126.17	270.12	177.01	58.72	3.54	285.08
V		87.38	15.25	294.23	51.17	59.84	42.68	28.89	95.63	71.21	23.45	82.63	198.24
Y		5.52	4.25	16.55	5.73	5.54	4.65	6.36	2.73	5.53	4.10	2.42	15.98
Zn		25.4	23.0	106.4	55.9	56.3	36.1	29.8	88.4	32.8	16.6	97.1	129.9
Zr		129.29	120.91	65.41	125.99	106.30	118.21	126.21	45.45	122.19	100.43	52.03	114.25
As		bd	bd	bd	bd	bd	bd	bd	370.04	bd	bd	970.42	bd
B		1602	954	3584	2508	2759	1299	1264	4875	1686	1377	2124	2579
Be		bd	bd	bd	bd	bd	bd	bd	bd	bd	bd	bd	bd
Co		bd	bd	bd	bd	bd	bd	bd	bd	bd	bd	bd	bd
Mo		0.21	0.40	0.15	0.21	0.41	0.28	0.13	0.44	0.21	0.17	0.32	0.14
Nb		2.20	2.40	1.85	3.27	2.45	2.93	3.53	0.48	2.15	1.72	1.28	3.44
Ni		50.56	16.83	137.76	7.94	19.23	24.16	5.79	1037.32	46.35	27.57	919.18	92.82
S		247	666	6211	1003	4000	1391	4420	712	2574	1751	375	3263
Sb		1.01	0.62	6.56	2.42	0.59	1.54	0.76	1.73	1.66	1.57	2.59	0.56
Sc		10.54	2.53	46.49	4.77	6.62	4.69	2.75	10.34	8.80	2.51	15.99	20.53
Si		16082	10201	37829	26301	28545	18212	22803	52679	18504	15099	23111	33803
Sn		0.76	0.65	0.47	0.60	0.53	0.55	0.48	0.19	1.51	0.52	0.18	0.62
Cd		0.08	0.25	0.27	0.15	0.11	0.28	0.15	0.20	0.24	0.11	0.16	0.39
Cs		3.65	5.34	5.60	8.58	7.29	10.11	9.00	0.12	8.84	5.95	16.10	5.37
Pb		12.45	6.34	11.53	26.60	9.64	17.98	17.38	3.35	30.85	10.05	bd	17.26
Hf		3.28	3.29	1.52	3.42	2.64	3.31	2.94	1.23	3.05	2.76	1.33	2.89
Rb		160.54	251.84	85.23	133.10	132.67	103.59	161.85	0.61	159.23	208.01	105.43	23.27
Ta		7.59	12.74	5.10	10.86	8.57	11.07	11.80	2.30	7.03	5.98	4.47	7.83
Th		8.21	8.80	0.14	3.62	3.19	3.38	9.30	0.07	4.59	3.41	2.01	13.81
U		1.74	2.42	0.09	1.24	0.99	1.01	3.04	0.07	0.99	0.92	0.47	2.36
W		42.59	76.10	58.40	93.57	88.79	103.81	77.05	6.03	57.78	50.56	49.60	38.70

		Komatiite			Basalt	Dyke	
Sample		PB 35-2	PB 36-1	PB 36-3	PB 35-1	BL 37-34	NGI 31-13
Depth (m)		219	50	61	233	32	
Al_2O_3	Wt. %	2.54	2.91	6.05	14.32	15.54	16.58
CaO		6.45	3.83	7.65	6.65	8.85	8.82
MgO		22.29	29.18	20.91	9.51	5.40	6.61
Na_2O		0.22	0.64	0.59	3.20	1.18	1.06
K_2O		0.01	0.01	0.02	0.35	2.92	0.74
Fe_2O_3		7.48	10.26	9.83	10.44	3.72	8.11
MnO		0.16	0.14	0.21	0.20	0.21	0.22
P_2O_5		bd	0.01	0.02	0.03	0.36	0.60
TiO_2		0.098	0.082	0.150	0.359	0.375	0.694
Ba	ppm	14.81	12.69	2.02	58.83	602.93	103.96
Cr		1143.32	3280.62	2077.22	196.59	54.30	166.57
Cu		9.24	19.40	1.91	19.84	3.81	74.47
Li		3.52	5.10	4.82	23.28	41.16	33.35
Sr		79.18	38.76	9.17	64.28	356.14	189.86
V		52.80	61.67	105.69	226.25	127.38	127.84
Y		2.63	2.39	10.46	9.35	14.82	13.99
Zn		54.3	51.5	63.4	517.1	27.9	64.2
Zr		9.22	55.00	86.37	45.89	115.96	190.12
As		bd	29.52	bd	bd	bd	11.75
B		2356	6336	5843	2508	1434	3479
Be		bd	bd	bd	bd	bd	bd
Co		bd	bd	bd	bd	bd	40.33
Mo		0.10	1.00	0.37	0.16	0.65	0.92
Nb		0.26	0.21	0.35	0.91	0.97	2.95
Ni		1090.56	1523.52	501.40	103.53	40.77	133.15
S		797	602	55	38	109	31109
Sb		0.77	13.32	1.28	0.36	1.47	0.62

		Komatiite			Basalt	Dyke	
Sample		PB 35-2	PB 36-1	PB 36-3	PB 35-1	BL 37-34	NGI 31-13
Sc	ppm	10.71	15.18	24.07	47.81	19.05	16.07
Si		34265	68321	69311	28105	15928	31981
Sn		0.15	0.23	0.25	0.46	0.52	0.95
Cd		0.23	0.07	0.22	3.15	0.35	0.23
Cs		0.14	1.63	0.17	3.23	3.79	10.72
Pb		6.08	2.41	0.91	13.34	28.79	20.10
Hf		0.19	1.27	2.02	0.93	3.00	4.59
Rb		0.76	1.08	0.65	21.00	178.58	70.38
Ta		2.17	1.88	2.65	3.53	4.43	0.26
Th		0.00	0.01	0.06	0.20	15.41	19.26
U		0.03	0.06	0.08	0.09	1.98	4.21
W		11.46	8.80	10.69	34.93	86.25	51.56

Appendix 1.2: Whole rock rare earth element geochemical data

Carbonate (unit - ppb)																
Sample	NGI 31-34	NGI 31-15	BL 38-1	BL 37-3	PB 32-1	PB 34-13	PB 34-27	PB 35-4	PB 36-8B	PB 36-11	RL-18A-C	RL-18B-C	RL-23-C	RL-24-C	HB-5	LK-11
Depth (m)	11	71	20	198	269	48	75	209	74	78	O/C	O/C	O/C	O/C	O/C	O/C
La	0.32	0.99	1.27	1.66	0.58	1.17	2.04	0.35	9.37	0.54	3.21	3.70	2.18	2.09	1.87	7.37
Ce	0.65	1.85	1.73	2.67	0.81	1.85	3.98	0.38	14.51	0.79	4.19	5.05	3.92	2.75	3.01	13.03
Pr	0.09	0.23	0.20	0.31	0.06	0.22	0.47	0.05	1.52	0.09	0.52	0.54	0.50	0.29	0.32	1.57
Nd	0.41	0.98	0.81	1.27	0.19	0.92	1.82	0.22	5.62	0.40	2.06	2.14	2.21	1.08	1.09	6.35
Sm	0.12	0.21	0.16	0.25	0.03	0.21	0.30	0.04	0.77	0.10	0.40	0.41	0.63	0.19	0.18	1.45
Eu	0.03	0.10	0.12	0.15	0.02	0.13	0.25	0.02	0.27	0.04	0.25	0.28	0.30	0.15	0.07	0.51
Gd	0.14	0.27	0.28	0.40	0.05	0.32	0.33	0.05	0.86	0.13	0.63	0.63	0.96	0.29	0.22	1.97
Tb	0.02	0.04	0.04	0.06	0.01	0.05	0.04	0.01	0.09	0.02	0.09	0.09	0.16	0.04	0.03	0.30
Dy	0.11	0.25	0.25	0.36	0.04	0.33	0.20	0.04	0.35	0.12	0.56	0.53	0.96	0.24	0.14	1.82
Ho	0.02	0.05	0.06	0.09	0.01	0.09	0.04	0.01	0.05	0.03	0.13	0.13	0.22	0.06	0.03	0.38

Carbonate (unit - ppb)																
Sample	NGI 31-34	NGI 31-15	BL 38-1	BL 37-3	PB 32-1	PB 34-13	PB 34-27	PB 35-4	PB 36-8B	PB 36-11	RL-18A-C	RL-18B-C	RL-23-C	RL-24-C	HB-5	LK-11
Er	0.06	0.16	0.17	0.28	0.03	0.31	0.13	0.04	0.14	0.07	0.41	0.40	0.71	0.20	0.08	1.18
Tm	0.01	0.02	0.03	0.04	0.00	0.04	0.02	0.01	0.02	0.01	0.06	0.05	0.10	0.03	0.01	0.17
Yb	0.06	0.14	0.13	0.23	0.02	0.30	0.11	0.03	0.09	0.07	0.33	0.34	0.65	0.17	0.07	1.12
Lu	0.01	0.02	0.02	0.04	0.00	0.06	0.02	0.01	0.01	0.01	0.05	0.06	0.11	0.03	0.01	0.18

Partial carbonate (unit - ppb)																						
Sample	RL-18A-C	HB-1	RL-18B-C	PB 36-11_	PB 35-4	RL-LI	HB-5	RL-24-C	PB 34-27	RL-23-C	LK-11	PB 36-8	NGI 31-15	BL 38-7	RL2 - 10	BL 38-1	BL 37-3	PB 32-1	PB 34-13	BL 38-7	NGI 31-34	TB -2
Depth (m)	O/C	O/C	O/C	O/C	O/C	O/C	O/C	O/C	75	bd	bd	74	71	3	O/C	20	198	269	48	3	11	O/C
La	4.85	10.86	5.02	0.50	0.41	7.80	3.53	4.81	2.16	4.01	8.33	14.28	1.40	0.65	1.15	1.55	1.67	0.63	2.01	0.69	0.21	0.90
Ce	6.99	19.60	6.91	0.37	0.23	12.20	5.58	6.38	4.39	7.69	15.20	22.09	2.17	1.07	1.62	2.09	2.70	0.74	3.20	0.94	0.34	1.66
Pr	0.77	2.06	0.75	0.04	0.03	1.26	0.57	0.64	0.52	0.95	1.76	2.31	0.26	0.12	0.17	0.24	0.31	0.08	0.41	0.10	0.04	0.19
Nd	3.18	7.48	2.96	0.14	0.12	4.51	2.03	2.42	1.97	4.32	7.28	8.20	1.06	0.44	0.64	1.00	1.25	0.28	1.75	0.38	0.16	0.76
Sm	0.62	1.51	0.57	0.02	0.02	0.83	0.32	0.42	0.32	1.27	1.91	1.12	0.21	0.08	0.09	0.19	0.24	0.05	0.40	0.07	0.03	0.20
Eu	0.36	0.49	0.40	0.02	0.02	0.24	0.14	0.37	0.29	0.66	0.78	0.38	0.15	0.07	0.04	0.16	0.15	0.03	0.22	0.07	0.02	0.07
Gd	1.00	2.37	0.92	0.05	0.06	1.30	0.41	0.72	0.38	2.15	2.97	1.23	0.30	0.12	0.16	0.32	0.38	0.08	0.67	0.11	0.05	0.26
Tb	0.14	0.47	0.13	0.01	0.01	0.22	0.05	0.10	0.05	0.36	0.48	0.12	0.05	0.02	0.02	0.04	0.06	0.01	0.11	0.01	0.01	0.04
Dy	0.87	3.60	0.80	0.04	0.05	1.48	0.26	0.59	0.22	2.32	3.02	0.46	0.27	0.10	0.14	0.26	0.32	0.06	0.70	0.08	0.04	0.29
Ho	0.19	0.99	0.19	0.01	0.01	0.36	0.05	0.15	0.05	0.52	0.66	0.06	0.06	0.02	0.03	0.06	0.08	0.01	0.19	0.02	0.01	0.06
Er	0.60	3.48	0.60	0.05	0.04	1.25	0.14	0.46	0.13	1.57	2.02	0.18	0.17	0.06	0.13	0.18	0.24	0.04	0.61	0.06	0.03	0.18
Tm	0.08	0.58	0.08	0.01	0.01	0.21	0.02	0.06	0.02	0.23	0.29	0.02	0.02	0.01	0.02	0.03	0.03	0.01	0.09	0.01	0.00	0.03
Yb	0.50	4.34	0.51	0.03	0.04	1.41	0.11	0.39	0.09	1.48	1.96	0.11	0.13	0.05	0.13	0.14	0.21	0.03	0.60	0.05	0.02	0.19
Lu	0.08	0.76	0.08	0.01	0.01	0.23	0.02	0.07	0.02	0.24	0.31	0.02	0.02	0.01	0.02	0.02	0.03	0.01	0.11	0.01	0.00	0.03

Chert (unit - ppb)							
Sample	NGI 31-14	EBL 27-88	EBL 28-1	EBL 28-7	EBL 28-28	EBL 28-31	EBL 28-44
Depth (m)	73	17	4	26	97	107	137
La	0.20	0.94	0.04	0.32	1.91	bd	0.01
Ce	0.29	1.18	0.15	0.80	3.12	bd	0.00

Chert (unit - ppb)							
Sample	NGI 31-14	EBL 27-88	EBL 28-1	EBL 28-7	EBL 28-28	EBL 28-31	EBL 28-44
Pr	0.03	0.11	bd	0.07	0.28	bd	bd
Nd	0.14	0.44	0.00	0.25	0.90	bd	0.01
Sm	0.03	0.06	0.01	0.03	0.13	bd	0.00
Eu	0.01	0.02	0.01	0.01	0.10	bd	bd
Gd	0.04	0.07	0.01	0.04	0.16	bd	0.00
Tb	0.01	0.01	0.00	0.01	0.02	bd	0.00
Dy	0.03	0.05	0.01	0.02	0.06	0.00	0.00
Ho	0.01	0.01	0.00	0.00	0.01	0.00	bd
Er	0.02	0.03	0.01	0.01	0.03	0.01	0.00
Tm	0.00	0.00	0.00	0.00	0.00	0.00	0.00
Yb	0.02	0.03	0.01	0.01	0.02	0.01	0.00
Lu	0.00	0.01	0.00	0.00	0.00	0.00	0.00

Magnetite (unit - ppb)																					
Sample	NGI 31-12	NGI 31-11	NGI 31-10	NGI 31-7	NGI 31-9	NGI 31-8	NGI 31-6	NGI 31-4	NGI 31-3	NGI 31-2	EBL 27-89	EBL 27-80	EBL 27-79	EBL 27-78	EBL 27-77	EBL 27-75	EBL 27-74	EBL 27-22	EBL 27-62	EBL 27-30	EBL 29-44
Depth (m)	82	86	88	98	91	95	103	109	119	122	12	47	50	57	59	74	77	80	124	125	45
La	0.30	4.93	2.49	1.53	2.50	3.73	4.47	0.63	1.86	6.19	0.90	3.04	2.14	3.54	2.16	6.00	2.61	8.99	2.50	0.19	0.26
Ce	0.63	9.99	5.02	3.08	5.36	6.74	9.48	1.39	3.81	12.79	1.54	5.62	4.22	6.98	4.27	9.29	4.69	17.02	4.41	0.41	0.43
Pr	0.08	1.21	0.62	0.38	0.63	0.77	1.20	0.19	0.46	1.55	0.19	0.66	0.51	0.83	0.54	1.06	0.55	2.07	0.54	0.05	0.04
Nd	0.40	5.03	2.66	1.58	2.62	3.17	4.92	1.06	2.07	6.36	0.91	2.74	2.31	3.40	2.33	4.41	2.26	8.71	2.70	0.27	0.22
Sm	0.17	1.16	0.63	0.40	0.56	0.71	1.03	0.30	0.55	1.43	0.21	0.58	0.65	0.70	0.49	0.93	0.48	2.09	1.10	0.11	0.06
Eu	0.11	0.82	0.43	0.23	0.36	0.50	0.40	0.19	0.26	1.03	0.14	0.30	0.38	0.34	0.30	0.55	0.23	1.23	0.74	0.04	0.03
Gd	0.39	1.74	1.00	0.57	0.75	1.09	1.20	0.57	0.98	1.82	0.26	0.82	1.01	0.93	0.88	1.36	0.62	2.95	1.76	0.22	0.10
Tb	0.08	0.28	0.18	0.09	0.11	0.17	0.16	0.09	0.17	0.27	0.04	0.13	0.16	0.15	0.17	0.19	0.08	0.43	0.30	0.05	0.02
Dy	0.68	1.72	1.17	0.57	0.67	1.12	0.77	0.61	1.03	1.50	0.20	0.81	1.05	0.94	1.21	1.14	0.42	2.36	1.88	0.33	0.13
Ho	0.18	0.39	0.28	0.13	0.15	0.26	0.15	0.15	0.22	0.33	0.04	0.19	0.24	0.22	0.31	0.26	0.08	0.49	0.41	0.07	0.03
Er	0.57	1.20	0.91	0.46	0.53	0.84	0.46	0.50	0.69	1.09	0.13	0.62	0.83	0.72	1.05	0.82	0.26	1.46	1.27	0.20	0.11
Tm	0.09	0.20	0.15	0.07	0.08	0.13	0.07	0.08	0.10	0.19	0.02	0.09	0.14	0.11	0.17	0.12	0.04	0.21	0.18	0.03	0.02
Yb	0.59	1.26	1.02	0.45	0.62	0.86	0.58	0.53	0.65	1.39	0.15	0.64	0.96	0.81	1.09	0.80	0.30	1.48	1.12	0.23	0.12
Lu	0.10	0.21	0.18	0.08	0.11	0.15	0.11	0.09	0.11	0.24	0.03	0.11	0.17	0.15	0.18	0.14	0.05	0.25	0.19	0.04	0.02

Magnetite (unit - ppb)																					
Sample	EBL 29-45	EBL 29-46	EBL 29-49	PB 32-23	PB 32-18	PB 34-3	PB 34-18	PB 34-21	PB 34-25	PB 34-27A	PB 35-44	PB 35-43	BL 37-41	BL 37-40	BL 38-4	EBL 28-4	RL-18A-M	RL-18B-M	RL-23-M	RL-24-M	BLO-1
Depth (m)	46	48	52	138	168	14	63	66	72	75	32	40	10.5	11	14	17	O/C	O/C	O/C	O/C	O/C
La	0.82	2.69	0.48	0.29	1.64	0.25	1.34	3.11	0.39	1.37	0.38	3.20	0.85	0.22	0.34	5.96	2.47	0.49	4.95	1.21	3.79
Ce	1.11	3.55	1.02	0.40	1.61	0.42	2.01	5.11	0.55	2.30	0.58	5.50	1.19	0.23	0.34	11.15	3.32	0.73	9.58	1.50	7.76
Pr	0.11	0.37	0.11	0.04	0.15	0.04	0.25	0.58	0.06	0.26	0.07	0.59	0.12	0.03	0.03	1.33	0.34	0.08	1.18	0.16	0.92
Nd	0.50	1.60	0.49	0.14	0.52	0.17	1.04	2.36	0.24	1.07	0.26	2.13	0.55	0.12	0.12	5.54	1.33	0.29	4.84	0.65	3.99
Sm	0.10	0.27	0.11	0.03	0.07	0.03	0.20	0.46	0.05	0.25	0.05	0.32	0.10	0.03	0.02	1.36	0.25	0.06	1.21	0.12	0.88
Eu	0.04	0.10	0.04	0.01	0.03	0.02	0.10	0.30	0.02	0.16	0.02	0.13	0.05	0.01	0.02	0.60	0.14	0.03	0.53	0.06	0.53
Gd	0.15	0.36	0.14	0.04	0.12	0.04	0.30	0.62	0.06	0.37	0.07	0.38	0.14	0.04	0.03	2.00	0.38	0.07	1.68	0.18	1.13
Tb	0.03	0.05	0.02	0.01	0.02	0.01	0.05	0.09	0.01	0.06	0.01	0.05	0.02	0.01	0.01	0.35	0.06	0.01	0.29	0.03	0.18
Dy	0.16	0.31	0.15	0.03	0.10	0.03	0.29	0.54	0.07	0.40	0.07	0.26	0.10	0.04	0.03	2.24	0.39	0.07	1.79	0.16	1.11
Ho	0.04	0.07	0.03	0.01	0.03	0.01	0.07	0.13	0.02	0.10	0.02	0.06	0.02	0.01	0.01	0.50	0.10	0.02	0.39	0.04	0.26
Er	0.14	0.24	0.13	0.03	0.09	0.03	0.23	0.42	0.07	0.34	0.06	0.18	0.09	0.03	0.02	1.52	0.35	0.05	1.21	0.13	0.89
Tm	0.02	0.04	0.02	0.00	0.01	0.01	0.03	0.06	0.02	0.05	0.01	0.03	0.01	0.01	0.00	0.21	0.06	0.01	0.17	0.02	0.15
Yb	0.16	0.27	0.13	0.03	0.08	0.04	0.20	0.44	0.08	0.37	0.07	0.17	0.10	0.03	0.02	1.38	0.38	0.06	1.07	0.13	1.07
Lu	0.03	0.04	0.03	0.01	0.02	0.01	0.03	0.08	0.02	0.07	0.01	0.03	0.02	0.01	0.01	0.23	0.07	0.01	0.15	0.02	0.19

Pyrite (unit - ppb)								Pyrrhotite (unit - ppb)					
Sample	EBL 27-8	EBL 27-9	EBL 27-10	EBL 27-11	PB 32-4	PB 32-6	PB 33-17	EBL 27-7	EBL 27-31	PB 32-5	PB 32-5	PB 33-29	PB 33-20
La	6.21	1.28	1.13	4.89	1.46	1.79	0.84	1.94	4.27	0.87	1.31	5.48	0.97
Ce	12.57	2.41	2.31	10.10	2.86	3.32	1.54	3.71	6.59	1.83	2.57	10.59	1.94
Pr	1.39	0.27	0.24	1.22	0.32	0.36	0.16	0.40	0.72	0.22	0.29	1.15	0.22
Nd	5.22	1.05	0.85	5.11	1.14	1.39	0.56	1.48	2.88	0.85	1.11	4.18	0.90
Sm	1.07	0.20	0.11	1.10	0.22	0.28	0.08	0.29	0.51	0.18	0.22	0.84	0.18
Eu	0.21	0.06	0.03	0.29	0.03	0.06	0.02	0.07	0.23	0.07	0.05	0.20	0.08
Gd	1.16	0.25	0.11	1.05	0.22	0.32	0.10	0.34	0.67	0.23	0.23	0.86	0.20
Tb	0.15	0.03	0.01	0.13	0.02	0.04	0.01	0.05	0.09	0.03	0.03	0.11	0.02
Dy	0.84	0.17	0.05	0.62	0.11	0.19	0.05	0.27	0.48	0.17	0.13	0.54	0.12
Ho	0.17	0.03	0.01	0.12	0.02	0.03	0.01	0.05	0.10	0.03	0.02	0.10	0.02
Er	0.49	0.09	0.03	0.46	0.05	0.09	0.03	0.16	0.28	0.10	0.07	0.27	0.07
Tm	0.07	0.01	0.01	0.07	0.01	0.01	0.00	0.03	0.04	0.01	0.01	0.04	0.01
Yb	0.37	0.07	0.03	0.60	0.06	0.10	0.03	0.15	0.27	0.11	0.09	0.22	0.07
Lu	0.05	0.01	0.00	0.11	0.01	0.02	0.01	0.02	0.04	0.02	0.02	0.04	0.01

Black slate (unit - ppb)																			
Sample	EBL 27-6	EBL 27-16	EBL 27-32	EBL 27-33	PB 32-10	PB 32-6	PB 32-5	PB 32-4	PB 33-31	PB 34-29	PB 34-30	PB 34-33	PB 34-34	PB 35-29	PB 35-25	PB 35-21	PB 35-19	PB 36-8A	PB 36-10
Depth (m)	24	43	128	136	210	239	247	254	91	79	80	88	92	93	101	110	114	74	75
La	19.92	35.19	10.49	40.15	18.27	13.99	14.58	13.93	22.72	2.46	13.16	16.16	21.25	21.54	7.45	13.88	23.89	12.74	25.24
Ce	39.51	72.57	20.10	72.75	38.08	26.96	29.01	28.22	46.39	4.96	27.93	32.02	42.49	43.77	14.16	27.89	45.74	25.22	52.02
Pr	4.49	8.56	2.21	8.29	4.50	3.12	3.30	3.21	5.41	0.55	3.33	3.69	4.88	4.99	1.61	3.20	5.10	2.77	5.86
Nd	16.88	32.66	8.06	30.72	17.47	11.88	12.79	12.24	20.63	1.98	12.96	13.72	18.30	18.86	6.19	12.22	18.81	10.23	22.30
Sm	3.50	6.60	1.67	4.86	3.75	2.31	2.59	2.41	4.33	0.37	2.94	2.58	3.48	3.51	1.14	2.39	3.28	1.78	4.04
Eu	1.22	1.84	0.73	0.76	1.13	0.74	0.99	1.18	1.45	0.20	1.01	0.80	1.04	0.87	0.65	0.78	1.38	0.54	1.25
Gd	4.51	6.69	1.96	5.05	4.49	2.45	2.81	2.65	4.89	0.38	3.58	2.69	3.62	3.66	1.16	2.49	3.03	1.99	3.98
Tb	0.68	0.79	0.27	0.55	0.70	0.30	0.34	0.35	0.69	0.05	0.60	0.34	0.48	0.49	0.15	0.32	0.34	0.27	0.50
Dy	3.94	3.74	1.51	2.45	4.10	1.52	1.67	1.94	3.70	0.29	3.72	1.69	2.50	2.52	0.72	1.63	1.52	1.49	2.35
Ho	0.80	0.68	0.30	0.43	0.82	0.28	0.31	0.38	0.70	0.06	0.77	0.31	0.45	0.47	0.14	0.32	0.28	0.30	0.44
Er	2.41	2.12	0.87	1.25	2.54	0.86	0.94	1.23	2.11	0.20	2.27	0.94	1.44	1.48	0.48	0.97	0.91	0.89	1.29
Tm	0.35	0.31	0.12	0.17	0.36	0.13	0.14	0.20	0.31	0.03	0.32	0.14	0.22	0.22	0.08	0.15	0.15	0.13	0.18
Yb	2.28	2.18	0.85	1.14	2.56	0.98	1.14	1.49	2.08	0.22	2.14	0.97	1.54	1.46	0.53	1.03	1.10	0.89	1.32
Lu	0.36	0.35	0.13	0.17	0.43	0.18	0.21	0.26	0.33	0.04	0.34	0.16	0.26	0.24	0.09	0.17	0.19	0.14	0.22

Siliciclastics-Sandstone and Siltstone (unit - ppb)												
Sample	EBL 28-6	EBL 28-59	BL 37-2	BL 37-1	PB 32-9	PB 34-1	PB 34-22	PB 34-38	PB 35-35	PB 35-16	PB 36-6	PB 36-12
Depth (m)	22	179	201	203	218	11	68	100	71	128	69	80
La	16.59	21.86	2.22	17.35	10.36	15.38	14.80	1.34	13.98	18.62	5.89	71.01
Ce	33.94	36.31	6.54	35.26	21.31	29.85	27.19	2.99	28.39	40.20	12.50	144.69
Pr	3.91	3.47	1.01	4.15	2.47	3.24	2.87	0.37	3.17	4.61	1.38	17.04
Nd	14.94	11.47	5.35	16.02	9.41	11.86	10.32	1.72	11.76	16.96	5.12	64.45
Sm	2.53	1.73	1.79	2.75	1.65	1.96	1.73	0.44	1.98	2.46	0.86	9.14
Eu	0.68	0.53	0.63	1.10	0.62	0.69	0.80	0.17	0.86	0.69	0.21	2.61
Gd	2.25	1.79	2.56	2.61	1.73	2.01	1.78	0.59	2.03	2.17	0.84	8.24
Tb	0.25	0.19	0.46	0.30	0.22	0.24	0.22	0.10	0.25	0.23	0.10	0.87
Dy	1.11	0.83	2.98	1.38	1.11	1.06	1.15	0.63	1.22	0.96	0.48	3.67
Ho	0.20	0.14	0.61	0.22	0.20	0.19	0.21	0.13	0.21	0.16	0.09	0.61
Er	0.58	0.39	1.71	0.64	0.58	0.51	0.64	0.41	0.61	0.47	0.27	1.82

Siliciclastics-Sandstone and Siltstone (unit - ppb)												
Sample	EBL 28-6	EBL 28-59	BL 37-2	BL 37-1	PB 32-9	PB 34-1	PB 34-22	PB 34-38	PB 35-35	PB 35-16	PB 36-6	PB 36-12
Tm	0.08	0.05	0.25	0.08	0.08	0.07	0.10	0.07	0.09	0.06	0.04	0.23
Yb	0.54	0.35	1.56	0.57	0.53	0.44	0.65	0.43	0.56	0.42	0.29	1.55
Lu	0.09	0.06	0.24	0.09	0.08	0.07	0.11	0.07	0.08	0.06	0.05	0.23

	Komatiite (unit - ppb)			Basalt (unit - ppb)	Dyke (unit - ppb)	
Sample	PB 35-2	PB 36-1	PB 36-3	PB 35-1	BL 37-34	NGI 31-13
Depth (m)	219	50	61	233	32	
La	0.64	0.53	0.69	1.77	81.04	60.17
Ce	1.57	1.08	2.22	4.05	164.39	127.33
Pr	0.22	0.15	0.44	0.56	20.23	16.04
Nd	1.10	0.69	2.67	2.71	77.67	62.22
Sm	0.35	0.21	1.15	0.84	10.80	9.23
Eu	0.14	0.09	0.14	0.32	2.56	2.13
Gd	0.49	0.33	1.64	1.19	9.31	7.99
Tb	0.09	0.06	0.29	0.22	0.93	0.84
Dy	0.57	0.43	1.90	1.52	3.49	3.28
Ho	0.12	0.10	0.40	0.34	0.53	0.52
Er	0.34	0.30	1.15	1.07	1.54	1.55
Tm	0.05	0.05	0.18	0.16	0.18	0.19
Yb	0.34	0.30	1.16	1.13	1.17	1.24
Lu	0.05	0.05	0.18	0.18	0.18	0.19

Appendix 1.3: $\delta^{34}S$ isotope and multiple sulfur isotopes data

$\delta^{34}S$ isotope analysis (G.G.Hatch Lab, Ottawa)		
Sample ID	**$\delta^{34}S$ vcdt ‰**	**S %**
EBL 27-6	5.3	1.3
EBL 27-7	3.0	17.6
EBL 27-8	-1.1	42.6
EBL 27-9	2.5	27.4
EBL 27-10	-1.2	46.6
EBL 27-11	-7.5	31.8
EBL 27-12	0.4	32.5
EBL 27-18	1.1	11.6
EBL 27-19	0.6	13.7
EBL 27-22	1.1	7.6
EBL 27-24	0.6	11.1
EBL 27-30	2.6	2.2
EBL 27-32	-1.5	1.2
EBL 27-33	5.4	0.7
PB 32- 3	-1.4	24.8
PB 32- 4	-0.6	2.9
PB 32- 5	0.2	30.3
PB 32- 6	2.8	10.1
PB 32- 10	4.3	2.8
PB 33-17	-4.5	13.9
PB 33-18	-3.9	12.4
PB 33-25	0.1	24.5
PB 33-31	0.1	1.0
PB 34-29	1.2	0.5
PB 34-30	3.6	1.1
PB 34-33	4.1	0.8

$\delta^{34}S$ isotope analysis (G.G.Hatch Lab, Ottawa)		
Sample ID	**$\delta^{34}S$ vcdt ‰**	**S %**
PB 34-34	5.4	1.3
PB 35-9	1.0	27.9
PB 35-19	5.8	3.1
PB 35-21	3.8	1.5
PB 35-25	7.3	2.4
PB 35-28	6.2	15.4
PB 35-29	4.8	1.5

Multiple sulfur isotopes analysis (European Institute for Marine Studies, France)			
Sample name	**$\Delta^{33}S$ ‰**	**$\Delta^{36}S$ ‰**	**$\delta^{34}S$ vs CDT ‰**
27-8-Py-CRS	-0.061	-0.60	-1.69
27-9-Py-CRS	1.200	-2.44	3.45
27-10-Py-CRS	-0.652	-0.10	-2.82
27-11-Py-CRS	-0.353	-0.16	-7.63
27-16-Py-CRS	0.441	-1.07	-0.52
32-4-Py-CRS	0.332	-0.74	1.47
33-17-Py-CRS	-0.417	-0.30	-8.83
33-29-Py-CRS	-0.332	0.22	-3.49
27-31-Po-AVS	-0.033	-0.22	3.85
32-5-Po-AVS	0.137	-0.56	0.36

Appendix 1.4: Organic carbon isotope data - European Institute for Marine Studies, France

Sample ID	δ ^{13}C ‰ VPDB	TOC %
PB32-03	-27.61	0.07
PB32-04	-25.08	5.38
PB32-06	-24.44	4.93
PB32-10	-21.20	4.35
PB33-17	-21.70	2.40
PB33-25	-27.99	0.16
PB33-31	-22.42	3.55
PB34-29	-19.15	1.30
PB34-30	-18.98	3.71
PB34-33	-21.19	2.34
PB34-34	-21.41	3.16
PB35-09	-24.90	0.15
PB35-19	-23.47	2.31
PB35-21	-23.93	2.81
PB35-25	-23.40	1.57
PB35-28	-22.64	1.61
PB35-29	-22.95	2.72
EBL27-06	-28.91	3.35
EBL27-07	-29.37	2.54
EBL27-09	-30.15	3.24
EBL27-12	-30.03	0.64
EBL27-16	-26.70	4.65
EBL27-18	-18.77	1.37
EBL27-19	-17.76	2.66
EBL27-24	-21.15	1.88
EBL27-32	-20.39	1.69
EBL27-33	-19.78	2.57

Appendix 1.5: Inorganic carbon and oxygen isotopes data – European Institute for Marine Studies, France and G.G.Hatch Lab, Ottawa

Inorganic carbon isotope analysis (European Institute for Marine Studies, France)		
Sample ID	**$\delta^{13}C$ VPDB ‰**	**$\delta^{18}O$ VPDB ‰**
BL 37-3	-0.03	-15.36
BL 38-1	-0.24	-15.11
BL 38-7	-0.61	-14.21
PB 32-1	-0.29	-14.83
NGI 31-15	-0.66	-14.96
NGI 31-34	0.62	-13.63
PB 34-13	-1.06	-11.38
PB 36-8B	-3.53	-9.36
PB 34-27B	-0.70	-13.24
PB 35-4	0.60	-10.85
PB 36-11	-0.03	-14.25
RL-Li	0.67	-11.99
LK-11	0.51	-13.15
MRL-18A	0.95	-12.27
MRL-23	0.69	-13.55
RL2-10	-2.43	-13.66
HB-5	-0.14	-13.54
TB-2	-2.70	-14.19

Inorganic carbon isotope analysis (G.G. Hatch Lab, Ottawa)		
Sample ID	**$\delta^{13}C$ VPDB ‰**	**$\delta^{18}O$ VPDB ‰**
MRL-18B	1.1	-11.0
MRL-21	-0.1	-13.4
MRL-23A	1.2	-12.2
MRL-24	0.7	-13.2
MRL-S	0.3	-13.3
MRL-S1	-0.8	-13.7
HB-1	0.2	-13.5
LK-6A	0.9	-11.6

Appendix 1.6: CNS analysis- Lakehead university instrumentation lab

Sample	N%	C%	S%
EBL27-6	0.06	3.47	1.60
EBL27-7	0.08	1.51	17.34
EBL27-8	0.06	1.24	42.30
EBL27-9	0.07	3.30	28.22
EBL27-10	0.06	0.48	48.15
EBL27-11	0.05	0.16	35.55
EBL27-12	0.07	0.33	37.39
EBL27-16	0.05	4.02	7.04
EBL27-18	0.07	1.55	12.16
EBL27-19	0.02	1.71	14.64
EBL27-22	0.03	0.06	7.76
EBL27-24	0.05	1.60	11.93
EBL27-30	0.06	0.25	2.68
EBL27-32	0.07	1.38	1.41
EBL27-33	0.05	2.08	0.80
EBL27-81	0.06	4.65	17.64
EBL28-4	0.06	0.14	2.66
PB32-3	0.04	0.07	25.69
PB32-4	0.04	4.97	3.29

Sample	N%	C%	S%
PB32-5	0.06	0.56	33.47
PB32-6	0.07	5.12	11.08
PB32-10	0.05	4.44	3.23
PB33-17	0.04	2.34	13.99
PB33-18	0.05	0.58	12.11
PB33-25	0.04	1.74	24.87
PB33-29	0.03	0.18	26.83
PB33-31	0.04	3.66	1.79
PB34-29	0.04	1.50	0.67
PB34-30	0.05	4.09	1.22
PB34-33	0.07	2.44	1.00
PB34-34	0.05	3.33	1.32
PB35-9	0.07	0.23	25.35
PB35-19	0.03	2.22	5.02
PB35-21	0.05	2.87	2.19
PB35-25	0.06	1.89	2.73
PB35-28	0.06	2.73	15.37
PB35-29	0.06	2.62	1.92
PB36-8	0.06	4.06	1.13
PB36-10	0.06	1.34	1.76